HAL
open science

Numerical study of pump-turbine instabilities : pumping mode off-design conditions

Uroš Ješe

To cite this version:

Uroš Ješe. Numerical study of pump-turbine instabilities : pumping mode off-design conditions. Fluids mechanics [physics.class-ph]. Université Grenoble Alpes, 2015. English. NNT : 2015GREAI090 . tel-01272738

HAL Id: tel-01272738

https://theses.hal.science/tel-01272738v1

Submitted on 23 Feb 2016

HAL is a multi-disciplinary open access archive for the deposit and dissemination of scientific research documents, whether they are published or not. The documents may come from teaching and research institutions in France or abroad, or from public or private research centers.

L'archive ouverte pluridisciplinaire **HAL**, est destinée au dépôt et à la diffusion de documents scientifiques de niveau recherche, publiés ou non, émanant des établissements d'enseignement et de recherche français ou étrangers, des laboratoires publics ou privés.

UNIVERSITÉ GRENOBLE ALPES

THÈSE

Pour obtenir le grade de

DOCTEUR DE L'UNIVERSITÉ GRENOBLE ALPES

Spécialité : **Mécanique des fluides, Procédés, Énergétique**

Arrêté ministériel : 7 août 2006

Présentée par

Uroš JEŠE

Thèse dirigée par **Regiane FORTES-PATELLA**
et codirigée par **Matevž DULAR**

préparée au sein du **Laboratoire des Ecoulements Géophysiques et Industriels (LEGI)**
et de **l'École Doctorale I-MEP2**

Numerical study of pump-turbine instabilities: Pumping mode off-design conditions

Thèse soutenue publiquement le **13/11/2015**,
devant le jury composé de :

M, Stéphane AUBERT
Prof., EC Lyon, Président du jury
M, François AVELLAN
Prof., EPFL (Switzerland), Rapporteur
M, Antoine DAZIN
Maître de conférences, ENSAM Lille, Rapporteur
Mme, Regiane FORTES-PATELLA
Prof., Grenoble-INP, Directrice de thèse
M, Matevž DULAR
Assoc. Prof., University of Ljubljana (Slovenia), Codirecteur de thèse

Acknowledgements

Presented PhD study wouldn't be possible without my supervisors Prof. Regiane Fortes-Patella and Asst. Prof. Matevž Dular. Funding has been provided by Slovene Human Resources Development and Scholarship Fund and Laboratory for Geophysical and Industrial Flows (LEGI).

I would like to start my thankyou-list with Regiane Fortes-Patella. Not only that she was the best scientific supervisor one could only wish for, she was much more than that to me. When I came to France, I couldn't speak any French (except merci, oui, non, bonjour and maybe a few words more). She helped me with the assimilation, she has been honestly concerned about how I feel and if I'm happy in Grenoble...and it meant a lot to me. She was supportive, honest, fair and enthusiastic during the whole studies. I really appreciated all the discussions related or not related to the PhD work. As I said, much more than just a supervisor. Thank you, Regiane.

I would like to thank also my thesis co-director Matevž Dular. He introduced me to scientific work during my master studies and he shared with me important comments, suggestions and views during my PhD thesis. Moreover, he showed me that science can be very funny and very interesting as well as the life of a scientist. Without him, I probably wouldn't start my PhD studies. Thank you, Matevž.

Beside my supervisors, I need to thank also the other members of the thesis jury: Prof. Stéphane Aubert, Prof. François Avellan and Assoc. Prof. Antoine Dazin for their remarks, opinions, demanding question and most of all for the interesting and indepth debate during the thesis defence. Thank you.

Next ones on the list are all my friends from LEGI and from Grenoble. You know exactly who you are. Because of you, I really enjoyed my 3 years in Grenoble. I loved playing football for LEGI team and drinking coffee in LEGI cafeteria. I loved spending time outside in the mountains and I enjoyed Grenoble city life, especially on Friday or Saturday evenings. We spent incredible time together. Without all of you, my life would be so much emptier. Thank you, all.

Finally, I would like to thank also my dearest. Firstly, Tina, that supported me three years from another country and spent hours and days during these years on visiting Grenoble. As a consequence, I need to thank Gaia that didn't cry the night before the thesis defense...quite an achievement for a 6 weeks old baby. Thank you.

Some of you know the story about Schrödinger's cat (named after Erwin Schrödinger, quantum physicist). It's a thought experiment, so no actual cats have been injured during the experiment. The experiment setup contains a cat that is placed in a sealed box along with a radioactive sample, a Geiger counter and a bottle of poison. If the Geiger counter detects that the radioactive material has decayed, it will trigger the smashing of the bottle of poison and the cat will be killed. If radioactive material could have simultaneously decayed and not decayed in the sealed environment (according to Copenhagen interpretation), then it follows the cat too is both alive and dead until the box is opened. It is a

bit similar to the PhD work, since the PhD work is a process and is validated only at the end with the PhD defense. Therefore, we can not know during the process what will be the output of the work. I believe that it is worth trying, despite all the uncertainties of the work and unknown results. It is why I love science, because of the process, because I like to be curious and sometimes even uncertain. However, now, at the end, when the box is opened, I'm still very happy that to see that the cat is alive. If by any coincidence, any younger PhD students will read this text, I could offer an advise. Stay curious, keep moving forward and never forget why you started with this uncertain period of your life.

Abstract

Flexibility and energy storage seem to be the main challenges of the energy industry at the present time. Pumped Storage Power Plants (PSP), using reversible pump-turbines, are among the most cost-efficient solutions to answer these needs. To provide a rapid adjustment to the electrical grid, pump-turbines are subjects of quick switching between pumping and generating modes and to extended operation under off-design conditions. To maintain the stability of the grid, the continuous operating area of reversible pump-turbines must be free of hydraulic instabilities.

Two main sources of pumping mode instabilities are the presence of the cavitation and the rotating stall, both occurring at the part load. Presence of cavitation can lead into vibrations, loss of performance and sometimes erosion. Moreover, due to rotating stall that can be observed as periodic occurrence and decay of recirculation zones in the distributor regions, the machine can be exposed to uncontrollable shift between the operating points with the significant discharge modification and the drop of the efficiency. Both phenomena are very complex, three-dimensional and demanding for the investigation. Especially rotating stall in the pump-turbines is poorly addressed in the literature. First objective of the presented PhD study has been to develop the cost-efficient numerical methodology in order to enable the accurate prediction and analysis of the off-design part load phenomena.

The investigations have been made on the reduce-scaled high head pump-turbine design ($n_q = 27$) provided by Alstom Hydro. Steady and unsteady numerical calculations have been performed using code FINE/Turbo^{TM} with barotropic cavitation model implemented and developed before in the laboratory. Some of the numerical results have been compared to the experimental data. Cavitating flow analysis has been made for various flow rates and wide range of cavitation levels. Flow investigation has been focused on the cavitation influence on the flow behavior and on the performance of the machine. Main analyses include incipient cavitation values, head drop curves and cavitation forms prediction for wide ranges of flow rates and NPSH values. Special attention has been put on the interaction between cavitation forms and the performance drop (hump zone) caused by the rotating stall. Cavitation results showed good agreement with the provided experimental data.

Second part of the thesis has been focused on the prediction and analysis of the rotating stall flow patterns. Computationally fast steady simulations have been presented and used to predict stable and unstable operating regions. The analyses have been done on 4 different guide vanes openings and 2 guide vanes geometries. In order to get detailed information about the unsteady flow patterns related to the rotating stall, more exact unsteady simulations have been performed. Local flow study has been done to describe in details the governing mechanisms of the rotating stall. The analyses enable the investigations of the rotating stall frequencies, number of stalled cells and the intensity of the rotating stall. Moreover, the unsteady calculations give very good prediction of the pump-turbine performance for both, stable and unstable operating regions. Numerical results

give very good qualitative and quantitative agreement with the available experimental data.

The approach appears to be very reliable, robust and precise. Even though the numerical results (rotating stall frequencies, number of cells...) on the actual geometry should be confirmed experimentally, author believes that the methodology could be used on any other pump-turbine (or centrifugal pump) geometry. Moreover, the simulations can be used industrially to study the effects of the guide vanes geometries, guide vanes opening angles and influence of the gap between the impeller and the distributor in order to reduce or even eliminate the negative effects of the rotating stall.

Keywords: Pump-turbine, Instabilities, CFD, Rotating Stall, Cavitation, Hump zone, Off-design, Part load

Résumé

Actuellement, la flexibilité et le stockage de l'énergie sont parmi les principaux défis de l'industrie de l'énergie. Les stations de transfert d'énergie par pompage (STEP), en utilisant des turbines-pompes réversibles, comptent parmi les solutions les plus rentables pour répondre à ces besoins. Pour assurer un réglage rapide du réseau électrique, les turbines-pompes sont sujettes à de rapides changements entre modes pompage et turbinage. Elles sont souvent exposées à un fonctionnement prolongé dans des conditions hors nominal. Pour assurer la stabilité du réseau, la zone d'exploitation continue de turbines-pompes réversibles doit être libre de toute instabilité hydraulique.

Deux sources principales d'instabilités en mode pompage peuvent limiter la plage de fonctionnement continu. Il s'agit de la présence de cavitation et de décollement tournant, tous deux survenant à charge partielle. La cavitation peut conduire à des vibrations, des pertes de performance et parfois même à l'érosion de la turbine-pompe. En outre, en raison de décollements tournants (apparition et décomposition périodique de zones de recirculation dans les régions du distributeur), la machine peut être exposée à un changement incontrôlable entre les points de fonctionnement, avec une modification de charge et une baisse significative des performances. Les deux phénomènes sont très complexes, tridimensionnels et délicats à étudier. Surtout le phénomène de décollement tournant dans les turbines-pompes est peu abordé dans la littérature. Le premier objectif de l'étude du doctorat présenté a été d'utiliser un code numérique, testé au laboratoire, et de développer une méthodologie de calcul pour permettre la prévision des phénomènes à charge partielle.

L'étude a été faite sur une géométrie à échelle réduite d'une turbine-pompe de haute chute ($n_q = 27$) fournie par Alstom Hydro. Des calculs numériques ont été effectués en utilisant le code FINE/Turbo^{TM} avec le modèle de cavitation barotrope qui a été développé au laboratoire. L'analyse des écoulements cavitants a été faite pour des débits et de niveaux de cavitation différents. Les principales analyses portent sur des valeurs naissantes de cavitation, des courbes de chute de performance et sur la prédiction des formes de cavitation pour différents débits et valeurs de NPSH. Une attention particulière a été portée sur l'interaction entre les formes de cavitation à l'entrée de la roue et la baisse de performance (zone de feston), causée par le décollement tournant qui apparaît dans la région du distributeur. Les résultats numériques ont montré un bon accord avec les données expérimentales disponibles.

La deuxième partie de la thèse a concerné la prédiction et l'analyse de décollements tournants. Des simulations ont été utilisées pour prédire les régions d'exploitation stables et instables de la machine. La méthodologie mentionnée pourrait fournir des résultats globaux précis pour différents points de fonctionnement avec un faible coût de calcul.

Afin d'obtenir des informations détaillées sur les écoulements instables, des simulations instationnaires plus précises ont été réalisées. L'analyse locale des écoulements a permis la description des mécanismes gouvernant le phénomène de décollement tournant. Les

analyses permettent l'étude du nombre, de l'intensité et des fréquences de rotation des cellules tournants. En outre, les calculs instationnaires donnent une très bonne prédiction de la performance de la turbine-pompe.

L'approche proposée est fiable, robuste et précise. La méthodologie de calcul proposée peut être utilisée sur plusieurs géométries de turbine-pompe (ou pompe centrifuge), pour une large gamme de débits et de géométries de directrices. Les simulations proposées peuvent être utilisées à l'échelle industrielle pour étudier les effets de géométrie, d'angles d'ouverture de directrices ou de l'influence du jeu entre la roue et le distributeur afin de réduire ou même éliminer les effets négatifs des décollements tournants.

Mots-clés: Turbine-pompe, Instabilitiés, CFD, Décollement tournant, Feston, Cavitation, Hors nominal, Charge partielle

Contents

I Introduction **1**

1 Overview **3**
1.1 Energy industry . . . 3
1.2 Pumped-storage power plants (PSP) . . . 5
1.3 Reversible pump-turbine . . . 7
1.4 Pumping mode instabilities . . . 7
1.4.1 Centrifugal pump characteristic . . . 7
1.4.2 Part load flows in centrifugal pumps . . . 10
1.4.3 Flow separation and rotating stall . . . 11
1.4.4 Hump shaped performance curve . . . 12
1.5 Cavitation . . . 14
1.5.1 History of cavitation . . . 15
1.5.2 Cavitation origins . . . 15
1.5.3 Hydrodynamic cavitation . . . 16
1.5.4 Non-dimensional parameters . . . 18
1.5.5 Cavitation in turbines . . . 18
1.5.6 Cavitation in pumps . . . 21
1.6 Numerical simulation overview . . . 24
1.6.1 CFD approaches . . . 25
1.6.2 CFD tradition in LEGI . . . 26
1.7 Thesis objectives . . . 26
1.8 Document organization . . . 27

II Tools and Methodology **29**

2 Physical and numerical modeling **31**
2.1 Navier-Stokes' equations . . . 32
2.1.1 Unsteady RANS . . . 33
2.2 Turbulence modeling . . . 33
2.2.1 Turbulence model $k - \epsilon$ . . . 34
2.2.2 Turbulence model $k - \omega$ . . . 35
2.3 Cavitation modeling . . . 35
2.3.1 Homogeneous approach . . . 35
2.3.2 Barotropic model . . . 36
2.3.3 Bubble dynamic models . . . 37
2.4 Scaled pump-turbine numerical domain . . . 38
2.5 Meshing . . . 39
2.6 Boundary conditions . . . 41

2.6.1 Rotating blocks . . . 42
2.7 Convergence criteria and time discretization . . . 43
2.7.1 Steady simulations . . . 43
2.7.2 Unsteady simulations . . . 44
2.8 Applied numerical scheme . . . 45
2.8.1 Computational resources . . . 45
2.9 Comparison of experimental and numerical data . . . 47
2.9.1 Hysteresis effect . . . 47

III Results 49

3 Global results 51
3.1 Global results for non-cavitating regime . . . 51
3.1.1 Turbulence model tests . . . 52
3.1.2 Tests of the rotor/stator interfaces and the rotating blocks . . . 53
3.2 Validation of the cavitation model . . . 56
3.2.1 Incipient cavitation . . . 56
3.3 NPSH head drop curves . . . 57
3.4 Cavitation forms . . . 58
3.5 Comparison to the visualization data . . . 63
3.6 Cavitation influence on the hump zone . . . 63
3.7 Chapter discussion . . . 65

4 Steady partial load flow analysis 67
4.1 Guide vane opening 14° . . . 67
4.1.1 Hump zone analysis . . . 69
4.2 Guide vane opening 12° . . . 70
4.3 Guide vane opening 16° . . . 71
4.4 Guide vane opening 18° . . . 73
4.5 Analysis discussions . . . 74
4.6 Guide vanes geometry $GVII$ . . . 74
4.6.1 Experimental comparison . . . 74
4.6.2 $GVII$, opening 12° . . . 75
4.6.3 $GVII$, opening 14° . . . 76
4.6.4 $GVII$, opening 16° . . . 77
4.6.5 $GVII$, opening 18° . . . 77
4.7 Chapter discussion . . . 78

5 Rotating stall analysis 79
5.1 Global results 14° . . . 79
5.2 Global results 16° . . . 81
5.3 Local flow analysis at $\Phi = 0,0313$, GV opening 14° . . . 83
5.3.1 Impeller blades pressure distribution . . . 83
5.3.2 Draft tube conditions . . . 84
5.3.3 Distributor time-depending analysis . . . 84
5.4 Evolution of the rotating stall . . . 90
5.5 Chapter discussion . . . 91

IV Conclusions and perspectives 93

6 Conclusions and perspectives 95
6.1 Conclusions 95
6.2 Perspectives 97

Bibliography 99

Appendices 107

A Experimental data 107
A.1 Experimental test rig 107

B Résumé prolongé 111
B.1 Introduction 111
B.1.1 Les stations de transfert d'énergie par pompage (STEP) 112
B.1.2 Les instabilités en mode pompage 114
B.1.3 Séparation d'écoulement et décollement tournant 115
B.1.4 Feston cadre et courbe de performance 116
B.2 La cavitation 117
B.2.1 Cavitation dans les pompes 118
B.3 Objectifs de la thèse 121
B.4 Modélisation physique et numérique 121
B.4.1 Les approches CFD 122
B.4.2 Schéma numérique appliqué 122
B.4.3 Moyens de calcul 123
B.5 Les résultats globaux 124
B.5.1 Validation du modèle de cavitation 125
B.5.2 Cavitation naissante 125
B.5.3 Courbes de NPSH 126
B.5.4 Formes de cavitation, débit $\phi = 0,0348$ 127
B.5.5 Influence de la cavitation sur le feston cadre 128
B.6 Analyse stationnaire à débit partiel 129
B.6.1 GV ouverture 14° 129
B.7 Analyse du décollement tournant 131
B.7.1 Résultats globaux 14° 131
B.7.2 Évolution du décollement tournant 133
B.8 Conclusions 133
B.9 Perspectives 134

List of Figures

1.1 Global primary energy consumption (www.eia.gov) 3
1.2 Global primary energy sources (www.eia.gov) 4
1.3 Electricity produced by wind and solar power plants (Germany, 4/9 - 5/9/14, www.eex.com) 5
1.4 Pumped-storage power plant (Alstom Hydro) 6
1.5 Pumped-storage power plant (Alstom Hydro) 7
1.6 Velocity triangles at the inlet/outlet of the pump impeller; outlet triangles comparison for three flow rates 8
1.7 Specific energy transformation inside the pump-turbine, pumping mode [90] 9
1.8 Optimal types of pumps related to specific speed 9
1.9 Possible part load recirculation zones in centrifugal pump [9] 10
1.10 Flow separation on the airfoil, depending on the attack angle 11
1.11 Schematic representation of the rotating stall in the pump-turbine (isosurface $V_m = 4m/s$) 11
1.12 Pumping mode unstable characteristic due to distributor hump 13
1.13 Operating point control: a) Increasing system losses, b) Variation of static head, c) Pump speed variation. 14
1.14 $p - T$ and $p - v$ phase diagrams 15
1.15 Parsons' cavitation tunnel (1895) [90] 16
1.16 Types of cavitation a) Traveling bubble cavitation b) Sheet cavitation c) Cloud cavitation d) Supercavitation e) and f) Cavitating vortices [33] . . . 17
1.17 Cavitation number for turbine characteristics (Q = const.) 19
1.18 Types of cavitation, depending on operating point (hill chart) [60], [90] . . 20
1.19 a) trailing edge cavitation; b) leading edge cavitation; d) cavitation vortices [33] 20
1.20 Cavitation vortex and outlet velocity triangles [33] 21
1.21 Velocity triangles 21
1.22 Cavitation in centrifugal pump [90] 22
1.23 Position of the pump-turbine system 23
1.24 Typical pump-turbine $NPSH_R$ characteristics for Q = const. (head drop curve) 23
1.25 Flow rate influence on the $NPSH_R$ values 24

2.1 Barotropic state law 37
2.2 Numerical pump-turbine domain; left: 3D view, right: Meridional view . . 39
2.3 Mesh and $y+$ value at the inlet of the impeller (left) and at the distributor (right) 40
2.4 Boundary conditions - meridional view 41
2.5 Convergence criteria, RMS, steady simulations 44

2.6 Convergence criteria, RMS, unsteady simulations 45
2.7 Schematic representation of the hysteresis effect on the performance curve . 48

3.1 Global pump-turbine performance, losses in the distributor - lossOUT (Opening 14°, basic GV geometry, non-cavitating regime) 52
3.2 Comparison between turbulence models $k-\epsilon$ (Extended wall functions) and $k-\omega$ (SST) 53
3.3 Influence and definition of the rotating blocks 54
3.4 (left) Influence of the different types of interface; (right) Position of the interface 54
3.5 Comparison of the data transfer for the used interface and the mixing plane interface at the entrance of the impeller 55
3.6 Incipient cavitation values 56
3.7 NPSH head drop curves 58
3.8 Suction side cavitation forms for $\phi = 0,0348$ ($\alpha = 0,05$) 59
3.9 Provided energy along the impeller blade for $\phi = 0,0348$ and various NPSH values 59
3.10 Suction side cavitation forms for $\phi = 0,0278$ ($\alpha = 0,05$) 60
3.11 β_1 and β_2 for 3 different NPSH values for $\phi = 0,0278$ 60
3.12 Suction side cavitation forms for $\phi = 0,0435$ ($\alpha = 0,05$) 61
3.13 Suction side cavitation forms for $\phi = 0,0487$ ($\alpha = 0,05$) 62
3.14 Pressure side cavitation forms for $\phi = 0,0487$ ($\alpha = 0,05$) 62
3.15 Stagnation point for 3 different discharges 62
3.16 Comparison of cavitation forms to visualization data (Alstom Hydro) for $\phi = 0,0304$ 63
3.17 Cavitation influence on the hump zone 64
3.18 Changed losses in the distributor and changed performance of the impeller due to cavitation, compared to the non-cavitating regime 64

4.1 Pumping performance curve for GV opening 14°, GV I geometry; flow patterns analysis 68
4.2 a) Investigated area between the GV channels for mass flow analysis; b) Hump zone performance curve, GVI, opening 14°; c) Flow rate variation between various GV channels (GVC) around the distributor (normalized by average flow rate Q_{avg}) 69
4.3 Static pressure guide vanes loading: a) Guide vanes numbers; b)-f) Static pressure on suction and pressure side of the guide vanes 70
4.4 Pumping performance curve for GV opening 12°, GV I geometry; flow patterns analysis 71
4.5 Pumping performance curve for GV opening 16°, GV I geometry; flow patterns analysis 72
4.6 Pumping performance curve for GV opening 18°, GV I geometry; flow patterns analysis 73
4.7 Experimental comparison of performance curve between guide vanes geometries GVI and $GVII$ for 4 different openings 75
4.8 Guide vanes geometry GV II, opening 12°, compared to the experimental data (a) and to the guide vane geometry GV I (b) 76
4.9 Guide vanes geometry GV II, opening 14°, compared to the experimental data (a) and to the guide vane geometry GV I (b) 76

4.10 Guide vanes geometry GV II, opening 16°, compared to the experimental data (a) and to the guide vane geometry GV I (b) 77
4.11 Guide vanes geometry GV II, opening 18°, compared to the experimental data (a) and to the guide vane geometry GV I (b) 78

5.1 Pumping performance curve for GV opening 14°, rotating stall analysis . . 80
5.2 Pumping performance curve for GV opening 16°, rotating stall analysis . . 82
5.3 Pressure distribution around 4 consecutive impeller blades at a given time 83
5.4 a) Static pressure at the draft tube; b) Tangential velocity in the draft tube 84
5.5 a) Flow rate fluctuations through one guide vanes channel b)-j) Mid-span vorticity with velocity vectors inside the guide vane channel for various time steps 85
5.6 a) Flow rate fluctuations through one guide vanes channel b)-j) Mid-span static pressure distribution inside the guide vane channel for various time steps 87
5.7 a) Flow rate fluctuations through guide vanes channel b)-i) Radial velocity at $D/Dout = 1,127$ (GV leading edge) for various time steps 88
5.8 a) Flow rate fluctuations through guide vanes channel b)-i) Radial velocity at $D/Dout = 1,156$ for various time steps 89
5.9 a) Flow rate fluctuations through guide vanes channel b)-i) Radial velocity at $D/Dout = 1,195$ for various time steps 90
5.10 a) Flow rate fluctuations through guide vanes channel b)-i) Radial velocity at $D/Dout = 1,233$ (GV trailing edge) for various time steps 91

6.1 Mesh size (N° of cells) and CPU time for various types of simulations . . . 96

A.1 Schematic closed test rig for pump-turbines (pumping mode) 107
A.2 Position of the sensors during the measurements (Alstom Hydro) 109

B.1 Sources mondiales d'énergie primaire (www.eia.gov) 111
B.2 Station de transfert d'énergie par pompage (Alstom Hydro) 113
B.3 Triangles de vitesse 115
B.4 Séparation d'écoulement sur le profil d'aile, en fonction de l'angle d'attaque 116
B.5 Représentation schématique du décollement tournant 116
B.6 Caractéristique instable en mode pompage à cause du feston 117
B.7 $p - T$ et $p - v$ dans les diagrammes de phase 118
B.8 Cavitation dans les pompes centrifuges [90] 119
B.9 Caractéristique $NPSH_R$ typique pour Q = const. 120
B.10 Influence du débit sur les valeurs de $NPSH_R$ 120
B.11 La performance globale, les pertes dans le distributeur - lossOUT (ouverture 14°, géométrie GVI, régime non-cavitant) 125
B.12 Valeurs de cavitation naissante 126
B.13 Courbes de NPSH 127
B.14 Formes de cavitation de côté aspiration pour $\phi = 0,0348$ ($\alpha = 0,05$) 128
B.15 Influence de la cavitation sur le feston cadre 128
B.16 Variations des pertes dans le distributeur et des performances de la roue dues à la cavitation, par rapport au régime non-cavitant 129
B.17 Courbe de performance pour GV ouverture 14°; la géométrie GV I; analyse des configurations d'écoulement 130

B.18 Courbe de performance pour GV ouverture 14°, analyse du décollement tournant 132

Nomenclature

Latin

A	guide vane opening	$[°]$
A_S	system area	$[m^2]$
c_{min}	minimal sound velocity	$[m/s]$
c_p	pressure coefficient	$[/]$
C	critical point of water	$[/]$
C	loss coefficient	$[/]$
C_μ	turbulent model constant	$[/]$
D	diameter	$[m]$
f	external forces	$[N]$
f_N	nominal frequency	$[min^{-1}]$
g	gravitational constant	$[m/s^2]$
H	head difference	$[m]$
H_n	net head	$[m]$
H_0	nominal head	$[m]$
$H_{3\%}$	3% head drop	$[m]$
H_{loss}	head losses in the system	$[m]$
k	turbulent kinetic energy	$[m^2/s^2]$
K_S	system curve characteristic	$[m]$
L	characteristic length	$[m]$
n	rotating speed	$[min^{-1}]$
n_q	specific speed number	$[min^{-1} \cdot s^{-1/2} \cdot m^{3/4}]$
$NPSH$	net positive suction head	[m]
$NPSH_A$	available net positive suction head	[m]
$NPSH_R$	required net positive suction head	[m]
p	pressure	$[Pa]$
P	power	$[W]$
P_h	hydraulic power	$[W]$
P_m	mechanical power	$[W]$
Q	discharge	$[m^3/s]$
Q^*	normalized discharge	$[m^3/s]$
R	radius	$[m]$
Re	Reynolds number	$[/]$
t	time	[s]
T	temperature	$[K]$
T	torque	$[N \cdot m]$
Tr	triple point of water	$[/]$

u	velocity component	$[m/s]$
U	circumferential velocity	$[m/s]$
v	velocity	$[m/s]$
V	absolute velocity	$[m/s]$
V_m	meridional velocity	$[m/s]$
V_r	radial velocity	$[m/s]$
V_t	tangential velocity	$[m/s]$
W	relative velocity	$[m/s]$
y^+	non-dimensional wall distance	$[/]$
z	position	$[m]$
Z	position	$[m]$

Greek

α	void ratio	$[/]$
α	absolute flow angle	$[°]$
β	relative flow angle	$[°]$
ϵ	turbulent dissipation rate	$[m^2/s^3]$
η	efficiency	$[/]$
η_0	nominal efficiency	$[/]$
μ	dynamic viscosity	$[kg/(s \cdot m)]$
μ_t	turbulent viscosity	$[kg/(s \cdot m)]$
π	constant	$[/]$
ρ	density	$[kg/m^3]$
σ	cavitation number	$[/]$
σ_i	incipient cavitation number	$[/]$
σ_p	allowed cavitation number	$[/]$
$\sigma_{1\%}$	cavitation number at 1% efficiency drop	$[/]$
τ	shear stress	$[Pa]$
τ	time needed for one impeller revolution	$[s]$
ϕ	flow rate coefficient	$[/]$
ψ	specific energy coefficient	$[/]$
ω	rotating speed	$[rad/s]$
ω	turbulent frequency	$[1/s]$
ω_S	rotating stall speed	$[rad/s]$

Subscripts

0	reference, nominal
1	pump inlet
2	pump outlet
avg	averaged
i	incipient
inl	inlet
l	liquid
m	mixture

min	minimal
ref	reference
out	outlet
v	vaporisation

Abbreviations

BEP	Best Efficiency Point
CFD	Computational Fluid Dynamics
CPU	Central Processing Unit
DNS	Direct Numerical Simulations
EPFL	Ecole Polytechnique Fédérale de Lausanne
GV	Guide Vanes
LDV	Laser Doppler Measurements
LEGI	Laboratory for Geophysical and Industrial Flows
LES	Large Eddy Simulations
PIV	Particle Image Velocimetry
PS	Pressure Side
PSP	Pumped Storage Power Plants
RANS	Reynolds Averaged Navier-Stokes
SAS	Scale-Adaptive Simulation
SS	Suction Side
SST	Shear Stress Transport
SV	Stay Vanes
URANS	Unsteady Reynolds Averaged Navier-Stokes

Definitions

$NPSH$	net positive suction head	$NPSH(m) = \frac{p_{ref} - p_v}{\rho_l \; g}$
ϕ	flow rate coefficient	$\phi = \frac{Q}{\pi \omega R^3}$
ψ	specific energy coefficient	$\psi = \frac{2gH}{\omega^2 R^2}$

Part I

Introduction

Chapter 1

Overview

1.1 Energy industry

In the last five decades, the population of our planet has increased by more than 100% to around 7,2 million in year 2014. The growth seems to be exponential, which means it will not stop for some time. Global primary energy consumption during the same period has increased by 338% to around 148 PWh (10^{15} Watt hour). The growth is very strong, therefore we will need more and more energy, especially in the developing countries with very fast economy growth (Figure 1.1, BRIC - Brazil, Russia, India, China).

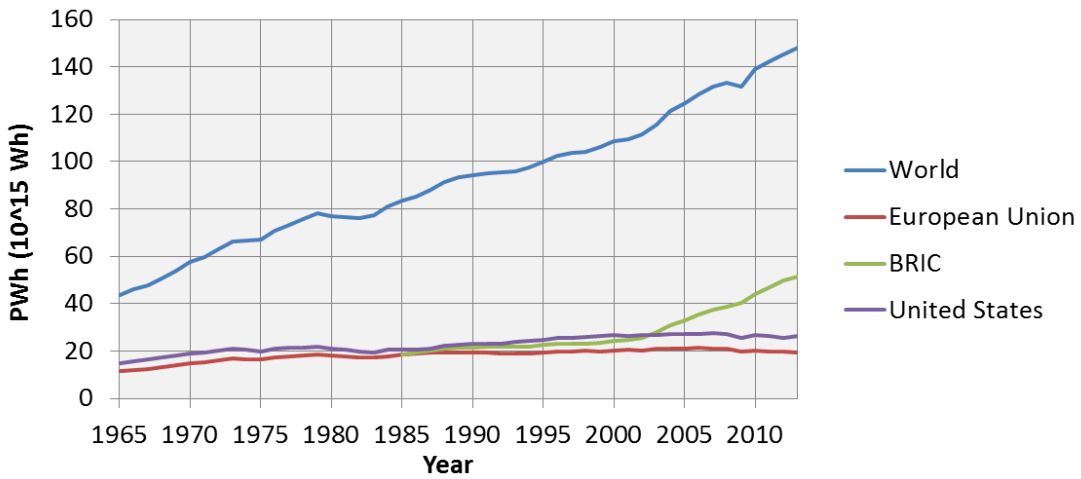

Figure 1.1: Global primary energy consumption (www.eia.gov)

The second problem related to the increasing energy consumption is the origin of energy. Figure 1.2 shows the dependence on oil, coal and natural gas. Together they represent 87% of all primary energy sources. Their combustion has low efficiency, moreover, as a side product we get the so called greenhouse gases that are harmful to local and global environment. Since all of them are non-renewable, the stocks are limited and mostly estimated to less than one century. Another important source of energy are nuclear power plants. However, due to its possible effect on the environment and on the safety of the people, many countries decided to reduce and abandon this energy source.

Traditionally, hydroelectricity represents the major part in renewable sources. It is flexible and clean. Using water potential energy with the efficiency of over 90% it is also

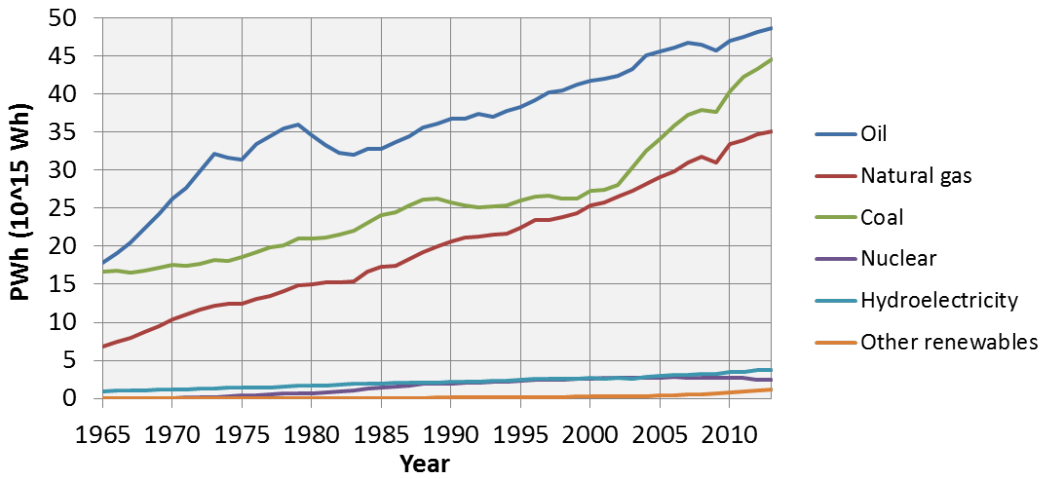

Figure 1.2: Global primary energy sources (www.eia.gov)

considered as the most efficient way to produce electricity. Around 17% (3,7 PWh/year) of the world electrical energy is currently generated by hydropower. According to IEA (International Energy Agency), the technical potential for hydropower is estimated to around 16 PWh/year, therefore we are using approximately 23% of the available potential (in 2013). The countries with the highest technical potential for hydroelectricity are China, US, Russia, Brazil and Canada.

Another advantage of hydro power plants is their durability. The expected life time of a plant is estimated to be around 40 years, however, there are many hydro power plants that were built more than 50 or even 100 years ago. Therefore, some upgrades and renovation can significantly extend the lifetime of power plants and consequently reduce the price of the electricity provided by hydropower. Moreover, the renovation can significantly improve the overall efficiency of the hydro power plants and increase the electricity production.

Besides hydroelectricity, the most widely used renewable energy sources are solar and wind power plants. The global percentage of the mentioned sources is still low, however, in several western European countries, the wind and solar power plants together already provide more than 20% of electricity demands. Indeed, in 2013, Spain became the first country in the world where the leading source of energy is wind. It accounted for 20,9% of the country electricity, according to Spanish Wind Energy Association (AEE).

The drawback of the wind and solar power plants is the negative effect on the electrical grid stability. As seen on figure 1.3, the electricity generated by solar and wind power plants can change every hour, even every minute. The electrical grids nowadays are not very flexible, which means that there can not be significant variation between the demand and the supply side of the grid. On the supply side, the sudden decrease of wind intensity or/and unpredicted cloud can cause the decrease of electrical power in the grid and therefore cause instabilities. On the other hand, the main instabilities on the demand side are caused during industrial operating hours. To balance and adjust the electrical grid system, a fast and reliable solution must be provided in order to store the energy during the production peak and use the same energy, when the energy consumption is higher than the production. So far, the pumped-storage power plants are the best solution that enable us flexibility.

Moreover, the provided energy storage can be enormous, since it depends only on the

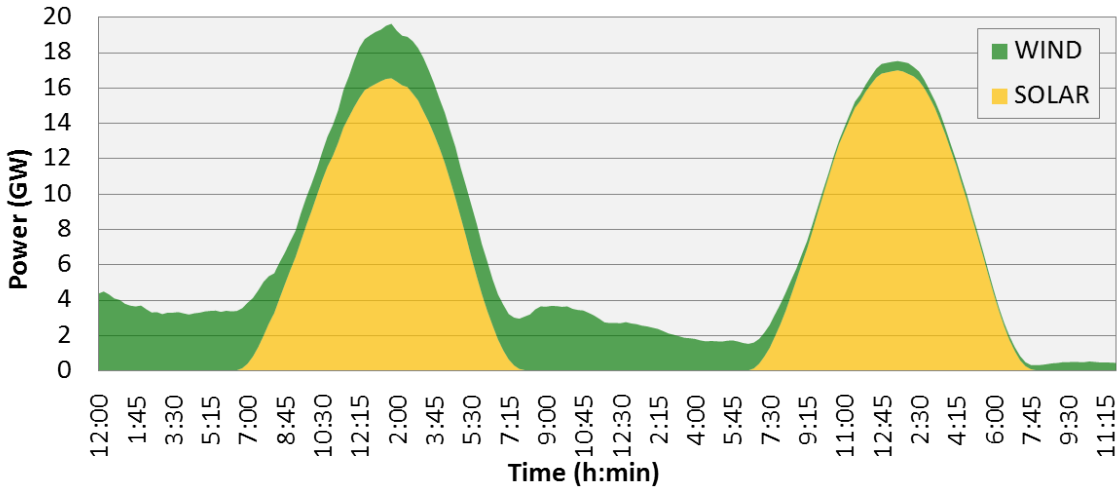

Figure 1.3: Electricity produced by wind and solar power plants (Germany, 4/9 - 5/9/14, www.eex.com)

size of the upper reservoir. This kind of energy storage is very efficient compared to the other types of storage, because is does not lose the stored energy as in case of the thermal or other kinds of energy storage.

1.2 Pumped-storage power plants (PSP)

Generally, we can divide hydro power plants into several groups. The most typical approach is to build a dam to store and accumulate water. Usually in the lower part of the dam, one or several turbines are connected by penstock to the water storage behind the dam and to the generator that transforms mechanical energy of the turbine to electricity. This kind of hydro power plants are called storage power plants and they can be partly regulated depending on the available water supply and energy requirements of the electrical grid.

The other approach is used on so called 'Run-of-river' schemes. The dam on the river is still necessary, however, there is low or no capacity for water storage behind the dam. The turbine uses almost constant flow rate of the river and therefore produces a constant amount of electricity.

The third type of hydro power plants are called Pumped-storage power plants. As presented on figure 1.4, they consist of two reservoirs connected by penstock. The lower one can be part of classical hydro power plant as described above. The conventional systems normally contain two separate hydraulic systems. One with a pump that pumps water to the higher reservoir and the other one with a turbine that, through a generator, generates electricity. Another option is to have one hydraulic system, but still separate pump and turbine machine [5], [68]. In that case, the pump can help regulating the pressure around the turbine in the generating mode, which is especially useful in the case of Pelton turbines.

However, due to the reduction of the cost and the technology improvement, we usually nowadays use just one system with reverse pump-turbine machine (figure 1.4). When we have too much energy available, the machine works in the pumping mode, therefore it pumps water in the higher reservoir. On the contrary, when we have a lack of electricity

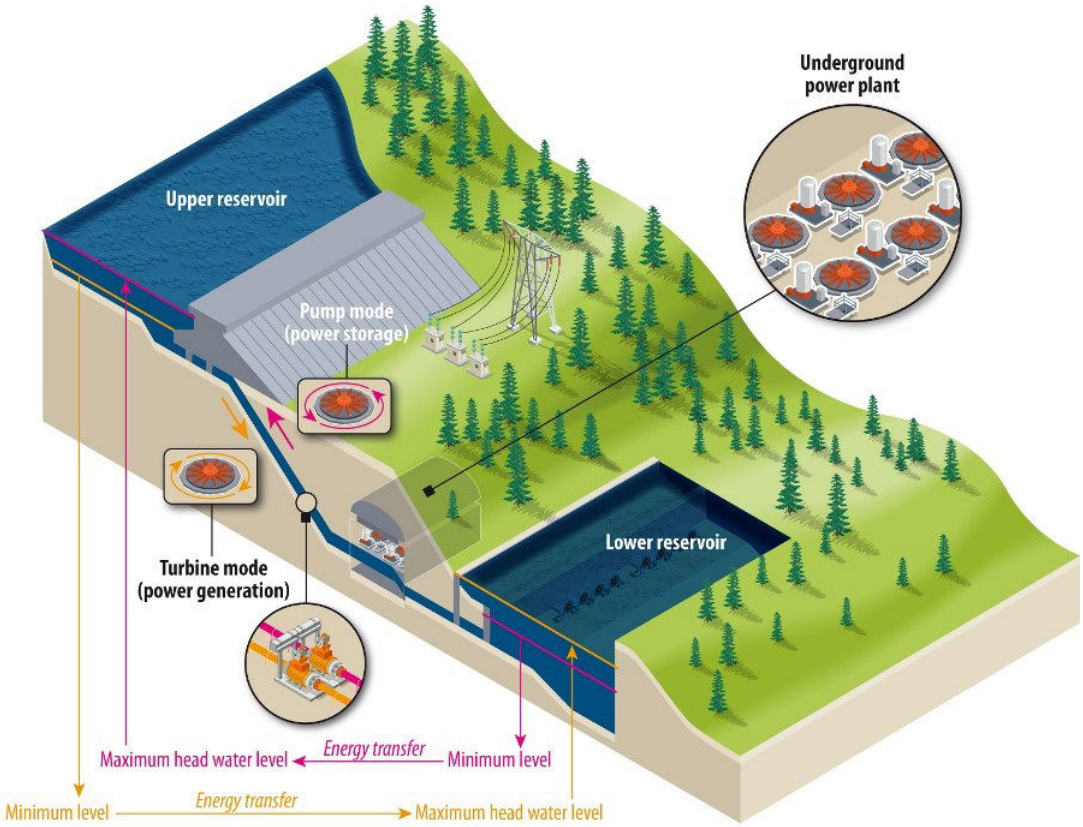

Figure 1.4: Pumped-storage power plant (Alstom Hydro)

in the grid, the machine rotates in the other direction and generates electricity.

The overall efficiency of the process of pumping water into a higher reservoir and using potential energy of water to generate electricity is up to 80%. However, pump-turbines are economically cost-effective as well. Indeed, when the demand of electricity is lower than supply, usually during the night, the price of electricity is low. On the contrary, when the supply is lower than the demand, typically in the morning, the electricity price increases. The daily difference between the highest and the lowest price can be even more than 100%. To use the availability of the pumped-storage power plant as well as possible, regular switching from pumping to generating mode and vice versa is mandatory. Pumped-storage power plant systems have been originally built to use and store the extra energy during the night provided by nuclear power plants. The switching between the generating and pumping mode occurred around 3 - 4 times per day. During the last years, the described switching increased to more than 10 times, since the main role of the PSP is to provide the stability of the grid, that is strongly influenced by the unstable energy sources, such as solar and wind power plants.

Like the other turbomachines, reversible pump-turbines are also designed for one optimal constant flow rate Q and net head H, that are given by the geographical position of both reservoirs. However, the regular changing between pumping and generating regime and the specific electricity demands of the grid, are the reasons that in reality, the pump-turbine needs to operate regularly at off-design conditions. Extended operating at off-design conditions can cause a significant efficiency drop, vibrations and can even seriously damage the machine. To avoid this scenario, it is essential to extend the operating range, therefore to study the origins of the instabilities.

1.3 Reversible pump-turbine

Figure 1.5 represents the basic parts of the reversible pump-turbine. Impeller is connected to the generator by the generator shaft. In generating mode, the generator produces electricity and in pumping mode, it delivers power to the pump.

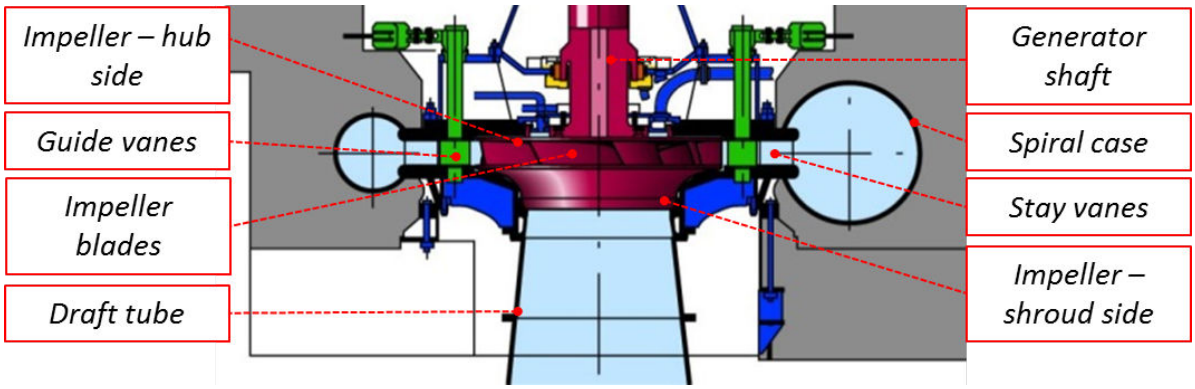

Figure 1.5: Pumped-storage power plant (Alstom Hydro)

In generating mode, spiral case is designed to guide the water to the stay vanes and later to the guide vanes as evenly as possible. Opening of the guide vanes can be regulated and optimized according to discharge through the machine.

The pump-turbine must operate efficiently in both, pumping and generating modes. Stable and efficient operating range is quite narrow in both cases, therefore a design compromise that suits all regimes, including off-design, must be found. Balancing of such hydraulic behavior is important for any kind of reversible pump-turbines.

The main features of unstable behavior areas can be divided into generating and pumping modes. The main instability in the generating mode can be described as a S-shaped turbine characteristic. It occurs at low load off-design operating points close to runaway (no-load) conditions. The phenomenon has been investigated numerically as well as experimentally by several authors [35], [42], [45], [89], so far the most extensive study on the generating mode instabilities was made by Hasmatuchi [41] during his thesis work.

1.4 Pumping mode instabilities

The main reported instabilities in the pumping mode are related to the cavitation behaviour at the off-design flow rates. Moreover, at part load, the phenomenon of rotating stall can occur and cause humped-shaped performance curve, which is the origin of the instabilities. Cavitation and humped-shaped performance curve are the main subjects of investigation in the presented PhD dissertation. In order to understand the pumping mode part load instabilities, it is essential to explain the basics of centrifugal pump behavior.

1.4.1 Centrifugal pump characteristic

The use of centrifugal effect to transport water was first mentioned by Leonardo da Vinci (1452 - 1519). However, the most fundamental equation in the field of turbomachinery

was presented by Leonhard Euler (1707 - 1783). Euler's equation for turbomachines is based on the conservation of angular momentum. The simplified linear Euler equation for specific hydraulic energy of the pump can be written as:

$$gH = U_2 V_{2u} - U_1 V_{1u}. \tag{1.1}$$

For a centrifugal pump, the average velocity triangles at the inlet and outlet are considered and the relative flow angles β_1 and β_2 are estimated as a constant (fig. 1.6). The inlet flow is assumed to have no circumferential component (absolute velocity projection $V_{1u} = 0$) for a centrifugal pump, the Euler's equation can be modified to:

$$gH = U_2 V_{2u} = U_2 \left(U_2 - \frac{V_{2m}}{tan(\beta_2)} \right). \tag{1.2}$$

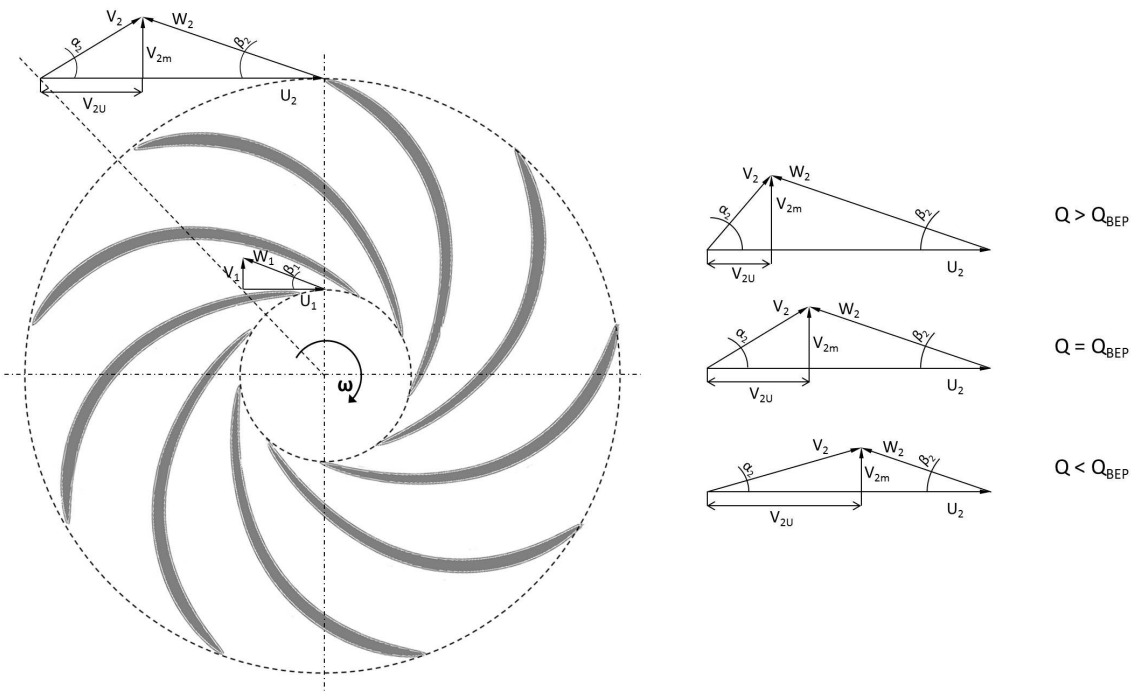

Figure 1.6: Velocity triangles at the inlet/outlet of the pump impeller; outlet triangles comparison for three flow rates

At the outlet of the pump impeller, the specific hydraulic energy gH_2 consists of the pressure component $\frac{p_2}{\rho}$ and velocity component $\frac{v_2^2}{2}$. The energy transformation from the velocity to the pressure component continues in the distributor (guide and stay vanes regions), as presented on the figure 1.7. The main objective of the centrifugal pump is to convert the mechanical power input P_m into hydraulic power P_h with maximum efficiency. P_m is defined by the multiplication of the torque on the shaft T and the rotating speed ω:

$$P_m = \omega T. \tag{1.3}$$

On the other hand, the hydraulic power is defined by the head difference H and the flow rate Q:

$$H = \frac{p}{\rho} + \frac{v^2}{2g} + z; \tag{1.4}$$

$$P_h = Q\rho(gH_2 - gH_1). \tag{1.5}$$

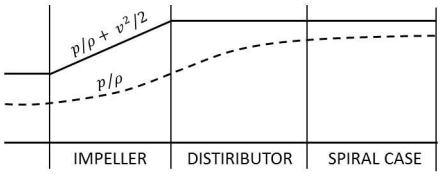

Figure 1.7: Specific energy transformation inside the pump-turbine, pumping mode [90]

In order to provide the maximum efficiency, the appropriate shape of the pump should be chosen. The typical criteria is a specific speed number n_q. Since the specific speed number definition can vary a lot in literature, it is important to define it clearly. In our case and in most industrial cases, the units are as follows: $n(min^{-1})$; $Q(m^3/s)$; $H(m)$.

$$n_q = n\frac{\sqrt{Q}}{H^{3/4}}. \tag{1.6}$$

Regardless of the definition, the lower specific speed value always represents a more centrifugal shape of the pump and on the contrary, higher values represent more axial vane shapes. Generally, the pumps can be divided into four groups, depending on the vane shape, as presented on the figure 1.8.

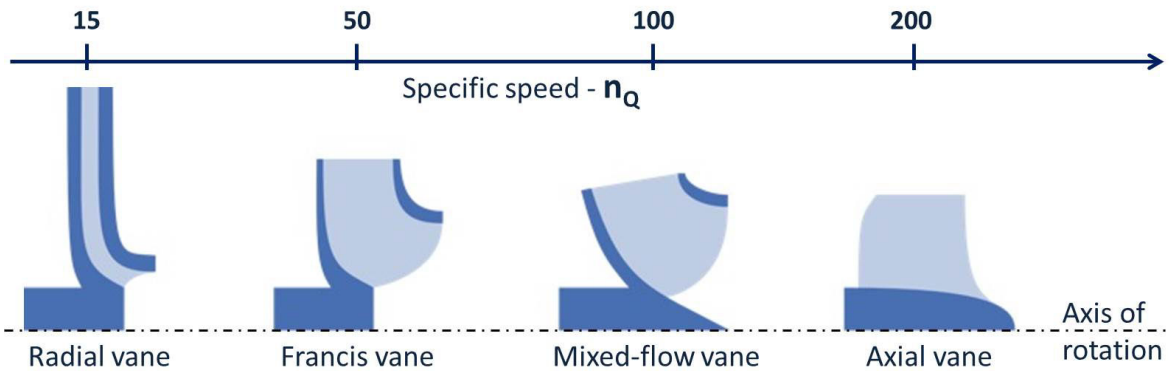

Figure 1.8: Optimal types of pumps related to specific speed

The other important non-dimensional numbers, widely used in literature, are the flow rate coefficient ϕ and the specific energy coefficient ψ that are defined as:

$$\phi = \frac{Q}{\pi\omega R^3}; \tag{1.7}$$

$$\psi = \frac{2gH}{\omega^2 R^2}. \tag{1.8}$$

Another important factor that must be taken into account to achieve high efficiency and low losses is the energy transformation inside the machine. It must be as smooth as possible (fig. 1.7). Therefore, the flow from the impeller must be adapted to the distributor. In case of a pump-turbine, the distributor contains two parts. On one hand, the guide vanes opening angle can be modified and adapted to the flow and on the other hand, the stay vanes are fixed.

The importance of adapting angle of guide vanes opening is even clearer, because the triangles of velocity at the outlet of impeller are changing significantly, depending on the flow rate. Figure 1.6 shows the difference in absolute flow angle α_2 at the outlet of the impeller for three different flow rates. In order to reduce the losses in the distributor, the α_2 angle should match the opening angle of the guide vanes.

However, that is not the case at part flow rate, where unadapted attack angle at the inlet of the distributor causes the flow separation and consequently rotating stalls.

1.4.2 Part load flows in centrifugal pumps

The flow gets very unstable at part load. Moreover, several recirculation zones and secondary flows occur that consequently lead into increased vibrations and pressure fluctuations. Horlock [44] presented analytical approach for the secondary flows description. Off-design conditions for centrifugal pumps have been studied lately by [9] who showed different possible recirculation zones inside and around the pump impeller (fig. 1.9).

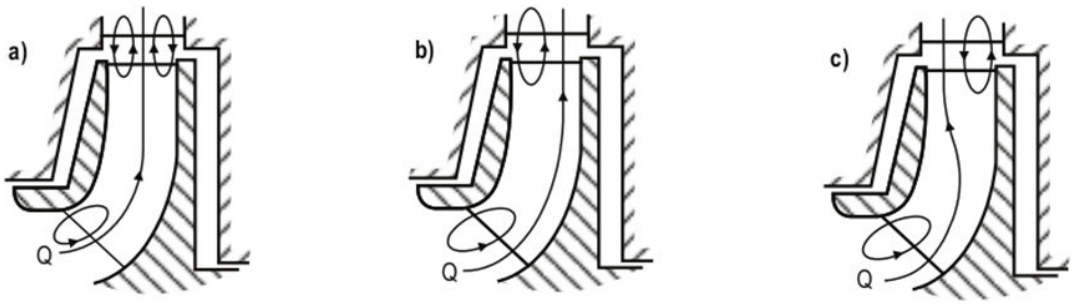

Figure 1.9: Possible part load recirculation zones in centrifugal pump [9]

According to [9], the recirculation zones at the inlet of the impeller occur due to:

- deceleration of relative velocity in the impeller throat,
- incidence at the impeller leading edge,
- pressure gradients perpendicular to the main flow.

The recirculation zones at the inlet of the impeller affect the efficiency of the machine, they increase the pressure fluctuations and vibrations and can consequently damage the mechanical parts of the machine. Some authors, including Zangeneh [96] suppose that the recirculation zones at the outlet of the impeller are influenced by the inlet conditions. They analyzed numerically different impellers with the same meridional shape, but different pressure distributions around the impeller blades in order to optimize the velocity profile at the trailing edge of the impeller that would reduce the recirculation zones at the impeller outlet regions.

1.4.3 Flow separation and rotating stall

Kline [54] gave the first explanations about the stall origins. It is defined as a recirculation zone on the internal or external walls. The initial flow separation can be caused by several flow phenomena, such as:

- an obstacle on the flow path,
- an unadapted attack angle on the leading edge of the blade (fig. 1.10),
- strong pressure gradients, normal to the flow direction.

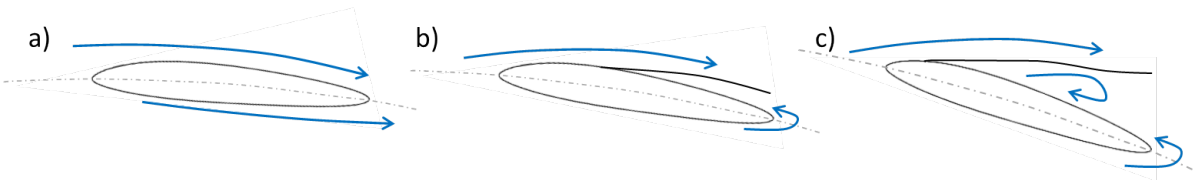

Figure 1.10: Flow separation on the airfoil, depending on the attack angle

The first detailed explanation of the rotating stall was given by Emmons [27] in 1959. At the beginning, the phenomenon was studied in a case of axial and centrifugal compressors ([34], [43], [46], [62]). Indeed, the rotating stall investigations on the centrifugal pump geometry were performed much later. Around 1990, Arndt [2], [3] was investigating the rotor stator interactions, and the study showed that the pressure fluctuations were strongly influenced by a radial gap between the trailing edge of the impeller and the leading edge of the diffuser. Moreover, the pressure fluctuations have been much higher on the suction side of the diffuser vanes.

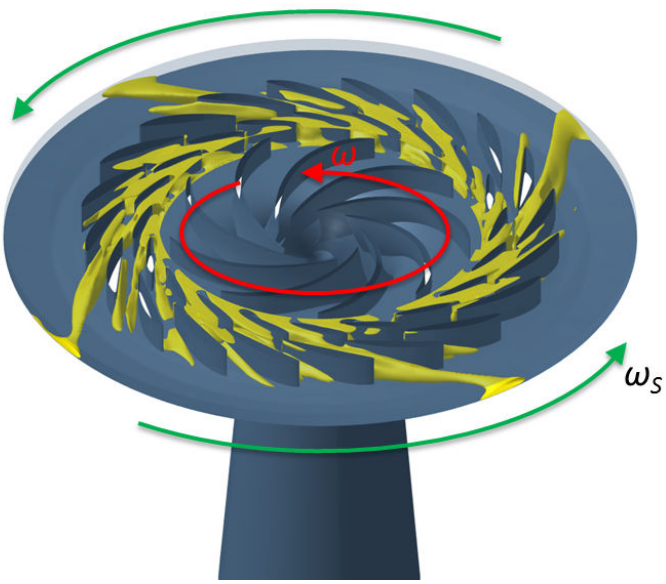

Figure 1.11: Schematic representation of the rotating stall in the pump-turbine (isosurface $V_m = 4m/s$)

Rotating stall is usually seen as cells of increased and decreased flow rate inside the distributor. Figure 1.11 represents the rotating stall inside a pump-turbine. 4 cells of increased flow rate are rotating around the distributor in the same direction as the impeller with the frequency ω_S from 2% to 6% of the operating frequency of the impeller ω. For the centrifugal pump applications, the rotating stall can also have the opposite direction than the pump. Studies on the radial gap influence on the forward/backward rotating stall have been made by Sano et al. [81], [82] in 2002. They state that a larger radial clearance between the impeller and the diffuser causes an easier occurrence of the diffuser rotating stall due to the decoupling of the impeller/diffuser flow.

Most of the experimental studies of the rotating stall in pumps and pump-turbines took place in the last 20 years. The main approach was to use PIV (Particle Image Velocimetry) method and was firstly used by Sinha et al. [86], [87]. The radial clearance between the impeller and the diffuser was around 10% of the impeller diameter. He assumed that a larger clearance would increase the stall intensity and the probability of stall occurrence as it was originally stated by Yoshida [94]. Similar experimental studies, using PIV method, were performed later by [72] and [91].

The most extensive project regarding the pump-turbine geometry in pumping mode was set up in Lausanne during Hydrodyna project. Part-load flow behavior in the centrifugal pumps as well as in the pump-turbines was investigated numerically and experimentally by Braun [10] during his thesis. The LDV (Laser Doppler Measurements) method was used in order to analyze the velocity components between the guide vane channels and in the vaneless gap between the impeller and the distributor. During the visual observation of the experiment, confirmed by noise analysis, some kind of cavitation vortex appeared in the region of the guide vanes, despite the fact that it is located in the high pressure area. Similar behaviors were observed in some cases of industrial centrifugal pumps. Braun assumed that the origin of the vortex is the flow separation on the hub side of the distributor and can reach the area of the impeller as well. Another study about the cavitation influence on the hump shaped performance curve was made by Amblard [1] in 1985.

Numerically, steady and unsteady 3-dimensional simulations were performed using RANS (Reynolds Averaged Navier-Stokes) equations [10], [93]. Additional numerical studies were performed lately in the EPFL by Pacot [69], [70], who used LES (Large Eddy Simulation) to investigate the rotating stall behavior. The global rotating stall behavior in one operating point was caught quite well, including the area and the frequency of the stall. Those kind of calculations are very demanding regarding computational time. They were done on one of today's fastest supercomputers (more than 700000 cores), called K computer, which is located in Japan.

1.4.4 Hump shaped performance curve

The appearance of the described rotating stall phenomena significantly increases the losses in the distributor and, therefore, causes a positive differential slope on the performance curve as presented on the figure 1.12. The green and the red lines represent the characteristics of the system. The normal, stable operating range for the pump-turbine is between the green lines. In a stable area, the pump-turbine provides one corresponding flow rate for every given net head of the system. On the contrary, in the area of the unstable characteristics due to the phenomenon of the rotating stall, the pump-turbine can provide three different flow rates for the given system characteristic, as shown by the red curve. In reality, that means that the flow rate through the pump-turbine varies

completely uncontrollably. Behavior like this drastically increases the losses. Moreover, it also causes very strong vibrations that can damage and in the worst case even destroy the machine.

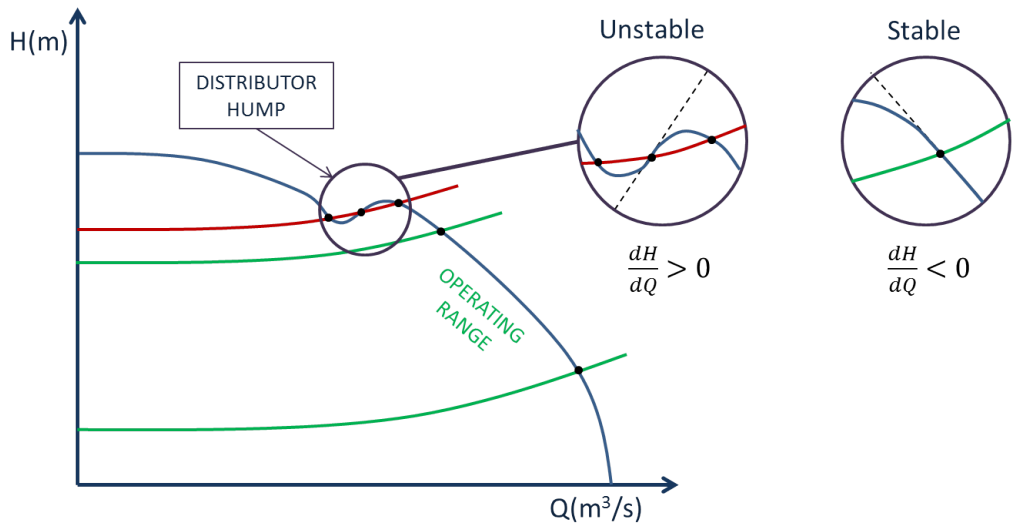

Figure 1.12: Pumping mode unstable characteristic due to distributor hump

Obviously, the pump-turbine should not operate in the area of the distributor hump. However, since the pump-turbine needs to change the regime several times per day and must be as adaptable as possible, there is no possibility to completely avoid the problematic unstable area. Some of the general control options of the operating point for pumping system are presented on figure 1.13. The system curve characteristic is proportional to the squared flow rate and to a loss coefficient C:

$$K_S \propto C \frac{Q^2}{A_S}. \tag{1.9}$$

The first option is to increase or decrease the losses in the system. It is often used in the industrial application to control the provided head. In pump-turbine systems it is partly used during the start-ups and the shut-downs for the changing from pumping to generating mode and vice versa. It is not used for normal operating.

The second option is the variation of the static head. This kind of control is very useful in tidal application, where the relative difference between the water levels can be large. For PSP system that means the variation of the water level between the upper and the lower reservoir, which is relatively small. The head variation in case of PSP must be taken into account, but can not be used to control the operating points.

The third option is to control the speed of the pump-turbine. The technology is called variable speed technology for the pump-turbines. It is a rather new approach in the field of the PSP. Detailed description and advantages were provided by [11]. The technology is already used by Alstom Hydro in several installations around the world. It enables the variation of the pump-turbine rotating speed and consequently different performance curves as seen on the part c) of the figure 1.13. Several advantages of the variable speed technology comparing to fixed speed are:

- For a fixed static head (water level of the reservoirs), the absorbed power can vary (up to 30%). Therefore, it can be used for the grid regulation when necessary.

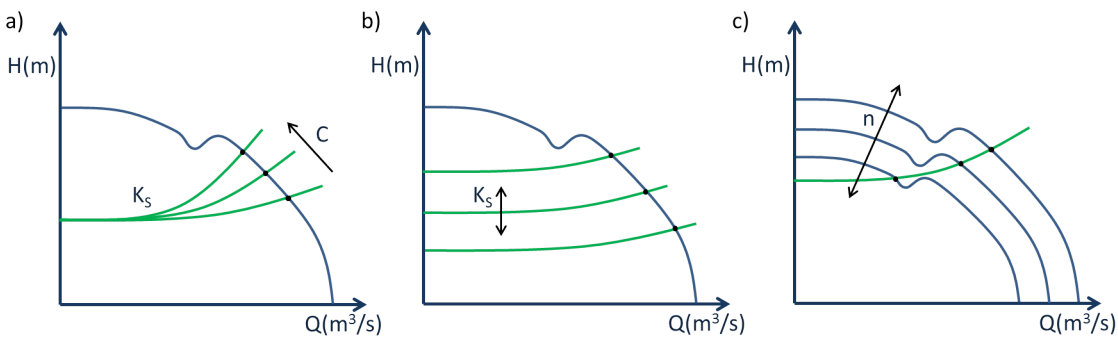

Figure 1.13: Operating point control: a) Increasing system losses, b) Variation of static head, c) Pump speed variation.

- Optimizing the efficiency. For a single speed machine the BEP (Best efficiency point) is a point at a given head and a given discharge. If the rotating speed of the machine is changed, the BEP also changes, which means that we can achieve better efficiency for the non-optimal flow rates, especially at the part load flow.

- Since the technology enables for higher flexibility, depending on the grid demands, the pump-turbine can operate longer. Therefore, the economic amortization time of the whole PSP system is shorter.

- Variable speed technology can be used to avoid the unstable operating points, such as the described distributor hump region and regimes, where the cavitation phenomenon is present.

1.5 Cavitation

The most common description of the term 'cavitation' is the appearance of vapor bubbles inside an initially homogeneous liquid medium. Usually, it is seen as a transition from the liquid to the vapor phase and again back to the liquid. The reason for the appearance of cavitation is a local decrease of pressure, where the temperature remains approximately constant. The vapor pressure can be explained in a classical thermodynamic point of view. On the $p-T$ phase diagram for water (fig. 1.14), the line between the triple point of water Tr and the critical point C separates the liquid phase from the vapor phase. The vapor pressure p_v means that crossing the curve under static conditions causes the change of the phase (in our case, evaporation). As seen from figure 1.14, the vapor pressure p_v is a function of the temperature. As mentioned before, the cavitation in cold water usually occurs at the almost constant temperature, when local pressure is decreased and later increased again. A similar phenomenon is called boiling, where the vaporisation occurs at the constant pressure when the temperature is increased.

The last stage of the cavitation process occurs when the pressure returns back to the initial one (above the p_v) and the bubbles start to implode. The bubble 'void' is filled again with the surrounding liquid. During the bubble collapse, strong pressure waves can be emitted, and one of the consequences can be serious damage of the nearby solid walls.

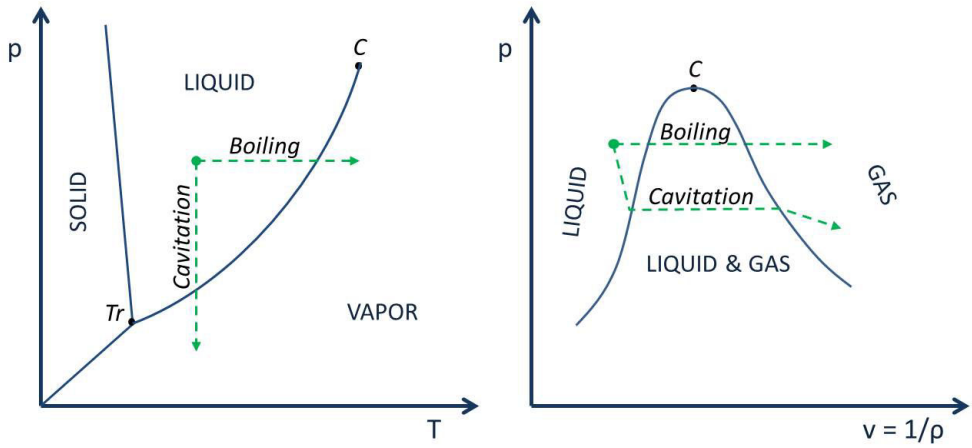

Figure 1.14: $p - T$ and $p - v$ phase diagrams

1.5.1 History of cavitation

Isaac Newton was most likely the first person who mentioned bubble formations in low pressure areas between a lens and a flat glass in his book Optics [67] that was originally published in 1704. He was not aware that the origin of the bubbles, extracted from the water, was the local pressure decrease. This phenomenon is nowadays called 'cavitation'.

The research activity increased in the nineteenth century, when engineers noticed that ship propellers turn 'into an empty'. This phenomenon has been predicted by Euler in his work about turbine machines in year the 1754. Reynolds showed with boat model in 1873 that bubbles appear behind the propeller even when the propeller is completely submerged below the water level. He noticed that bubbles do not appear when the propeller is deep enough [32], [90].

The term 'cavitation' has been first mentioned in an article in 1893, when Barnaby, Parsons and Thornycroft explained the phenomenon (suggestion for the phenomenon name was given by Froude *lat. cavitas - cave, empty space*). First cavitation test rig was built by Pearson, where he tested propellers (fig. 1.15).

Dimensionless cavitation number σ (also Th), which describes the level of cavitation, has been suggested by Thoma in 1925. Research on cavitation was boasted after 1940, when technology for high speed recording of the phenomenon became available. Experimental results stimulated the development of the bubble dynamic theory, which has been set by Rayleigh [78] in 1917 and supplemented by Plesset in 1949 [73]. The basic equation, which has been later supplemented few times, is known as the Rayleigh - Plesset equation of bubble dynamics [32].

1.5.2 Cavitation origins

According to Franc [32], [33], the cavitation can be divided according to four different types of origin:

- **Hydrodynamic cavitation**. Caused by the geometry of the submerged body (profile, rotor blades, propeller).
- **Acoustic cavitation**. Caused by the sound waves, which spread through fluid.

Figure 1.15: Parsons' cavitation tunnel (1895) [90]

- **Optic cavitation**. Caused by the photons or laser light.
- **Cavitation of particles**. Caused by other elementary particles, e.g. protons.

The hydrodynamic and the acoustic cavitation commence because of the tensions in the fluid; on the other hand, the optical cavitation and the cavitation of particles start because of a local energy input into the fluid. In the field of hydraulic machines, the hydrodynamic cavitation is the most important, and therefore deserves an additional analysis.

1.5.3 Hydrodynamic cavitation

Hydrodynamic cavitation occurs due to one or several effects that increase the possibility of cavitation:

- **Geometry of the submerged body**, which causes an increase of local velocity and an indirect decrease of the local static pressure.
- **Boundary layer between flows with two different speed**.
- **Surface roughness**.
- **Vibrations of submerged bodies**, when the fluid can not follow high speed frequencies of the body.

Different types of cavitation can be observed depending on the flow conditions and the geometry of the submerged body. It is common to distinguish between the different types of cavitation, each having its distinctive characteristics. Franc [32], Knapp [55] and Young [95] describe five different types of cavitation as presented on the figure 1.16.

- **Transient isolated bubbles.** A type of cavitation where individual bubbles form in the liquid and move with the flow. They appear in low pressure regions, travel with the flow and implode in the regions with high pressure. (fig. 1.16, part a)

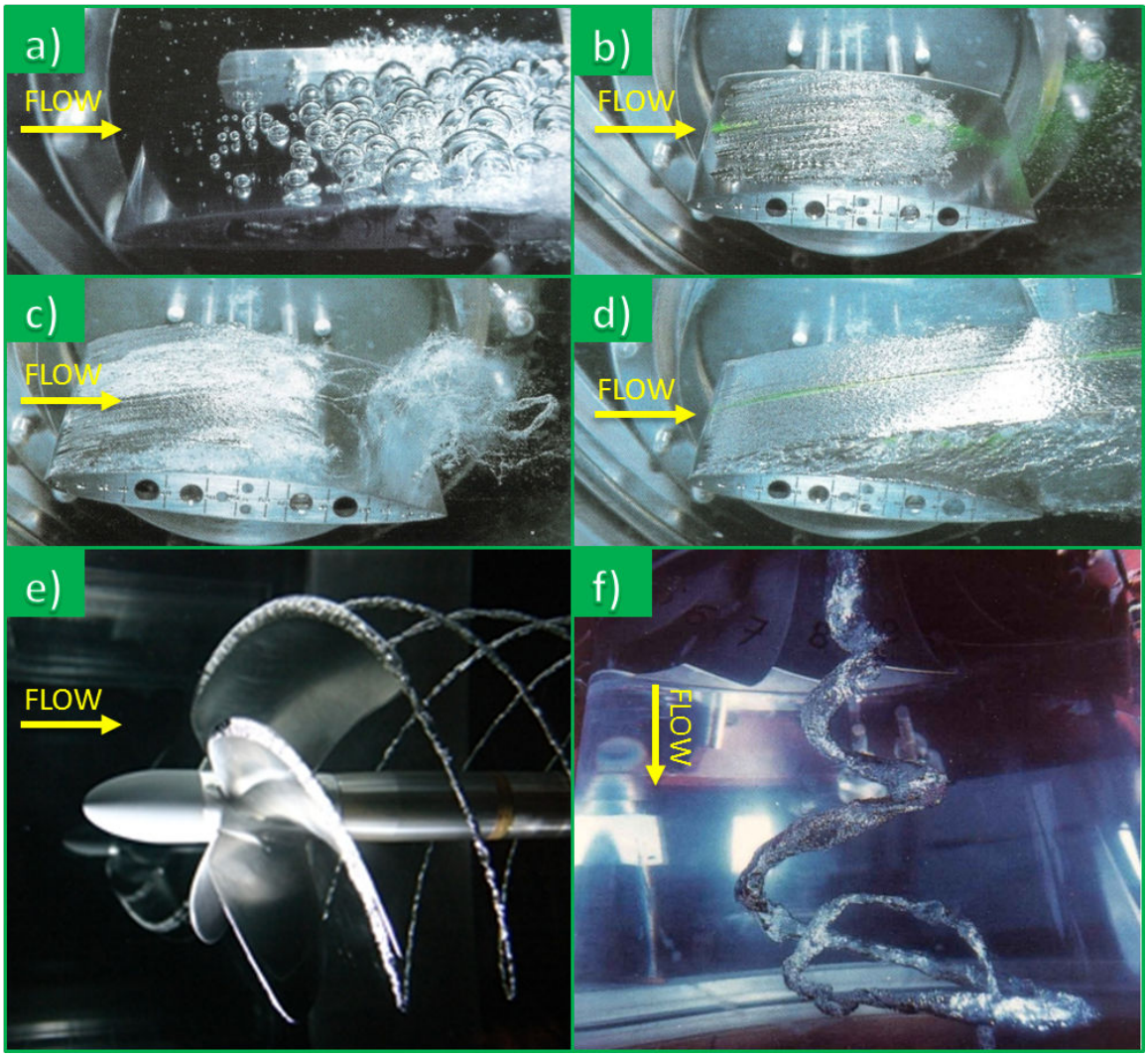

Figure 1.16: Types of cavitation a) Traveling bubble cavitation b) Sheet cavitation c) Cloud cavitation d) Supercavitation e) and f) Cavitating vortices [33]

- **Sheet cavitation.** The shape of the sheet can change with time. It is attached to the leading edge of the submerged bodies, i.e. low pressure side of blades and foils (fig. 1.16, part b).
- **Cloud cavitation.** Cloud cavitation is the origin of the most engineering problems related with hydrodynamic cavitation, including erosion, vibrations and noise. It is created by the vorticity in the flow field. The periodic shedding of cavitation clouds is caused by the re-entrant jet as measured and described by Dular [22], [23]. (fig. 1.16, part c)
- **Supercavitation.** Supercavitation appears when the sheet cavitation grows in such way, that envelopes the whole submerged solid body. (fig. 1.16, part d)
- **Cavitating vortices.** Usually occurs as a result of high shear stresses in the region inside the low-pressure cores of the vortices. It is most commonly observed on the tips of the rotating blades or behind the outlet of a turbine. (fig. 1.16, part e and f)

1.5.4 Non-dimensional parameters

The basic condition for cavitation occurrence is when local minimal static pressure p_{min} reaches the vaporisation pressure p_v:

$$p_{min} = p_v. \tag{1.10}$$

If we use a reference point where the pressure and velocity equals p_0 and v_0, the pressure coefficient $c_p(\vec{r}, t)$ for a random local point and a random time can be defined as:

$$c_p(\vec{r}, t) = \frac{p(\vec{r}, t) - p_0}{\frac{\rho v_0^2}{2}}. \tag{1.11}$$

On the other hand, the cavitation number σ can be written as a relation between a reference and a vaporisation pressure:

$$\sigma = \frac{p_0 - p_v(T)}{\frac{\rho v_0^2}{2}}. \tag{1.12}$$

When the cavitation number σ is low enough for the cavitation occurrence, it can be marked as an incipient cavitation number σ_i. Normally, a simplified explanation states that the vaporisation commences when the local static pressure reaches the vaporisation pressure. However, in reality, the vaporisation conditions are much more difficult to define. The fact is that c_p is influenced by several other factors such as friction, turbulence level, boundary layers and others. Moreover, even σ_i is influenced by some parameters such as amount of dissolved gas in the water. Still, in many circumstances, including the ones presented in this document, especially for numerical modeling of cavitating flows, following estimation is taken for σ_i:

$$\sigma_i = -c_{p,min}. \tag{1.13}$$

1.5.5 Cavitation in turbines

Cavitation behavior in different types of hydraulic machines has been studied and presented by [4], [28]. As mentioned before, the cavitation in the turbine occurs when the local pressure drops under the critical vaporisation pressure. To characterize the level of cavitation, the cavitation number σ is used. Lower cavitation number means more intensive cavitation, however it does not tell us about the forms of cavitation that are present inside the turbine.

On the figure 1.17 we can observe how the cavitation level influences the turbine performance. Several typical values of the cavitation number are marked on the chart according to IEC 60193 [12]:

- σ_i represents the incipient cavitation value. Experimentally, it is set by a visual observation; numerically, usually by the comparison of the lowest local pressure in the domain and a vaporisation pressure. Incipient cavitation value is lower when the flow is close to optimal value $Q/Q_{BEP} = 1$, therefore the attack angle is well adapted to the blades. On the contrary, for increased or decreased flow rate, the value increases due to either too high or too low attack angles.

- σ_p represents the lowest value of the cavitation number when the machine is still allowed to operate.

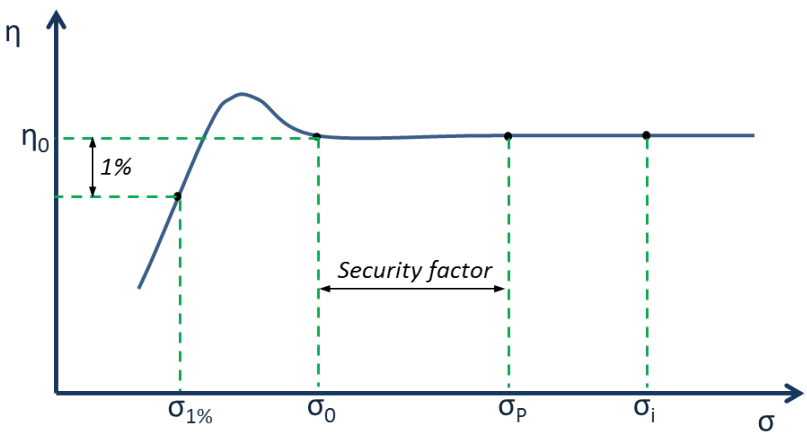

Figure 1.17: Cavitation number for turbine characteristics (Q = const.)

- σ_0 shows the smallest cavitation number value when the level of the cavitation does not influence the turbine performance curve.
- $\sigma_{1\%}$ marks the level of the cavitation that causes 1% of the machine efficiency drop $\eta_{1\%}$.

In the figure 1.17 we can also notice the efficiency increase during high cavitating flow lower than σ_0. This kind of behavior is not always present and usually occurs at the part load operating. The origin of the phenomenon is a better flow adaptation to the blades due to the presence of the cavitation sheets on the turbine blades.

Similarly to the pumps, the turbines are generally divided into two groups. In the radial machines, the flow is mostly perpendicular to the rotation axis, on contrary, in the axial machines, the flow is mostly parallel to the rotation axis. Due to our field of research, just the radial machines with the typical example of a Francis turbine, are going to be described.

Forms and locations of cavitation inside the turbine vary widely. The main influence factor (except cavitation number) is the operating point of the turbine. Five different types of cavitation are presented on the figure 1.18. On the hill chart (up-right fig. 1.18), the appearance of specific cavitation forms can be observed in dependence on a relative flow rate ϕ/ϕ_0, a relative specific energy ψ/ψ_0 and a relative guide vane opening A/A_0.

Here-below, a short description of different forms of cavitation in the Francis turbine according to [33], [90] is presented:

- Cavitation in region (a) (fig. 1.18 and 1.19) occurs due to over load. The cavitation appears along the runner blade.
- In region (b) (fig. 1.18 and 1.19) the cavitation occurs close to leading edge, on the suction side of the runner. Although the area is small, this kind of a cavitation is very aggressive and can seriously damage the machine.
- Cavitation in the region (c) starts at the leading edge of the runner, close to the shroud (fig. 1.18). It has a shape of a vortex that grows between the runner blades. It can be very difficult to take a picture of it.

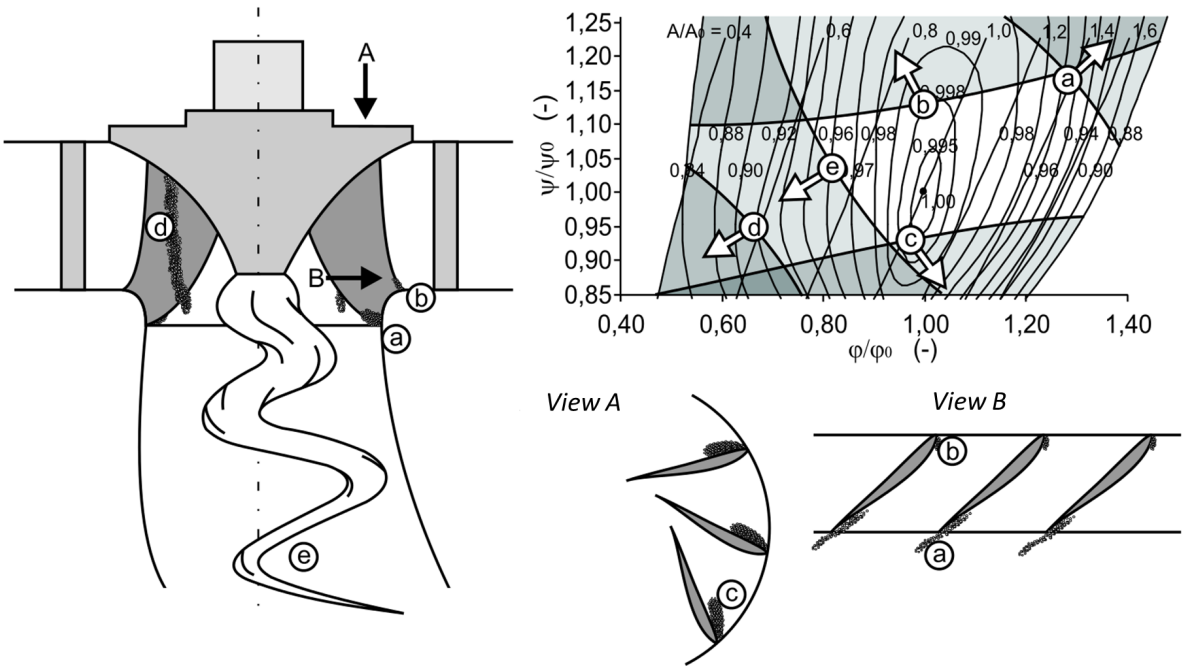

Figure 1.18: Types of cavitation, depending on operating point (hill chart) [60], [90]

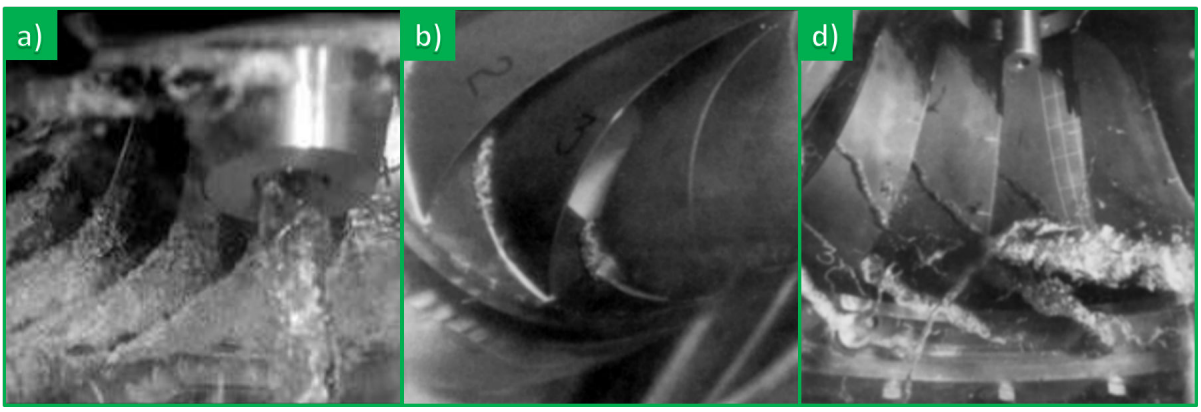

Figure 1.19: a) trailing edge cavitation; b) leading edge cavitation; d) cavitation vortices [33]

- In the region (d), both, the specific energy and flow rate factor are low. The attack angle is not well adapted and causes the flow separation and consequently some cavitation vortices (fig. 1.18 and 1.19). This type of cavitation results in increased vibrations of the machine.

- At part load region (e), the cavitation vortex occurs in the draft tube (fig. 1.18 and 1.20) as a result of a water circulation at the turbine outlet. It causes strong, low-frequency vibrations and changes the hydraulic condition. The size of the vortex depends mostly on the cavitation number. On the other hand, the vortex shape depends on the relative flow rate ϕ/ϕ_0. For high flow rates, the shape is almost axi-symmetric and the rotation is opposite to the turbine rotation (fig. 1.20, left). On the contrary, for low flow rates, the rotation has the same direction as the turbine

and the vortex is rotating around the draft tube (fig. 1.20, right). Typical rotating vortex frequency is between 25% and 35% of the turbine rotation frequency.

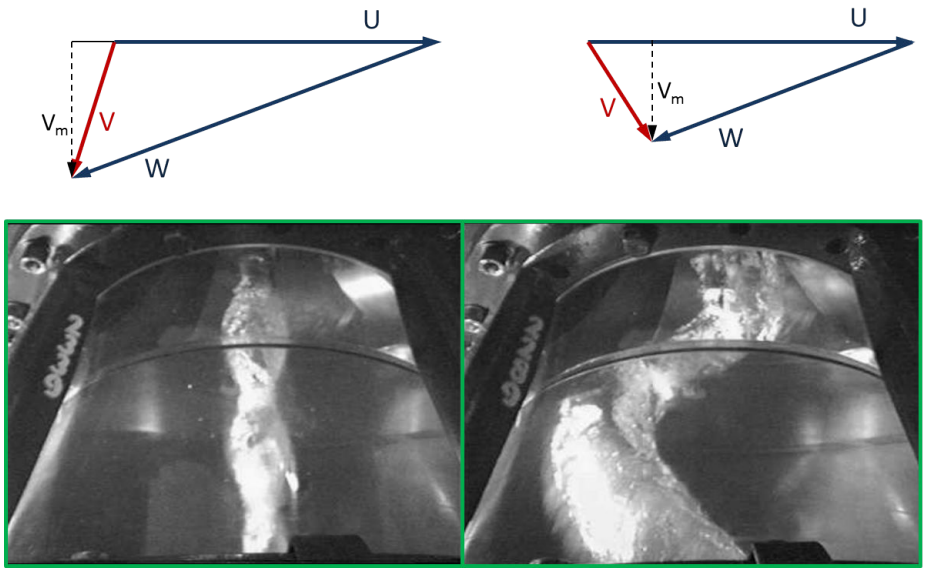

Figure 1.20: Cavitation vortex and outlet velocity triangles [33]

1.5.6 Cavitation in pumps

Cavitation in pumps occurs mostly on both sides of the impeller blades, depending on the attack angle at the impeller leading edge. As seen on the figure 1.21, in the case of the reduced flow rate, the cavitation appears firstly on the suction side of the blade. On the contrary, when the flow rate is increased, the cavitation typically occurs on the pressure side.

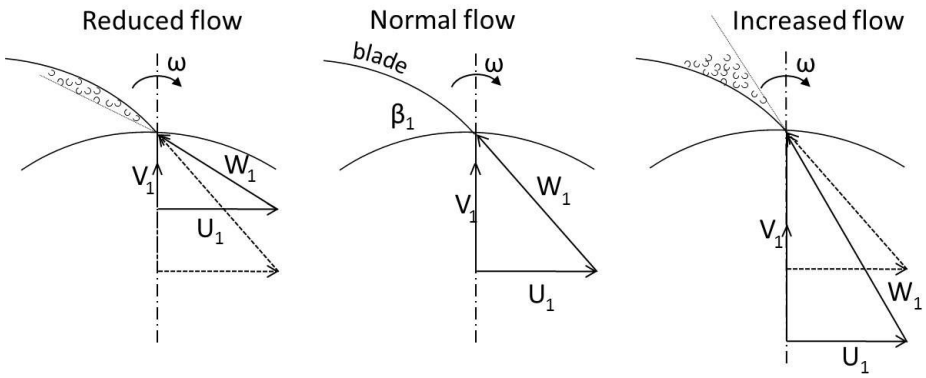

Figure 1.21: Velocity triangles

On the figure 1.22 we can see all different forms of cavitation in the centrifugal pump. The cavitation forms (on the suction side (a) and on the pressure side of the blade) originate in the non-adapted flow attack angle. On the other hand, the cavitation in the

(c) region (sealing gap) occurs due to secondary flows that cause local pressure decrease. In special cases of increased flow rate, the cavitation can be present also in the region (d), on the spiral case tongue (centrifugal pumps) [6]. Similarly, in the case of the increased flow rate in the pump-turbine, the cavitation can occur on the pressure side of guide vanes, if the guide vanes opening angle is not adapted to the flow.

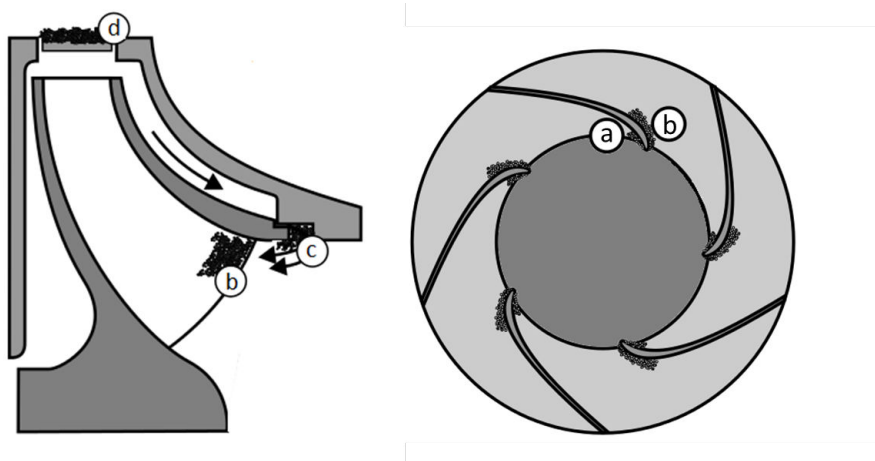

Figure 1.22: Cavitation in centrifugal pump [90]

Generally, the presence of the developed cavitation forms in a pump can lead into:

- reducing the pump performance (reducing net head H_n), if the flow rate Q and rotating speed n remain constant;
- decrease of the efficiency η;
- changing the velocity and the pressure profile inside the pump;
- damage of the pump due to cavitation erosion.

The intensity and effects of the cavitation depend mostly on the NPSH (net positive suction head) number, which is comparable parameter to the cavitation number σ for the case of the turbines of single profiles.

NPSH number definition

Net positive suction head number can be given for the system as well as for the machine. When we try to describe and compare the system probability for the cavitation occurrence, available NPSH number ($NPSH_A$) can be calculated as:

$$NPSH_A(m) = \frac{p_0 - p_v}{\rho g} + \frac{v_0^2}{2g} + \Delta Z - H_{loss}. \tag{1.14}$$

Index 1 in the equation 1.14 refers to conditions at the lower reservoir. It is important to stress that ΔZ has positive value, if the level of the pump-turbine is lower than the lower reservoir of the PSP system, as seen on the figure 1.23. H_{loss} represents the losses in the system between the machine and the lower reservoir. Kinetic energy component is usually estimated to 0, since the water level in the reservoirs changes very slowly.

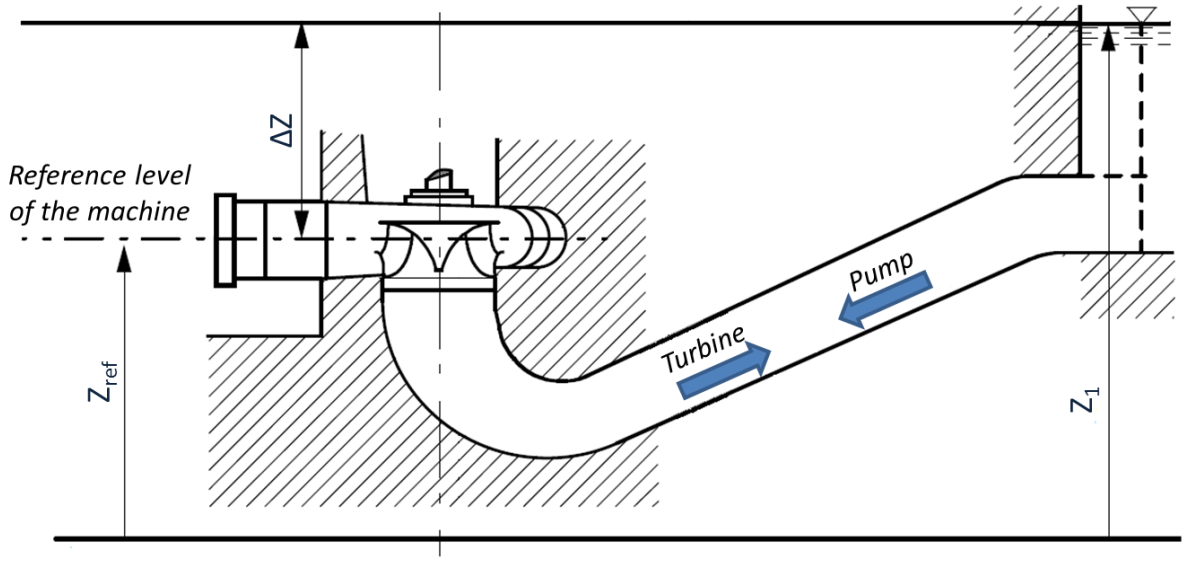

Figure 1.23: Position of the pump-turbine system

According to the equation 1.14 and the figure 1.23, the level of the water in the lower reservoir influences the cavitation level in the pump-turbine. Therefore, in order to minimize or avoid cavitation, the position of the pump-turbine is generally significantly under the level of the lower reservoirs.

On the other hand, the required NPSH value ($NPSH_R$) is used to define various levels of developed cavitation inside the machine. Some of the typical values are presented on the figure 1.24 and are defined as:

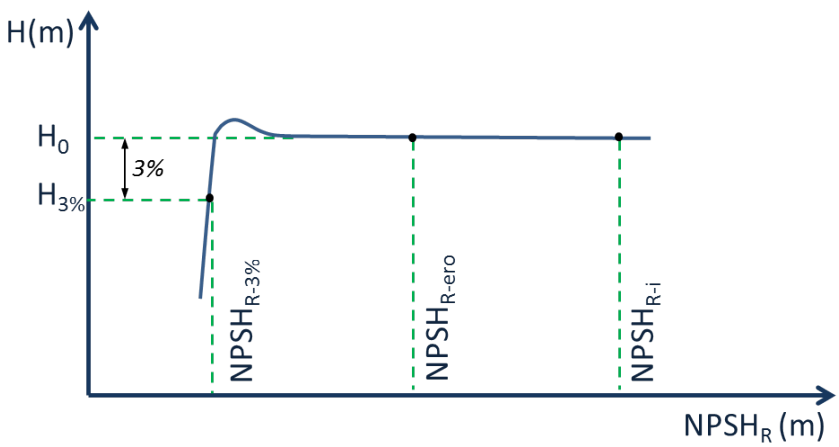

Figure 1.24: Typical pump-turbine $NPSH_R$ characteristics for Q = const. (head drop curve)

- $NPSH_{R-i}$ represents the incipient cavitation value. Experimentally, it can be obtained by the visualization measurements in the pump (pump-turbine).

- $NPSH_{R-ero}$ represents the value, where the cavitation intensity is high enough to cause the erosion on the blades of the pump.
- $NPSH_{R-3\%}$ represents the cavitation value, when the head drop, due to presence of the cavitation, reaches 3% of reference no-cavitation head H_0. $NPSH_{R-3\%}$ value can be obtained by the global measurements of the pump (pump-turbine) performance that are described in the international standard IEC 60193 [12].

Slight increase of the performance can be sometimes observed on $NPSH_R$ head drop curve for a reduced flow rate, similar as for the turbine cavitation characteristics (fig. 1.17). Also the origin of the improvement is the same. Therefore, an attack angle at the leading edge of the blade is optimized due to the cavitation sheet, attached to the blade. As mentioned, the $NPSH_R$ values are usually obtained through measurements and visualization. However, numerical simulations can be as well used to predict the NPSH values and forms of cavitation for certain values, which is also one of the several objectives of the presented PhD work.

$NPSH_R$ values are significantly influenced by the flow rate. The incipient cavitation value curve has the lowest value at the optimal flow rate, as presented on the figure 1.25. Due to velocity triangles (fig. 1.21), the incipient cavitation at the reduced flow rate occurs on the suction side of the blades. On the contrary, at the increased flow rate it occurs on the pressure side of the blade. Cavitation on the pressure side of the blade has a more significant effect on the performance of the pump-turbine than the cavitation on the suction side. Indeed, the $NPSH_{R-3\%}$ value is higher for the increased flow rate than for the part load as seen on the figure 1.25.

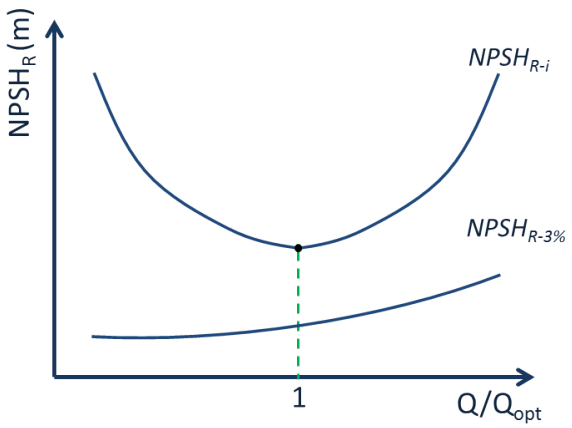

Figure 1.25: Flow rate influence on the $NPSH_R$ values

Several times in the presented PhD work, $NPSH$ value is mentioned without indicators R (required) or A (available). It should be underlined that since one of the objectives of the work is to study numerically the influence of the cavitation intensity inside the pump-turbine, $NPSH$ value always represents required $NPSH$ value ($NPSH_R$).

1.6 Numerical simulation overview

Computational fluid dynamics (CFD) is taking a strong part in the field of fluid mechanics. Development of the computers and the software provided the academics and the industry

with useful tools to analyze, predict and improve the flow behavior. Comparing to the experiments, CFD approach is normally cheaper and can provide more detailed information about the phenomena that scientists and engineers are interested in. However, it still has its limits in the computational power and the accuracy of the given results, therefore an evaluation of the calculated data is always necessary. Typically, a good combination of the experimental and the numerical studies gives the best and the most cost-efficient results.

1.6.1 CFD approaches

To achieve good results from the numerical simulations, it is important to know which types of simulations are available and what are their limitations. Generally, three different approaches are available to simulate the flow behavior. Direct Numerical Simulation (DNS) solves unsteady Navier-Stokes equations and computes the turbulence forms on all scales. If the time and space discretization are good enough, the DNS simulations should provide the most exact results. Kolmogorov [56] made a study on the appropriate spatial discretization for high Reynolds turbulent flows in 1941. However, when performing DNS, the limits are set with the available computational time. So far, even the fastest and the largest supercomputers are capable to calculate only the simple geometries with low Reynolds numbers. Taking into account the expected development of the computational power, the DNS simulations for complex geometries with high Reynolds number will not be available for a few decades.

Second approach is known as a Large Eddy Simulation (LES). It is a compromise between DNS and RANS simulations. It computes the turbulent forms, but not on all scales. Therefore, with a filter selection, one must choose the size of the turbulent structures that will still be calculated. The challenge is to find a good compromise between the accuracy and the discretization. The turbulence production occurs on the large scale, but dissipates on the small scales, therefore, it is essential to find the appropriate time and spatial discretization. Additionally, the modeling of the boundary layers may be very demanding due to need for very dense mesh close to the walls. Feasibility study on the mesh size should be performed before actual numerical simulations. LES approach is getting more and more popular in last years in academics, however it is not completely ready yet to be used for industrial applications. The most extensive study in the field of the turbomachinery was recently performed by Pacot [69]. The computation for one operating point lasted around 12 days for 40 impeller revolutions on an about 10000 computational cores. It is clear that this amount of computational capacity is not widely available. On the other hand, the LES simulations have shown potential for predicting the flow behavior.

The only remaining approach is to solve Reynolds Averaged Navier-Stokes (RANS) equations. So far it is extensively used in the industry as well as in the academics. The approach is economical, since it can be used for a wide range of application even on a casual PC. The drawback is that the RANS approach provides statistically averaged solutions for the turbulent behavior. Choosing appropriate turbulent model is very important. The RANS equations can be modified to Unsteady RANS (URANS) equations to perform the unsteady calculations. More about the RANS and URANS approach follows in the chapter 2.

1.6.2 CFD tradition in LEGI

Tradition of the numerical simulations in the LEGI laboratory has a long history, especially in the field of the cavitation modeling. The initial model was based on a barotropic law approach and developed for 2D non-viscous flows [21]. Successive improvements of the 2D numerical and physical models were carried out during the last decades, concerning mainly the turbulence modeling and the compressibility effects on turbulence [14], [19]. The application of the numerical tool to study different unsteady cavitating flow configurations allowed very reliable experimental validation [30], [31], [61], [79], [80].

To analyse 3D complex flows, especially in the field of the turbomachinery, the cavitation model was implemented in the 3D URANS code Fine/TURBO^{TM} in the scope of a very fruitful collaboration between the LEGI and Numeca International [15], [16]. Mainly during the thesis works of Pouffary [74] and Coutier-Delgosha [13], many steady and unsteady calculations were performed for cavitating inducers, in collaboration with the CNES and the rocket engine division of SNECMA-Moteurs, with successful experimental validation in cold water applications [18], [37], [75], [76] . The final objective was providing assistance to the design and prevision of operating range of rocket engine turbopumps, taking into account the hydrodynamic instabilities of cavitating flows. Other applications of unsteady cavitation modeling have also been investigated in the research team, for example in the field of cavitation erosion [29], [57].

The presented work is part of this overall context. It took into account the previous research team's know-how on numerical calculations and flow analyses in turbomachines. Based on this know-how, the code Fine/TURBO^{TM} and the barotropic cavitating model have been applied to study the flows inside of the considered pump-turbine geometry.

For the research team, it was the first time that this type of machine and the associated unsteady and instable phenomena were studied. The methodology developed during this thesis to mesh, to calculate and to analyze these complex mechanisms is a major contribution to the future works, mainly in the scope of the storage program at the Supergrid institute.

1.7 Thesis objectives

CFD simulations provide us a useful, cost-efficient tool for analyzing the flow phenomena in hydraulic machines. Presented study focuses on the predicting and analyzing the flow under the complex, part load pumping mode off-design conditions. The studied geometry is a reduced-scale high head pump-turbine model ($n_q = 27$). At the part load regimes, the continuous operation of the machine can be limited by the rotating stall and the cavitation. The objectives of the thesis are the following:

- The first objective is to use a commercial code, tested before in the laboratory, to develop a numerical simulations approach allowing the accurate prediction of off-design part load phenomena in pumping mode operating regions. The main goal is to predict accurately the cavitation forms, drop of performance due to cavitation and to carry out local analysis of the flow patterns in cavitating flow. Moreover, a global analysis of the cavitation impact on the rotating stall flow patterns will be performed. The code should give an accurate global prediction of the hump zone on the performance curve caused by the rotating stall. It should also enable the analysis of the unsteady flow pattern for wide range of the flow rates and the NPSH

values. Therefore, the simulations should be numerically stable and robust, but still accurate.

- Another objective is to develop the computationally cheap global methodology using steady RANS equations that will detect the stable and the unstable pumping mode operating regions. Mentioned methodology can be very useful for fast, practical flow analysis of the variables such as guide vane opening angles, guide and stay vanes geometry, the size of the radial gap between the impeller and the distributor and others. It should provide accurate global results for a large amount of the operating points for a relatively low computational cost.

- The final objective is to make a detailed analysis of the rotating stall behavior and origins by performing full geometry unsteady simulations. The analysis should include the investigations of the velocity and pressure fields in the distributor regions. Moreover, the influence of the flow rate, guide vanes opening angles, guide vanes geometry and radial clearance gaps should be studied in detail in order to give the global image about the phenomenon. The analysis, the developed tools and methodology could be an important basis for the future studies of the unsteady off-design flow phenomena, not only on the presented pump-turbine geometry, but on the other kind of pump-turbines and centrifugal pumps as well.

1.8 Document organization

The document consists of three parts. **Part I** has described the background of the study. It started with the introduction to the energy sector challenges, showed the importance of the pumped storage power plants (PSP) for the electrical grid and presents the rentability of the PSP systems. The operation of the reversible pump-turbine has been explained by presenting the basic laws, principles and classifications for centrifugal pumps and pump-turbines. Additionally, the unsteady, off-design flow phenomena has been presented and explained. An important part of the **Part I** was the presentation of the cavitation that starts with a basic explanation of the phenomenon and continues with describing the appearance in the hydraulic machines and the related challenges.

Part II will describe the used tools and methodologies. It will start with a short description of the background of the experimental measurements that have been done in the Alstom Hydro laboratory in Grenoble. It presents the possible sources of discrepancies between the experimental and the numerical data. **Part II** continues with the presentation of the numerical setup. Numerical domain and methodology is presented starting with the governing equations and continuing with the turbulence and cavitation modeling, meshing and a brief description of the applied numerical scheme.

Part III presents the results. These are divided into three chapters. The first one is focused on global results of the steady simulations on the periodic mesh including the analysis of the cavitating flow. The second one presents the approach to detect the stable and the unstable operating points that depend on the guide vane openings and geometry. The third chapter shows the results of the unsteady simulations followed by the detailed analysis of the rotating stall phenomenon.

Part II

Tools and Methodology

Chapter 2

Physical and numerical modeling

The idea behind the CFD simulations is to have a tool that can provide us with detailed information about the flow behavior in reasonable time and computational cost. Moreover, the cost and the time of the computations are the biggest CFD advantage compared to the experiments. The constant development of the computers enables us larger and cheaper computations in a shorter time. Indeed, for the field of hydraulic turbomachines, we can already obtain a great amount of reliable results in one or a few days, using just a normal personal computer. On the other side, preparing and performing an experiment can take lot of time (weeks), large testing rigs, expensive equipment and great amount of working hours. The experiments are also limited by the amount and the position (mostly on solid walls) of the measuring points, whereas numerically we can get the data in all calculated domains. However, if performed accurately, the experimental results are probably still more reliable than the numerical ones.

CFD simulations consist of three important parts:

- **Preprocessing** is used to define the problem. During the procedure, one needs to:
  - define the physical bounds (geometry),
  - set the spatial discretization (mesh),
  - choose the governing equations,
  - define the boundary conditions.
- **Simulation** is the longest part of the CFD, when the equations are solved iteratively for a steady state or a transient solution.
- **Postprocessing** is used for analyzing and visualizing the obtained results.

Important part of the CFD simulation is also the evaluation of the results. Small difference in the settings can lead into completely different results. Therefore, one needs to evaluate if the results are physical or they are affected by some numerical error or inaccuracy. When choosing the best models to describe the certain problems, extensive study of the literature can play an important role. Moreover, the comparison with the experimental data is always very welcome. Firstly, to confirm the numerical results and secondly, to confirm the numerical code that enables to provide the data for various operating points in a short time.

2.1 Navier-Stokes' equations

The motion of the fluid is governed by the mass (eq. 2.1) and the momentum (eq. 2.2, derived from Newton's second law) conservation laws. The flow is a result of the external forces, such as gravity, pressure, the shear stress that origins in the movement of the solid surface close to the fluid and the rotation induced body forces, such as Coriolis force. Governing equations are known as Navier-Stokes equations. For incompressible Newtonian fluid with a constant density in a Cartesian coordinate system, they can be written in the following way:

$$\frac{\partial u_i}{\partial x_i} = 0, \tag{2.1}$$

$$\frac{\partial u_i}{\partial t} + u_j \frac{\partial u_i}{\partial x_j} = \frac{1}{\rho}\left(-\frac{\partial p}{\partial x_i} + \frac{\partial \tau_{ij}}{\partial x_j}\right) + f_i. \tag{2.2}$$

For a viscous Newtonian fluid, the shear stress τ can be expressed by the strain rate tensor D_{ij} and the dynamic viscosity μ:

$$\tau_{ij} = 2\mu D_{ij} \qquad ; \qquad D_{ij} = \frac{1}{2}\left(-\frac{\partial u_i}{\partial x_j} + \frac{\partial u_j}{\partial x_i}\right). \tag{2.3}$$

By introducing τ into the equation 2.2 we get the incompressible Navier-Stokes equation for Newtonian fluids:

$$\frac{\partial u_i}{\partial t} + u_j \frac{\partial u_i}{\partial x_j} = \frac{1}{\rho}\left(-\frac{\partial p}{\partial x_i} + \mu \frac{\partial^2 u_i}{\partial x_i \partial x_j}\right) + f_i. \tag{2.4}$$

Navier-Stokes equations can be solved analytically for the laminar flow. The value that defines if the flow is laminar or turbulent flow is a dimensionless Reynolds number Re. On one hand, the laminar flow occurs at the low Reynolds numbers, where the viscous forces are dominant. It can be observed as a smooth, constant fluid motion. On the other hand, the turbulent flow occurs at high Reynolds numbers, where the inertial forces are dominant. It is characterized as chaotic and it produces vortices, eddies of various sizes and other flow instabilities. Reynolds number is therefore defined as a relation between the inertial and the viscous forces and can be written as:

$$Re = \frac{inertial\ forces}{viscous\ forces} = \frac{\rho v L}{\mu} = \frac{\rho U_2 D_2}{\mu}. \tag{2.5}$$

For the case of the pump-turbines, the velocity component v can be substituted with U_2 (figure 1.6) and characteristic length L with an outer diameter D_2. The critical value, where the laminar flow changes into turbulent inside the pipes, is between $Re = 1700$ and $Re = 2300$, according to the literature [25]. In our pump-turbine case the Re reaches around $Re = 3,6 \cdot 10^6$, which means that the turbulence is fully developed.

Modeling the turbulent flow becomes much more demanding than the laminar. As already mentioned, the DNS and mostly also the LES approaches are still computationally too expensive. The remaining and most widely used is therefore the RANS approach. The idea is to use Reynolds decomposition and separate the flow variable u (in case of velocity) into the mean component $\bar{u}$ and the fluctuating component u':

$$u(\vec{x},t) = \bar{u}(\vec{x}) + u'(\vec{x},t). \tag{2.6}$$

By introducing the equation 2.6 into the incompressible Navier-Stokes equation (eq. 2.4) we can get the Reynolds averaged Navier-Stokes equations:

$$\frac{\partial \bar{u}_i}{\partial t} + \bar{u}_j \frac{\partial \bar{u}_i}{\partial x_j} = \frac{1}{\rho}\left(-\frac{\partial \bar{p}}{\partial x_i} + \mu \frac{\partial^2 \bar{u}_i}{\partial^2 x_j}\right) - \frac{\overline{\partial u_i' u_j'}}{\partial x_j} + f_i. \tag{2.7}$$

For the steady RANS equations there is no time dependence, therefore, the time depending part equals 0:

$$\frac{\partial \bar{u}_i}{\partial t} = 0. \tag{2.8}$$

Due to Reynolds stress term $\overline{u_i' u_j'}$ we get 6 new unknowns, which means that the system of the equations is not anymore closed. At that point it is necessary to involve turbulence modeling that can be done by several approaches.

2.1.1 Unsteady RANS

The difference between the classical RANS equations and the Unsteady RANS equations is the definition of the Reynolds decomposition. The mean component $\bar{u}$ is in the case of the URANS equations, not only function of the space, but also of the time. Therefore, Reynolds decomposition can be written as:

$$u(\vec{x},t) = \bar{u}(\vec{x},t) + u'(\vec{x},t). \tag{2.9}$$

Mean value $\bar{u}$ can be defined as:

$$\bar{u}(\vec{x},t) = \frac{1}{\Delta t}\int_t^{t+\Delta t} \bar{u}(\vec{x},t)dt. \tag{2.10}$$

It is important to define correctly the integral time Δt. It should be long enough to have representative mean value, and on the other hand it should be short enough to calculate the changing of the flow behavior.

Final URANS equation is therefore eq. 2.7 with the space and time depending variables $\bar{u}_i = \bar{u}_i(\vec{x},t)$, $\bar{p} = \bar{p}(\vec{x},t)$ and $\overline{u_i' u_j'} = \overline{u_i' u_j'}(\vec{x},t)$.

2.2 Turbulence modeling

Choosing the right turbulent model might be one of the most important decision during the process of CFD preprocessing. Different approaches of modeling the turbulence have been tested and developed through the last decades. The typical approach for RANS equations is to substitute the Reynolds stress term in equation 2.7 with the eddy viscosity expression (eq. 2.11).

$$\frac{\partial \overline{u_i' u_j'}}{\partial x_j} = \mu_T \left(\frac{\partial \bar{u}_i}{\partial x_j} + \frac{\partial \bar{u}_j}{\partial x_i}\right). \tag{2.11}$$

However, in the literature one can find several different ways of modeling the eddy viscosity. Turbulent models are usually divided into groups, depending on the number of the additional equations they are using. Some of the turbulent model groups are:

- Algebric (0-equation) models are typically used, when fast and numerically stable calculations are required. However, to simulate more precisely the turbulent quantities with good rate of convergence, the higher level turbulence models are advised. Typical example of the algebric model is Baldwin-Lomax model [7].
- 1-equation models, like Spalart-Allmaras model [88], are widely used due to their robustness and ability to treat complex flows. They can be seen as a good compromise between the 0-equation and the 2-equations models. According to [63], they are a very popular choice for simulating aerodynamic external flows.
- 2-equations models are the most widely chosen options in the last decades. Two additional transport equations are used to define the turbulence intensity and length scale. Most famous groups of models for the industrial and academic applications are based on the $k-\epsilon$ and the $k-\omega$ models.
- Reynolds Stress Models (RSM), also known as a second order closure models, are the most complex classical turbulence models. Six separate transport equations are used for the Reynolds stress term. It is the most general of all turbulence models that works relatively well for a wide range of engineering problems. However, it is computationally very expensive and requires high mesh quality. Moreover, comparing to 2-equations models, it is more demanding to achieve the satisfying converged solution.

According to the literature and the previous know-how of the laboratory, the best turbulence modeling compromise for the application of turbomachinery seems to be one of the 2-equations models.

2.2.1 Turbulence model $k-\epsilon$

The standard model has been initially proposed by [50]. Turbulent eddy viscosity μ_t is expressed as a function of turbulent kinetic energy k and the dissipation ϵ (eq. 2.12):

$$\mu_t = \rho C_\mu \frac{k^2}{\epsilon} \qquad ; \qquad C_\mu = 0,09. \tag{2.12}$$

When the production and the dissipation of turbulent kinetic energy k are balanced, it can be assumed that the dissipation rate ϵ is related to the turbulent kinetic energy by the turbulent length scale L:

$$\epsilon \approx \frac{k^{3/2}}{L}. \tag{2.13}$$

The model gives typically good results for industrial application, especially in the free stream areas away from the walls. However, the weakness of the model is the turbulence prediction and therefore the flow separation in the boundary layers close to the walls. In order to avoid the problem, several modifications were proposed to model the boundary regions [71], [84], [92].

The model used in the present PhD study has been developed and presented in 2000 by Hakimi et al. [40] and is implemented in the Numeca CFD solver FINE^{TM}/Turbo. It is a improved $k-\epsilon$ model that uses a novel set of wall functions for the turbulent kinetic energy and the turbulent dissipation based on DNS data of Kim et al. [53]. This $k-\epsilon$ model with wall functions uses a single damping function for the eddy viscosity similar to that used in the low Reynolds $k-\epsilon$ model of Yang and Shih [92] and wall functions for the shear stress and the heat flux similar to those used in the standard model with wall functions. The derived model insures that k, ϵ and the Reynolds stress term $\overline{u_i'u_j'}$ fit to the DNS data.

To sum up, the difference between the used model and a classic low Reynolds model is that in the used $k-\epsilon$ (Extended wall function) model, the turbulent equations are not solved in the first layer next to the wall. Instead, wall functions derived from DNS data are used to define the values of k and ϵ in the first cell next to the wall.

2.2.2 Turbulence model $k-\omega$

The standard $k-\omega$ model uses turbulent frequency ω to define turbulent viscosity μ_t:

$$\mu_t = \rho\frac{k}{\omega} \qquad ; \qquad \omega = \frac{\sqrt{k}}{C_\mu L}. \tag{2.14}$$

The model gives better results than standard $k-\epsilon$ in the boundary regions but is less exact in the free stream flow. Considering that, the combined model that uses $k-\omega$ approach in the boundary regions and the $k-\epsilon$ in the free stream flow away from the walls has been developed. It is known as a $k-\omega$ (SST). The advantages and experiences are described by [65]. Nowadays, $k-\omega$ (SST) is probably the most widely used turbulence model in the field of turbomachinery, especially with the optimization of the turbulent viscosity called SST-SAS model that enables resolving more detailed structures of the flow patterns (introduced by Menter [64] and Egorov [26]).

Both, $k-\omega$ (SST) and $k-\epsilon$ (Extended wall function), have been tested during the present work. The comparison between the models is presented in the chapter 3.

2.3 Cavitation modeling

Numerical modeling of the cavitating flow can be done in several different ways. Most of the cavitation models consider two aggregate phases (liquid and vapour) as a homogeneous liquid-vapour mixture.

2.3.1 Homogeneous approach

Cavitating flow is a mixture of liquid and vapour phases. Since hydrodynamic cavitation occurs at high velocities, one can assume that there is a negligible velocity slip [52] on the border between the phases, which means that the flow can be considered as homogeneous. The properties of the flow depend on the local void ratio α:

$$\alpha = \frac{vapour\ volume}{cell\ volume}. \tag{2.15}$$

The density and dynamic viscosity of the mixture phase can be simply expressed as initially proposed by [8]. Index m represents mixture, l liquid phase and v vapour phase:

$$\rho = \rho_m = \alpha\rho_v + (1-\alpha)\rho_l, \tag{2.16}$$

$$\mu = \mu_m = \alpha\mu_v + (1-\alpha)\mu_l. \tag{2.17}$$

Modeling of the cavitating flow using homogeneous approach requires to modify the Navier-Stokes equation for mass conservation (2.1). Since the density is not constant anymore, it can be written as:

$$\frac{\partial\rho}{\partial t} + \frac{\partial(\rho u_i)}{\partial x_i} = 0. \tag{2.18}$$

Mass and momentum conservation equations have to be solved by using variables for mixture flow ($\rho_m,\ \mu_m,\ u_m$). The difference between the cavitation models is in the modeling of the evaporation and the condensation process. Two different approaches have been proposed through the last decades. Moreover, they have been extensively tested in the laboratory.

- **Barotropic model** defines the mixture density by local pressure.
- **Bubble dynamic models** use source terms and are usually based on Rayleigh-Plesset equation for bubble dynamics. Similar approaches are based on the mass conservation for vapour and liquid phase.

2.3.2 Barotropic model

Barotropic model was initially proposed by Delannoy and Kueny [21] and was also used by Coutier-Delgosha [13] [14], Fortes-Patella [31], Pouffary [74], [75], [76], Reboud [79], Hofmann [17] and others to study steady and unsteady cavitating flows in turbomachinery.

Fluid is defined by density ρ that is calculated for each cell. If the mixture density ρ equals to the density of the liquid ρ_l, we can suppose that the full cell is filled by liquid. On the contrary, if the density in the cell ρ equals the density of the vapour phase ρ_v, the cell is filled by vapour. The law that defines the density variation in the cells is called barotropic state law and is presented on the figure 2.1.

Density in the cell is directly related to the local pressure p. When the local pressure p is lower than $p_v - \Delta p/2$, the whole cell is filled with vapour. On the contrary, when the local pressure is higher than $p_v + \Delta p/2$, the whole cell is filled with liquid.

The mixture region $p_v - \Delta p/2 < p < p_v + \Delta p/2$ is defined by the minimal sound velocity in the liquid-vapour mixture c_{min} that can be written as $c_{min}^2 = \frac{\partial p}{\partial \rho}$. To provide a smooth density transition from the liquid to the vapour phase, the density ρ is described by a sinus function (eq. 2.19):

$$\rho = \frac{\rho_l + \rho_v}{2} + \frac{\rho_l + \rho_v}{2} sin\left(\frac{p - p_v}{c_{min}^2}\frac{2}{\rho_l - \rho_v}\right). \tag{2.19}$$

The size of mixture zone is therefore defined by the value $\frac{1}{c_{min}}$. A smaller c_{min} represents smaller mixture region. However, during the modeling one does not have direct access to the parameter c_{min}. If the density ratio between the liquid and the vapour phase

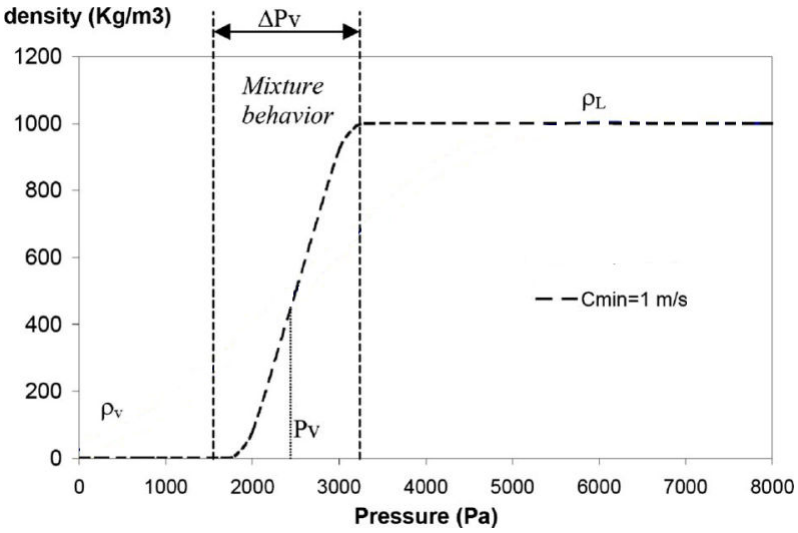

Figure 2.1: Barotropic state law

is considered very high ($\rho_v << \rho_l$), then the parameter A_{min} is used instead of c_{min} and can be calculated as (eq. 2.20):

$$A_{min} = \sqrt{\frac{\rho_l - \rho_v}{2} c_{min}^2}. \tag{2.20}$$

Local void ratio α is defined by the local density of the mixture (eq. 2.21):

$$\alpha = \frac{\rho - \rho_l}{\rho_v - \rho_l}. \tag{2.21}$$

The density of the vapour ρ_v changes significantly with the temperature. The typical value for $20°C$ and 100 % humidity is $\rho_v = 17,3g/m^3$. However, authors have often used different values for the vapour pressure ρ_v, everything between $1g/m^3 < \rho_v < 100g/m^3$ in order to increase the robustness of the simulations. Detailed analysis and influence study of the parameters have been described by Pouffary during his PhD thesis work [74].

Working with barotropic state law for the modeling of cavitation has normally shown very good matching with the experimental data. However, there was often the problem of the numerical robustness and stability that could lead into a not satisfying convergence or even non-converged solution. To set good parameters, it often requires knowledge and some experience with the parameters. Pouffary [74] and Coutier [13] have also shown that turbulence models based on $k - \epsilon$ work better with the barotropic state law than turbulence models based on $k - \omega$.

In the presented work, the barotropic model is used in all cases of the cavitating flow with the constant $c_{min} = 1m/s$ as it has been proposed by Reboud [80] and later thermodynamically proved by Goncalves and Fortes-Patella [36]. Additionally, the ratio between the vapour and the liquid density has been set to 0,01 and A_{min} to 23. The values remained constant for all the cavitating simulations.

2.3.3 Bubble dynamic models

The model is typically based on the Rayleigh-Plesset equation and has been initially used by Kubota [58]. It describes the radius of the bubbles in relation to the local pressure.

The radius is defined by the void ratio and therefore the density. A similar approach, based on more complex relation between the bubble radius and local pressure, has been proposed by Schnerr and Sauer [83]. Both cases and several others as well include the predefined parameters such as the density of the bubbles and the bubble radius that are hard or even impossible to estimate. The simulations based on the described models therefore depend on the input parameters that can give very wide range of results.

Void ratio transport equation models

The approach is based on the mass conservation for the vapour or the liquid phase. The advantage is that the model takes into account the time influence on the mass transport through the empirical equation for the source term. It also enables for the modeling of the internal forces influence on the cavitation structures, which can affect the extension and the transport of the cavitation bubbles and clouds. The approach has been developed and used by Merkle [66], Kunz [59] and Singhal [85]. Optimization of the model for the rapidly changing pressure field has been proposed by [98].

Another advantage of the model is that we don't need to estimate the parameters about the density of the bubbles or bubble radius, however, we still need to estimate the constants regarding appearance and sink of the bubbles, which might be a difficult task as well and may vary from case to case.

For a detailed information about the available cavitation models, see [20].

2.4 Scaled pump-turbine numerical domain

Numerical geometry for the presented PhD work has been provided by Alstom Hydro together with some available experimental data. The investigated machine is a reduced-scale high head pump-turbine model with the presented characteristics (tab. 2.1). More detailed information about the geometry are not available due to confidential aspects. All the presented calculations have been done in a pumping mode regime.

Specific speed n_q	27
Number of impeller blades	9
Number of guide vanes	20
Number of stay vanes	20
Rotational speed n	1000 rpm
Operating range ϕ	0,034 - 0,045

Table 2.1: Pump-turbine characteristics

As presented on figure 2.2, the domain consists of a draft tube cone, an impeller with 9 blades, 20 guide vanes, 20 stay vanes and a convergent expansion instead of a spiral case. Two main advantages of the convergent expansion are to enable the periodicity condition for whole domain (if necessary) and due to convergent shape avoiding numerical instabilities at the outlet of the domain. The draft tube (cone) length is around 3 times longer than inlet diameter D_1.

Probably one of the most important information about the geometry is the radial gap between the outlet of the impeller and the inlet of the distributor. Various opening angles $(12°, 14°, 16°, 18°)$ and 2 different guide vane geometries have been studied and the radial

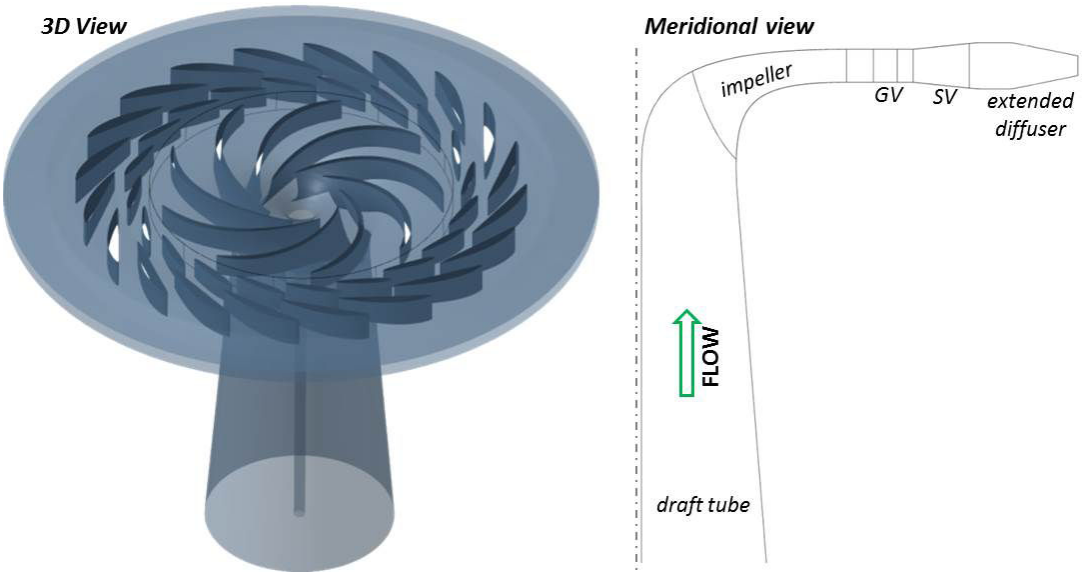

Figure 2.2: Numerical pump-turbine domain; left: 3D view, right: Meridional view

gap has changed for each opening as well. The gap sizes, relative to the outer impeller diameter D_2 for all used opening and both geometries could be seen in the table 2.2.

opening angle	GV I - basic geometry	GV II - new geometry
12°	13,3 %	12,9 %
14°	12,6 %	12,2 %
16°	11,3 %	11,6 %
18°	10,7 %	11,0 %

Table 2.2: Relative gap size for 2 guide vane geometries and 4 guide vane openings

It can be seen from table 2.2 that the relative gap size changes significantly with the opening angle. For the basic geometry the changing of the GV opening angle from 18° to 12° leads into increasing the size of the gap for 24,3%. The influence of the gap size on the flow behavior will be additionally presented and analyzed in the results.

2.5 Meshing

Meshing, together with the boundary conditions, represents one of the most essential parts in CFD. In our case, the Numeca's software AutoGRID 5 has been used to create a fully structured mesh that consists of only hexahedral cells. Several feasibility studies and optimizations have been made to find an adequate mesh. The mesh in our case has to be refined in distributor region to give accurate results in zone of hump-shaped performance curve and rotating stall. Nevertheless, it must be coarse enough in the cavitating regions to enable robust simulations and converged results. Moreover, the number of mesh cells should not be too high in order to avoid the computationally too expensive simulations.

Another important aspect of meshing is to keep the same (or very similar) mesh during all the studies to enable reliable comparison of all the obtained results. Several parts of the mesh have been changed during the studies in our case due to changed guide vanes

opening angle, guide vanes geometry and the periodicity conditions between the blades. However, the quality of mesh remained almost the same for all the presented cases.

Mesh characteristic in table 2.3 refers to the initial periodic mesh for guide vanes opening 14° and for basic guide vane geometry (GV I).

When the periodicity has not been used as a boundary condition between the either impeller blades or distributor vanes, one needs to multiply the number of nodes by 9 in the impeller and by 20 in the distributor.

Component	Number of nodes	Min. skewness	Max. expansion ratio	y^+_{mean}
Impeller	320'000	35°	$1,76$	$7,4$
Distributor	520'000	27°	$1,52$	$8,7$
Draft tube	30'000	41°	$1,06$	$6,0$
Total	870'000	27°	$1,76$	$7,5$

Table 2.3: Periodic mesh characteristics

Dimensionless number $y+$ is a widely used criteria for the estimation of the mesh quality close to the walls. It depends on the size of the first cell on the wall y, the kinematic viscosity ν and the friction velocity u_τ at the nearest wall (eq. 2.22).

$$y+ = \frac{y\ u_\tau}{\nu} \tag{2.22}$$

Mean $y+$ value for the whole domain is below 10 (tab. 2.3). The highest value is reached between the outlet of the impeller and the inlet of the guide vanes (fig. 2.3 - right), where the flow has the highest velocity. However, even in that region the value is below 30, which is still sufficient for the applied turbulence model.

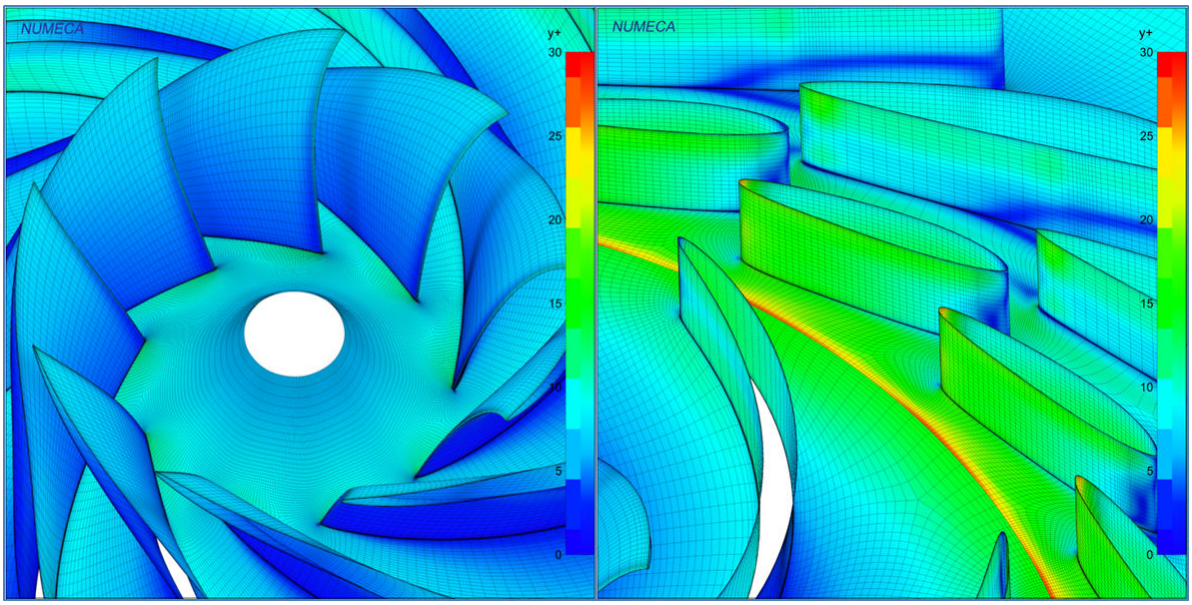

Figure 2.3: Mesh and $y+$ value at the inlet of the impeller (left) and at the distributor (right)

As already mentioned, the mesh in the distributor region has to be finer than in the impeller region in order to get exact detection of the flow separation on the guide vanes. The reason is related to the higher velocities (Re numbers) in this region. If the mesh is

too coarse, the first flow separation that leads into the rotating stall phenomenon does not occur at the correct flow rate.

On the other hand, at the inlet of the impeller, where the cavitation typically occurs, mesh should be coarser in order to be coherent with the homogeneous cavitation model. The applied model is robust and can give good converged results about the average cavitation forms (cavitation clouds) and the loss of the performance due to the cavitation. Nevertheless, the model is not capable to calculate very small forms, such as individual cavitation bubbles. Therefore, if the mesh in the cavitating region is too fine, the code will not reach the convergence that is necessary for reliable results.

2.6 Boundary conditions

Boundary conditions are very important for the stability of the simulations. Moreover, in some cases they have also significant influence on the obtained results, especially at the non-optimal flow conditions, such as part load.

In our case, constant mass flow rate Q has always been set at the inlet of the domain, and at the outlet of the domain, static pressure p_s has been imposed. It is also very important to define correctly rotating and stationary walls of the machine that should be set as similarly as possible to the actual physical conditions, otherwise they can affect the obtained solution, especially at the part load. In our case it was necessary to modify several blocks to get a good definition of the rotating and the stationary no-slip walls as seen on the figure 2.4.

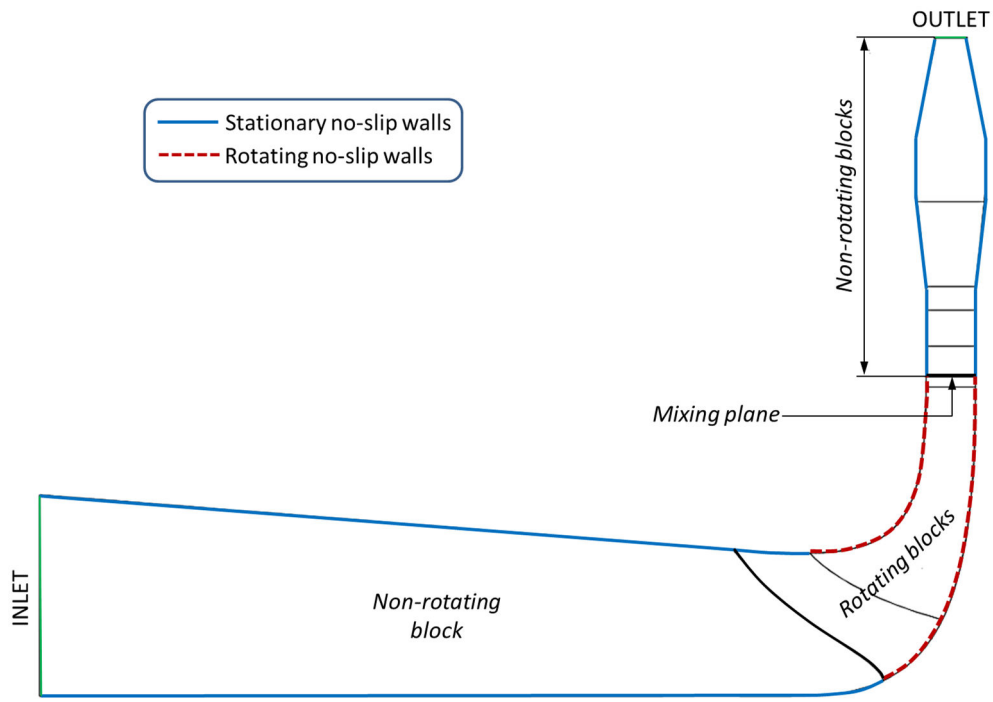

Figure 2.4: Boundary conditions - meridional view

2.6.1 Rotating blocks

Another issue related to the boundary conditions is to define the rotating blocks. Theoretically, it has nothing to do with the physical nature of the machines, where the rotation of the machine leads into the rotation of the fluid inside the machine. However, the definition of the rotating and non-rotating blocks has a strong influence on the numerical aspects of the problem, since numerical codes need this information to calculate the flow behavior inside the machine and around the machine as well.

Applied solver Fine/TURBO^{TM} solves the governing RANS equations for the turbomachinery application for the relative velocity components in the relative system [47] (optional, it can be set to solve for the absolute velocity components in the relative system). When the rotation of the blocks is set to 0, the source term that takes into account the contribution of the centrifugal and the Coriolis force equals 0. The question of the rotating blocks is therefore the following: In which regions do we need to take into account the contribution of the Coriolis and the centrifugal forces and in which regions we should not calculate them?

In most regions of the domain it is very clear which blocks are rotating and which are not. As seen from the figure 2.4, the regions after the impeller (guide vanes, stay vanes, extension) consist of non-rotating blocks. The same should apply to the draft tube and in all the other parts of the domain upstream of the machine (in case of larger domain). Between the rotating and the non-rotating domains in case of steady simulations, the mixing plane can be used only if it is not too close to the impeller blades or guide vanes. The reason is not optimal information transfer from one side of mixing plane to the other (typically, certain velocity or pressure components are averaged). This problem occurs close to the leading edge of the impeller at the part load. The influence of the flow conditions at the inlet of the impeller on the global performance increases with the reducing of the discharge. The reason is that at the part load, the machine affects the conditions in the draft tube, even though the draft tube is located at the upstream side of the system, comparing to the machine.

It has been shown recently by Zhang [97] that the relative tangential velocity component in the region before the impeller does not exist at the nominal flow rate, but occurs at the part load. Moreover, it appears at the certain flow rates and then it doesn't change significantly for even lower flow rates. Zhang also claimed that the rotating stall, which occurs at the part load in the distributor region, origins in the bad flow conditions in the region close to the impeller inlet.

In our case, the interface between the rotating and non-rotating part coincide, which means that the cells on both sides are matching completely and the interface is adapted to the mesh and not the inverse. This kind of interface has been created by splitting the blocks in the draft tube after the whole domain has already been meshed. The advantage of the described approach with the coinciding mesh interface is that the transfer of the information (pressure and velocity fields) is not disturbed and changed (except adding relative velocity component). The detailed analysis will be presented later.

Classical numerical approach used by the majority of the authors uses the rotating block for most of the draft tube or mixing plane interface close to the leading edge of the impeller. As already mentioned, for the nominal and increased discharge, the global results are not significantly affected by the size of the rotating block and the type of the rotor-stator interface. However, it is not the case for the partial load. The tests of this different definition of the rotating blocks will be presented in chapter 3.

To sum up, the flow behavior in the distributor regions can be strongly influenced by

conditions at the inlet of the impeller. Therefore, setting the interface that divides the rotating and non-rotating blocks seems to be very important, especially at the part load operating points. The best way seems to be to create an unite mesh for the impeller and the draft tube (cone) and later split the blocks and create coinciding interface. The rotating and non-rotating regions can therefore be defined without interfering the information (pressure, velocity fields) transfer close to the leading edge of the impeller blades.

2.7 Convergence criteria and time discretization

Steady and unsteady simulations have been performed during the studies. In both cases it is necessary to have good convergence in order to obtain reliable results, which is not very hard for the operating points close to the BEP in non-cavitating regime. However, it gets much more complicated in the cavitation regime and especially at the unstable part load conditions.

2.7.1 Steady simulations

Global residuals are typically used as a convergence criteria for a steady simulations. It depends a lot on the initial conditions, therefore the convergence level cannot be completely quantified. What is more important than the value of the global residuals is the stability of the convergence curve. The simulation reached the convergent solution when it is stable and does not fluctuate too much.

Other criteria that might be even more important than the global residuals are:

- **Mass flow convergence**. The difference between the inlet and the outlet mass flow. For the stable operating points the difference is lower than $0,003\%$. On the other hand, for a very unstable operating points, the difference below 1% is still acceptable.

- **Head convergence**. The numerical head is defined as the total pressure difference between the inlet and the outlet of the numerical domain. The fluctuations of the converged solution are negligible at stable operating points. However, they might appear in unstable off-design regions. For the regions with stalled cells, it often occurs to have 'periodical' fluctuations in a range of a few percent, even for the steady simulations.

- **Torque convergence**. For stable operating points the fluctuations are less than $0,01\%$ and for unstable points, the satisfying convergence is less than $0,1\%$ of the fluctuations.

- **Efficiency convergence** can be difficult to estimate. For stable points, the convergence curve is usually very stable with less than $0,01\%$. However, for the cavitating regimes and if the rotating stall is present, the fluctuations can reach up to 1%.

The convergence difference between stable and unstable operating can be seen on the figure 2.5. Both curves represent a converged solution. However, the global residuals for the operating point with the rotating stall finishes with the 'periodic repetitions'. Similar behaviors could be seen also on the mass flow convergence curve, head convergence curve and others. It means that we have an unsteady phenomenon, which cannot be simulated correctly by the steady approach. The solution may slightly vary depending on the final

iteration. This kind of analysis can help us to detect the stable and the unstable operating regions. Additional analysis on the convergence will be shown in the **Part III**.

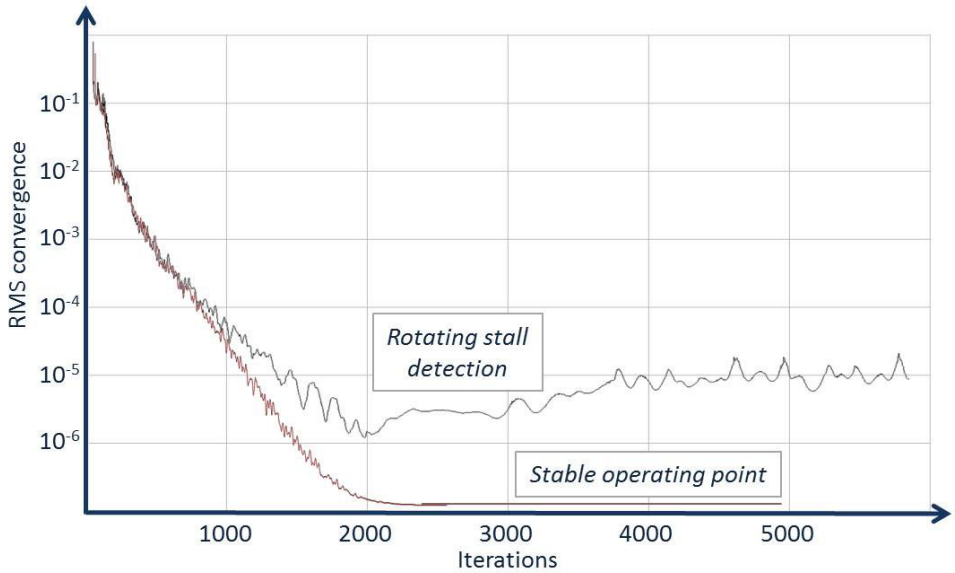

Figure 2.5: Convergence criteria, RMS, steady simulations

2.7.2 Unsteady simulations

Choosing the time step can significantly influence the length of the simulations and also the precision of the results at the end of the simulations. Typical time discretization choices for hydraulic machines are 1° or 2° of the rotation of the machine. One must be aware that the discretization of 1° would result in a calculation twice as long as in the case of 2°.

In the case of unsteady simulations it is important to know, before the simulations, which kind of results are we interested in. The time step choice depends on this information. For example, if we are interested in the pressure fluctuations around the region between the impeller and the distributor, the critical effect would be the interaction between the impeller blades and the guide vanes. In our case of 9 impeller blades and 20 guide vanes it would mean 180 interactions per revolution of the machine. Therefore, the discretization should be 1° (360 time steps per revolution) or even $0,5°$ (720 time steps per revolution). Similar conclusions have been proposed by [10] and [41]. They showed that the discretization of 1° is enough to simulate precisely pressure fluctuations in the region between the impeller and the distributor.

On the other hand, if the goal is to detect, predict and analyze the rotating stall, the time step can be different. The frequency of the stall is usually around 3% of the rotating frequency of the machine, which means that the time discretization of 2° should be enough to catch the correct frequency and forms of the rotating stall.

No matter which discretization time is used, one still needs to provide good convergence for each time step. The approach is called Dual Time Stepping and is similar to the steady simulations for each time step. The number of so called internal iterations can be defined by setting the satisfying convergence level (global residuals) or by limiting the number of iterations for each time step. The convergence is good, when several consecutive iterations

have the same level of convergence. In our case, the number of internal iterations has been limited to 35. The RMS convergence for the already converged solution can be seen on the figure 2.6.

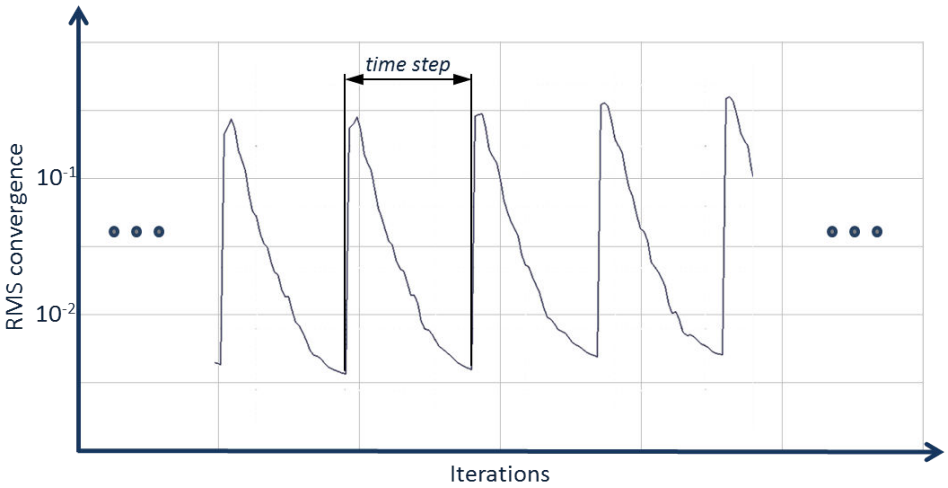

Figure 2.6: Convergence criteria, RMS, unsteady simulations

2.8 Applied numerical scheme

Numeca's Commercial code FINE^{TM}/Turbo has been used as a solver for all presented numerical simulations.

Table 2.4 summarizes already described information about the numerical scheme. Both, steady and unsteady numerical simulations have been performed using RANS and URANS equations. Turbulence model $k - \epsilon$ (Extended Wall Function) has been used for all the simulations, since it has been proven the most accurate for our kind of simulations. Simulations of the cavitating flow have been performed only for steady simulations using the barotropic state law for the mass transfer. For the case of the cavitating operating points, non-cavitating results have been used as initial solution. Mixing plane has been used on the interface between the impeller and the guide vanes for the steady simulations. On the contrary, between the impeller and the draft tube, the interface that enables continuous data transfer has been created. The solver is using central spatial discretization scheme [47]. Local time stepping is used for the steady simulations and dual time stepping for the unsteady simulations (described in [47]).

Chosen time step for the unsteady simulations is 2° of the impeller revolution, what corresponds to 0,00033 s for a rotation speed of 1000 rpm. The number of internal iterations is limited to 35 for each time step. A satisfying convergence for steady simulations is usually reached after around 2000 iterations for stable operating points and up to 15000 iterations for the unstable operating points that are influenced by the cavitation, rotating stall or other kinds of instabilities.

2.8.1 Computational resources

Using numerical simulations for predicting and analyzing the complex flow behavior can bring us very fast to the limits of our computational resources. Several different mesh

Type of Simulation	Steady	Unsteady
Physical model	RANS	URANS
Turbulence model	$k-\epsilon$ (Ext. Wall Function)	$k-\epsilon$ (Ext. Wall Function)
Cavitation model	Barotropic	/
Spatial discretization	Central (2nd order)	Central (2nd order)
Temporal discretization	Local time stepping	Dual time stepping
Time step	/	2° of the revolution
Max iterations/time steps	2000 - 15000 iterations	up to 2700 time steps

Table 2.4: Numerical scheme

settings were analyzed during the presented work. However, for the final analysis and results only one type of mesh has been used in order to have a good comparison between the various boundary conditions and different types of simulation. In other words, in all cases the mesh density does not change, the numerical domain does not change, the periodicity between the blades changes and the type of simulations (steady and unsteady) changes as well.

Approximate estimation of the necessary computational resources for non-cavitating operating points are presented in the table 2.5. Column 'periodic' represents fully periodical mesh that is typically used in the field of turbomachinery. It means that just one channel of the impeller and one channel of the distributor are calculated. The 'combined' mesh consists of one meshed channel in the region of the impeller and a fully meshed distributor. The term 'Full mesh' or 'full domain' represents the type of mesh where periodicity was not used at all. The entire domain (impeller, draft tube and distributor) is 360° meshed and calculated.

	periodic	combined	full domain	full domain
type	steady	steady	steady	unsteady
mesh cells	0,87 M	10,7 M	13,4 M	13,4 M
CPU h	7 - 20	250	320	270/rev
Output	0,2 Gb	1,9 Gb	2,3 Gb	1,7 Gb/ts

Table 2.5: Mesh analysis, CPU time, data size

Simulations of the cavitating flow require from 2 - 5 times more CPU hours, comparing to non-cavitating operating points. The calculation time depends significantly on the intensity of the cavitation, therefore, it is difficult to make a general estimation.

As seen from the table 2.5, the size of mesh differs significantly. On one hand, the calculations on the periodic mesh can be easily performed on the normal personal computer, since only 7 - 20 CPU hours are necessary to reach good convergence for the non-cavitating flow. On the other hand, for the combined and for the full domain, one needs several additional processors and more than 250 CPU hours for steady simulations. Moreover, the typical size of random-access memory (RAM) in a personal computer is not sufficient anymore.

Optimal type of simulation for the exact prediction of the rotating stall is most likely unsteady simulation with a full-meshed geometry. However, in that case, the computational requirements become very demanding. For good stall detection, one needs to use rotating angle 2° of impeller revolution or less, this means at least 180 time steps per one revolution of the machine. Since every time step provides us around 1,7 Gb of data, we

need around 300 Gb of storage to save data and around 270 CPU computational hours per one revolution of the pump-turbine. Nevertheless, to detect the stall characteristic frequency, which is normally between 2% and 6% of the nominal frequency of the machine, more than 10 revolutions should be calculated for each operating point. By multiplying the numbers, it becomes clear that the computational cost and demanding data storage for that kind of simulation is high and not easily affordable.

One of the goals of the study is to find cost-efficient computational approach to simulate part load unstable operating points in pumping mode. Therefore, all our calculations have been performed on the server in LEGI on the maximum of the 12 cores. The calculation time of the longest of the presented simulations has been around 2 weeks. It means that all the calculations in the presented work are fast and repeatable on widely accessible computers.

To conclude, it is necessary to estimate which kind of simulations do we need for good results at each operating point. Moreover, one needs to be aware of the advantages and disadvantages of each type of simulation.

2.9 Comparison of experimental and numerical data

To validate the numerical simulations, they have been compared to the provided experimental data. Comparison was mostly based on the global performance. Head difference has been evaluated numerically as the average total pressure difference between the outlet and the inlet of the numerical domain. Gravitation has been neglected.

Experimentally, the head difference information comes from the pressure sensors that have been installed upstream and downstream of the machine. Position of the pressure sensors on the test rig can be seen in the Appendix 1 (fig. A.2). Comparison of the experimental and numerical (fig. 2.4) position of the pressure reference sections shows that in the numerical domain the spiral case and the draft tube elbow are not taken into account. On the other side, the convergent extension exists only in the numerical domain. It means that the calculated performance cannot be completely the same, because the losses depend also on the domain.

Another effect that has not been taken into account numerically is the leakage flow. In physical machines there is small part of the flow that go around the machine from the high pressure region of the pump-turbine to the low pressure region. It is considered as a loss and it can slightly affect the pump-turbine performance curve. The leakage flow in the centrifugal pump has been studied experimentally and numerically by [24].

However, despite all the mentioned differences, the comparison between the numerical and the experimental data is still possible. If the goal is to have a detailed quantitative comparison of the results, then additional impact factors (leakage, sensors position,...) including mentioned losses and differences should be considered and taken into account. However, since the main idea in our case is to have a good qualitative description of the part load flow phenomena, those factors have not been taken into account. Nevertheless, even in our case, various quantitative comparisons and conclusions have been done and are presented in the thesis **Part III**.

2.9.1 Hysteresis effect

Hysteresis phenomenon represents the differences in the performance curve depending if the flow rate is decreasing or increasing. It occurs typically during the experiments.

Especially the hump zone can be significantly influenced by the hysteresis. Figure 2.7 shows the difference in the hump zone position. If one starts to measure the pump-turbine performance at the increased discharge and than gradually reduces it, the hump zone might occur at a lower discharge than if the measurements are performed at lower discharge first, which is later gradually increased.

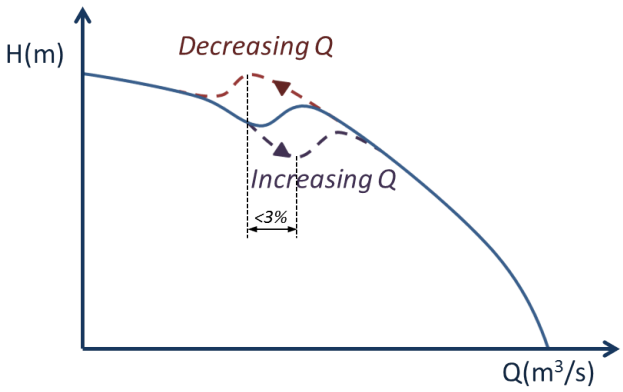

Figure 2.7: Schematic representation of the hysteresis effect on the performance curve

The hysteresis effect has been studied experimentally and numerically on the centrifugal pump geometry by [51] and on the pump-turbine geometry (pumping mode) by [77]. In their cases, the difference between the increasing and the decreasing performance curve do not exceed 3% of the nominal discharge.

During the experiment in the Alstom Hydro's laboratory, the hysteresis effect has not been taken into account. It means that we should take into account the appropriate tolerance for the measured position of the hump zone. Nevertheless, as already mentioned, the aims of the presented study are more qualitative than quantitative. Therefore, the mentioned tolerance is acceptable for the comparison with the numerical simulations and as well for the final analysis and the conclusions.

Part III

Results

Chapter 3

Global results

This chapter focuses mainly on the analysis of the cavitation phenomenon. All the performed calculations represent steady simulations and have been performed on the described periodic mesh. Applied guide vanes opening angle is 14° in all cases. Most of the results have been presented in [48].

The beginning of the chapter also includes the tests of the already presented turbulence models and the chosen boundary conditions. The cavitation analysis is mostly focused on the prediction of the incipient cavitation values, head drop curves, cavitation forms and on the effects of the cavitation appearance on the performance curve.

3.1 Global results for non-cavitating regime

The first global results, presented on the figure 3.1, have been obtained for steady non-cavitating regime. The comparison between the experimental and the numerical data can be analyzed qualitatively and quantitatively as well. The curve is a basis for all further analysis of the cavitating flow. The first source of difference between the experimental and the numerical performance values occurs due to different total pressure (net head) measurement spots between the experimental and the numerical domain. The position of sensors in the experiment are marked on the figure A.2 (Appendix A). On the other hand, the numerical reference points are defined as a inlet and outlet of the numerical domain. Additionally, mechanical and volumetric losses have not been estimated and taken into account numerically.

As shown on the figure 3.1, the position of the hump zone can be detected numerically by the accuracy of 2% on flow rate value. It is a good matching considering the possible hysteresis effect on the experimental curve that has not been taken into account since the information about it has not been provided. The hump amplitude prediction matches well; in the cases of the experimental and numerical curve the specific energy coefficient ψ drops for around 1%.

The comparison between the experimental and the numerical performance curves shows good matching for all the operating points at the normal operating range close to BEP and for the increased discharge as well (for $\phi = 0,0315$ and higher). The discrepancy between the experimental and the numerical curve is around 1%.

The performance decrease, known as a hump zone (fig. 3.1; $\phi = 0,031$, numerically; $\phi = 0,032$, experimentally) occurs due to the flow separation in the distributor area, which later leads into the phenomenon called the rotating stall. The phenomenon will be described in detail in the next two chapters. However, it is important to stress that ac-

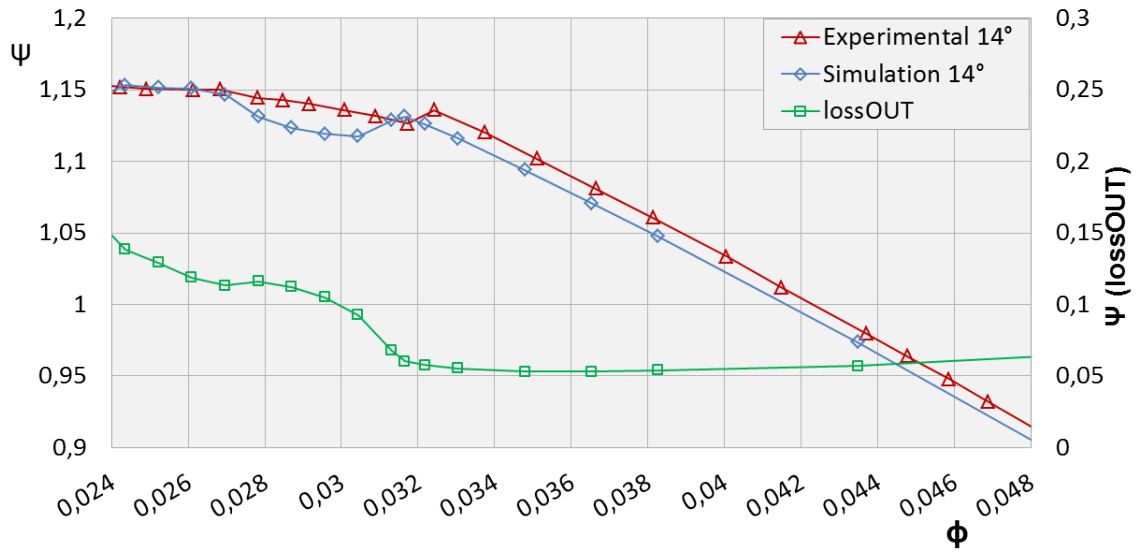

Figure 3.1: Global pump-turbine performance, losses in the distributor - lossOUT (Opening 14°, basic GV geometry, non-cavitating regime)

cording to the performed calculations, the head decrease occurs due to the increased losses in the distributor regions (line lossOUT, fig. 3.1, represents the losses in the distributor regions).

The flow behavior at the significantly decreased discharge (around $\phi = 0,026$) is very complex and 3-dimensional in the distributor regions. Using a periodicity as a boundary condition between the guide and the stay vane channels might not be appropriate. Unsteady simulations that have been performed on full mesh will be analyzed in the chapter 5.

3.1.1 Turbulence model tests

Comparison of the $k - \epsilon$ (Extended wall functions) turbulence model and the $k - \omega$ (SST) model (fig. 3.2) shows that the $k - \epsilon$ (Extended wall functions) model predicts the global performance curve more accurately than the $k - \omega$ (SST) model comparing to the experimental data.

Even though our comparisons are more qualitative than quantitative, there are still two main differences between the models. One is the trend of the line for all the flow rates higher than hump zone, where the trend of the performance curve is more exact in the case of the $k - \epsilon$ (Extended wall functions) model. The other indicator is the prediction of the hump zone. On one hand, the zone is predicted at almost the same discharge and has a similar amplitude for the case of the $k - \epsilon$ (Extended wall functions) and experimental data. On the other side, the $k - \omega$ (SST) model predicts the hump zone at the around 12% lower discharge and has smaller amplitude. The prediction of the hump zone seems to be strongly related to the accuracy of the prediction of the flow separation in the distributor region. From this point, for all presented simulations, turbulence model $k - \epsilon$ (Extended wall functions) has been used.

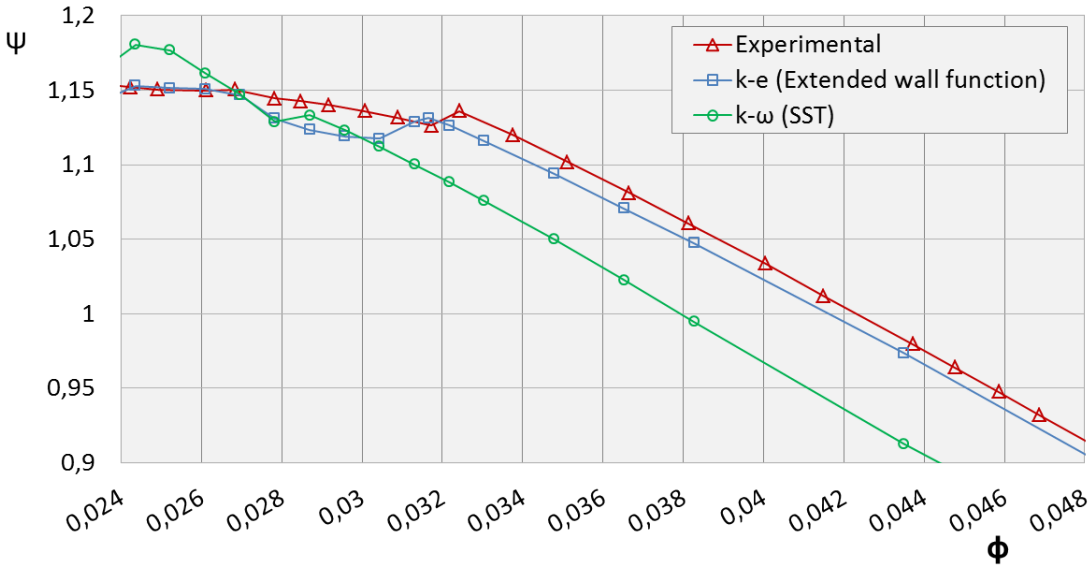

Figure 3.2: Comparison between turbulence models $k - \epsilon$ (Extended wall functions) and $k - \omega$ (SST)

3.1.2 Tests of the rotor/stator interfaces and the rotating blocks

The definition of the rotating blocks and the interfaces around the impeller influence the global prediction of the pump-turbine performance, including the prediction of the hump zone. In our case, the blocks have been defined as shown on the figure 2.4. Figure 3.3 shows the influence of the rotation of the blocks on the global performance comparison and corresponding definitions of the rotating blocks. Definition of rotating and non-rotating blocks is mathematically related to the calculation of the Coriolis and centrifugal forces. If the rotation speed of the block is defined as 0, then the possible Coriolis and centrifugal forces will not be calculated in this block.

If the border between the rotating and the non-rotating blocks is set very close to the leading edge of the impeller (No prerotation - fig. 3.3), the performance prediction is not good for any operating points. It gets worse with reducing the discharge, moreover, hump zone cannot be predicted. On the other hand, if the border is set far away from the impeller (Full prerotation - fig. 3.3), the prediction is good at optimal discharge and at increased discharge. At the part load, the discrepancies increase significantly and the trend of the performance curve is not well predicted. The hump zone still occurs, but at the lower discharge and with a higher hump amplitude.

For comparison, the blue line (Partial prerotation - fig. 3.3) represents the results, where the border between the rotating and non-rotating blocks is set at the distance of around $D_{inl}/4$ from the leading edge of the impeller. The border (interface) is almost parallel to the leading edge as seen on the figure 3.4. As mentioned before, the interface between the rotating and non-rotating part match perfectly, which means that the cells on both sides are matching completely and the interface is adapted to the mesh and not the inverse. This kind of interface has been created by splitting the blocks in the draft tube after the whole domain has been already meshed. Prediction of the performance curve is in this case relatively good for all discharges, the prediction of the hump zone is accurate as well.

The advantage of the described approach with the coinciding mesh interface is that the

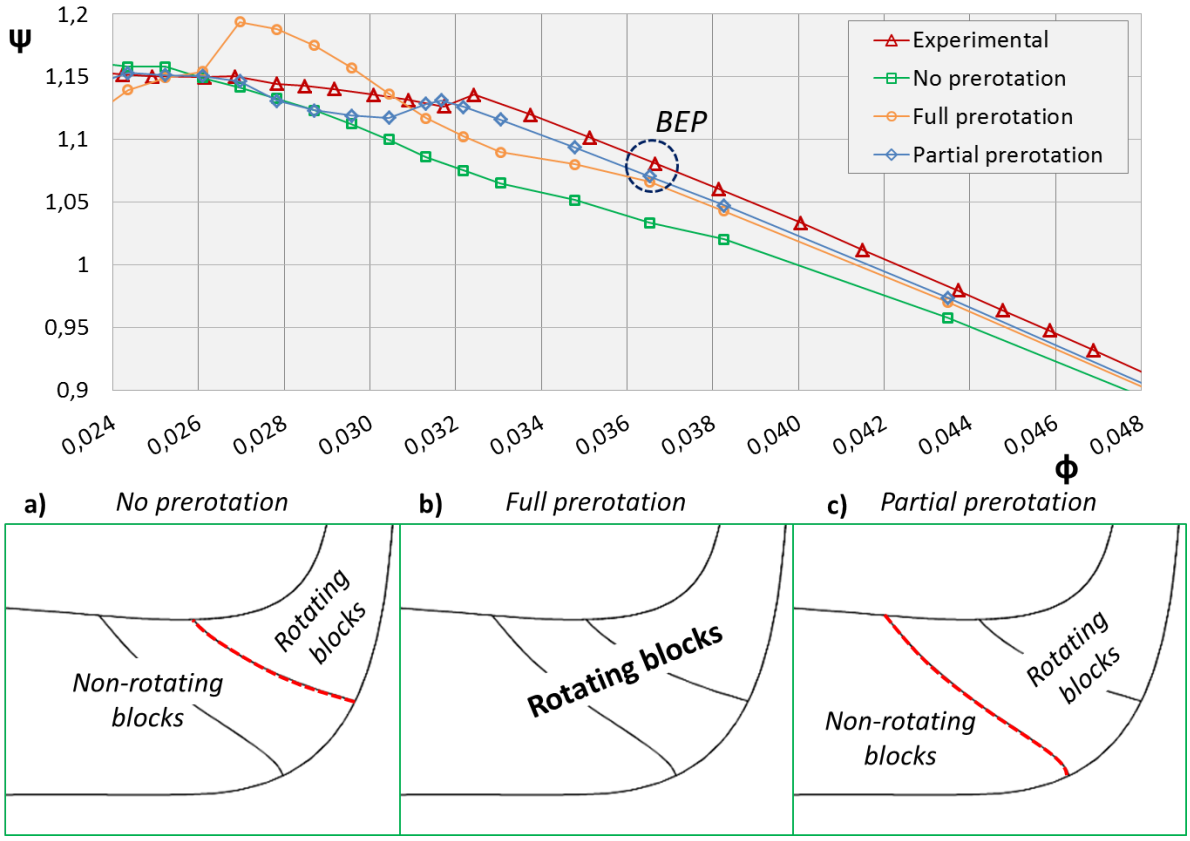

Figure 3.3: Influence and definition of the rotating blocks

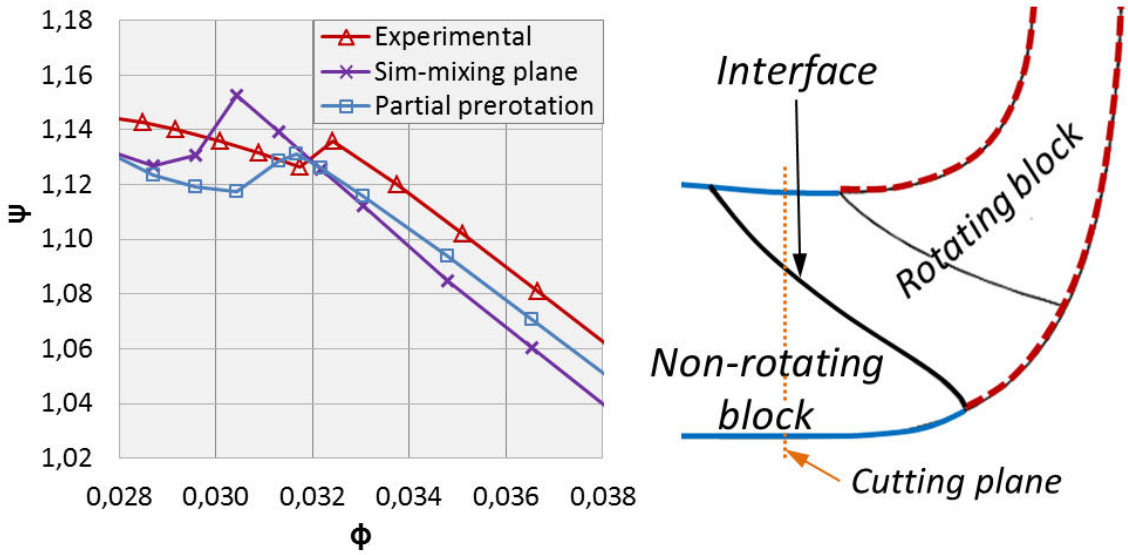

Figure 3.4: (left) Influence of the different types of interface; (right) Position of the interface

transfer of the information (pressure and velocity fields) is not disturbed and changed (except adding relative velocity component). For comparison, using mixing plane approach

on the same interface causes numerical losses and not continuous transfer of the information. On the performance curve (Sim-mixing plane - fig. 3.4) it is seen as a non-optimal trend of the curve and less exact prediction of the hump zone.

Figure 3.5 shows the data transfer in the case of the used described interface and in the case of using mixing plane. The cutting plane is perpendicular to the axis of the machine and is set close to the leading edge of the impeller as it is shown on the figure 3.4. The middle circle on the images on the figure 3.5 represents the interface between the rotating and non-rotating blocks. It can be seen in the case of the static pressure, radial velocity and the tangential velocity that the using of the mixing plane causes very bad, not continuous data transfer. On the other hand, the interface that is applied in our case does not influence the transfer of the information.

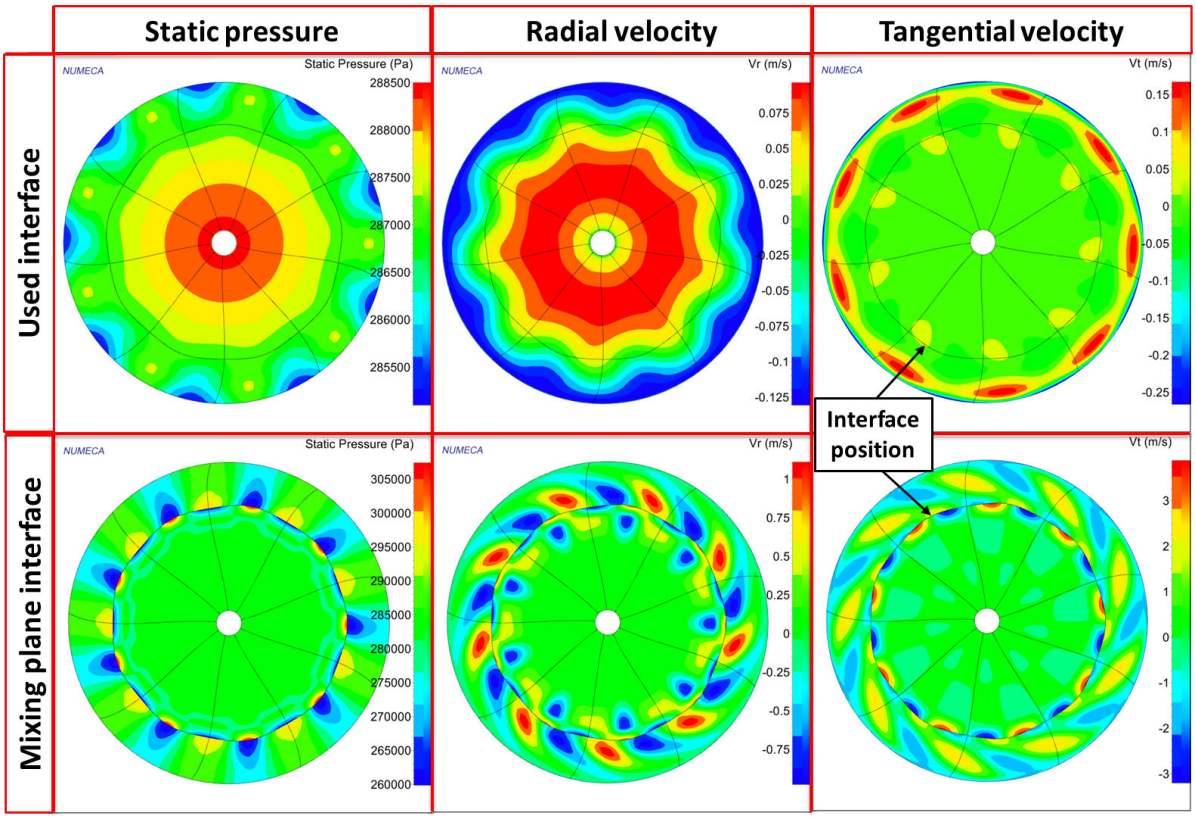

Figure 3.5: Comparison of the data transfer for the used interface and the mixing plane interface at the entrance of the impeller

As it has been shown by Zhang [97] and mentioned several times in the present work, the conditions at the inlet of the impeller, close to the leading edge, affect the conditions at the whole impeller domain and in the distributor as well, especially in the case of partial load. Therefore, the prediction of the hump zone on the performance curve and the forms of the rotating stall strongly depends on these conditions.

To summarize, the interface should be at the appropriate distance from the leading edge of the impeller to define accurately the rotating and non-rotating blocks (in our case around $D_{inl}/4$). Moreover, it should coincide in order to enable good data transfer between the blocks and consequently good hump zone and rotating stall prediction.

3.2 Validation of the cavitation model

To evaluate the level of the cavitation in the pumping regime, definition of the required NPSH value is important. In our case, it is calculated for each operating point as:

$$NPSH(m) = \frac{p_{ref} - p_v}{\rho_l \; g}. \tag{3.1}$$

In the equation 3.1, p_{ref} represents the total pressure value at the inlet of the domain, p_v the vaporization pressure of the water at $20°C$, ρ_l the density of the water and g is the gravitational constant. Numerical NPSH value has been calculated after each calculation.

Since the conditions at the inlet and the outlet of the numerical domain have been fixed, the NPSH value has been modified by changing the value of vaporization pressure p_v in order to keep the stability of simulations and similar level of the convergence, which plays even more important role in the calculations with the cavitation model and unstable operating points. A similar approach has been used and described in the thesis work by Pouffary [74] and Coutier-Delgosha [13].

3.2.1 Incipient cavitation

It is important that the numerical simulations in the cavitating regime can be validated and compared to the experimental results. The incipient cavitation value (fig. 3.6) is presented for the numerical simulations as well as for the experiment. Experimentally, the value is obtained by the visual observation of the pump-turbine impeller inlet. The value at different flow rates is defined as the appearance of the first cavitation bubbles.

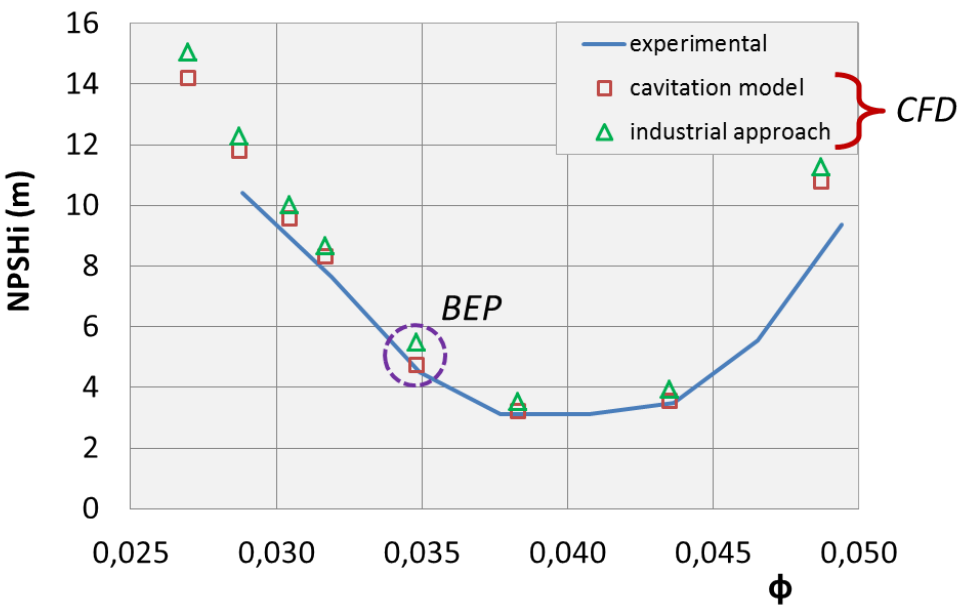

Figure 3.6: Incipient cavitation values

Classical numerical industrial approach does not use the cavitation model to predict the incipient cavitation value. It is simplified by defining the reference pressure p_{ref} (eq. 3.1) by the difference between the total pressure at the inlet of the domain and the minimal static pressure in the studied domain. The approach has been proved quite

precise to predict the incipient cavitation value. Nevertheless, it cannot give us any additional information if the cavitation is more developed.

When using the cavitation model, the criteria for the incipient cavitation condition can be defined by the void ratio α. In our case, when the void ratio in the first cavitating cell reached the value $\alpha = 0,2$ (20% of vapor in the cell), the corresponding NPSH value has been taken as the incipient cavitation value. The agreement between the industrial approach without cavitation model and the approach using the cavitation model for the mass transfer is very good. However, the simulations with the cavitation model can give us lots of additional information about the cavitating flow behavior comparing to the industrial numerical approach.

As presented on the figure 3.6, the matching between the numerical and the experimental values is good for the wide range of flow rates. The precision for both, numerical and experimental $NPSH_i$ values, is estimated to $\pm\ 0,5m$. Some deviation can be observed for the increased flow rate at the operating point around $\phi = 0,048$. The reason is most likely the experimental methodology for estimating the occurrence of the first bubble. In most of our studied operating points, the first cavitation bubble occurs at the leading on the suction side of the impeller blade. On contrary, at the $\phi = 0,048$, the cavitation firstly occurs on the pressure side of blade, which is experimentally more difficult to observe, which could explain the higher discrepancy in this area.

3.3 NPSH head drop curves

The robustness of the cavitation model allows us to provide results for a wide range of flow rates and a wide range of NPSH values.

The NPSH head drop curves could be made for various flow conditions. Figure 3.7 shows four different NPSH head drop curves for the four different operating regimes (flow rates). Curve $\phi = 0,0348$ represents the operating regime, close to the best efficiency point for the guide vane opening of 14°, which is also relatively close to the hump zone. $\phi = 0,0278$ represents the part load operating regime, which is at lower discharge than the hump zone. The curve at $\phi = 0,0435$ is close to the upper operational limit of the normal operating regime and the curve $\phi = 0,0487$ represents the operation point at the increased discharge. In these three cases, we can see experimental results for 1% head drop due to cavitation occurrence. Numerical results are in relatively good agreement with the experimental data.

As seen from the figure 3.7, the simulated head drop can reach up to 10% due to the cavitation on the pressure side of the impeller blades. All the points where the head drop occurs are considered dangerous, since the machine can be exposed to strong vibrations, erosion and non-controllable switching of the operating points due to the presence of the cavitation phenomenon.

In the case of the reduced discharge, a performance increase can be observed before the head drop at around NPSH = 2 m. The cavitation sheet at this point increases the incidence at the leading edge of the impeller blade and improves the performance.

It is known that the cavitation cloud at the low NPSH values is not a steady phenomenon. However, steady simulations enable us to get average size of cavitation sheet for each NPSH value and the estimated head drop. To evaluate the size of the cavitation clouds and the frequency of the cloud separation, high-cost unsteady simulations are required and have not been performed in these studies.

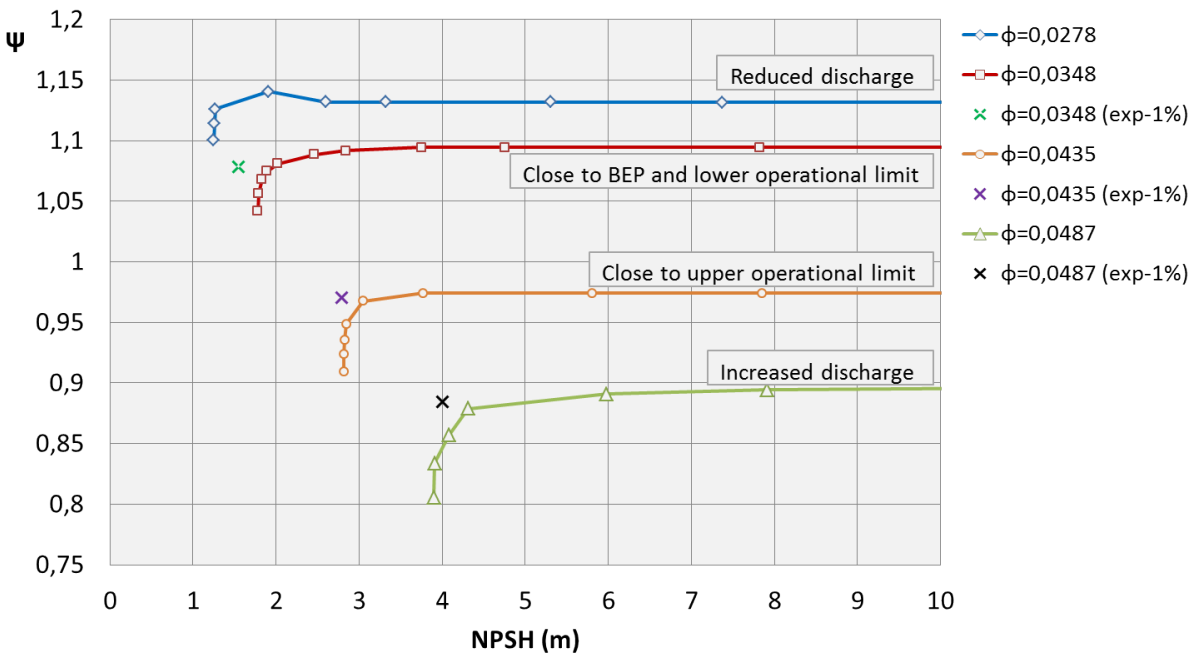

Figure 3.7: NPSH head drop curves

3.4 Cavitation forms

Discharge $\phi = 0,0348$ (close to BEP)

Related to figure 3.7, we can observe the cavitation forms for different flow rates. Figure 3.8 represents three different levels of cavitation inside the pump-turbine at the discharge $\phi = 0,0348$, which corresponds to the operating point close to the BEP for the considered opening. The incipient cavitation value for that case is around $NPSH_i = 4,8m$. The cavitation firstly occurs on the suction side of the impeller blade. By lowering the NPSH value, the cavitation is seen mostly on the large area on the suction side of the blade, closer to the shroud. At extremely low NPSH values ($NPSH = 1,78m$), one can observe the vapour sheets also on the pressure side of the blade. In case of $NPSH = 1,78m$ the head drop reaches around 5% of the nominal head for the corresponding discharge and guide vanes opening.

The cavitation forms in the channels between the impeller blades have an important impact on the provided energy by the impeller. The impeller blade has been divided into seven (D1 - D7, fig. 3.9, left) regions in order to observe the energy distribution along the impeller blade.

Line 'total' (3.9, right) represents the performance of the pump-turbine for the corresponding NPSH value including the losses in the distributor. At very low NPSH values, we can see that the regions closer to the leading edge of the impeller blades provide less energy because of the cavitation appearance. However, the blade regions D3 and D4 partially compensate the bad distribution at region D1. Provided energy in the regions D3 and D4 is even higher than in cases with higher NPSH values. It is interesting that even in the region D7, which is at the outlet of the impeller, the performance fluctuates for more than 10%. In fact, the performance in the region D7 is the best in the case of the $NPSH = 1,83m$.

Overall, as expected, the presence of the cavitation has negative influence on the per-

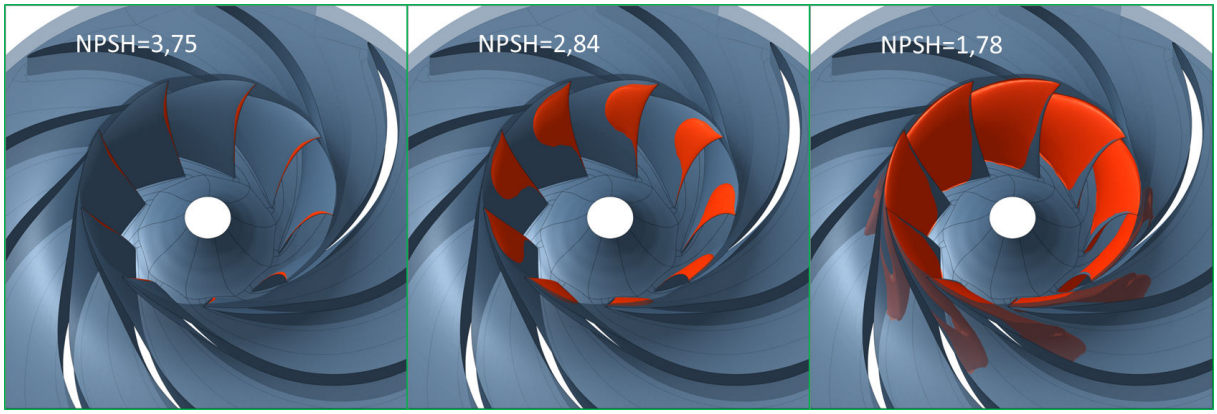

Figure 3.8: Suction side cavitation forms for $\phi = 0,0348$ ($\alpha = 0,05$)

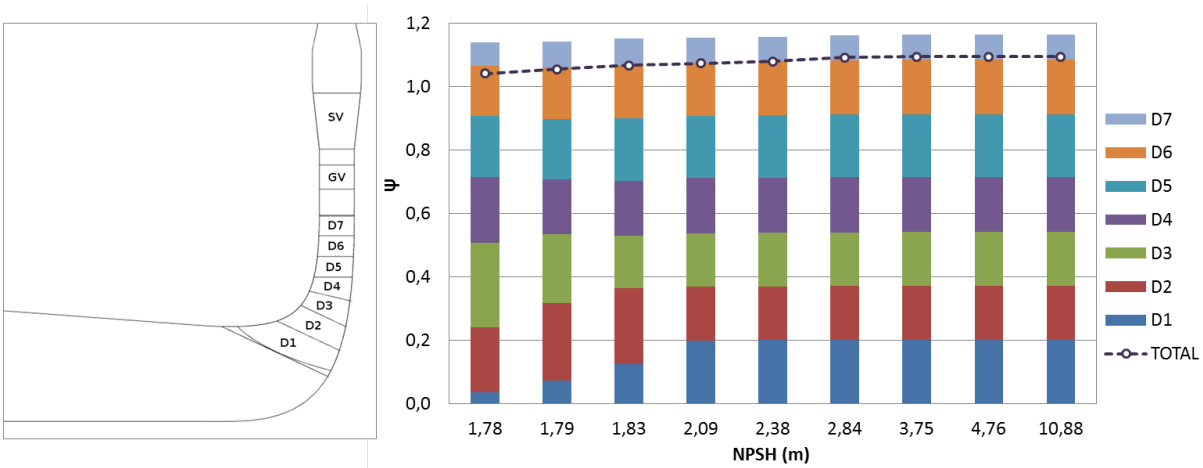

Figure 3.9: Provided energy along the impeller blade for $\phi = 0,0348$ and various NPSH values

formance of the pump-turbine (except in some cases of reduced discharge). Nevertheless, even though the cavitation forms appear at the inlet of the impeller close to the leading edge, they change the flow behavior (pressure fields, velocity fields) also at the other parts of the impeller, which can significantly influence the occurrence and the behavior of the rotating stall that occurs at the distributor regions.

Discharge $\phi = 0,0278$

Figure 3.10 shows the cavitation forms at the discharge, lower than the hump zone ($\phi = 0,0278$). The incipient cavitation occurs at the $NPSH_i = 13m$.

The incipient cavitation appears at the suction side of the impeller blades. With the reduction of the NPSH value, the cavitation sheet grows on the suction side of the blade to the level that it blocks the significant part of the channel between the blades. At around $NPSH = 1,28m$, the head drop reaches more than 5% of the nominal head for the corresponding discharge and guide vanes opening.

It is interesting to observe the cavitation sheet at the NPSH value close to $2m$. The cavitation form increases the performance of the pump-turbine (fig. 3.7) by the fictive changing of the inlet β angle on the impeller blade as it is presented on the figure 3.11.

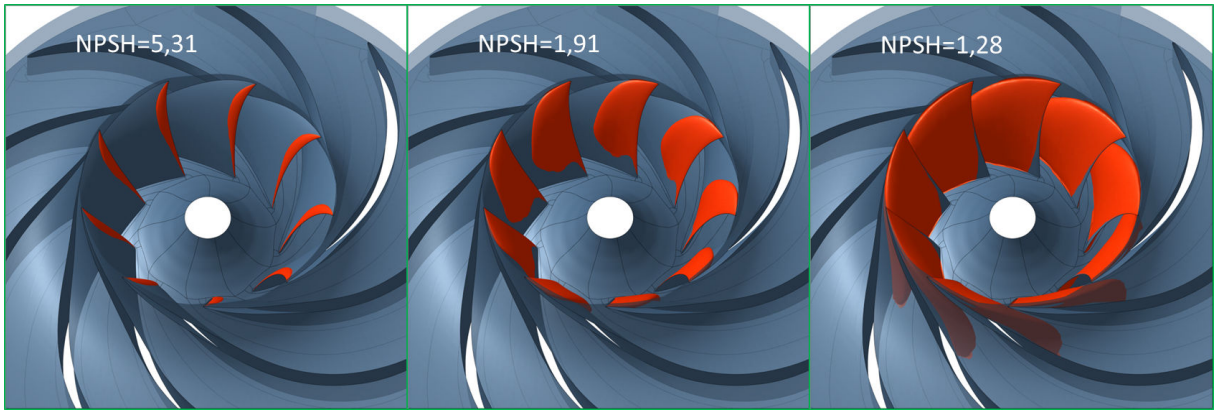

Figure 3.10: Suction side cavitation forms for $\phi = 0,0278$ ($\alpha = 0,05$)

The attached cavitation sheet can be assumed as a part of the impeller blade that has, in this case, a changed geometry and optimized operating conditions.

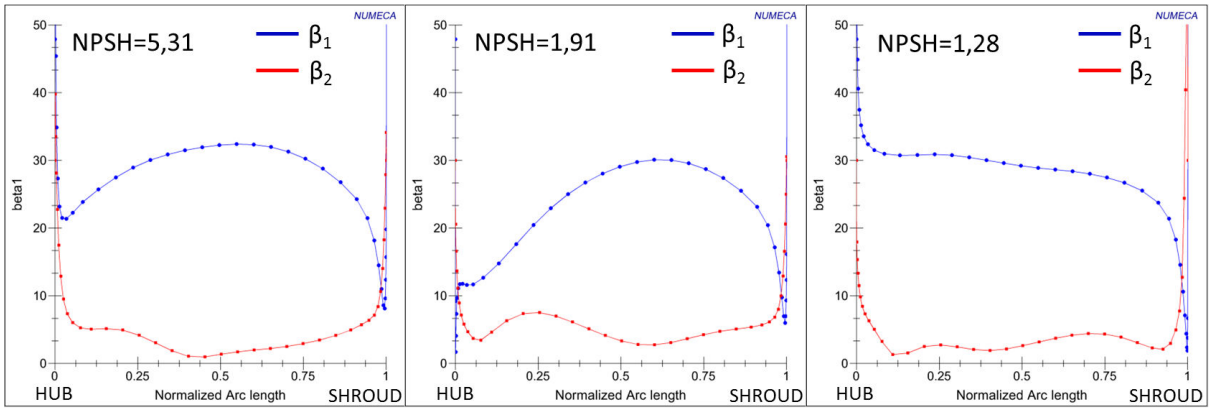

Figure 3.11: β_1 and β_2 for 3 different NPSH values for $\phi = 0,0278$

Figure 3.11 represents the impeller inlet and the outlet β angle for corresponding NPSH values presented on the figure 3.10. The operating point of the improved performance ($NPSH = 1,91m$) has lower beta value close to the hub, comparing to the case of small cavitation (with no influence on the performance).

It is clear that the cavitation changes the flow attack angle on the leading edge of the blade and changes the performance of the impeller. However, what is important is the changing of the beta angle at the trailing edge of the impeller. It proves that the conditions at the leading edge of the impeller affect the condition at the trailing edge of the impeller and consequently at the inlet of the distributor.

Similar conclusions have been made by [97]. This is very important for the study and the prediction of the rotating stall. Not only that it can be affected by the cavitation forms, but also by the velocity profile at the inlet of the impeller that must be therefore simulated as exactly as possible.

Discharge $\phi = 0,0435$

Figure 3.12 represents the cavitation forms for an operating point close to the upper operating limit. The incipient cavitation occurs at the value $NPSH_i = 3,6m$, which is more than $1m$ lower than in the case of operating point close to BEP ($\phi = 0,0348$). The cavitation occurs almost at the same time on the pressure and suction side of the impeller blades, which shows us that the flow attack angle is well adapted to the angle of the leading edge of the impeller blade.

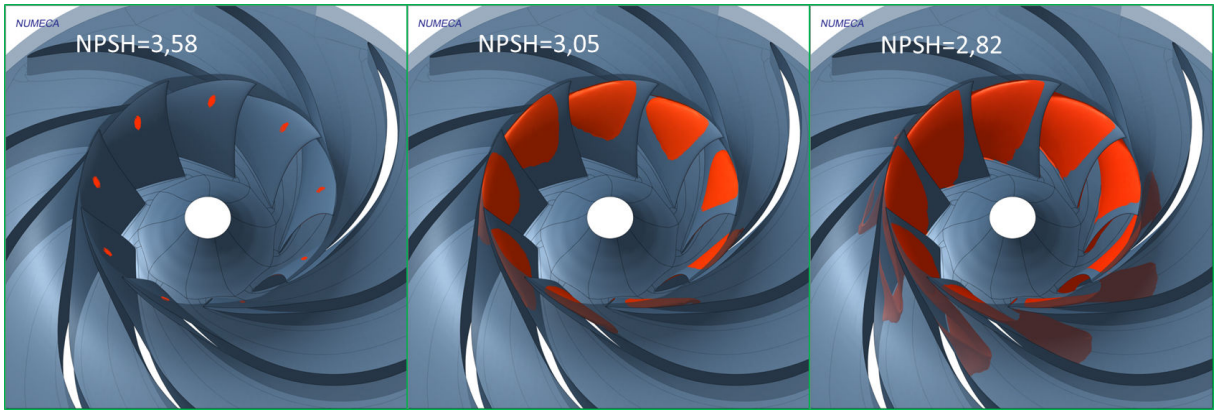

Figure 3.12: Suction side cavitation forms for $\phi = 0,0435$ ($\alpha = 0,05$)

On the suction side, cavitation firstly occurs far away from the leading edge of the impeller blade close to the shroud side of the impeller. At around $NPSH = 2,85m$, the cavitation sheets from the suction side and the pressure side join together at the shroud and at that point strong pressure drop occurs, because the cavitation already occupies significant part in the channel between the impeller blades. Operating point at the $NPSH = 2,82m$ represents the head drop of around 7% comparing to the nominal head for the considered discharge.

Discharge $\phi = 0,0487$

Figures 3.13 and 3.14 represent the cavitation forms at the suction and the pressure side of the impeller blade for the significantly increased discharge ($\phi = 0,0487$) and different NPSH values. The incipient cavitation appears at the $NPSH_i = 10,9m$ close to the leading edge on the pressure side of the impeller blade. At around $NPSH = 5m$, the cavitation occurs also on the suction side of the blade close to the shroud and far away from the leading edge of the impeller blade. With the lowering of the NPSH value, the cavitation sheet grows mostly on the shroud side of the impeller on both, pressure and suction side of the blade. Around the $NPSH = 4m$ the sheets from pressure and suction side of the blade join on the shroud side of the impeller.

Meanwhile, small cavitation forms occur also on the suction side of the guide vanes (fig. 3.14). Even though the guide vanes are in the high pressure region of the machine, the unadapted guide vane opening angle results in the position of the stagnation point far from the leading edge of the guide vane on the pressure side of the vane. Figure 3.15 represents the stagnation points close to the leading edge of the guide vanes for 3 different discharges. The static pressure scale is the same for all 3 figures.

In case of the operating point close to the BEP ($\phi = 0,0435$), the stagnation point almost matches the leading edge of the guide vane. Therefore, the pressure gradients are

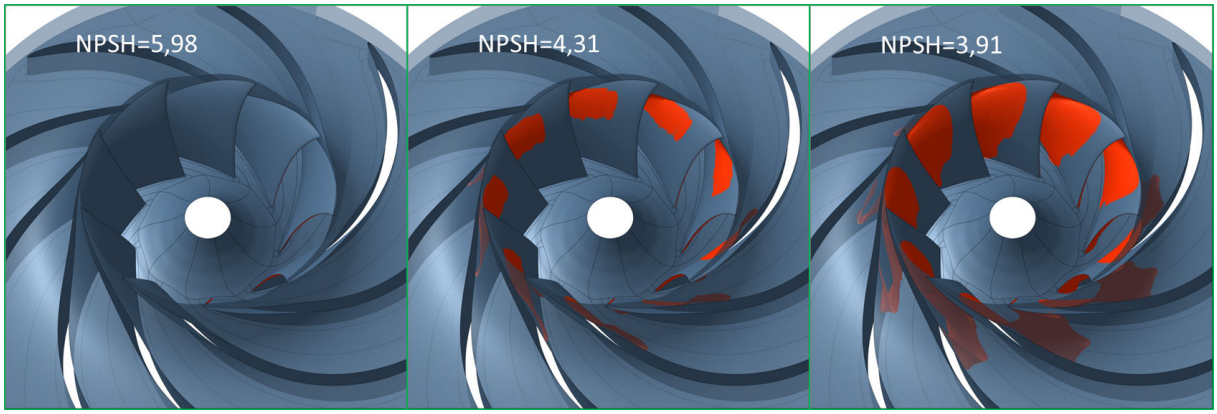

Figure 3.13: Suction side cavitation forms for $\phi = 0,0487$ ($\alpha = 0,05$)

Figure 3.14: Pressure side cavitation forms for $\phi = 0,0487$ ($\alpha = 0,05$)

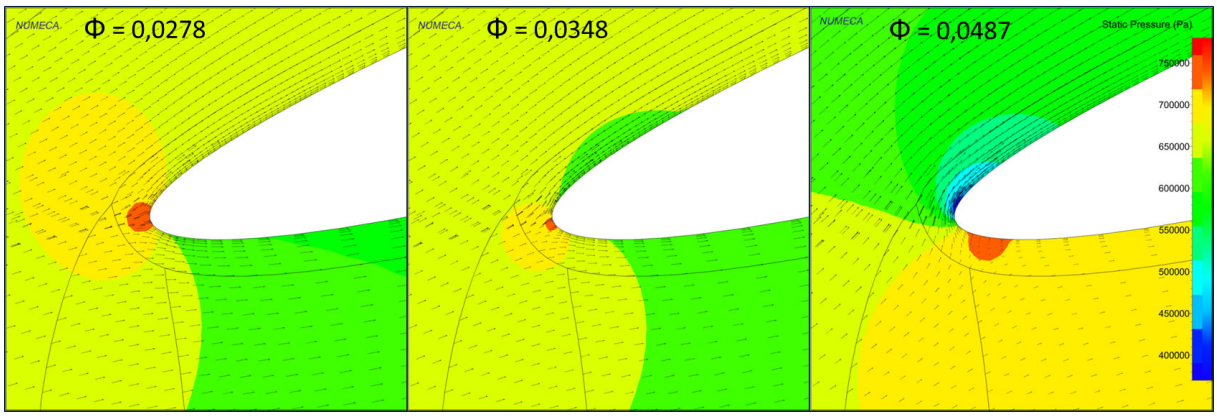

Figure 3.15: Stagnation point for 3 different discharges

low on both sides of the vane. At the part load ($\phi = 0,0278$), the attack angle of the flow changes and the stagnation point moves a bit towards the suction side of the guide vane. However, even though the local pressure on the pressure side reduces, it is still too high for the cavitation occurrence. On the other hand, for the increased discharge ($\phi = 0,0487$), the stagnation point moves towards the pressure side of the guide vanes. Consequently, the local pressure on the suction side of the guide vanes decreases significantly and reaches the

vaporization pressure as seen on the figure 3.15. Nevertheless, the form of the cavitation in the guide vane region does not change a lot with the NPSH value due to surrounding high pressure regions.

3.5 Comparison to the visualization data

The direct comparison of the cavitation forms between the numerical images and the experimental visualization has been possible for the discharge $\phi = 0,0304$, but (due to limited visualization data) only for two NPSH values. As seen from the figure 3.16, the cavitation structures for $NPSH = 6m$ and $NPSH = 7m$ match the forms, observed by visualization of the suction side of the pump-turbine impeller.

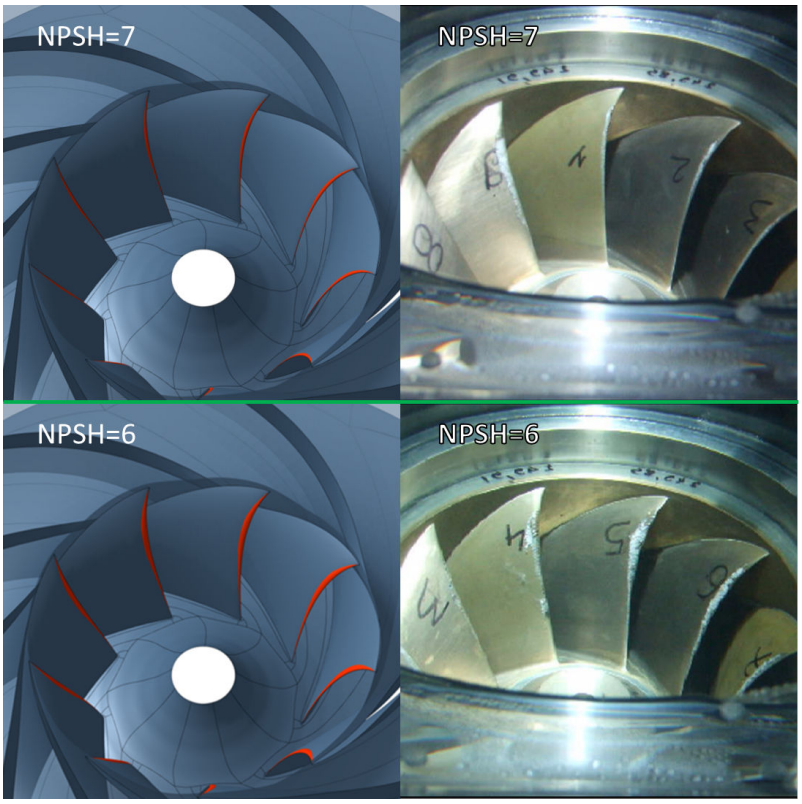

Figure 3.16: Comparison of cavitation forms to visualization data (Alstom Hydro) for $\phi = 0,0304$

3.6 Cavitation influence on the hump zone

Cavitation influence on the hump region has been investigated phenomenologically under the same numerical conditions for the same opening as previous cavitation analyses. Figure 3.17 presents the hump zone for non-cavitating conditions and under relatively strong, but constant cavitating conditions (constant NPSH values). Non-cavitating performance curve has been compared to the two constant NPSH performance curves. Both NPSH values ($NPSH = 2,7m$ and $NPSH = 2m$) affect the hump zone significantly.

The presence of the strong cavitation reduces the hump amplitude and the positive dH/dQ slope is not observed anymore for the cavitating regimes at $NPSH = 2,7m$ and

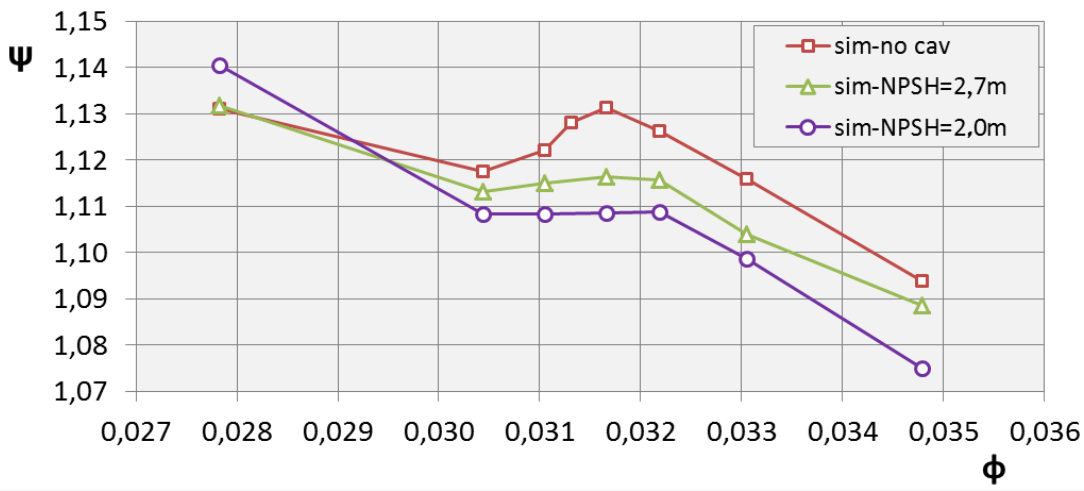

Figure 3.17: Cavitation influence on the hump zone

$NPSH = 2m$. Similar results have been presented by [1]. As already seen, in the case of $\phi = 0,0278$ and $NPSH = 2m$, the performance improves due to the optimized conditions in the impeller. Similar experimental and numerical results have been recently presented by [38], [39].

It could be expected that the developed cavitation forms increase the losses in the impeller. However, it is not obvious for the case of the distributor. The losses in the distributor and decreased performance in the impeller have been investigated for the cavitating operating points ($NPSH = 2,7m$ and $NPSH = 2m$) and have been compared to the non-cavitating regime (fig. 3.18). Negative values represent the increase of the losses ($\Delta\Psi$, fig. 3.18).

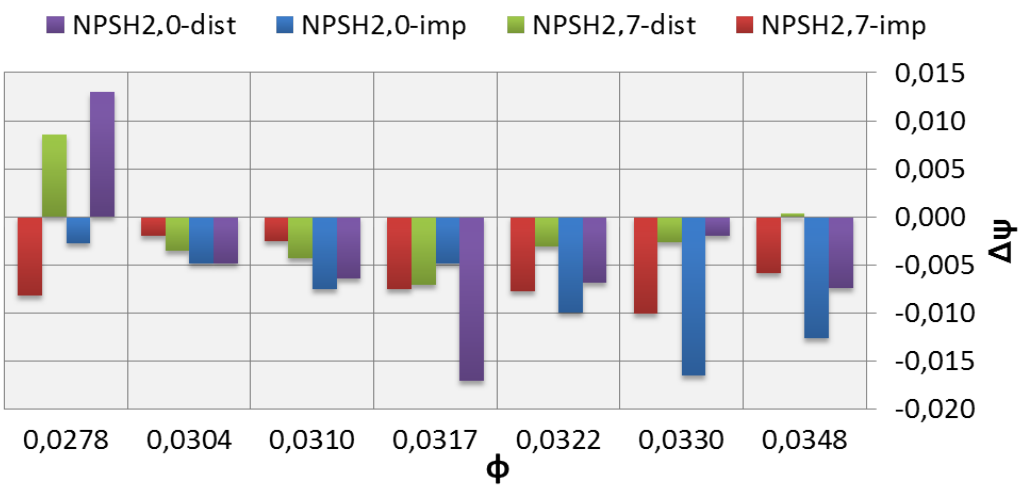

Figure 3.18: Changed losses in the distributor and changed performance of the impeller due to cavitation, compared to the non-cavitating regime

Cavitation effects on the performance are higher when the flow rate is higher. Sometimes, at the part load ($\phi = 0,0278$), the presence of the cavitation even improves the performance curve due to better conditions in the distributor, as seen on the figure 3.18.

Analysis also shows that in most cases, the cavitation appearance increases losses in the impeller and in the distributor as well, even though the cavitation occurs at the leading edge of the impeller blade.

3.7 Chapter discussion

To conclude, the effects of the cavitation and generally the conditions at the inlet of the impeller seem to be very complex. They have influence on the pressure and velocity fields in the parts of the domain that are very far from the region of actual cavitation appearance. It also means that the other unstable phenomena, such as the rotating stall, are strongly influenced by it. The detailed analyses and comparisons of the pressure and velocity fields should be made in the future for the cases of the cavitating and non-cavitating operating points.

Influence of the cavitation on the hump region can be improved by the unsteady calculations of the cavitating operating points. The simulations would be computationally more demanding, but would give detailed insights about the interaction between the two types of instabilities, rotating stall and cavitation.

Chapter 4

Steady partial load flow analysis

The results in the first part of this chapter have been analyzed for 4 different guide vanes openings and guide vanes geometry GVI (the opening is related to the relative angle to tangential direction). All the presented calculations are steady simulations for non-cavitating regime, performed on the periodic and on the combined mesh, where the periodicity has been applied in the impeller and not in the distributor. Results have been partly presented in [49].

Analyses have been focused on a global prediction of the hump position, on the amplitude of the hump and on the flow patterns in the distributor area. Moreover, the analysis has been used to predict the stable, fully unstable and slightly unstable operating points in relation with the corresponding guide vanes openings and flow rates.

The last part of the chapter presents the global performance curves for the changed guide vanes geometry $GVII$. Results have been obtained on the fully periodic mesh and steady simulations. They have been compared to the experimental curves and to the numerical results for the guide vanes geometry GVI.

4.1 Guide vane opening 14°

The line titled 'Sim-periodic 14°' (fig. 4.1) represents the calculations with the periodic mesh. The hump zone position has been detected with an accuracy of 2% on the flow rate axis. Head drop amplitude reaches around 1% in both cases, numerical and experimental one.

In chapter 3, it has been shown that the head drop in the hump zone was related to the losses which occur due to flow behavior inside the distributor. To study the effects of the periodicity, the combined mesh has been created (Sim-combined 14°, fig. 4.1), using a periodicity in the impeller area and full distributor mesh. The difference between the numerical results occurs only at the part load for the flow rates around $\Phi = 0,025$. In case of periodic mesh, flow separation can be detected only on one guide vane, which is not enough to represent the behavior in those operating points.

Several analyses of the flow patterns in the distributor of the combined mesh have been made on the mid-span cutting plane by comparing the meridional velocity distributions. The analysis showed a symmetrical distribution of the flow for all flow rates higher than $\Phi = 0,0317$ (i.e., case a, $\Phi = 0,0348$, fig. 4.1). On the contrary, for the part load at the hump region ($\Phi = 0,0313$), the instability is seen as an unsymmetrically distributed flow as shown on the fig. 4.1, case b. Moreover, the flow analysis shows 4 cells of the decreased flow rate next to the regions of the increased flow rate. The detected phenomenon is

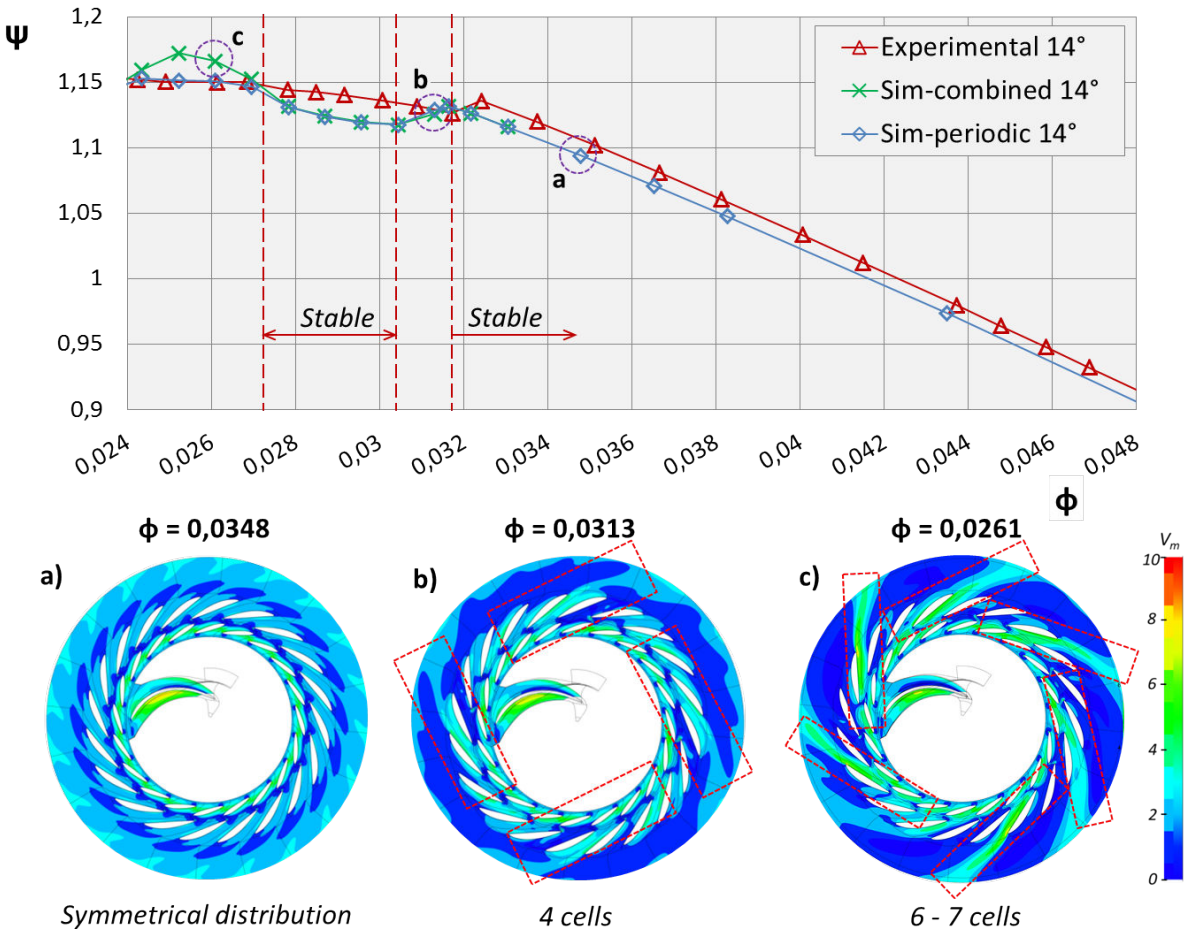

Figure 4.1: Pumping performance curve for GV opening 14°, GV I geometry; flow patterns analysis

related to an unsteady phenomenon of rotating stall that will be presented in details in the next chapter.

By reducing the flow rate, different shapes and number of the flow cells could be predicted. Between $\Phi = 0,0275$ and $\Phi = 0,0304$ the flow seems again almost symmetrically distributed around the distributor. Performance is slightly underpredicted as in all cases of stable operating regime. On the other hand, flow seems to be very unstable lower than $\Phi = 0,027$, which can be seen as 5 to 7 cells of increased flow rate (case c, $\Phi = 0,0261$, fig. 4.1).

Stable regions are marked on the figure 4.1. Stability is defined as a symmetrical distributed flow in the regions of the guide vanes and stay vanes. Operating regions that are not marked as stable are considered unstable. Therefore, there is high probability that the rotating stall will occur there.

Numerical steady results calculated on the combined mesh overpredict the performance for the very unstable part load operating points ($\Phi < 0,028$). For these points, the unsteady calculations should be performed, since the unsteadiness of the flow in the distributor plays an important role in the prediction of the losses in this part of the domain.

4.1.1 Hump zone analysis

The unstable region around the hump was additionally investigated by mass flow variation analysis through 20 channels between the guide vanes for three different operating points as shown on the figure 4.2b. Figure 4.2a shows the cutting plane though the guide vane channels close to the leading edge, at which the flow rate has been investigated.

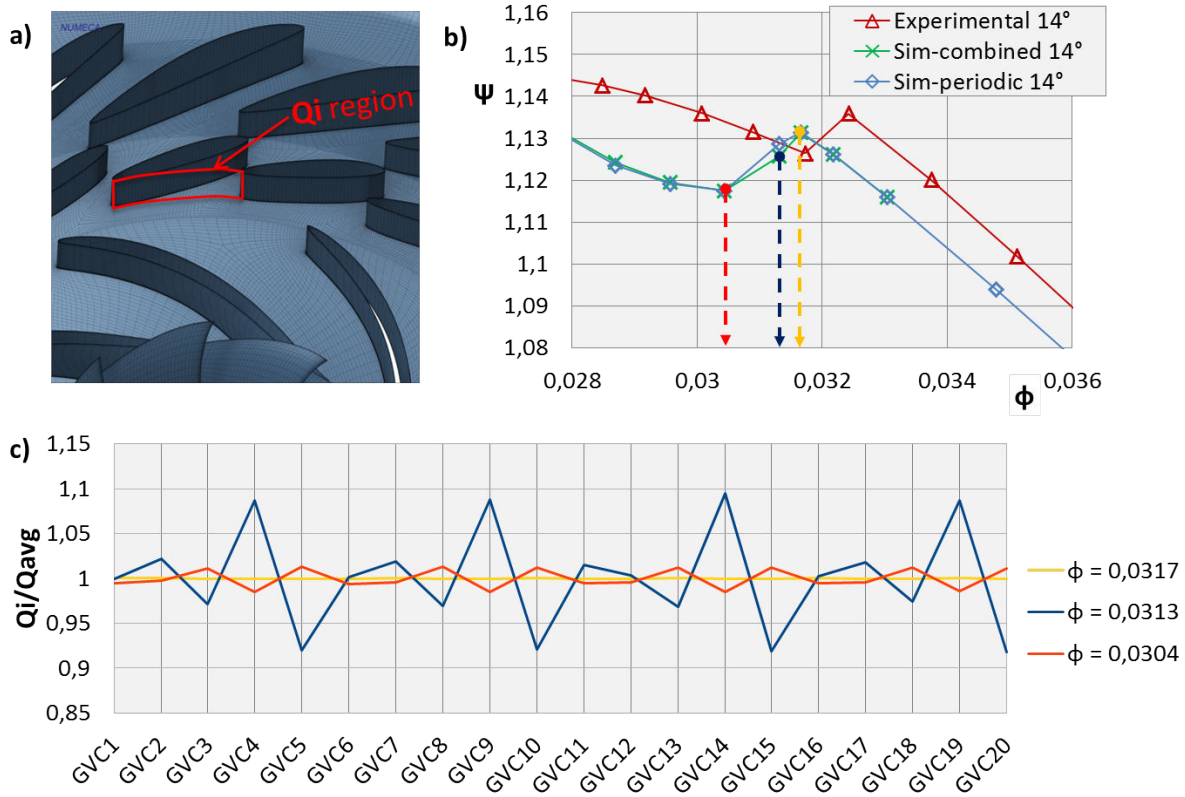

Figure 4.2: a) Investigated area between the GV channels for mass flow analysis; b) Hump zone performance curve, GVI, opening 14°; c) Flow rate variation between various GV channels (GVC) around the distributor (normalized by average flow rate Q_{avg})

Non homogeneous distribution of the flow rate, which can physically lead to the vibrations and uncontrollable changing of the operating points, are negligible for the discharge $\Phi = 0,0317$ and all higher flow rates. On the contrary, the flow rate fluctuations at the hump zone ($\Phi = 0,0313$) reach up to $\pm$ 10%, as seen on the figure 4.2 c. When the value of the dH/dQ on the performance curve is again negative ($\Phi = 0,0304$ and lower), the fluctuations decrease significantly ($\Phi = 0,0304$). They change less than 1% of the average flow rate between the channels.

Additional hump zone study has been done by analyzing the pressure distributions around the guide vanes. Static pressure distributions on 5 consecutive guide vanes (fig. 4.3a) have been analyzed for the discharge $\Phi = 0,0313$. Figures 4.3 show static pressure distributions for suction and pressure sides of guide vanes in three different positions (close to hub, in the middle, close to shroud). Meridional velocity distribution shows a flow separation that blocks an important part of the channel between the guide vanes 3 and 4. Consequently, the static pressure on the pressure side of GV 4 and on the suction side of GV 3 is increased. The flow deviation close to the leading edge of the GV 3 causes

an increased flow rate in the channel between the GV 2 and GV 3. Therefore, low pressure regions could be observed in the pressure side of GV 3 and in the suction side of GV 2.

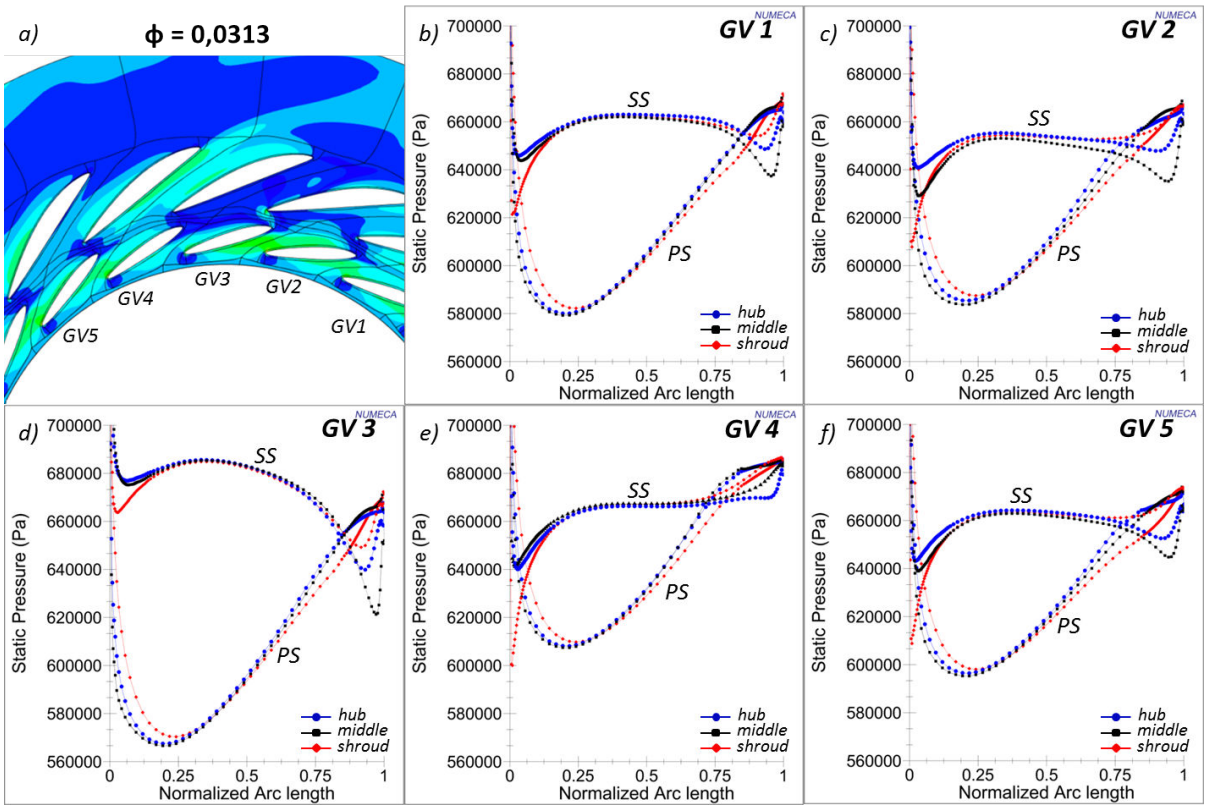

Figure 4.3: Static pressure guide vanes loading: a) Guide vanes numbers; b)-f) Static pressure on suction and pressure side of the guide vanes

To sum up, a steady, fully periodic mesh can give a good prediction of the hump shaped performance curve. Steady simulations on the combined mesh appear to be very useful to detect the stable and the unstable operating regions on the performance curve. Moreover, they can be used for several different steady analyses of the flow patterns in the distributor zone. In case of very unstable operating points, unsteady simulations should be performed in order to get more precise information about the distributor losses and consequently about the net head for corresponding discharge.

4.2 Guide vane opening 12°

The numerical hump detection for the 12° opening occurs at the same flow rate as experimental one, also the hump amplitude is similar, as seen on the figure 4.4. Flow is symmetrically distributed for the flow rates higher than $\Phi = 0,0325$ (fig. 4.4a). The hump seems to be less intensive comparing to the 14° opening. 4 cells of slightly increased flow rate can be observed at the hump zone ($\Phi = 0,0322$, fig. 4.4b). Between the $\Phi = 0,027$ and $\Phi = 0,0313$, the flow seems to be symmetrically distributed around the distributor (fig. 4.4c). By a considerable decrease of the flow rate, 6 cells of increased flow rate are formed between the $\Phi = 0,024$ and the $\Phi = 0,027$, as seen on figure 4.4d.

The difference between the periodic mesh and the combined mesh occurs at very unstable operating points, where the rotating stall seems to be very strong. The origin

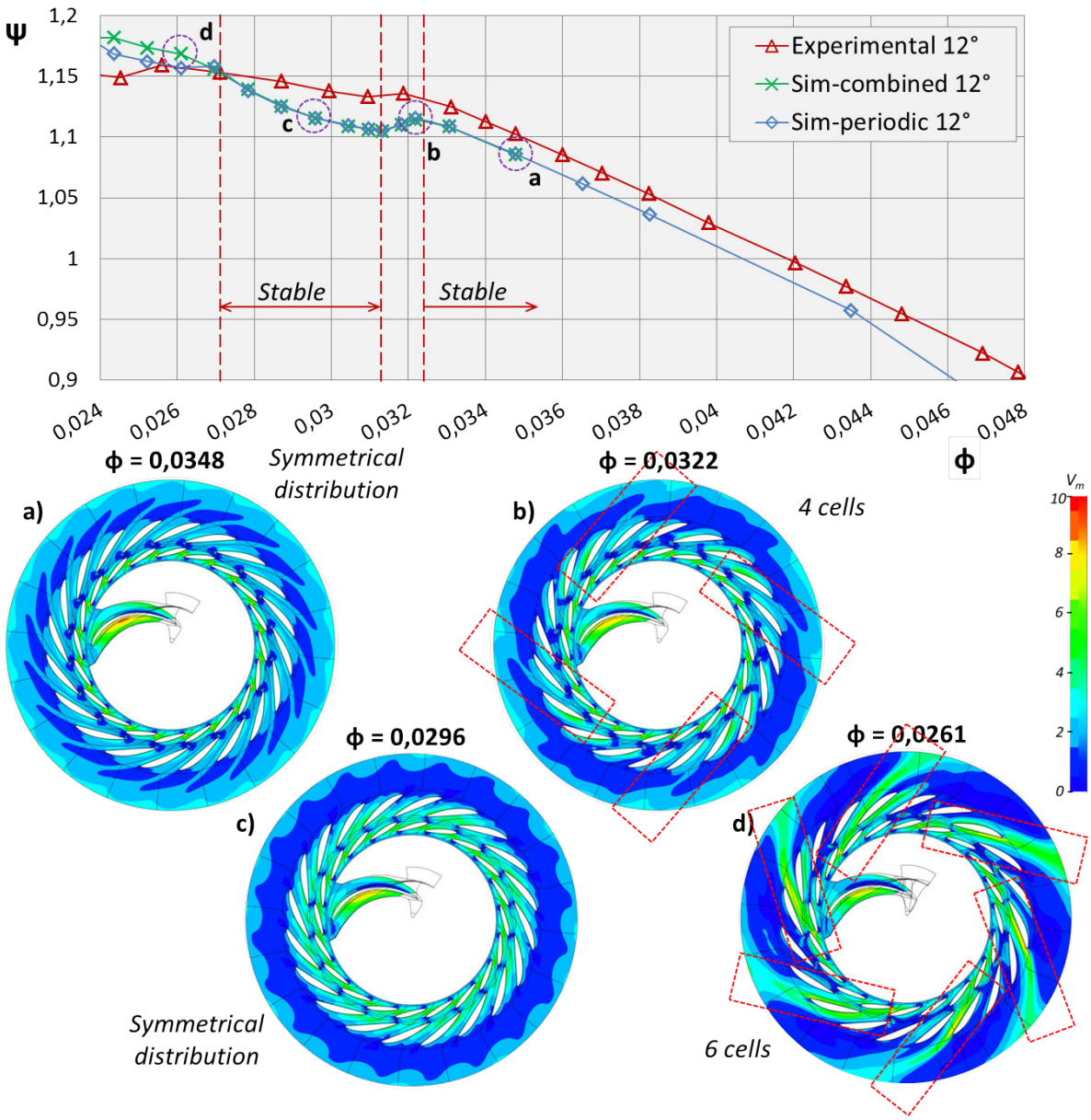

Figure 4.4: Pumping performance curve for GV opening 12°, GV I geometry; flow patterns analysis

of the discrepancies with the experimental results lies in the unsteadiness of the rotating stall that can not be simulated by the steady simulations. Same as for other openings, the periodic mesh in these cases can predict only flow separation on the guide vanes, the combined mesh can be used to predict the stall forms in the distributor. However, for detailed performance prediction and for the analysis of the unsteady components, unsteady simulations should be performed.

4.3 Guide vane opening 16°

Guide vane opening 16° shows experimental performance curve almost without hump (fig. 4.5). The tendency of the curve changes at around $\Phi = 0,0332$, where small hump occurs.

The tendency of the numerical curve is slightly different for the operating points higher than $\Phi = 0,0332$, compared to the experimental one. The difference occurs most likely due to the applied conditions on the rotor-stator interface between the impeller and the distributor. The influence of the applied mixing plane in the interface on the flow is higher, when the gap between the impeller and the guide vanes is lower. Moreover, the impact of the mixing plane and periodicity on the performance curve increases with the lowering of the discharge.

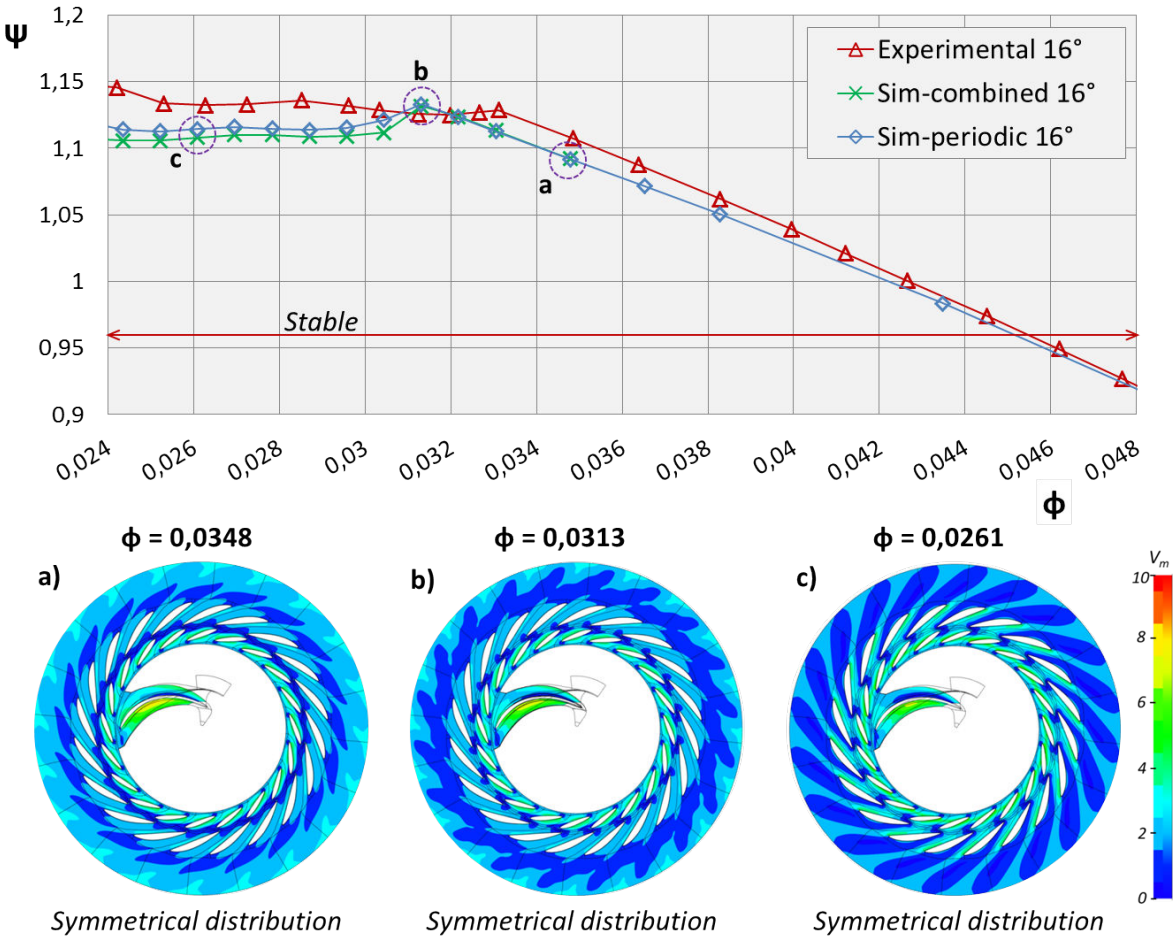

Figure 4.5: Pumping performance curve for GV opening 16°, GV I geometry; flow patterns analysis

Numerically, the flow seems to be stable and symmetrical for all the flow rates, as seen on the figure 4.5. The numerical hump occurs at the operating point $\Phi = 0,0313$. For this opening, around the hump zone, the full domain mesh should be used, preferably in combination with unsteady simulations. The reason is the reduction of the vaneless gap, which causes increased influence of the used mixing plane and the periodicity comparing to the smaller openings, where the gap is bigger.

The stall in case of opening 16° seems to be less intensive than in case of smaller openings. On the other hand, the losses in the distributor increase due to a less adapted angle of attack at the part load. The difference between the numerical simulations on the periodic mesh and on the combined mesh is very small. It occurs at the part load. The performance from the combined mesh is slightly under-predicted at the part load as in all cases of a stable behavior.

4.4 Guide vane opening 18°

The largest analyzed opening 18° does not have a very intensive hump region as seen on the figure 4.6. The stable regions with the symmetrical distribution occur at $\Phi \geq 0,0313$ (fig. 4.6a). For all the other part load discharges we can observe slightly unstable distributions that is seen as a high number of stalled cells (fig. 4.6b, c, d). In case of $\Phi = 0,0304$, $\Phi = 0,0278$ and $\Phi = 0,0244$ we can see around 8 cells of increased and decreased flow rate.

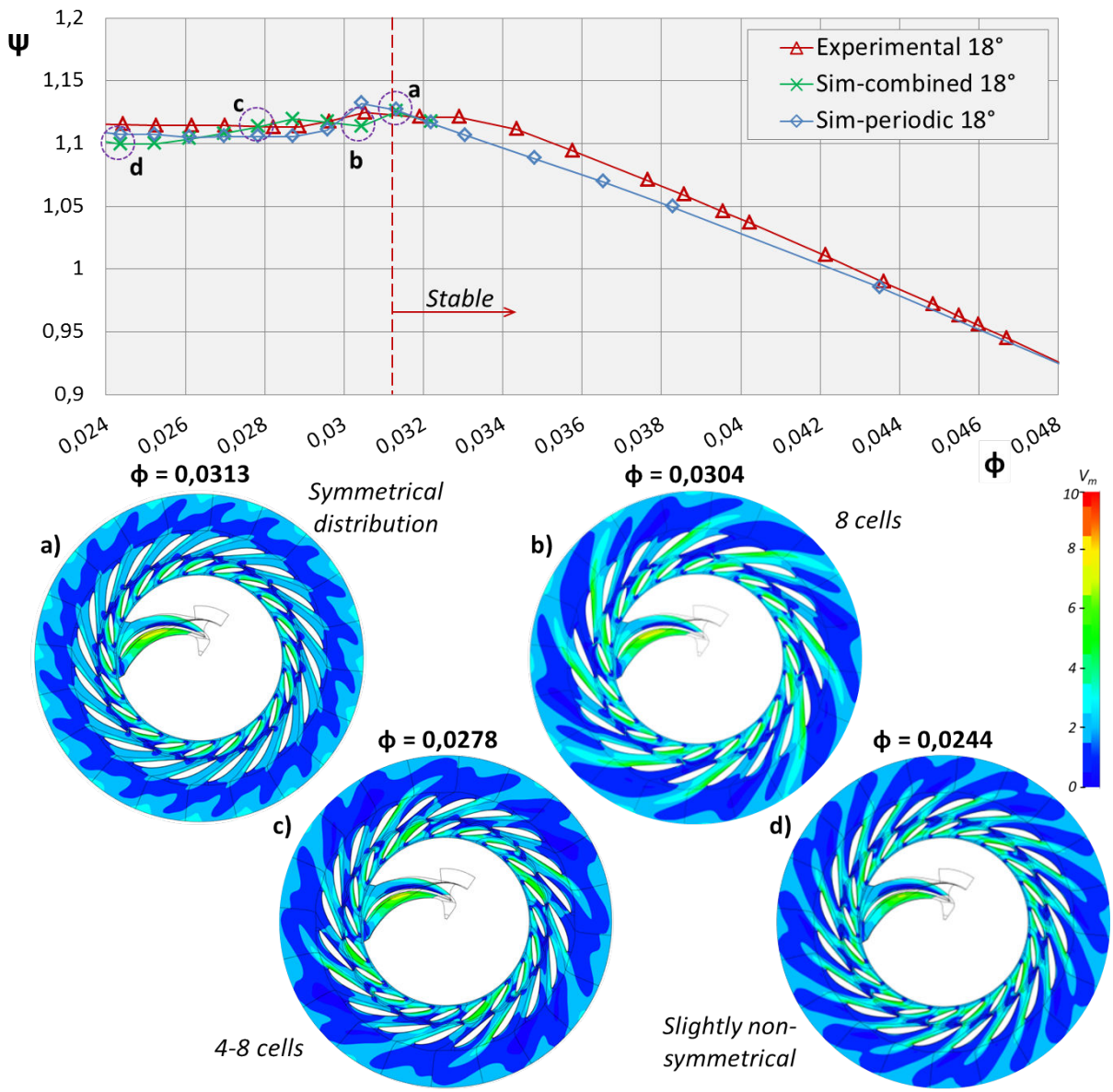

Figure 4.6: Pumping performance curve for GV opening 18°, GV I geometry; flow patterns analysis

The issue with the results for guide vane opening 18° is the same as with the opening 16°. The gap between the impeller and the distributor becomes very small and is therefore very sensitive to the rotor-stator conditions. That is the origin of the slight difference between the numerical and the experimental performance curve tendency. Probably, it would be more appropriate to use full impeller geometry in this case, since the flow

patterns in the guide vane regions might affect the flow at the outlet of the impeller. Moreover, using mixing plane and steady simulations is probably not the optimal solution for the calculations with the small gap between the impeller and the distributor.

Apart the mentioned issues, the simulations still seem to be very useful for the prediction of the stable and the unstable operating points. This kind of simulations confirms the finding that the stall appears to be more intensive for the smaller opening and higher gaps. On the other hand, the higher openings increase the losses in the distributor due to unadapted angle of attack at the leading edge of the guide vanes.

4.5 Analysis discussions

General findings about the presented analysis are that the code detects well the stable and the unstable operating regions. However, some discrepancies occur at the prediction of the performance for certain operating points. For all 4 different guide vanes openings, numerically the performance is a bit over predicted in the case of unstable, very low part load regions (where cells of increased and decreased flow rate occur) and a bit underpredicted in stable part load regions. The difference between the periodical mesh and the combined mesh results are seen only in the unstable, part load regions, where rotating stall presumably appears.

For the higher openings, the using of the mixing plane on the rotor-stator interface and the periodicity at the impeller regions seems to be a bit problematic. The influence of the aforementioned parameters on the flow prediction increases due to the reduced gap between the impeller and the distributor. For the cases of a small gap, the flow from the guide vane regions influences the flow in the impeller and not only the inverse.

In any case, the presented results imply very cost-efficient solution that provides ample information about the flow behavior at the part load. In order to obtain more detailed results and improved analysis, steady and unsteady calculations in the full domain should be used.

4.6 Guide vanes geometry $GVII$

The results in this section demonstrate the comparison between the guide vanes geometry GVI and the modified geometry $GVII$. All the calculations in this section are steady simulations that have been made on the fully periodic mesh for 4 different guide vanes openings. The information about the relative gap size between the impeller and the distributor can be found in the table 2.2 in the chapter 2.

The analysis in this section is only global and can provide us information about the position of the hump zone. Moreover, it can be used to detect safe stable operating regions that are mostly located at the discharges higher than the hump zone and where the stall is not present. It is worth to note that stalled cells can still occur even though in some cases the hump zone is not experimentally seen as a positive value of the dH/dQ on the performance curve.

4.6.1 Experimental comparison

Figure 4.7 presents experimental comparison between guide vanes geometries GVI and $GVII$ for 4 different openings. In all cases geometry $GVII$ shows better performance at partial load comparing to the geometry GVI. Hump zone position, defined as a changing

of the performance curve tendency, is located at lower discharge in case of $GVII$ for all 4 openings. Indeed, in case of 12°, it occurs at 6% lower discharge, in case of 14° at 7% lower discharge, in case of 16° at 3,5% lower discharge and in case of 18° at 1,5% lower discharge as seen on the figure 4.7.

In the case of the GVI and $GVII$, opening 12°, we can observe another strong hump zone on the experimental curve at very low discharge ($\Phi = 0,025$, fig. 4.7a). However, this hump is not related to the flow behavior in the distributor, but, according to several recent studies, it is related to the backflow in the impeller inlet, it occurs for some openings and should be investigated additionally in detail in a further study. On the contrary, so called distributor hump zone is located at the discharge around $\Phi = 0,03$ for $GVII$ and is seen as a changed tendency of the performance curve.

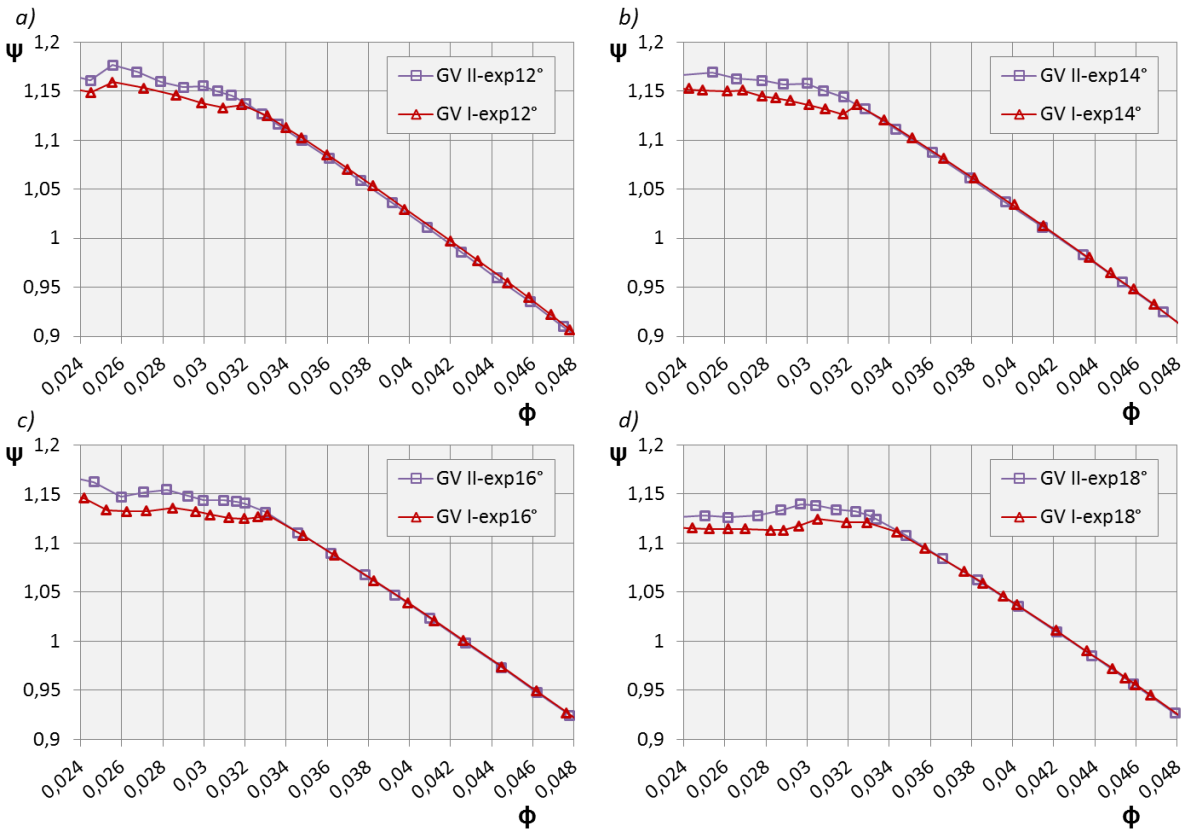

Figure 4.7: Experimental comparison of performance curve between guide vanes geometries GVI and $GVII$ for 4 different openings

The performance is improved also from the hump amplitude point of view. We can observe a positive dH/dQ value on the performance curve for geometry GVI and openings 12° and 14°. On the other hand, in case of geometry $GVII$, dH/dQ value remains negative, which means that each net head value corresponds to exactly one discharge. Consequently, there is no uncontrollable changing of the operating points that might damage the machine.

4.6.2 $GVII$, opening 12°

In the case of the $GVII$, opening 12°, numerical distributor hump occurs at around $\Phi = 0,03$ and is seen as a strong increase of the losses. The tendency of the curve for the flow

rates higher than hump zone is predicted correctly. Comparing to the guide vane geometry GVI (fig. 4.8b), the distributor hump zone occurs at an around 3% lower discharge, which is a correct trend, even though the difference is a bit higher experimentally. It should be stressed that the gap between the impeller and the GV is smaller in case of $GVII$ (tab. 2.2), comparing to GVI. Results presented in the next chapter will show the relations and the trends between the steady simulations with periodic geometry and the unsteady simulations with the full meshed geometry. We can assume that, in this case, the prediction of the hump zone position and the size of the hump zone would be significantly improved if we perform the unsteady simulations on full domain.

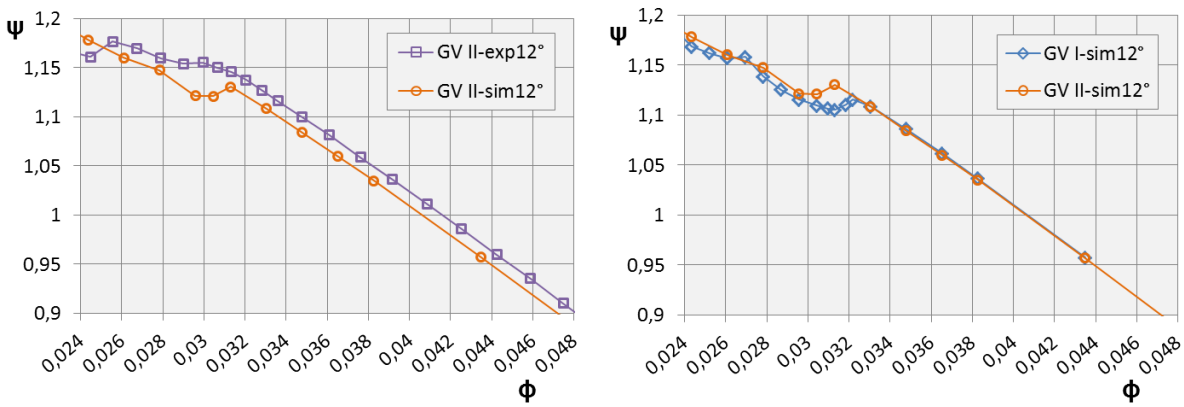

Figure 4.8: Guide vanes geometry GV II, opening 12°, compared to the experimental data (a) and to the guide vane geometry GV I (b)

4.6.3 $GVII$, opening 14°

Experimental performance curve for the opening 14° shows a distributor hump as a changing of the curve tendency at discharge around $\Phi = 0,03$, as seen from the figure 4.9a. The tendency of the numerical curve for the flow rates higher than hump zone matches the experimental one. Numerically, we can observe the distributor hump at the same discharge as experimentally, but the amplitude is higher.

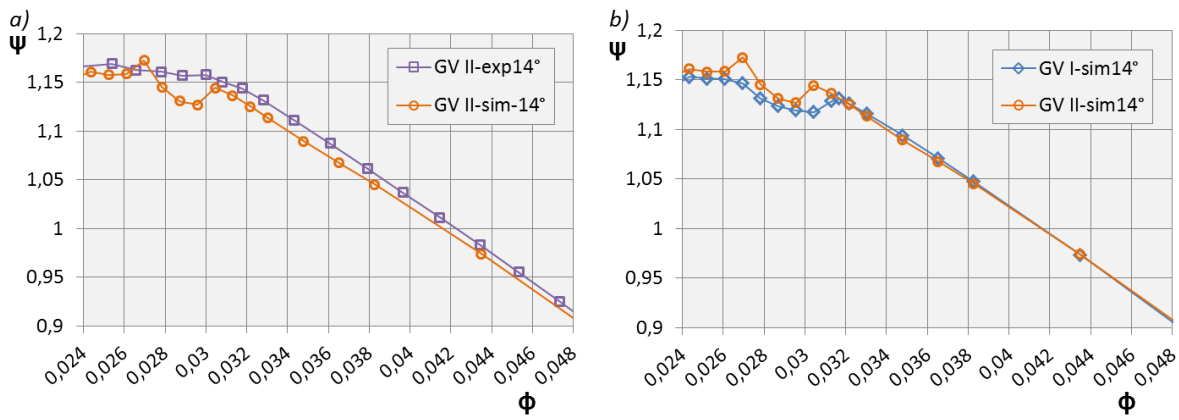

Figure 4.9: Guide vanes geometry GV II, opening 14°, compared to the experimental data (a) and to the guide vane geometry GV I (b)

Numerical calculations with the modified guide vanes geometry $GVII$ have been compared to the guide vane geometry GVI (fig. 4.9b). Gap size between the impeller and the GV is smaller in case of $GVII$ (tab. 2.2), comparing to GVI. The distributor hump for geometry $GVII$ occurs at around 5% lower discharge comparing to the case of the geometry GVI, which is a correct prediction according to the experimental data.

4.6.4 $GVII$, opening 16°

Hump zone for the guide vanes opening 16° for geometry $GVII$ can be seen as the changing of the experimental performance curve tendency at around $\Phi = 0,032$ (fig. 4.10a). Comparing to the experimental curve for the guide vane geometry GVI, the curve tendency changes at the discharge 3% lower than in case of geometry GVI (fig. 4.7c).

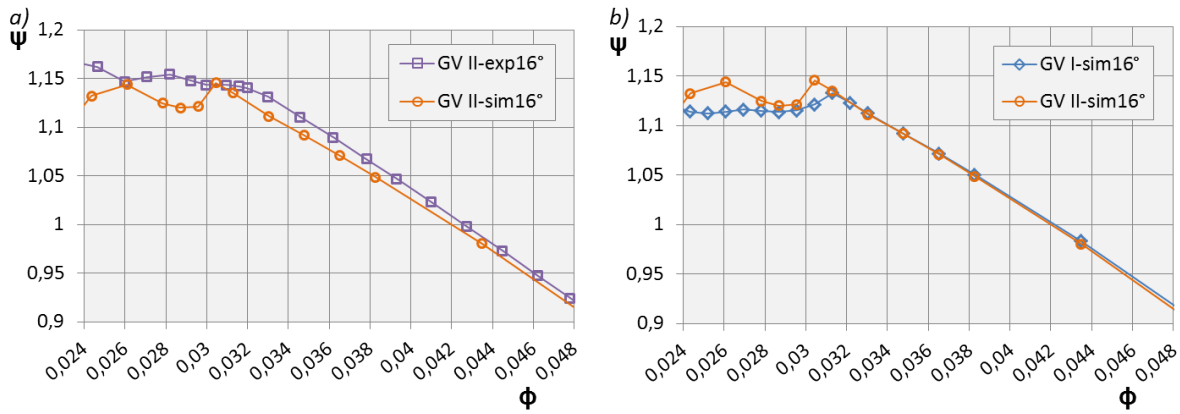

Figure 4.10: Guide vanes geometry GV II, opening 16°, compared to the experimental data (a) and to the guide vane geometry GV I (b)

Numerically, we can observe distributor hump at $\Phi = 0,0305$, which is lower than experimentally. However, it should be stressed again that with the higher guide vanes openings, the gap between the impeller and the distributor reduces. This indicates that the influence of the conditions, such as the mixing plane at the rotor-stator interface and the periodicity, increases. Gap is higher in case of $GVII$ compared to the GVI. The gap size also explains the slight change of the numerical performance curve tendency for flow rates higher than the hump zone, comparing to the experimental curve.

Comparison of the numerical curves for both guide vane geometries (fig. 4.10b) shows a similar behavior as for the other openings. The hump zone for modified geometry $GVII$ occurs at an around 3% lower discharge compared to the guide vane geometry GVI.

4.6.5 $GVII$, opening 18°

Experimentally at the guide vanes opening 18°, the hump zone occurs at around $\Phi = 0,033$ and is seen as a changing of the experimental performance curve tendency. The difference between the experimental performance curves for guide vane geometries GVI and $GVII$ is only in the part load losses as seen on the fig. 4.7d. Numerically, the hump is predicted at discharge $\Phi = 0,0304$ as shown on fig. 4.11. Numerical comparison of the geometries GVI and $GVII$ does not show significant differences. Gap is higher in case of $GVII$,

comparing to the GVI (tab. 2.2). However, we can assume that the differences might occur if we would not use periodicity as boundary condition. Behavior like this can be seen for the geometry GVI and simulations made on the combined mesh (fig. 4.6).

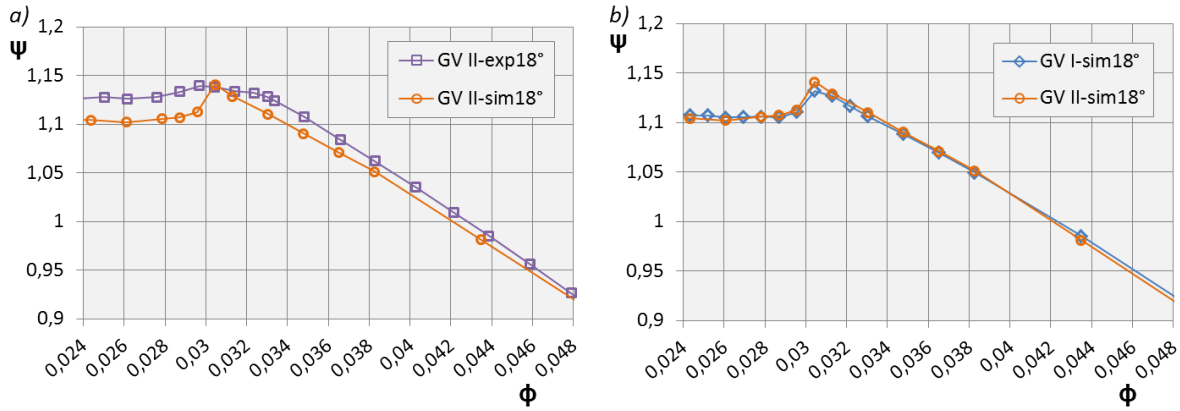

Figure 4.11: Guide vanes geometry GV II, opening 18°, compared to the experimental data (a) and to the guide vane geometry GV I (b)

4.7 Chapter discussion

To conclude, it should be pointed out that the presented steady simulations on the periodic mesh predict relatively well the position of the hump zone for both guide vanes geometries, GVI and $GVII$. The approach is completely satisfying for all the discharges higher than the hump zone. The simulations are computationally very cheap and robust, which means that we can obtain results for a wide range of operating points in a short time. The accuracy is better for smaller openings, where the size of the gap between the impeller trailing edge and the guide vanes leading edge is larger. It means that the influence of the distributor flow on the flow inside the impeller is lower. The advantage of the simulations on the combined mesh is the fast stability detection for each operating point. In other words, using low-cost simulations, each operating point can be defined as stable, unstable or slightly unstable.

The issue related to the steady simulations and the vaneless gap size is using the mixing plane on the rotor-stator interface between the impeller and the distributor. The influence of the mixing plane is higher in case of partial flow rate and in case of smaller gap. The impact is seen as a slightly changed performance curve tendency for larger openings and less exact prediction of the hump zone. All of the described issues can be avoided by using full geometry mesh and unsteady simulations. However, they are less cost-efficient, which means that it need to be determined firstly, which kind of information about flow behavior and results precision needs to be obtained.

Chapter 5

Rotating stall analysis

The results in this chapter have been obtained by performing the unsteady simulations on fully meshed domain for a non-cavitating regime. The time step is the same for all presented simulations and is defined as 2° of the impeller revolution. The number of inner iterations has been fixed to 35 for each time step. All calculations have been initialized from steady simulations on the full mesh geometry. From 2 to 3 revolutions have been necessary to stabilize the calculations, after that around 10 - 15 revolutions have been performed to analyze the rotating stall phenomenon.

Simulations have been performed for guide vanes geometry GVI and guide vanes openings 14° and 16°. Unsteady flow behaviors such as rotating stall frequency and rotating stall intensity have been investigated and analyzed. Rotating stall intensity has been mentioned several times in this chapter. It should be stressed that the parameter 'intensity' is qualitative and up to interpretation. However, the author assume that the rotating stall is more intensive if the size of stalled cells is bigger and thus the number of cells is lower. Moreover, it is also assumed that the higher rotating stall frequency corresponds to a higher intensity of the rotating stall. The assumption should be verified experimentally. In the future, a dimensionless number could be proposed to quantify the rotating stall intensity.

The detailed analysis of the time dependent local flow has been made for the discharge $\Phi = 0,0313$ and opening 14° in order to analyze the governing instability phenomena.

5.1 Global results 14°

Global unsteady results for the GV opening 14° have been compared to the experimental data and to the already presented steady simulations as seen on the figure 5.1. Additionally, we can see that the steady results on the full mesh geometry do not differ from the steady results on the combined mesh. The finding shows that for the presented GV opening and geometry, periodicity in the impeller region can be applied for the steady simulations. Unsteady results show significant improvement in the prediction of the performance curve, comparing to the steady simulation. Moreover, the comparison between the experimental data and the unsteady simulations shows very good agreement in both stable and unstable operating regions.

Flow analysis for unsteady calculations shows slightly different results for some points, comparing to the already presented steady results on the combined mesh (fig. 4.1). Flow distribution analyses have been made on the mid-span cutting plane by comparing the meridional velocity patterns. Figure 5.1a shows symmetrically distributed flow for

the discharge $\Phi = 0,0348$. Similar behavior has been observed for the operating point $\Phi = 0,0325$ and according to the other results, we can assume that the same symmetrical distribution could be observed for all discharges higher than the hump zone.

In the hump zone (fig. 5.1b; $\Phi = 0,0313$), 4 rotating cells of increased and decreased flow rate have been observed. The cells seem to be more developed than in case of the steady simulations. The rotating frequency of the cells is around 3,5% of the operating frequency of the pump-turbine (tab. 5.1). The discharge $\Phi = 0,0313$ has been chosen for a detailed local flow analysis of the rotating stall that will be presented later in this chapter. Specific energy fluctuations for this discharge reach around $\pm 0,5\%$ and indicate an unstable, potentially dangerous operating point.

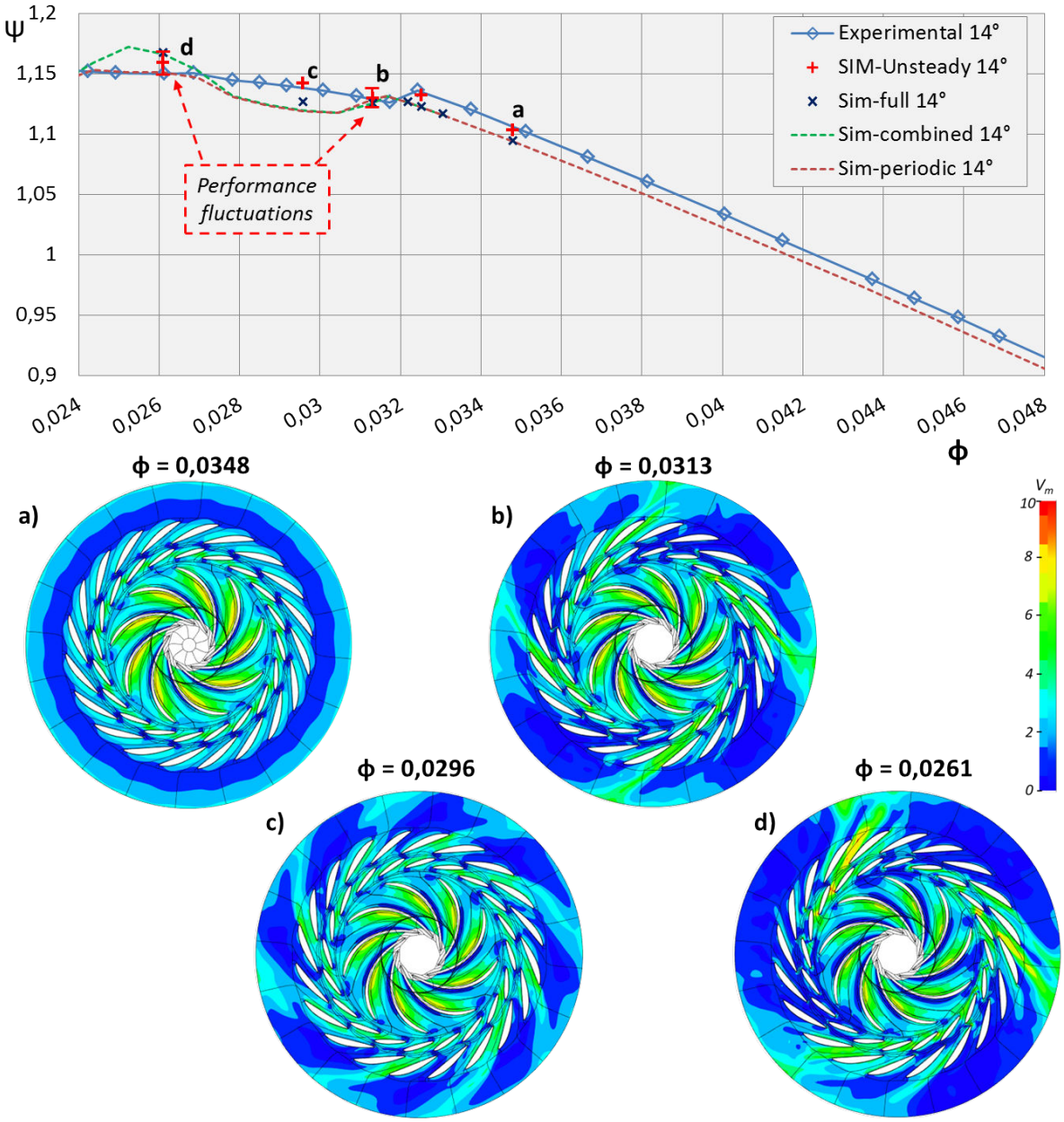

Figure 5.1: Pumping performance curve for GV opening 14°, rotating stall analysis

By additional lowering of the discharge, we can observe 8 rotating stall cells at $\Phi = 0,0296$. Rotating stall frequency is lower, comparing to $\Phi = 0,0313$ and reaches around

Discharge	N° of cells	Frequency	Intensity
$\Phi = 0,0348$	/	/	0
$\Phi = 0,0325$	/	/	0
$\Phi = 0,0313$	4	3,5%	++
$\Phi = 0,0296$	8	2%	+
$\Phi = 0,0261$	3	5,5%	+++

Table 5.1: Rotating stall cells, frequency and intensity for opening 14°

2% of the operational frequency (fig. 5.1c; tab. 5.1). Moreover, the rotating cells also seem to be less intensive for this case and there are no performance fluctuations. Comparing to the steady simulations on the combined mesh (fig. 4.1), the flow at $\Phi = 0,0296$ shows slightly more unstable behavior. The findings are the same for most of the operating points.

The flow becomes even more unstable at the very low partial load at $\Phi = 0,0261$. Three rotating cells of the strongly increased and decreased flows can be observed (fig. 5.1d). The frequency of the rotating stall cells reaches 5.5% of the operational frequency (tab. 5.1). The fluctuation of the specific energy coefficient Ψ are around $\pm 0,5\%$, which is another indicator of a very unstable operating point. Steady simulations for this discharge (fig. 4.1d) showed a higher number and smaller stalled cells, which confirms the general findings that the unsteady simulations on the full mesh geometry predict slightly more unstable flow patterns. Therefore, they are required for a precise prediction of the rotating stall.

5.2 Global results 16°

Global unsteady results for the GV opening 16° around the hump zone have been compared to the experimental data and to the already presented steady simulations, as seen on the figure 5.2. Steady results on the full mesh geometry do not show significant improvement in the performance prediction, comparing to the steady results on the combined mesh. Similar as for the GV opening 14°, the unsteady results show very good agreement with the experimental data for all simulated operating points. The improvement in the prediction of the performance curve is significant, comparing to the steady simulations. Hump zone position and amplitude, seen as a changed tendency of the performance curve, matches the experimental data almost completely. Comparisons of the flow patterns have been made on the mid-span cutting plane by analyzing the meridional velocity profile for several different discharges.

At the discharge $\Phi = 0,0348$, symmetrical flow distribution that corresponds to a stable operating point can be observed (fig. 5.2a). The flow is stable until the discharge $\Phi = 0,0330$, where the performance curve changes its tendency. At the discharge $\Phi = 0,0322$ (fig. 5.2b), we can see that the flow starts to be slightly unsymmetrically distributed, but still very stable.

By additional flow rate lowering, we can observe 4 cells of the locally increased and decreased flow rate at the discharge $\Phi = 0,0313$ (fig. 5.2c). It is interesting to compare this point to the same discharge at the GV opening 14° (fig. 5.1b). We can see the same number of rotating stall cells, but intensity at the GV 14° seems to be much higher. It confirms our hypothesis that the increase of GV opening causes a smaller gap between the impeller and the distributor, which consequently leads into the less intensive rotating

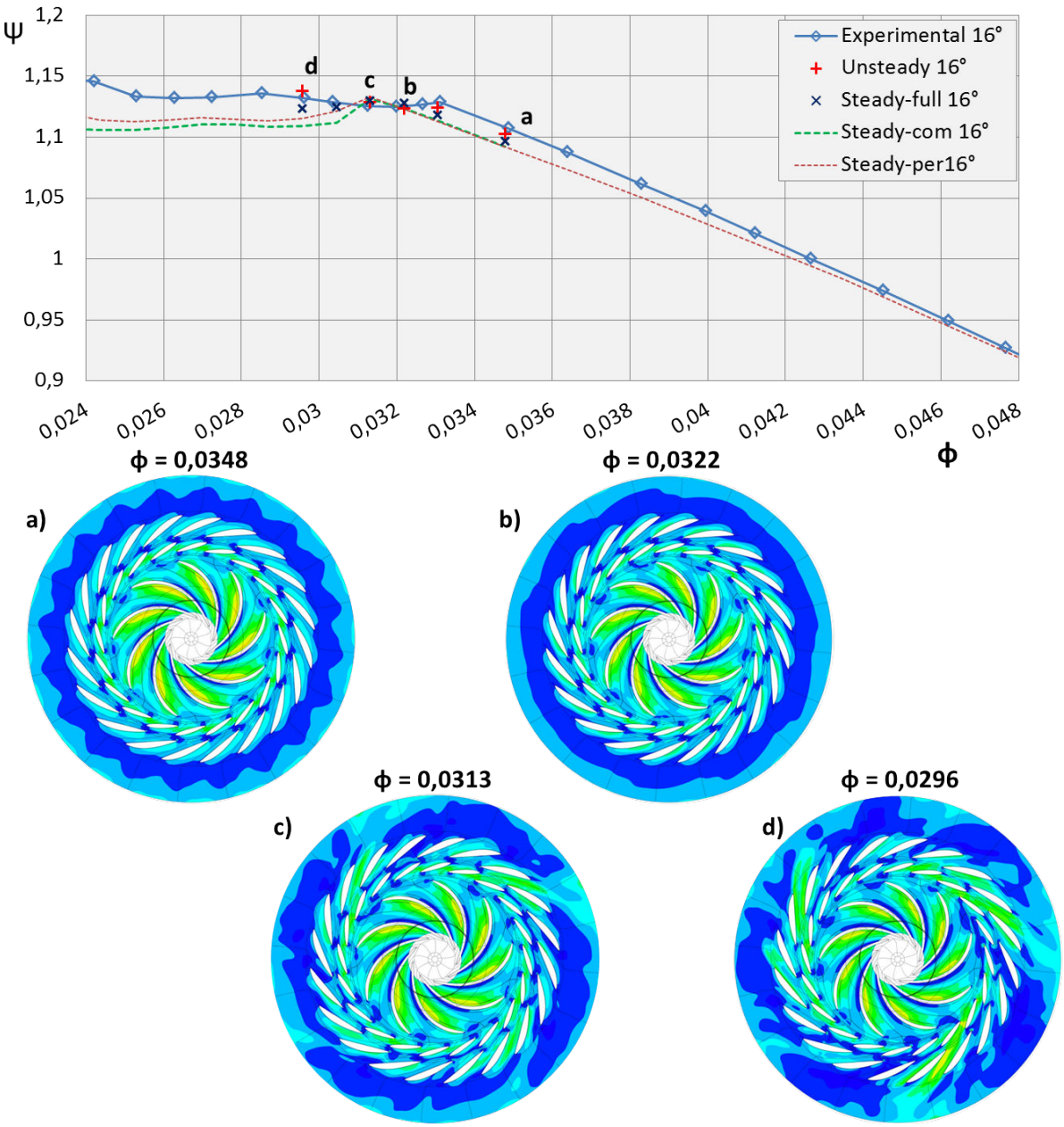

Figure 5.2: Pumping performance curve for GV opening 16°, rotating stall analysis

stall. At the flow rate $\Phi = 0,0296$, the flow keeps slightly unstable behavior, similar as in the case of the opening 14°.

To sum up, the first difference between the larger and smaller opening at the partial load is in the distributor losses that are higher in the case of larger opening due to less adapted attack angle at the leading edge of the guide vanes. On the other hand, the rotating stall is less intensive for the larger opening. The reason is smaller gap between the impeller and the guide vanes that does not allow high fluctuations of the attack angle. Moreover, also the hump zone seems to be smoother for the larger openings, which is seen as a smaller or in some cases even no hump amplitude. Unsteady simulations for the GV opening 16° confirmed the improvement in the performance prediction and in the rotating stall analysis, comparing to the steady simulations.

5.3 Local flow analysis at $\Phi = 0,0313$, GV opening 14°

Detailed flow analyses have been made for opening 14°, guide vane geometry GVI and discharge $\Phi = 0,0313$ that represents an operating point at the hump zone, where the rotating stall occurs. After stabilization period, around 15 revolutions of the pump-turbine impeller have been calculated and analyzed.

5.3.1 Impeller blades pressure distribution

Static pressure distributions have been analyzed on 4 consecutive impeller blades. This analysis is important because it can show us the impact of the developed rotating stall on the flow patterns in the upstream regions such as impeller and even draft tube. Static pressure has been analyzed on the mid-span cutting plane on the impeller blades (fig. 5.3a). Figure 5.3b shows the difference in the static pressure distribution on both, pressure and suction sides of the blades. It should be taken into account that the relative position of the 4 impeller blades is not the same and can influence the pressure distribution around the blade, but it is estimated that it is lower than the rotating stall influence.

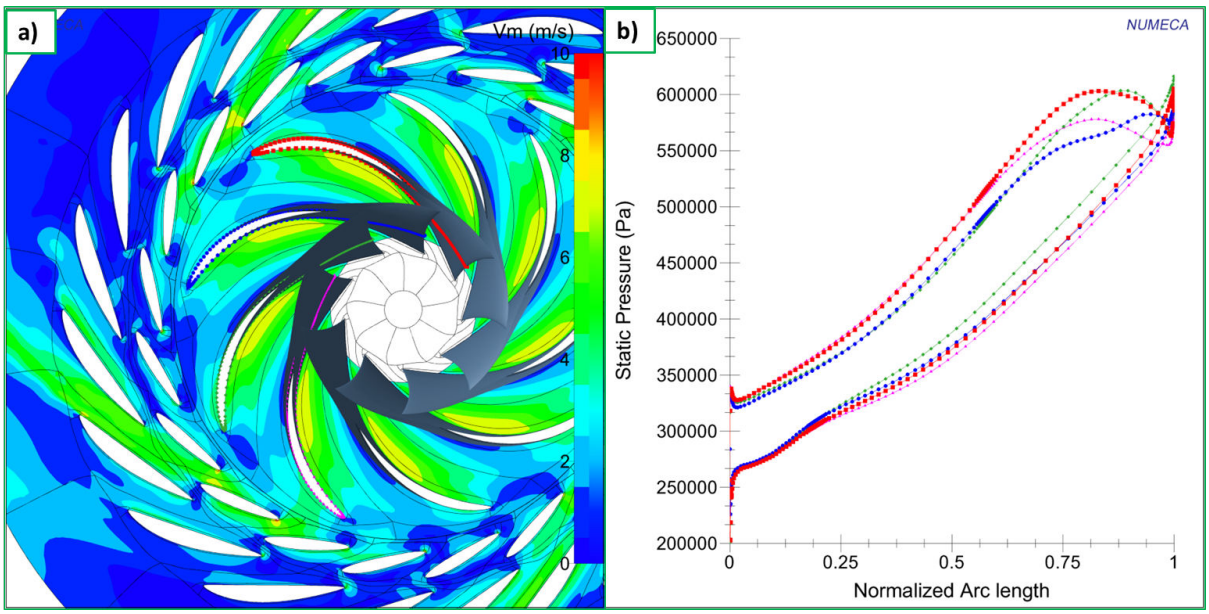

Figure 5.3: Pressure distribution around 4 consecutive impeller blades at a given time

Rotating stall influence, seen as a change in pressure distribution, is the highest close to the trailing edge of the impeller blades. However, the difference can be observed also on the suction side of the blades and even close to the impeller blades leading edges, which are located very far from actual occurrence of the rotating stall in the distributor regions. Pressure fields around the blades have a strong influence on the velocity fields in the impeller channel. It should be stressed that the influence can also be inverse, therefore, the conditions close to the leading edge of the impeller can have an impact on the rotating stall patterns in the distributor.

5.3.2 Draft tube conditions

Conditions at the draft tube have been analyzed on the cutting plane close to the impeller leading edge at a given time (fig. 5.4). The cutting plane is marked on the figure 3.4. Static pressure and tangential velocity fields show unsymmetrical distribution, which means that the rotating stall that occurs in the distributor regions influences the conditions far back upstream in the draft tube and as well inverse. Consequently, the modeling of the conditions at the inlet of the impeller can have an important influence on the prediction of the partial load performance and flow patterns, as it has been already stressed in this document.

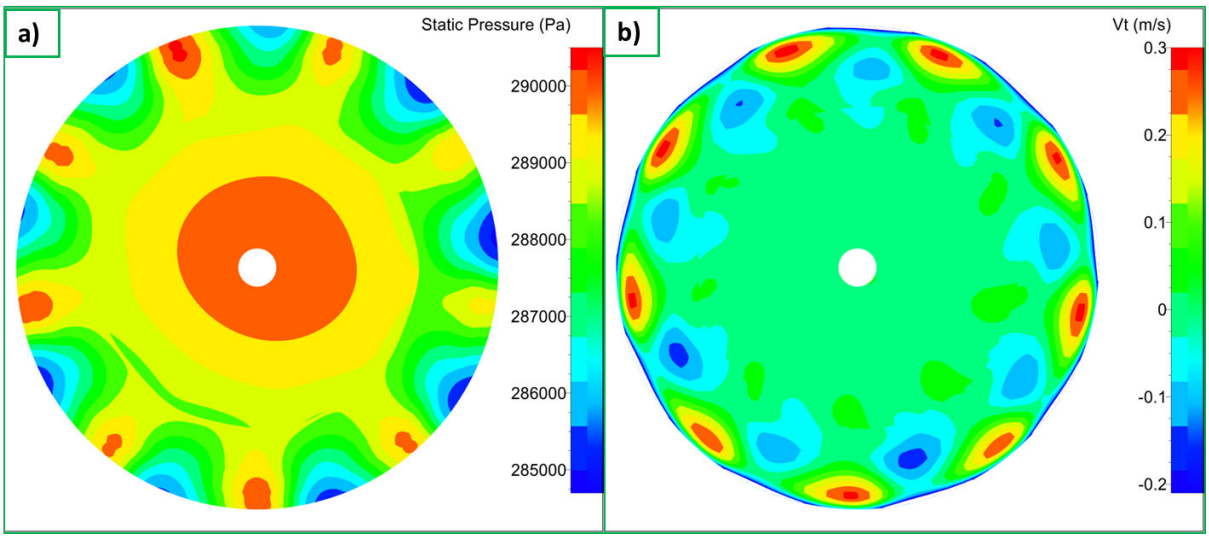

Figure 5.4: a) Static pressure at the draft tube; b) Tangential velocity in the draft tube

5.3.3 Distributor time-depending analysis

Local flow analysis between the guide vanes channels has been made for several time steps. Flow separation on the guide vanes (mid-span cutting plane) together with the velocity vectors have been compared to the local flow rate fluctuations through the guide vane channel (fig. 5.5). Moreover, static pressure fields have been analyzed for the same time steps and on the same mid-span cutting plane (fig. 5.6).

Several cuts have been chosen inside the guide vane channel in order to investigate the local flow patterns and secondary flows. Cutting planes have been made for 4 different constant diameter values. Radial velocity has been investigated on these planes in order to detect the backflow regions inside the guide vanes channels.

Flow separation

Figure 5.5a shows the flow rate fluctuations through one guide vane channel. It can be observed that the flow rate values fluctuate between 45% and 130% of the mean value. The reference plane for flow rate fluctuations has been put at the constant radius, close to the leading edge of the guide vanes. τ represents the time needed for one revolution of the pump-turbine. One cycle of increased and decreased flow rate needs about 7,2 revolutions of the pump-turbine impeller, which corresponds to a rotating stall frequency around 3,5% of the nominal frequency of the machine.

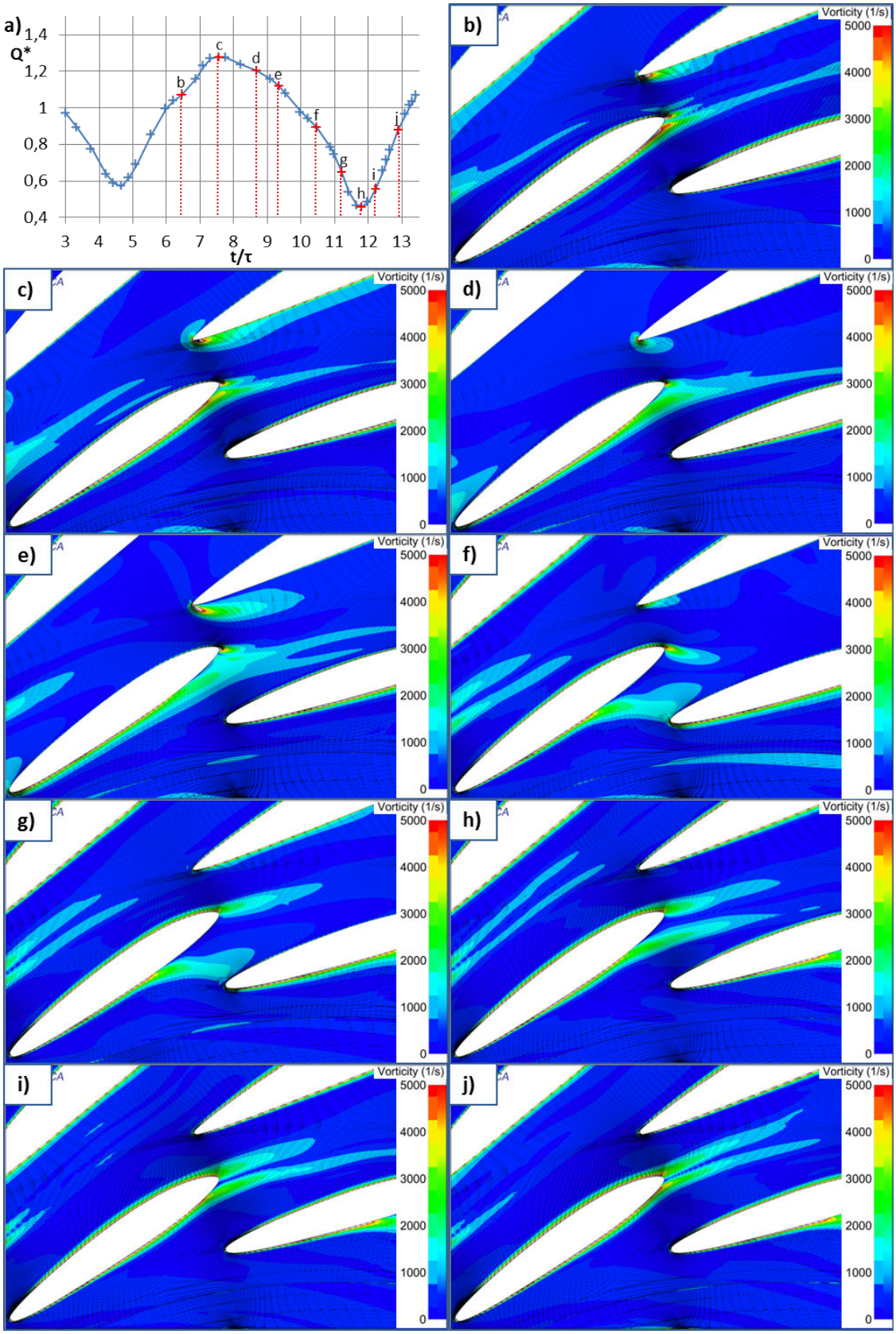

Figure 5.5: a) Flow rate fluctuations through one guide vanes channel b)-j) Mid-span vorticity with velocity vectors inside the guide vane channel for various time steps

Figure 5.5'b'-'j' shows the vorticity and velocity vectors on the mid-span cutting plane. Flow rate through the channel is the highest at the time step 'c'. At this time, the separation occurs only at the trailing edge of the guide vane. Time steps 'd' - 'g' show the growing region of the flow recirculation inside the guide vanes channel. Velocity vectors show the deviation of the flow to the downstream channel. At the time step 'e', we can observe increased separation and flow deviation on the pressure side of the stay vane, which leads the flow back to the guide vanes regions and consequently causes increased backflow close to the guide vane leading edge. Flow recirculation on the mid-span seems to be the highest in the time steps 'f' and 'g'. However, the flow rate continues to reduce due to unfavorable conditions.

The flow rate is the lowest at the time step 'h', even though the recirculation zone already starts to reduce on the mid-span cutting plane. It means that the flow patterns are very complex and three-dimensional. Since, only mid-spans are shown on the figure 5.5, additional analyses have been done to verify that the tendency of the flow is different closer to the hub and the shroud. At the time steps 'i' and 'j', the recirculation zone in the guide vane channel continues to reduce and also the flow rate inside the channel starts to increase again.

As expected, it seems that the flow rate through the guide vane channel depends on the size of the flow separation and recirculation zone between the two consecutive guide vanes. However, the dependence is not completely linear. It seems that there is a delay between the size of the recirculation zone and flow rate, which is caused by the flow behavior closer to the hub and shroud side of the machine.

Static pressure fields

Under normal, stable operating points, static pressure distribution along the guide vanes channel should not change in time. However, at the partial load, when the rotating stall is present, the pressure distribution can vary significantly and is related to the flow rate inside the channel. Moreover, the relation between the static pressure and the velocity along the channel can be described by the Bernoulli's principle (eq. 5.1) as the friction by viscous forces can be negligible.

$$\frac{v^2}{2} + gZ + \frac{p}{\rho} = const. \tag{5.1}$$

The relation can be applied to any reference point on the streamlines inside the channel. Still, when explaining the phenomenon, we need to pay lots of attention, since the flow is 3-dimensional and the recirculation zones can cause complex flow patterns along the channels.

Figure 5.6 represents the static pressure fields on the mid-span cutting plane inside the guide vanes channels for various time steps. Time steps and cutting plane are the same as on the figure 5.5, where the vorticity is presented and can therefore be directly compared. Time step 'c' represents the highest flow rate in the guide vane channel. The static pressure value in the channel is very low, which is to be expected, according to Bernoulli's principle. A small static pressure peak can be seen close to the trailing edge of the guide vane at the time steps 'b', 'c' and 'd'. It corresponds to the small recirculation zone that has been observed also on the figure 5.5.

At the time steps from 'd' to 'f', the flow rate in the channel reduces, the recirculation zone increases and consequently the static pressure increases. Increasing of the static pressure in the channel causes strong adverse pressure gradient around the downstream

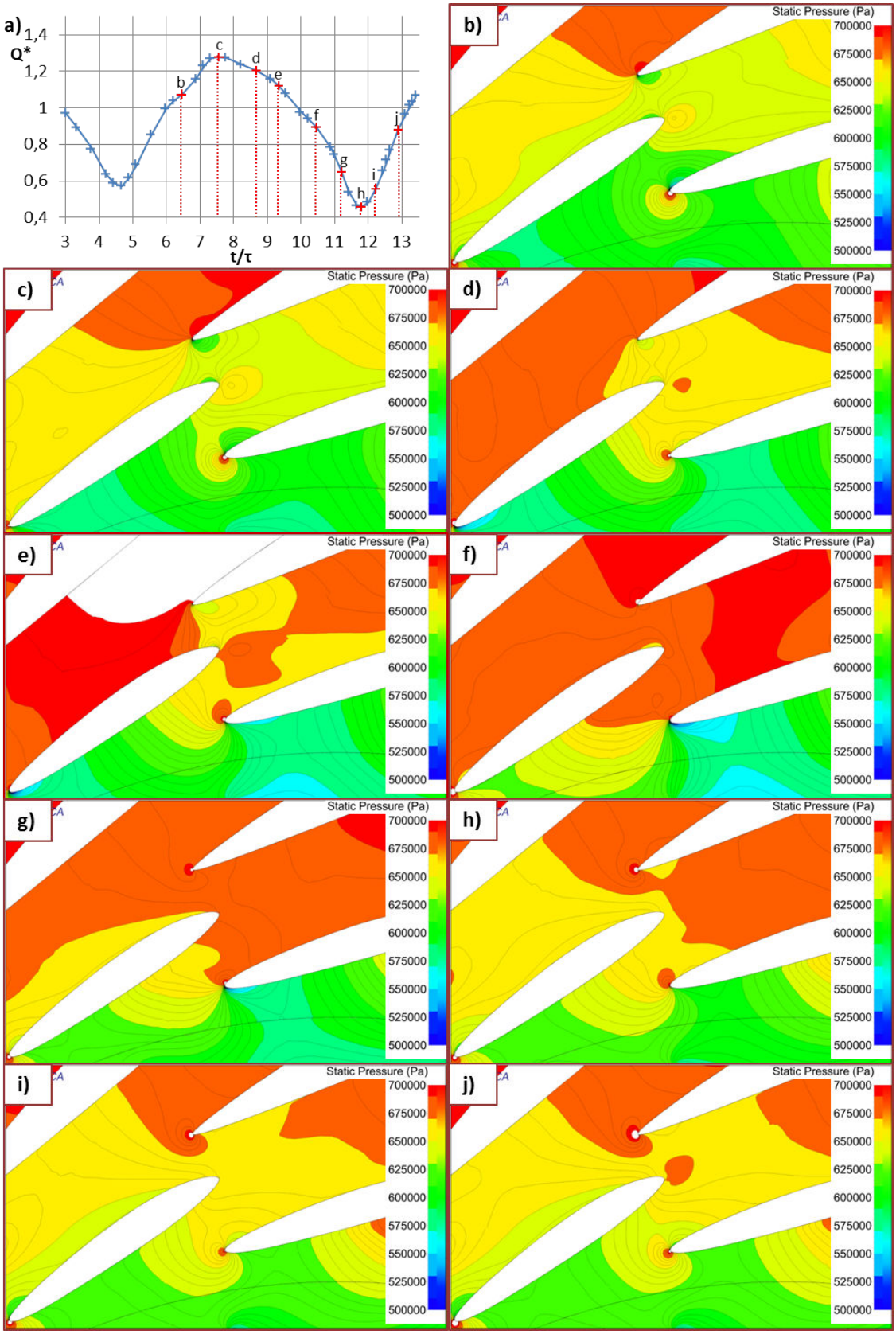

Figure 5.6: a) Flow rate fluctuations through one guide vanes channel b)-j) Mid-span static pressure distribution inside the guide vane channel for various time steps

guide vane leading edge that even increases the flow deviation to the downstream channel as seen at the time step 'f'. Consequently, the flow rate continues to reduce even more. Slowly, adverse gradient starts to neutralize and with some delay (time step 'h' and 'i'), the flow rate starts to increase again. The stall meanwhile moves to the downstream channel as it can be seen on the right side of figures 5.5j and 5.6j. At time step 'j', a small static pressure peak can be observed close to the trailing edge of the guide vanes, which means that the recirculation zone is reduced again to a very small region close to the trailing edge.

Guide vanes channel sections

Radial velocity has been investigated on 4 different cuts in the GV regions (fig. 5.7 - fig. 5.10). The cuts have been made on the constant diameter values along the GV channels. The diameters are defined relatively to the outer diameter of the impeller D_{out}. Time steps remain the same as for the figures 5.5 and 5.6. Since the radial velocity is proportional to the flow rate, the analysis provides an insight of the flow distribution between the hub side and the shroud side of the machine.

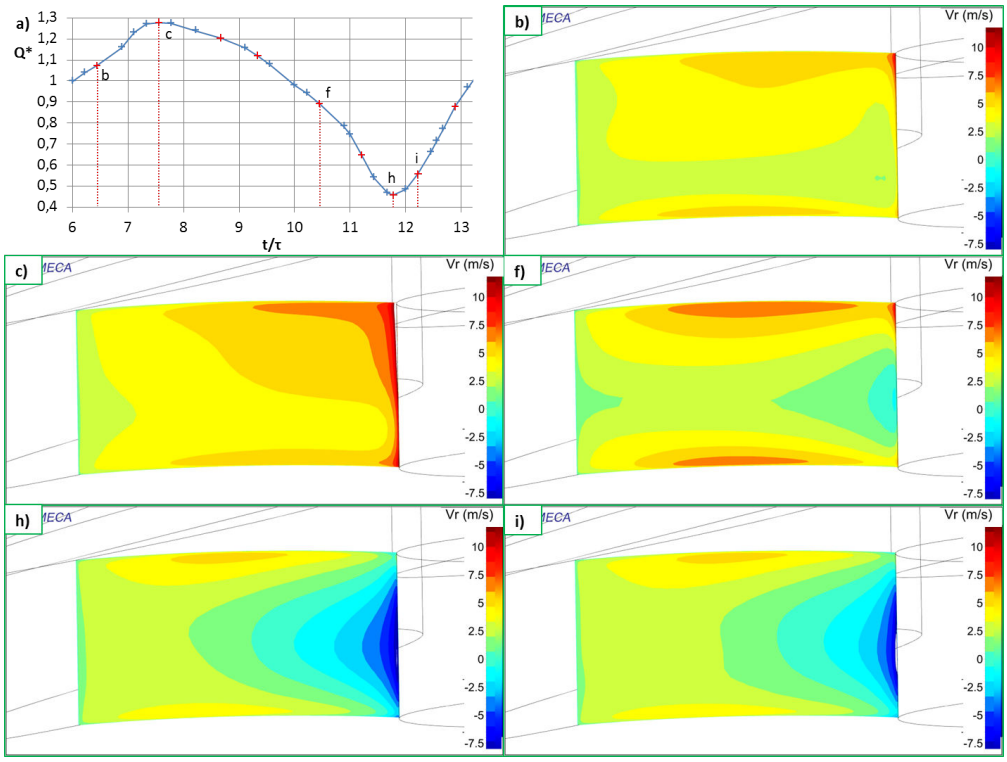

Figure 5.7: a) Flow rate fluctuations through guide vanes channel b)-i) Radial velocity at $D/Dout = 1,127$ (GV leading edge) for various time steps

Figure 5.7 shows the radial velocity profile at the leading edge of the guide vane channel for five different time steps. Time step 'b' shows the region of increasing flow rate through the channel. The flow rate increases mostly at the hub and shroud side of the channel. Later it also increases close to the downstream guide vane and it reaches maximum at the time step 'c'.

Time step 'f' represents the highest recirculation zone seen on figure 5.5f. Flow rate is still high close to the hub and the shroud. Small backflow region can be observed close

to the downstream vane in the mid-span. Backflow and flow deviation to the downstream vane increase until the time step 'h', where the flow rate through the channel is the lowest. Later, at time step 'i', the flow rate through the channel slowly increases again by the reduction of the backflow zone close to the downstream vane.

Figure 5.8 shows the radial velocity distribution at around 1/3 of the guide vane channel ($D/D_{out} = 1,156$). At time step 'b', the flow rate increases almost proportionally around the channel. At time step 'c', it reaches the maximum. From 'c' to 'f', the recirculation zone seen on figure 5.5 starts to grow. At time step 'f', we can see that the majority of the flow goes close to the hub and shroud side of the channel. Figure 5.8f matches with the figure 5.5f, where we can see on mid-span that the center of the channel is blocked by the recirculation zone. Flow rate continues to reduce in all regions and it reaches the minimum at the time step 'h'. Backflow region seen close to the downstream guide vane on figure 5.7h is now located in the middle of the channel. At time step 'i', we can see that the flow rate starts to increase again in all regions of the channel.

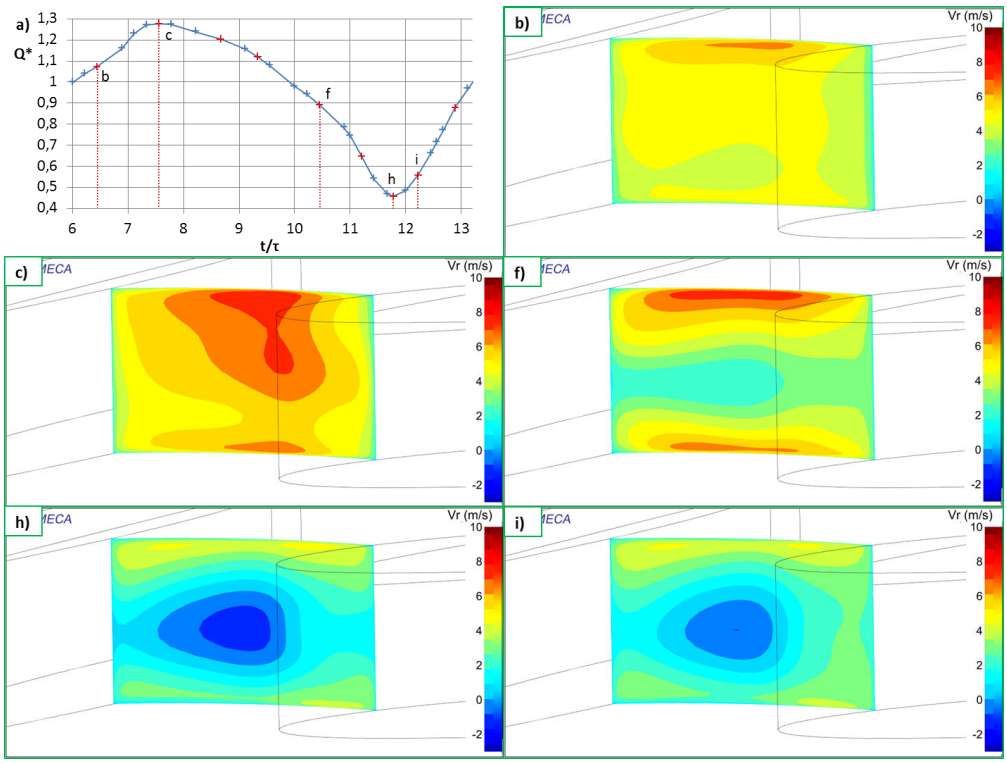

Figure 5.8: a) Flow rate fluctuations through guide vanes channel b)-i) Radial velocity at $D/Dout = 1,156$ for various time steps

Figure 5.9 shows the radial velocity distribution at around 2/3 of the guide vane channel. It can be seen at time steps 'b' and 'c' that the flow rate increase happens at the shroud side of the channel, close to the upstream guide vane. Time step 'f' shows that the recirculation zone occurs firstly in the middle of the channel and the flow is still strong at the shroud and hub side of the channel. At the minimum flow rate (time step 'h'), a strong backflow region occurs close to the upstream vane. At the time step 'i', flow rate starts to increasing again all over the channel.

Cutting plane on figure 5.10 is located at the trailing edge of the guide vane channel. From time step 'b' to 'c' we can see the increased flow rate region close to the shroud. The backflow regions start at the upstream vane close to the shroud and hub (fig. 5.10b and

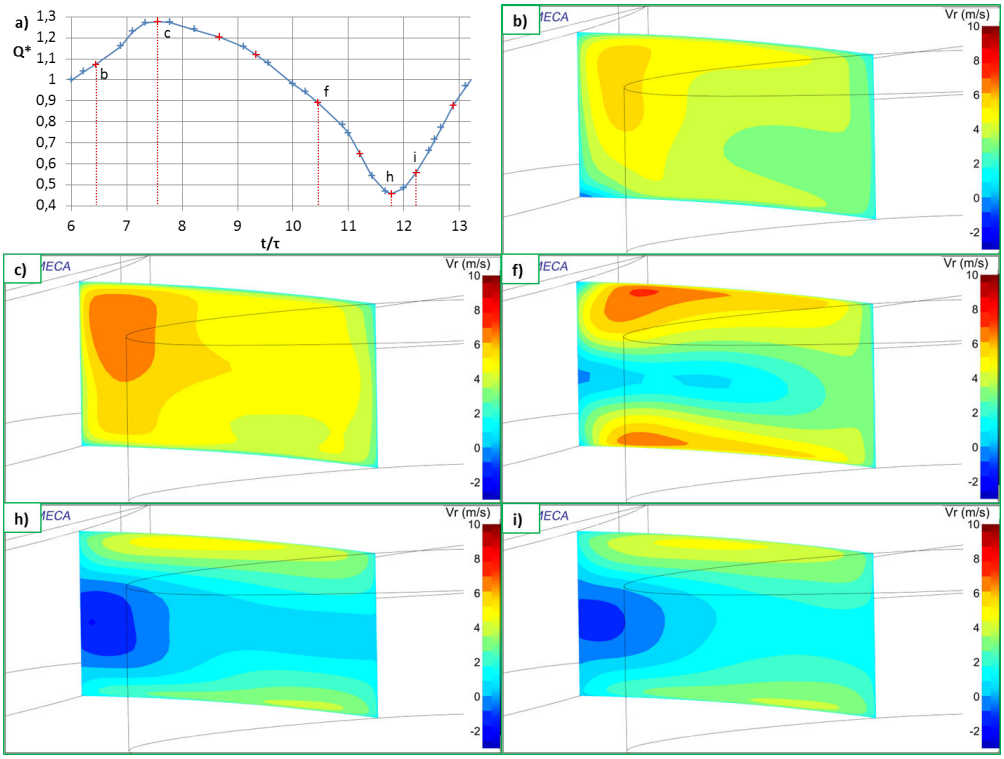

Figure 5.9: a) Flow rate fluctuations through guide vanes channel b)-i) Radial velocity at $D/Dout = 1,195$ for various time steps

c). Recirculation region starts to grow in the middle of the channel, close to the upstream vane (time step 'f'). At this time, the most of the flow passes close to the shroud and hub sides. Minimum flow rate is reached at the time step 'h', when also the flow rates at the hub and shroud sides reduce. At time step 'i', the flow rate through the channel starts to grow again by reducing the recirculation zone close to the upstream guide vane.

5.4 Evolution of the rotating stall

Evolution of the rotating stall can be described in a simplified way as an occurrence and a decay of the stalled cells.

- **Phase 1.** Flow increases in the channel due to favorable conditions, such as low pressure in the middle of the channel (fig. 5.6b) and angle of attack adapted to the guide vanes (fig. 5.5b). Slowly, it reaches maximum value of around 130% of the nominal flow through the channel.

- **Phase 2.** Angle of attack at the entrance of the channel (seen as velocity vectors) starts to turn slowly to the downstream channel (fig. 5.5d). Meanwhile, static pressure in the channel starts to increase and causes strong adverse pressure gradient between the middle region of the channel and the region close to the leading edge of the downstream guide vane on the pressure side of the vane (fig. 5.6d, e, f). It leads into strong flow separation in the channel, growth of the recirculation zone and deviation of the flow towards the downstream channel (fig. 5.5d, e, f, g). Flow rate reduction starts firstly in the middle of the channel and after that it reduces

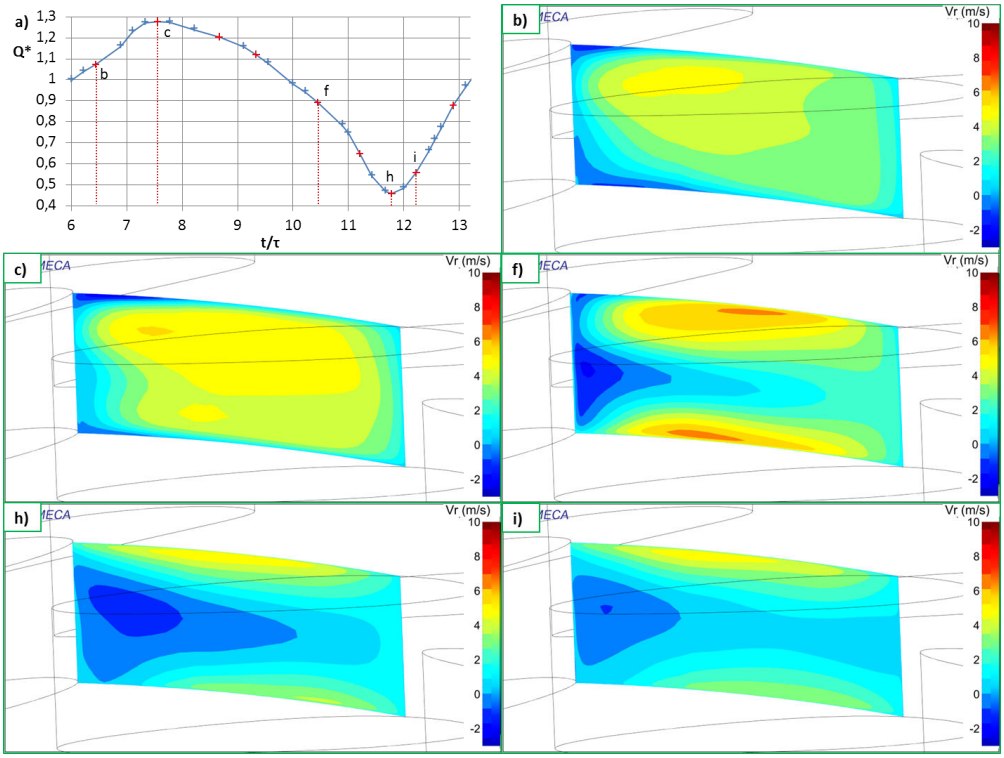

Figure 5.10: a) Flow rate fluctuations through guide vanes channel b)-i) Radial velocity at $D/Dout = 1,233$ (GV trailing edge) for various time steps

also at the hub side and shroud side of the channel, which leads into additional flow rate reduction (fig. 5.9f, h). It reaches minimum of around 45% of the nominal flow rate.

- **Phase 3.** Adverse pressure gradients start to reduce, together with the size of the recirculation zone and cause gradually more favorable conditions that lead more flow rate into the channel. The stalled cell moves to the downstream channel, which causes additional fast flow rate increase in the channel.

5.5 Chapter discussion

In this chapter it was shown that unsteady simulations can give very precise results. Accuracy of performance prediction has been improved significantly, comparing to the steady simulations. Additionally, the simulations are robust enough to give good results at very unstable operating points, where the rotating stall occurs. Various shapes of the rotating stall have been detected. Results and trends of rotating stall behavior appears to be similar to the experimental work of [10]. However, they cannot be compared directly, since the pump-turbine geometry is different in their case. It is important to say that the intensity of the rotating stall can vary. It could be parametrized by the number of rotating stall cells, rotating stall frequency and by the flow variation through the guide vane channel. As a perspective, non-dimensional parameter could be proposed in order to evaluate the rotating stall intensity for various geometries and openings.

Unsteady simulations presented in this chapter showed the relation between the number of rotating stall cells and the rotating stall frequency (tab. 5.1). At lower number

of cells results in higher stall frequency. Moreover, the discharge fluctuations are higher in the cases of lower number of cells. Even though the statement should be verified experimentally, it can be assumed that the conditions with less rotating stall cells are less favorable (more dangerous) for the machine, comparing to the more rotating stall cells or fully symmetrical distribution of the flow around the distributor.

Local flow analysis showed the mechanisms of the rotating stall. In a simplified way, the rotating stall can be described with the growth and decay of the stalled cell. Most important parameters for the stall evolution are the size of the flow separation and recirculation zones that completely change the flow conditions at the leading edge of the guide vanes. Pressure fields, especially the direction and magnitude of adverse pressure gradient, cause the deviation of the flow to the downstream channel, which consequently leads the rotation of the stalled cells around the distributor with its characteristic frequency.

Part IV

Conclusions and perspectives

Chapter 6

Conclusions and perspectives

6.1 Conclusions

CFD tools have been used in the presented work to predict and analyze pumping mode part load instabilities. All presented simulations have been performed in LEGI on maximum 12 processors, which is nowadays widely accessible computational power.

The first goal of the project has been to perform and to develop simulations of the cavitation phenomena in a pump-turbine geometry. Steady calculations on periodic mesh have been performed for various discharges and various NPSH values. Reliable results have been obtained even for very unstable off-design operating points. The agreement between the (unfortunately limited) experimental data and simulations is very good. The code is capable to predict accurately the incipient cavitation values, the NPSH head drop curves and the average cavitation forms in reasonably short time (max. 20 CPU hours).

Steady simulations on the periodic and combined mesh give good insight on the stability of the operating points. Calculations on the periodic mesh are very fast and relatively good in the prediction of the global performance curve. They are accurate enough to be used to analyze the global position of the hump zone and the influence of the various guide vanes geometries. Combined mesh with the periodicity in the impeller regions and full mesh at the distributor regions can be additionally used for the analysis of the stalled forms in the distributor. Stable, slightly unstable and fully unstable operating points can be detected by using this approach. It is a compromised solution between more costly, unsteady simulations on fully-meshed domain and steady simulations on the periodic mesh. However, they have their limits. The prediction of the hump zone is better if the gap between the impeller and the distributor is larger. The origins of the discrepancies are the periodicity in the impeller regions and using the mixing plane at the border between the impeller and the distributor. Indeed, for the case of larger guide vanes openings (smaller gaps), the flow patterns at the distributor regions influence the flow behavior at the impeller regions. Author would suggest to put special attention on the modeling of rotor-stator interactions, when the gaps between the impeller and the distributor are relatively small and the operating points are at the partial load. Moreover, for smaller gaps and partial loads, the periodicity between the blades would not be suggested in order to minimize the discrepancies between the numerical and the experimental results.

The results obtained by unsteady simulations, using URANS equations, are very good comparing to the results in the literature. Moreover, they prove that the developed CFD tools can be very exact in the prediction of the performance even under off-design conditions, such as partial load. Additionally, CFD simulations give us a detailed insight

into the flow patterns inside the machine that are experimentally very demanding or even impossible to get.

Developed and presented computational methodology with several types of calculations enables us to obtain various pieces of information progressively, depends on what we wish to get and what are our computational resources. Figure 6.1 shows the cost of each calculation presented in the document. On that basis one can start with the analysis of various operating points. During the process, more demanding points can be found and analyzed in details by performing more costly unsteady simulations or by using cavitation model. Author proposes following procedure:

1. Steady simulations without cavitation model; periodicity as boundary conditions
2. Steady simulations for cavitating flow; periodicity as boundary conditions
3. Steady simulations on full domain (with cavitation model or without)
4. Unsteady simulations on full domain (with cavitation model or without)

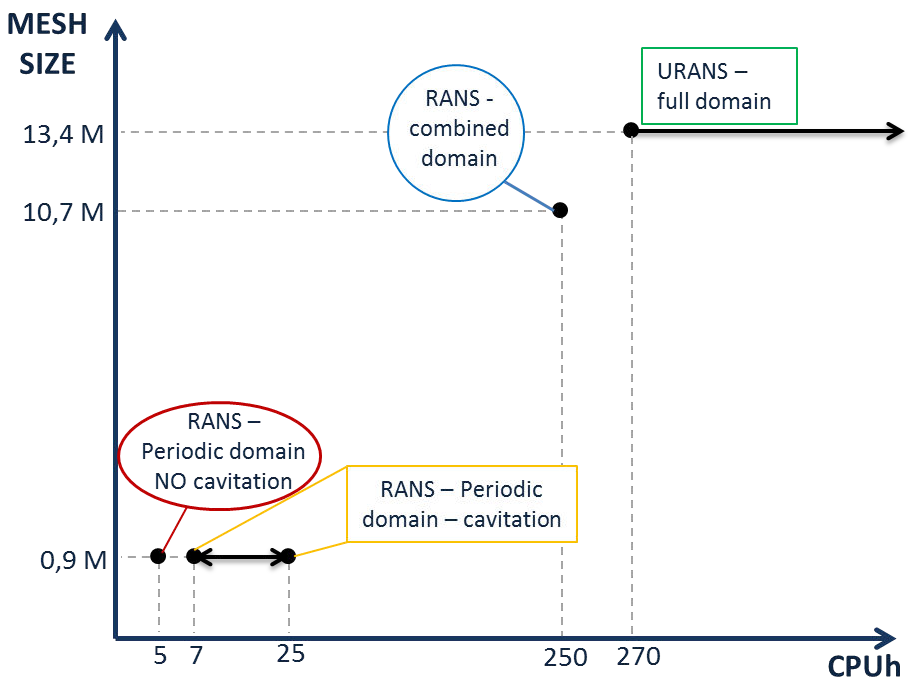

Figure 6.1: Mesh size (N° of cells) and CPU time for various types of simulations

Rotating stall can take various forms and intensity. The number as well as the frequency of the rotating stall cells can vary. Even though it should be confirmed experimentally, it seems like the lower number of rotating cells indicate higher rotating stall frequency and higher intensity that is seen as a larger cells of increased or decreased flow. Therefore, corresponding operating points seems to be more dangerous for the machine. Local flow analysis has shown that the rotating stall can be described as a growth and decay of the stalled cells and rotation of these cells around the distributor. Most important parameters for the stall evolution are the size of the flow separation and recirculation zones that completely change the flow conditions at the leading edge of the guide vanes.

Pressure fields, especially the direction and magnitude of adverse pressure gradient, cause the deviation of the flow to the downstream channels and are responsible for the so called rotation of the stalled cells. Taking into account all mentioned rotating stall mechanisms, we can highlight several possible ways to modify the effects of the rotating stall.

- **Decreasing GV opening angle** would increase the gap between the impeller and guide vanes and the gap between the guide vanes and stay vanes as well. Angle of attack would be in that case more adapted at the GV leading edge, but would be able to fluctuate more due to larger gap between the impeller and GV leading edge. Increased gap between the GV and the SV would make the flow deviation and the rotation of the cells around the distributor easier.

- **Increasing GV opening angle** would reduce the gap between the impeller and the guide vanes. Even though the attack angle would become less adapted, also the possible fluctuations of local attack angle would reduce. The losses in the distributor would increase, but the rotating stall intensity would reduce, which is good for the operating points stability.

- **Changing GV geometry** would change the velocity and pressure fields in the distributor regions, which could change completely the position and the amplitude of the hump zone as it has been shown also in this document. It should be stressed that the GV design around the GV leading edge can influence the ratio between the gap size and the opening angle, which is not linear. Design of the guide vanes is therefore a strong tool that can be used to modify rotating stall conditions at various operating points.

- **Reducing the impeller-distributor gap size** would reduce the intensity of the rotating stall. However, the relative gap size would change even more with the changing of the guide opening, if the guide vanes are positioned closer to the impeller. It should be mentioned that other kind of instabilities, such as strong pressure fluctuations due to rotor-stator interactions might appear in case of very small radial gap between the impeller and the guide vanes.

- **Changing impeller geometry** might have an influence on the rotating stall mechanisms. It was shown in this document that pressure and velocity fields in the impeller might have a strong influence on the rotating stall. Moreover, the flow angle at the trailing edge of the impeller seems to be a useful way to control and to influence the rotating stall conditions.

6.2 Perspectives

First of all, experimental tests should be performed to evaluate the precision of the presented numerical simulations. Accuracy of the rotating stall frequency and number of rotating stall cells prediction should be validated by the experimental measurements for the same geometry under the same operating conditions. Furthermore, in order to increase precision and enable various frequency analyses, additional revolutions of the machine should be simulated.

The presented results, especially unsteady calculations, demonstrate big potential to develop a general, widely accessible numerical tool that gives reliable results for a wide range of discharges, even under demanding off-design conditions, such as the appearance

of the cavitation and the rotating stall. To achieve that, unsteady simulations could be made also for the cavitating conditions. More importantly, the simulations should be validated for additional GV openings, GV geometries and even for completely different pump-turbine geometries.

Another perspective could be a more detailed analysis of the unsteady flow phenomena inside the impeller and the distributor. The phenomenon known as a runner hump exists for some geometries and is related with the partial load recirculation zones close to the leading edge of the impeller. In literature it has been poorly addressed, therefore it should be additionally investigated. Presented work can be a good basis to address this unstable behavior.

Finally, the main idea of the presented study was the investigation of the hump zone and related rotating stall in order to minimize its effects on the pump-turbine performance. At this moment, all the numerical tools to achieve this are available and can be used for any geometry that is facing the problem of the rotating stall. Additional study from industrial or academic point of view should be performed in order to propose practical solutions for reducing or eliminating the negative effects of the rotating stall on the pump-turbine performance and stability of the operating points.

Bibliography

[1] *H Amblard, P Henry, G Borciani, G Martin, P Guiton, and R Thalmann. Comportement des turbines Francis et des pompes-turbines à débit partiel. *La Houille Blanche*, (5):435–440, 1985.

[2] N Arndt, A J Acosta, C E Brennen, and T K Caughey. Rotor–stator interaction in a diffuser pump. *Journal of Turbomachinery*, 111(3):213–221, 1989.

[3] N Arndt, A J Acosta, C E Brennen, and T K Caughey. Experimental investigation of rotor-stator interaction in a centrifugal pump with several vaned diffusers. *Journal of Turbomachinery*, 112(1):98–108, 1990.

[4] F Avellan. Introduction to cavitation in hydraulic machinery. In *The 6th International Conference on Hydraulic Machinery and Hydrodynamics, Timisoara, Romania*, 2004.

[5] F Avellan. Evolution des groupes de pompage-turbinage. *Bulletin des SEV VSE Including Jahresheft*, 103(2):37, 2012.

[6] R Bachert, B Stoffel, and M Dular. Unsteady cavitation at the tongue of the volute of a centrifugal pump. *Journal of Fluids Engineering*, 132(6):061301, 2010.

[7] *B S Baldwin and H Lomax. *Thin layer approximation and algebraic model for separated turbulent flows*. American Institute of Aeronautics and Astronautics, 1978.

[8] *S G Bankoff. A variable density single-fluid model for two-phase flow with particular reference to steam-water flow. *Journal of Heat Transfer*, 82(4):265–272, 1960.

[9] S Berten. *Hydrodynamics of high specific power pumps for off-design operating conditions*. PhD thesis, EPFL, 2010.

[10] O Braun. *Part load flow in radial centrifugal pumps*. PhD thesis, EPFL, 2009.

[11] G D Ciocan, O Teller, and F Czerwinski. Variable speed pump-turbines technology. *University" Politehnica" of Bucharest Scientific Bulletin, Series D: Mechanical Engineering*, 74(1):33–42, 2012.

[12] International Electrotechnical Commission et al. Iec 60193. Hydraulic turbines, storage pumps and pump-turbines - model acceptance tests. *Chap. Dimensional Check of Model and Prototype*, 1999.

[13] O Coutier-Delgosha. *Modélisation des écoulements cavitants: étude des comportements instationnaires et application tridimensionnelle aux turbomachines*. PhD thesis, Grenoble, INPG, 2001.

[14] O Coutier-Delgosha, R Fortes-Patella, and J-L Reboud. Evaluation of the turbulence model influence on the numerical simulations of unsteady cavitation. *Journal of Fluids Engineering*, 125(1):38–45, 2003.

[15] O Coutier-Delgosha, R Fortes-Patella, J-L Reboud, N Hakimi, and C Hirsch. Numerical simulation of cavitating flow in 2d and 3d inducer geometries. *International Journal for Numerical Methods in Fluids*, 48(2):135–167, 2005.

[16] O Coutier-Delgosha, R Fortes-Patella, J-L Reboud, N Hakimi, and C Hirsch. Stability of preconditioned navier–stokes equations associated with a cavitation model. *Computers & Fluids*, 34(3):319–349, 2005.

[17] O Coutier-Delgosha, R Fortes-Patella, J-L Reboud, M Hofmann, and B Stoffel. Experimental and numerical studies in a centrifugal pump with two-dimensional curved blades in cavitating condition. *Journal of Fluids Engineering*, 125(6):970–978, 2003.

[18] O Coutier-Delgosha, P Morel, R Fortes-Patella, and J-L Reboud. Numerical simulation of turbopump inducer cavitating behavior. *International Journal of Rotating Machinery*, 2005(2):135–142, 2005.

[19] O Coutier-Delgosha, J L Reboud, and Y Delannoy. Numerical simulation of the unsteady behaviour of cavitating flows. *International Journal for Numerical Methods in Fluids*, 42(5):527–548, 2003.

[20] J Decaix. *Modélisation et simulation de la turbulence compressible en milieu diphasique: application aux écoulements cavitants instationnaires.* PhD thesis, Grenoble, INPG, 2012.

[21] Y Delannoy and J-L Kueny. Two phase flow approach in unsteady cavitation modelling. In *ASME Cavitation and Multiphase flow forum*, pages 153–158, 1990.

[22] M Dular, R Bachert, C Schaad, and B Stoffel. Investigation of a re-entrant jet reflection at an inclined cavity closure line. *European Journal of Mechanics-B/Fluids*, 26(5):688–705, 2007.

[23] M Dular, R Bachert, B Stoffel, and B Širok. Experimental evaluation of numerical simulation of cavitating flow around hydrofoil. *European Journal of Mechanics-B/Fluids*, 24(4):522–538, 2005.

[24] P Dupont, A-C Bayeul-Lainé, A Dazin, G Bois, O Roussette, and Q Si. Leakage flow simulation in a specific pump model. In *IOP Conference Series: Earth and Environmental Science*, volume 22, page 012012. IOP Publishing, 2014.

[25] B Eckhardt, T M Schneider, B Hof, and J Westerweel. Turbulence transition in pipe flow. *Annu. Rev. Fluid Mech.*, 39:447–468, 2007.

[26] Y Egorov, F R Menter, R Lechner, and D Cokljat. The scale-adaptive simulation method for unsteady turbulent flow predictions. part 2: Application to complex flows. *Flow, Turbulence and Combustion*, 85(1):139–165, 2010.

[27] *H W Emmons. A surway of stall propagation: experiment and theory. *Journal of Basic Engineering*, 81:409–416, 1959.

[28] X Escaler, E Egusquiza, M Farhat, F Avellan, and M Coussirat. Detection of cavitation in hydraulic turbines. *Mechanical Systems and Signal Processing*, 20(4):983–1007, 2006.

[29] R Fortes-Patella, A Archer, and C Flageul. Numerical and experimental investigations on cavitation erosion. In *IOP Conference Series: Earth and Environmental Science*, volume 15, page 022013. IOP Publishing, 2012.

[30] R Fortes-Patella, S Barre, and J-L Reboud. Experiments and modelling of cavitating flows in venturi. part II: unsteady cavitation. In *CAV 2006 Symposium*, 2006.

[31] R Fortes-Patella, O Coutier-Delgosha, J Perrin, and J-L Reboud. Numerical model to predict unsteady cavitating flow behavior in inducer blade cascades. *Journal of Fluids Engineering*, 129(2):128–135, 2007.

[32] J-P Franc and J-M Michel. *Fundamentals of cavitation*, volume 76. Springer, 2006.

[33] J-P Franc et al. *La cavitation: mécanismes physiques et aspects industriels*. Presses Universitaires Grenoble, 1995.

[34] *P Frigne and R Van den Braembussche. Distinction between different types of impeller and diffuser rotating stall in a centrifugal compressor with vaneless diffuser. *Journal of Engineering for Gas Turbines and Power*, 106(2):468–474, 1984.

[35] C Gentner, M Sallaberger, C Widmer, O Braun, and T Staubli. Numerical and experimental analysis of instability phenomena in pump turbines. In *IOP Conference Series: Earth and Environmental Science*, volume 15, page 032042. IOP Publishing, 2012.

[36] E Goncalves and R Fortes-Patella. Numerical simulation of cavitating flows with homogeneous models. *Computers & Fluids*, 38(9):1682–1696, 2009.

[37] N Gonzalo-Flores, E Goncalvès, R Fortes-Patella, J Rolland, and C Rebattet. Head drop of a spatial turbopump inducer. *Journal of Fluids Engineering*, 130(11):111301, 2008.

[38] L Gros, A Couzinet, and D Pierrat. Part load flow and hydrodynamic instabilities of a centrifugal pump–Part I: experimental investigations. In *Paper 33444, AJK Joint Fluid Engineering Conference 2015*, 2015.

[39] L Gros, A Couzinet, and D Pierrat. Part load flow and hydrodynamic instabilities of a centrifugal pump–Part II: Numerical simulations. In *Paper 33445, AJK Joint Fluid Engineering Conference 2015*, 2015.

[40] N Hakimi, C Hirsch, and S Pierret. Presentation and application of a new extended k–ε model with wall functions. *ECCOMAS, Barcelona*, 2000.

[41] V Hasmatuchi. *Hydrodynamics of a pump-turbine operating at off-design conditions in generating mode*. PhD thesis, EPFL, 2012.

[42] V Hasmatuchi, M Farhat, S Roth, F Botero, and F Avellan. Experimental evidence of rotating stall in a pump-turbine at off-design conditions in generating mode. *Journal of Fluids Engineering*, 133(5):051104, 2011.

[43] *U Haupt, U Seidel, A N Abdel-Hamid, and M Rautenberg. Unsteady flow in a centrifugal compressor with different types of vaned diffusers. *Journal of Turbomachinery*, 110(3):293–302, 1988.

[44] *J H Horlock and B Lakshminarayana. Secondary flows: theory, experiment, and application in turbomachinery aerodynamics. *Annual Review of Fluid Mechanics*, 5(1):247–280, 1973.

[45] J-B Houdeline, J Liu, S Lavigne, Y Laurant, and L Balara. Start-up improvement in turbine mode for high head PSP machine. In *IOP Conference Series: Earth and Environmental Science*, volume 15, page 042022. IOP Publishing, 2012.

[46] M Inoue, M Kuroumaru, S Yoshida, and M Furukawa. Short and long length-scale disturbances leading to rotating stall in an axial compressor stage with different stator/rotor gaps. *Journal of Turbomachinery*, 124(3):376–384, 2002.

[47] NUMECA International. Theoretical manual FINE^{TM}/Turbo v8.9. 2011.

[48] U Ješe, R Fortes-Patella, and S Antheaume. High head pump-turbine: Pumping mode numerical simulations with a cavitation model for off-design conditions. In *IOP Conference Series: Earth and Environmental Science*, volume 22, page 032048. IOP Publishing, 2014.

[49] U Ješe, R Fortes-Patella, and M Dular. Numerical study of pump-turbine instabilities under pumping mode off-design conditions. In *Paper 33501, AJK Joint Fluid Engineering Conference 2015*, 2015.

[50] W P Jones and B Launder. The prediction of laminarization with a two-equation model of turbulence. *International Journal of Heat and Mass Transfer*, 15(2):301–314, 1972.

[51] K A Kaupert, P Holbein, and T Staubli. A first analysis of flow field hysteresis in a pump impeller. *Journal of Fluids Engineering*, 118(4):685–691, 1996.

[52] I Khlifa, O Coutier-Delgosha, S Fuzier, M Hočevar, A Vabre, and K Fezzaa. Velocity measurements in cavitating flows using fast X-ray imaging. In *Congrés Français de Mécanique (21; 2013; Bordeaux)*, 2013.

[53] J Kim, P Moin, and R Moser. Turbulence statistics in fully developed channel flow at low Reynolds number. *Journal of fluid mechanics*, 177:133–166, 1987.

[54] S J Kline. *On the nature of stall.* Stanford University, Dept. of Mechanical Engineering, 1958.

[55] R T Knapp, J W Daily, and F G Hammitt. *Cavitation.* Institute of hydraulic research, University of Iowa, 1979.

[56] A N Kolmogorov. The local structure of turbulence in incompressible viscous fluid for very large Reynolds numbers. In *Dokl. Akad. Nauk SSSR*, volume 30, pages 299–303, 1941.

[57] L Krumenacker, R Fortes-Patella, and A Archer. Numerical estimation of cavitation intensity. In *IOP Conference Series: Earth and Environmental Science*, volume 22, page 052014. IOP Publishing, 2014.

[58] A Kubota, H Kato, and H Yamaguchi. A new modelling of cavitating flows: A numerical study of unsteady cavitation on a hydrofoil section. *Journal of Fluid Mechanics*, 240(1):59–96, 1992.

[59] R F Kunz, J W Lindau, M L Billet, and David R Stinebring. *Multiphase CFD modeling of developed and supercavitating flows.* Defense Technical Information Center, 2001.

[60] *S C Li. *Cavitation of hydraulic machinery*, volume 1. Imperial College Press London, 2000.

[61] H Lohrberg, B Stoffel, R Fortes-Patella, O Coutier-Delgosha, and J L Reboud. Numerical and experimental investigations on the cavitating flow in a cascade of hydrofoils. *Experiments in fluids*, 33(4):578–586, 2002.

[62] N M McDougall, N A Cumpsty, and T P Hynes. Stall inception in axial compressors. *Journal of Turbomachinery*, 112(1):116–123, 1990.

[63] F R Menter. Eddy viscosity transport equations and their relation to the k-ε model. *Journal of Fluids Engineering*, 119(4):876–884, 1997.

[64] F R Menter and Y Egorov. The scale-adaptive simulation method for unsteady turbulent flow predictions. part 1: theory and model description. *Flow, Turbulence and Combustion*, 85(1):113–138, 2010.

[65] F R Menter, M Kuntz, and R Langtry. Ten years of industrial experience with the sst turbulence model. *Turbulence, Heat and Mass Transfer*, 4(1), 2003.

[66] C L Merkle, J Feng, and P E Buelow. Computational modeling of the dynamics of sheet cavitation. In *3rd International Symposium on Cavitation, Grenoble, France*, volume 2, pages 47–54, 1998.

[67] *I Newton. *Opticks or, a Treatise of the reflexions, refractions, inflexions and colours of light. Also two treatises of the species and magnitude of curvilinear figures.* London, printed for Sam. Smith and Benj. Walford, 1704.

[68] C Nicolet, Y Vaillant, B Kawkabani, P h Allenbach, J J Simond, and F Avellan. Pumped storage units to stabilize mixed islanded power network: a transient analysis. *Proceedings of HYDRO*, pages 6–9, 2008.

[69] O Pacot. *Large scale computation of the rotating stall in a pump-turbine using an overset finite element large eddy simulation numerical code.* PhD thesis, EPFL, 2014.

[70] O Pacot, C Kato, and F Avellan. High-resolution les of the rotating stall in a reduced scale model pump-turbine. In *IOP Conference Series: Earth and Environmental Science*, volume 22, page 022018. IOP Publishing, 2014.

[71] V C Patel, W Rodi, and G Scheuerer. Turbulence models for near-wall and low reynolds number flows-a review. *AIAA Journal*, 23(9):1308–1319, 1985.

[72] N Pedersen, P S Larsen, and C B Jacobsen. Flow in a centrifugal pump impeller at design and off-design conditions–part I: particle image velocimetry (PIV) and laser Doppler velocimetry (LDV) measurements. *Journal of Fluids Engineering*, 125(1):61–72, 2003.

[73] M S Plesset. The dynamics of cavitation bubbles. *Journal of Applied Mechanics*, 16:277, 1949.

[74] B Pouffary. *Simulation numérique d'écoulements 2d/3d cavitants, stationnaires et instationnaires: analyse spécifique pour les turbomachines*. PhD thesis, Grenoble, INPG, 2004.

[75] B Pouffary, R Fortes-Patella, J-L Reboud, and P-A Lambert. Numerical analysis of cavitation instabilities in inducer blade cascade. *Journal of Fluids Engineering*, 130(4):041302, 2008.

[76] B Pouffary, R Fortes-Patella, J-L Reboud, and P-A Lambert. Numerical simulation of 3d cavitating flows: analysis of cavitation head drop in turbomachinery. *Journal of Fluids Engineering*, 130(6):061301, 2008.

[77] H J Ran, X W Luo, Y L Chen, H Y Xu, and M Farhat. Hysteresis phenomena in hydraulic measurement. In *IOP Conference Series: Earth and Environmental Science*, volume 15, page 062048. IOP Publishing, 2012.

[78] L Rayleigh. On the pressure developed in a liquid during the collapse of a spherical cavity. *The London, Edinburgh, and Dublin Philosophical Magazine and Journal of Science*, 34(200):94–98, 1917.

[79] J-L Reboud, R Fortes-Patella, M Hofmann, H Lohrberg, G Ludwig, and B Stoffel. Numerical and experimental investigations on the self oscillating behavior of cloud cavitation. In *ASME Paper FEDSM99-7259, Proceedings of 3rd ASME/JSME Joint Fluids Engineering Conference*, 1999.

[80] J-L Reboud, B Stutz, and Olivier Coutier-Delgosha. Two-phase flow structure of cavitation: experiment and modelling of unsteady effects. In *3rd International Symposium on Cavitation CAV1998, Grenoble, France*, volume 26, 1998.

[81] T Sano, Y Nakamura, Y Yoshida, and Y Tsujimoto. Alternate blade stall and rotating stall in a vaned diffuser. *JSME International Journal Series B*, 45(4):810–819, 2002.

[82] T Sano, Y Yoshida, Y Tsujimoto, Y Nakamura, and T Matsushima. Numerical study of rotating stall in a pump vaned diffuser. *Journal of Fluids Engineering*, 124(2):363–370, 2002.

[83] *G H Schnerr and J Sauer. Physical and numerical modeling of unsteady cavitation dynamics. In *Fourth International Conference on Multiphase Flow, New Orleans, USA*, volume 1, 2001.

[84] *T-H Shih, W W Liou, A Shabbir, Z Yang, and J Zhu. A new k-epsilon eddy viscosity model for high Reynolds number turbulent flows: Model development and validation. 1994.

[85] A K Singhal, M M Athavale, H Li, and Y Jiang. Mathematical basis and validation of the full cavitation model. *Journal of Fluids Engineering*, 124(3):617–624, 2002.

[86] M Sinha and J Katz. The onset and development of rotating stall within a centrifugal pump with a vaned diffuser. In *Paper FEDSM99-7198, The 3rd ASME/JSME Joint Fluid Engineering Conference*, pages 1–7, 1999.

[87] M Sinha, A Pinarbasi, and J Katz. The flow structure during onset and developed states of rotating stall within a vaned diffuser of a centrifugal pump. *Journal of Fluids Engineering*, 123(3):490–499, 2001.

[88] P R Spalart and S R Allmaras. A one-equation turbulence model for aerodynamic flows. *AIAA Journal*, 1992.

[89] T Staubli, F Senn, and M Sallaberger. Instability of pump-turbines during start-up in turbine mode. *Hydro2008, Ljubljana, Slovenia, Paper*, (9.6), 2008.

[90] B Širok, M Dular, and B Stoffel. *Kavitacija*. Ljubljana, 2006.

[91] G Wuibaut, G Bois, P Dupont, G Caignaert, and M Stanislas. PIV measurements in the impeller and the vaneless diffuser of a radial flow pump in design and off-design operating conditions. *Journal of Fluids Engineering*, 124(3):791–797, 2002.

[92] *Z Yang and T H Shih. New time scale based k-epsilon model for near-wall turbulence. *AIAA Journal*, 31(7):1191–1198, 1993.

[93] Y Yangyang, X Yexiang, Z Wei, Z Liming, A S Hwang, and W Zhengwei. Numerical analysis of a model pump-turbine internal flow behavior in pump hump district. In *IOP Conference Series: Earth and Environmental Science*, volume 22, page 032040. IOP Publishing, 2014.

[94] Y Yoshida, Y Murakami, T Tsurusaki, and Y Tsujimoto. Rotating stalls in centrifugal impeller/vaned diffuser systems. In *Proc. First ASME/JSME Joint Fluids Engineering Conference*, pages 125–130, 1991.

[95] F R Young. *Cavitation*. World Scientific, 1999.

[96] M Zangeneh, A Goto, and H Harada. On the design criteria for suppression of secondary flows in centrifugal and mixed flow impellers. *Journal of Turbomachinery*, 120(4):723–735, 1998.

[97] Z Zhang. Rotating stall mechanism and stability control in the pump flows. In *IOP Conference Series: Earth and Environmental Science*, volume 12, page 012010. IOP Publishing, 2010.

[98] A Žnidarčič, R Mettin, and M Dular. Modeling cavitation in a rapidly changing pressure field–application to a small ultrasonic horn. *Ultrasonics Sonochemistry*, 22:482–492, 2015.

(*) Marked references have not been read by author directly (or only partly)

Appendix A

Experimental data

A.1 Experimental test rig

All the experimental data used in the presented studies have been provided by Alstom Hydro. The measurements have been carried out on the test rig in Alstom's laboratory in Grenoble according to international standard IEC 60193 [12]. Schematic representation of the closed test rig components can be seen on the figure A.1.

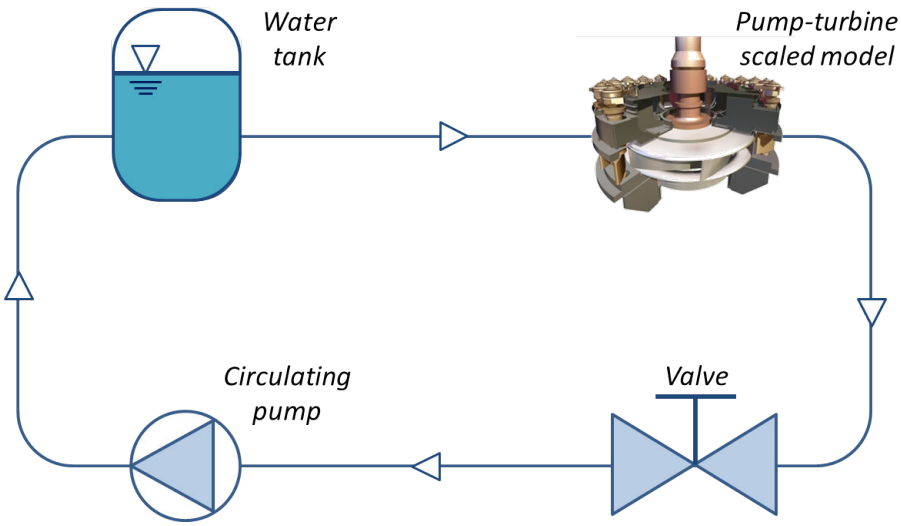

Figure A.1: Schematic closed test rig for pump-turbines (pumping mode)

The test rig consists of following components:

- **Circulation pumps** that take care for the flow circulation and compensate the losses in the closed loop. They are also used to control the operating points.
- **Valve**, which regulates the flow rate in the loop.
- **Water tank**, where the pump-turbine upstream pressure can be defined.
- **Scaled pump-turbine model** equipped with the experimental setup for the performance measurements and the visualization.

During the experiment on the closed test rig, one can set, measure and observe several system parameters that define the operating points of the machines. In the presented study, we used experimental data provided by the following instrumentation:

- **Flow meters** that are situated on the test rig away from the machine. Two different technologies are used at the same time to cross check measurements, when it is possible. The accuracy of the measurements is around 0,15%.
  - **Electromagnetic flow meters:** Water velocity through a magnetic field causes a difference of the potential in the water.
  - **Propeller flow meters:** The rotating speed of the propellers is proportional to the velocity of the flow.
- **Pressure sensors** on the draft tube and on the spiral case. On each side of the machine, there are four differential pressure sensors that measure static and dynamic components of the total pressure.
  - **Manometers** are used to measure the static pressure difference. Their precision is around 0,05%.
  - **Piezoelectric sensors** are used to measure the dynamic component of the pressure. The accuracy of the sensors is around 1%.
- **Shaft torque measurement equipment** is situated on the generator shaft.
- **High speed camera** close to the draft cone. Draft cone is made of Plexiglas, therefore it is possible to observe the cavitation forms on the suction side of the impeller blades, close to the leading edge.

Position of the pressure sensors section at the high and low pressure area is very important for the evaluation of the numerical results, since the numerical domain is not completely the same as the experimental one. Figure A.2 shows the position of the sensors and instrumentation.

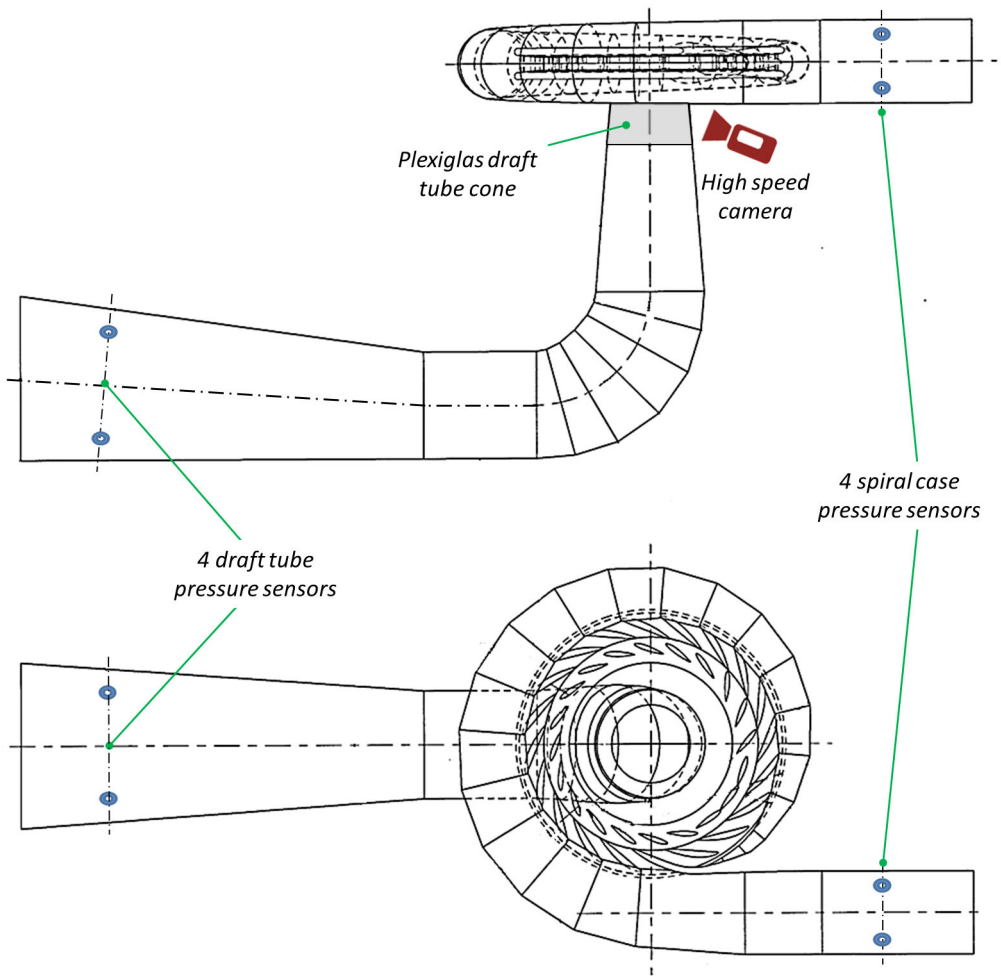

Figure A.2: Position of the sensors during the measurements (Alstom Hydro)

Appendix B

Résumé prolongé

B.1 Introduction

Les cinq dernières décennies, la population de notre planète a augmenté de plus de 100% à environ 7,2 milliard en 2014. La croissance semble être exponentielle, ce qui signifie qu'elle ne va pas s'arrêter avant un certain temps. La consommation mondiale d'énergie primaire au cours de la même période a augmenté de 338% à environ 148 PWh (10^{15} Watt heure). La croissance est très forte, donc nous aurons besoin de plus en plus d'énergie, en particulier dans les pays en développement avec une croissance très rapide de l'économie. Le deuxième problème lié à la consommation croissante d'énergie est la source de l'énergie. La figure B.1 montre la dépendance du pétrole, du charbon et du gaz naturel. Ensemble, ils représentent 87% de toutes les sources d'énergie primaire. Leur combustion a une faible efficacité et libère des gaz à effet de serre qui sont nuisibles à l'environnement local et mondial. Puisque toutes ces sources sont non-renouvelables, les stocks sont limités et estimés à moins d'un siècle. Une autre source importante d'énergie est l'énergie nucléaire. Toutefois, en raison de son effet possible sur l'environnement et sur la sécurité de la population, de nombreux pays ont décidé de réduire et d'abandonner cette source d'énergie.

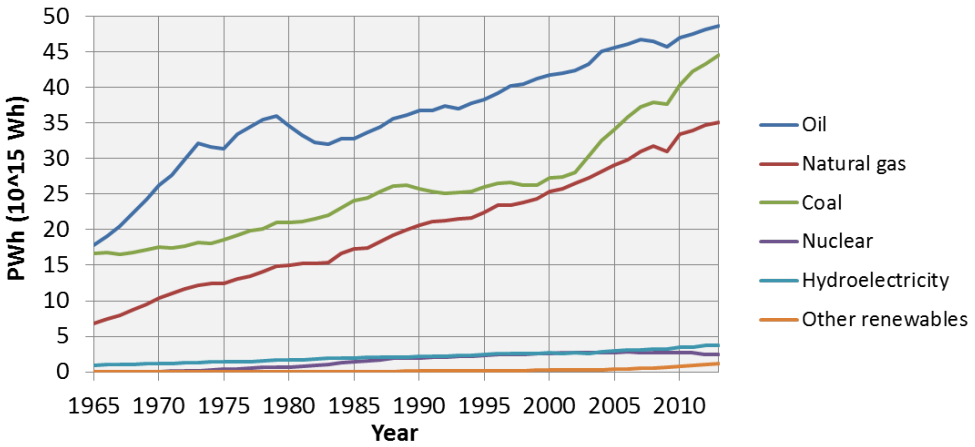

Figure B.1: Sources mondiales d'énergie primaire (www.eia.gov)

Traditionnellement, l'hydroélectricité représente la majeure partie de sources renouvelables. C'est une source flexible et propre. L'utilisation de l'énergie potentielle de l'eau

d'une efficacité supérieure à 90%, est également considérée comme le moyen le plus efficace pour produire de l'électricité. Autour de 17% (3,7 PWh/an) de l'énergie électrique mondiale est actuellement générée par l'énergie hydroélectrique. Selon l'AIE (Agence internationale de l'énergie), le potentiel technique de l'hydroélectricité est estimé à environ 16 PWh/an. Nous utilisons donc environ 23% du potentiel disponible (en 2013). Les pays avec le plus haut potentiel technique pour l'hydroélectricité sont la Chine, les États-Unis, la Russie, le Brésil et le Canada.

Un autre avantage des centrales hydroélectriques est leur durabilité. La durée de vie moyenne est estimée à environ 40 ans. Cependant, il y a beaucoup de centrales hydroélectriques qui ont été construites il y a plus de 50 ou même 100 ans. Par conséquent, certaines mises à niveau et rénovations peuvent prolonger considérablement la durée de vie des centrales et réduire par conséquent les coûts de l'électricité fournie par l'énergie hydroélectrique. Par ailleurs, la rénovation peut améliorer de manière significative l'efficacité globale des centrales hydroélectriques et augmenter leur production électrique.

Autre que l'hydroélectricité, les sources d'énergie renouvelable les plus largement utilisés sont les sources solaires et éoliennes. Le pourcentage global des sources mentionnées est encore faible, mais dans plusieurs pays d'Europe de l'Ouest, le vent et les centrales solaires fournissent ensemble déjà plus de 20% de la demande d'électricité.

L'inconvénient du vent et des centrales solaires est l'effet négatif sur la stabilité du réseau électrique. La quantité d'électricité produite par les centrales solaires et éoliennes peut changer toutes les heures, même à chaque minute. Les réseaux électriques ne sont aujourd'hui pas très flexibles, ce qui signifie qu'il ne peut y avoir de variation significative entre la demande et l'offre du réseau. Concernant l'offre, une baisse soudaine de l'intensité du vent et/ou l'apparition d'un nuage imprévu peut provoquer la diminution de l'énergie électrique dans le réseau et donc provoquer des instabilités. D'autre part, les principales instabilités sur la demande sont remarquées pendant les heures d'exploitation industrielles. Pour équilibrer et ajuster le système de réseau électrique, une solution rapide et fiable doit être fournie afin de stocker l'énergie pendant le pic de production et d'utiliser la même énergie, lorsque la consommation est plus élevée que la production. Jusqu'à présent, les stations de transfert d'énergie par pompage (STEP) sont la meilleure solution qui nous permet la flexibilité et le stockage d'énergie à grande échelle.

B.1.1 Les stations de transfert d'énergie par pompage (STEP)

Généralement, nous pouvons diviser les centrales hydroélectriques en plusieurs catégories. L'approche la plus classique consiste à construire un barrage pour stocker et accumuler de l'eau. Habituellement, dans la partie inférieure du barrage, une ou plusieurs turbines sont reliées par une conduite forcée, au stockage de l'eau derrière le barrage, et au générateur qui transforme l'énergie mécanique de la turbine en l'électricité. Ces centrales hydroélectriques sont appelées les centrales de stockage et elles peuvent être en partie réglées en fonction des besoins du réseau électrique et de l'approvisionnement en eau.

Les centrales au fil-de-l'eau sont un autre exemple d'aménagement hydraulique. Le barrage sur la rivière est toujours nécessaire, cependant, il n'y a que peu ou pas de capacité de stockage de l'eau derrière le barrage. La turbine utilise le débit presque constant de la rivière et produit donc une quantité constante d'électricité.

Le troisième type de centrales hydroélectriques est la station de transfert d'énergie par pompage (STEP). Comme présenté sur la figure B.2, il se compose de deux réservoirs, reliés par une conduite forcée. Celui du bas peut être une partie de l'usine hydroélectrique classique comme décrit ci-dessus. En raison de la réduction des coûts et de l'amélioration

de la technologie, nous avons l'habitude d'utiliser de nos jours, un seul système avec la machine turbine-pompe réversible (fig. B.2). Quand on a trop d'énergie disponible, la machine fonctionne en mode de pompage, et pompe donc l'eau dans le réservoir supérieur. Le contraire se passe quand nous avons un manque d'électricité dans le réseau, la machine tourne dans l'autre sens et génère de l'électricité.

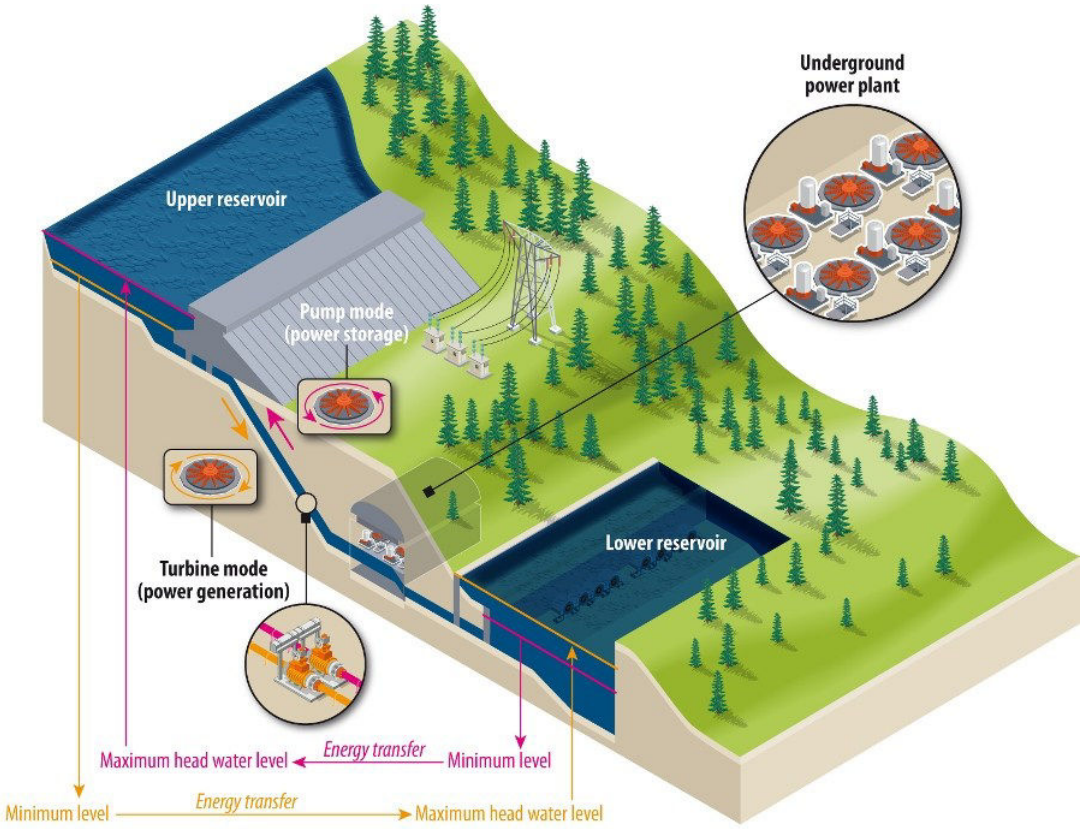

Figure B.2: Station de transfert d'énergie par pompage (Alstom Hydro)

L'efficacité globale du processus de pompage/turbinage de l'eau pour produire de l'électricité est au maximum de 80%. Cependant, les pompes-turbines sont aussi économiquement rentable. En effet, lorsque la demande d'électricité est inférieure à l'offre, généralement au cours de la nuit, le prix de l'électricité est faible. Au contraire, lorsque l'offre est inférieure à la demande, généralement dans la matinée, les prix de l'électricité augmente. La différence quotidienne entre le plus haut et le prix le plus bas peut être même plus de 100%. Pour utiliser la disponibilité des centrales STEP au mieux, il est obligatoire d'assurer une commutation régulière du mode pompage au mode génération et vice versa. Les systèmes d'une centrale STEP ont été construits à l'origine pour utiliser et stocker l'énergie supplémentaire fournie par les centrales nucléaires pendant la nuit. Initialement, la commutation entre le mode de production et de pompage survenait autour de 3 - 4 fois par jour. Au fils des dernières années, la commutation a augmenté de plus de 10 fois, puisque le rôle principal de la STEP est d'assurer la stabilité du réseau, qui est fortement influencée par les sources d'énergie intermittentes, telles que les centrales solaires et éoliennes.

Comme les autres turbomachines, les turbines-pompes réversibles sont également conçues pour un débit constant Q optimal, et une chute nette H optimale, qui sont donnés par la position géographique des deux réservoirs. Cependant, le changement régulier entre

le pompage et le régime de génération électrique, ainsi que les exigences spécifiques de l'électricité du réseau, sont les raisons pour lesquelles, en réalité, la turbine-pompe fonctionne régulièrement sous des conditions hors nominales. Un long fonctionnement sous des conditions de ce genre peut provoquer une chute importante de l'efficacité, des vibrations, ainsi que des dommages sévères sur la machine. Pour éviter ce scénario, il est essentiel d'étudier les origines des instabilités.

B.1.2 Les instabilités en mode pompage

Les principales instabilités remarquées dans le mode de pompage sont liées au comportement de cavitation lors des débits non-optimaux. De plus, à charge partielle, le phénomène du décollement tournant peut se produire et provoquer une forme de bosse sur la courbe de performance (phénomène appelé 'feston'), ce qui est à l'origine des instabilités. L'étude de la cavitation et du feston sont les principaux objectifs de la thèse de doctorat ici présentée. Afin de comprendre les instabilités du mode de pompage en charge partielle, il est essentiel d'expliquer les bases du comportement d'une pompe centrifuge.

L'utilisation de l'effet centrifuge pour transporter de l'eau a été proposée pour la première fois par Leonard de Vinci (1452 à 1519). Cependant, l'équation la plus fondamentale dans le domaine des turbomachines a été présentée par Leonhard Euler (1707 à 1783). L'équation d'Euler pour turbomachines est basée sur la conservation du moment angulaire. L'équation linéaire d'Euler simplifiée pour l'énergie hydraulique spécifique de la pompe peut être écrite comme:

$$gH = U_2 V_{2u} - U_1 V_{1u}. \tag{B.1}$$

Pour une pompe centrifuge, les triangles de vitesse moyens à l'entrée et à la sortie sont pris en compte et le rapport des angles d'écoulement β_1 et β_2 sont considérés constants (fig. B.3). L'écoulement d'entrée est supposé n'avoir aucune composante circonférentielle (projection de vitesse absolue $V_{1u} = 0$) pour une pompe centrifuge, l'équation d'Euler peut être modifiée en:

$$gH = U_2 V_{2u} = U_2 \left(U_2 - \frac{V_{2m}}{tan(\beta_2)} \right). \tag{B.2}$$

A la sortie de la turbine, l'énergie hydraulique spécifique gH_2 se compose de la pression $\frac{p_2}{\rho}$ et de la vitesse $\frac{v_2^2}{2}$. La transformation de l'énergie de vitesse en pression continue dans le distributeur. L'objectif principal de la pompe centrifuge est de convertir la puissance mécanique P_m en puissance hydraulique P_h avec une efficacité maximale. P_m est définie par la multiplication du couple T sur l'arbre et la vitesse de rotation ω de:

$$P_m = \omega T. \tag{B.3}$$

D'autre part, la puissance hydraulique est définie par la différence de chute H et le débit Q:

$$H = \frac{p}{\rho} + \frac{v^2}{2g} + z; \tag{B.4}$$

$$P_h = Q\rho(gH_2 - gH_1). \tag{B.5}$$

Les autres nombres adimensionnels importants, très utilisés dans la littérature, sont le coefficient débit ϕ et le coefficient d'énergie spécifique ψ qui sont définis comme suit:

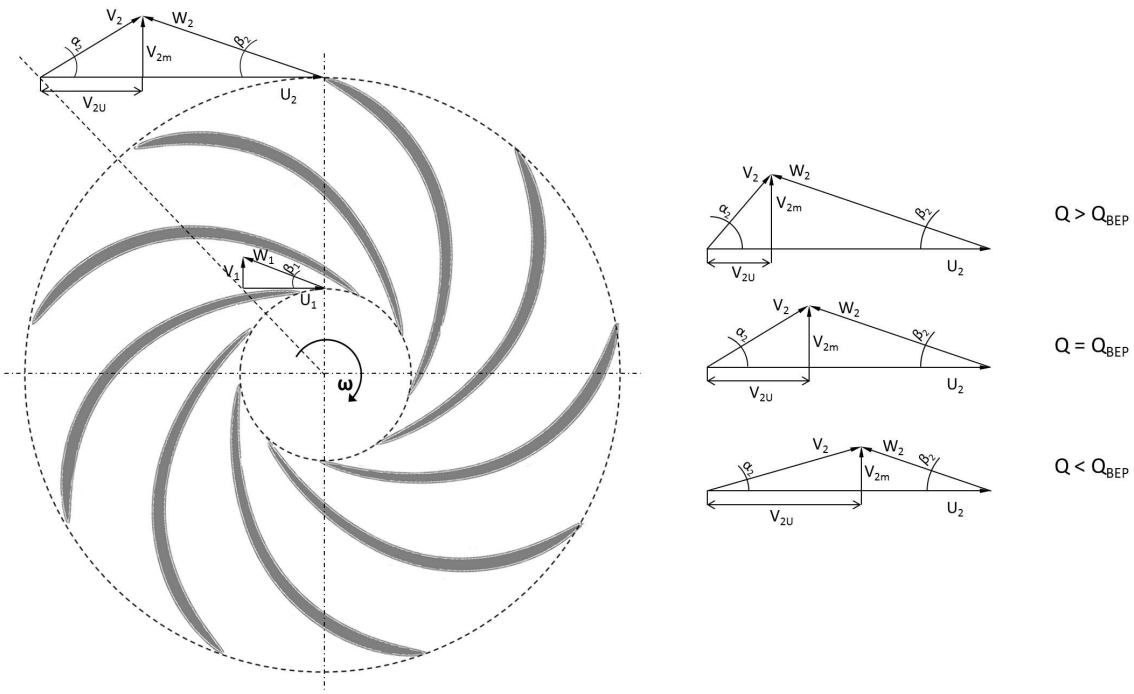

Figure B.3: Triangles de vitesse

$$\phi = \frac{Q}{\pi \omega R^3}; \tag{B.6}$$

$$\psi = \frac{2gH}{\omega^2 R^2}. \tag{B.7}$$

Afin d'atteindre un rendement élevé et de faibles pertes, la transformation de l'énergie à l'intérieur de la machine doit être aussi progressive que possible. Par conséquent, le débit de la turbine doit être adapté au distributeur. Dans le cas d'une turbine-pompe, le distributeur comporte deux parties. D'une part, l'angle d'ouverture des aubes directrices peut être modifié et adapté à l'écoulement et, d'autre part, les aubes avant-directrices sont fixes. L'adaptation de l'angle d'ouverture des aubes directrices est nécessaire parce que les triangles de vitesse à la sortie de la roue changent de façon considérable, en fonction de la vitesse d'écoulement. La figure B.3 montre la différence de l' angle d'écoulement absolu α_2 à la sortie de la roue pour trois débits différents. Afin de réduire les pertes dans le distributeur, l'angle α_2 doit correspondre à l'ouverture de l'angle des aubes directrices.

B.1.3 Séparation d'écoulement et décollement tournant

La séparation est définie comme une zone de recirculation sur les parois solides de la machine. La séparation de l'écoulement initial peut être provoquée par plusieurs phénomènes d'écoulement, tels que:

- un obstacle sur le trajet d'écoulement,
- un angle d'attaque inadapté au bord d'attaque de l'aube (fig. B.4),

- de forts gradients de pression, perpendiculaires à la direction de l'écoulement.

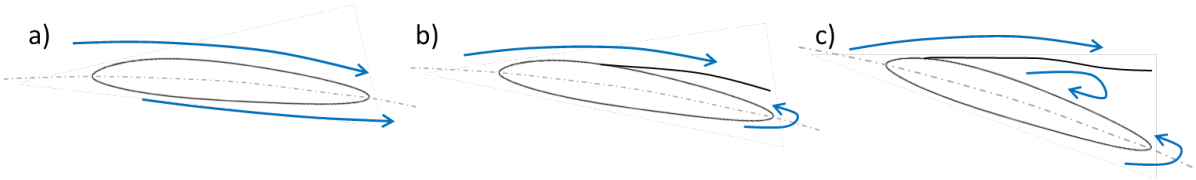

Figure B.4: Séparation d'écoulement sur le profil d'aile, en fonction de l'angle d'attaque

Le décollement tournant est généralement considéré comme des cellules de sur-débit et sous-débit à l'intérieur du distributeur. La figure B.5 représente le décollement tournant à l'intérieur d'une turbine-pompe. Quatre cellules de sur-débit sont en rotation autour du distributeur dans le même sens que la roue, à aubes à une fréquence correspondant à 2% à 6% de la fréquence de rotation de la roue. Pour les pompes centrifuges, le décollement tournant peut avoir également une direction de rotation opposée à celle de la pompe.

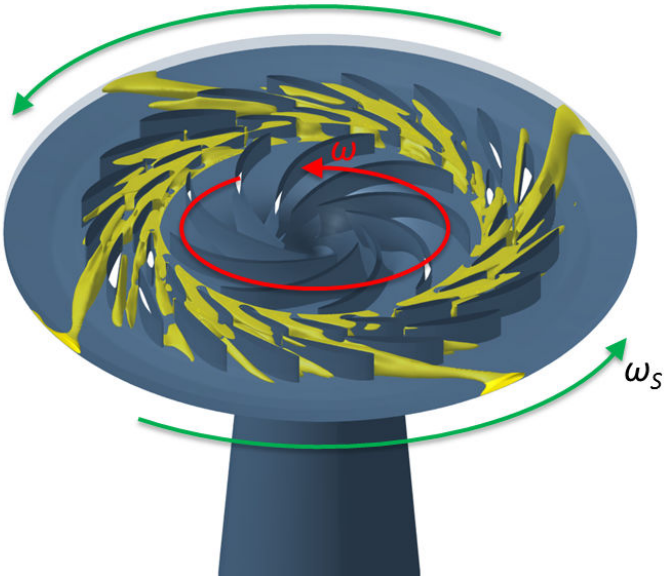

Figure B.5: Représentation schématique du décollement tournant

La plupart des études expérimentales du décollement tournant dans les pompes et pompes-turbines ont eu lieu au cours des 20 dernières années. L'approche principale était d'utiliser la méthode PIV (Vélocimétrie d'Image de Particules) et a d'abord été utilisée par Sinha et al. [86], [87]. Le jeu radial entre la roue et le diffuseur est d'environ 10% du diamètre de la roue. Il a supposé qu'un jeu plus important augmenterait l'intensité du décollement tournant et la probabilité d'apparition.

B.1.4 Feston cadre et courbe de performance

L'apparition des phénomènes de décollement tournant décrits augmente de manière significative les pertes dans le distributeur et, par conséquent, provoque une pente différentielle positive sur la courbe de performance tel que présenté sur la figure B.6. Les lignes verte

et rouge représentent les caractéristiques du circuit hydraulique. La plage de fonctionnement stable normale pour la turbine-pompe est entre les lignes vertes. Dans une zone stable, la turbine-pompe fournit pour chaque hauteur de chute nette du système un débit correspondant. Par ailleurs, dans la zone des caractéristiques instables causées par le phénomène de décollement tournant, la turbine-pompe peut fournir trois débits différents pour la caractéristique du circuit donnée, comme indiqué par la courbe rouge. En réalité, cela signifie que le débit à travers la turbine-pompe varie de manière complètement incontrôlable. Un tel comportement augmente considérablement les pertes. De plus, elle provoque de très fortes vibrations qui peuvent endommager et dans le pire des cas, même détruire la machine. De toute évidence, la turbine-pompe ne doit pas opérer dans la zone du feston cadre.

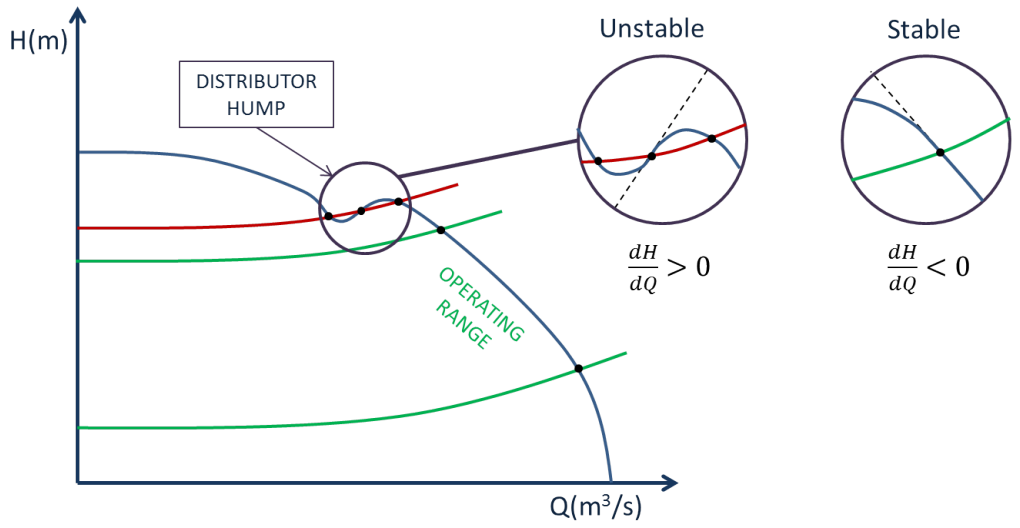

Figure B.6: Caractéristique instable en mode pompage à cause du feston

B.2 La cavitation

La description la plus commune du terme 'cavitation' est l'apparition de bulles de vapeur à l'intérieur d'un milieu liquide initialement homogène. Habituellement, c'est considéré comme un passage du liquide à la phase vapeur et puis de nouveau à la phase liquide. La raison de l'apparition de la cavitation est la diminution de la pression locale, avec une température qui reste sensiblement constante. La pression de vapeur peut être expliquée d'un point de vue thermodynamique classique. Sur le diagramme de phase $p - T$ de l'eau (fig. B.7), la ligne entre le point triple de l'eau Tr et le point critique C sépare la phase liquide de la phase vapeur. La pression de vapeur p_v indique la limite à partir de laquelle une diminution supplémentaire de pression statique (à température constante) provoquerait le changement de la phase (dans notre cas, l'évaporation). Comme le montre la figure B.7, la pression de vapeur p_v est une fonction de la température. Comme mentionné précédemment, la cavitation dans l'eau froide se produit généralement à température à peu près constante, lorsque la pression locale diminue et ensuite augmente de nouveau. Un phénomène similaire arrive au point d'ébullition, où la vaporisation se produit à pression constante quand la température augmente.

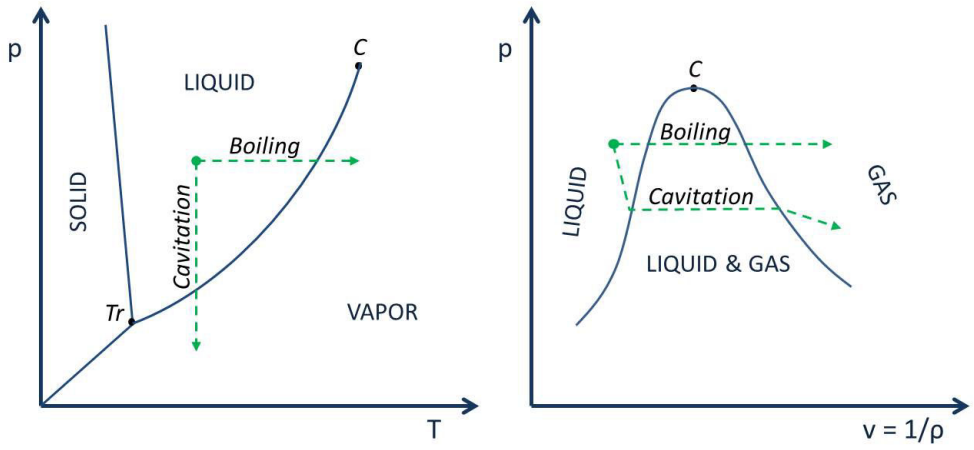

Figure B.7: $p - T$ et $p - v$ dans les diagrammes de phase

La dernière étape du processus de cavitation se produit lorsque la pression retourne à sa valeur initiale (au-dessus de la p_v) et les bulles commencent à imploser. La bulle de vapeur se remplit à nouveau avec le liquide environnant. Lors de l'implosion de la bulle, des ondes de pression de forte amplitude peuvent être émises, pouvant induire à l'endommagement des parois solides environnantes.

B.2.1 Cavitation dans les pompes

La cavitation dans les pompes se produit généralement sur les deux côtés des pales, en fonction de l'angle de l'écoulement au bord d'attaque de la roue. Dans le cas d'une vitesse d'écoulement réduite, la cavitation apparaît en premier sur le côté d'aspiration de la pale. En revanche, lorsque le débit augmente, la cavitation se produit généralement sur le côté pression de la pale.

Sur la figure B.8, nous pouvons voir toutes les différentes formes de cavitation dans la pompe centrifuge. Les formes de cavitation (sur le côté d'aspiration (a) et sur le côté pression de la pale) proviennent de l'angle d'attaque de l'écoulement non-adapté. D'autre part, la cavitation dans la région (c) (jeu) est due à des écoulements secondaires qui provoquent la diminution de la pression locale. Dans des cas particuliers de débit partiel, la cavitation peut être présente aussi dans la zone (d), dans la région du bec de volute (pompes centrifuges) [6]. De même, dans le cas de l'augmentation du débit de la turbine-pompe, la cavitation peut se produire du côté pression des aubes directrices, si l'ouverture de l'angle des aubes directrices n'est pas adaptée à l'écoulement.

Généralement, la présence de formes de cavitation développées dans une pompe peut conduire à:

- la réduction de la performance de la pompe (en réduisant la chute nette H_n), si le débit Q et la vitesse de rotation n restent constants;
- la diminution du rendement;
- la modification de la vitesse et du profil de pression à l'intérieur de la pompe;
- l'endommagement de la pompe dû à l'érosion de cavitation.

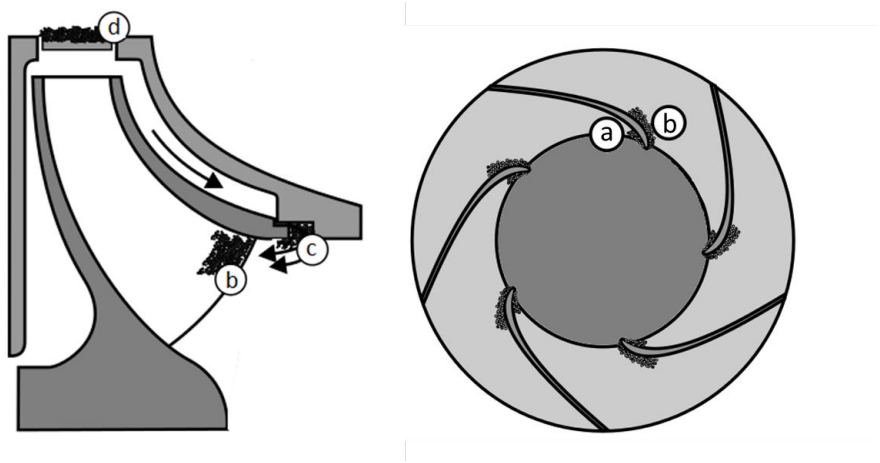

Figure B.8: Cavitation dans les pompes centrifuges [90]

Définition du nombre NPSH

La charge nette absolue à l'aspiration ($NPSH$) peut être attribuée au circuit ainsi qu'à la machine. Quand nous essayons de décrire et de comparer la probabilité de l'apparition de la cavitation dans un circuit, le nombre $NPSH$ présent ($NPSH_A$) peut être calculé comme suit:

$$NPSH_A(m) = \frac{p_0 - p_v}{\rho g} + \frac{v_0^2}{2g} + \Delta Z - H_{loss}. \tag{B.8}$$

L'index 1 dans l'équation B.8 se réfère aux conditions dans le réservoir inférieur. Il est important de souligner que ΔZ est positif si le niveau de la turbine-pompe est inférieur au réservoir inférieur de la centrale. H_{loss} représente les pertes dans le système entre la machine et le réservoir inférieur. L'énergie cinétique est généralement estimée à 0, car le niveau d'eau dans les réservoirs change très lentement. Selon l'équation B.8, le niveau de l'eau dans le réservoir inférieur influe sur le niveau de cavitation dans la turbine-pompe. Par conséquent, afin de réduire au minimum ou d'éviter la cavitation, la position de la turbine-pompe est en général nettement inférieure au niveau des réservoirs inférieurs.

D'autre part, la valeur du $NPSH$ requise ($NPSH_R$) est utilisée pour définir différents niveaux de cavitation développée à l'intérieur de la machine. Certaines des valeurs typiques sont présentées sur la figure B.9 et sont définies de la sorte:

- $NPSH_{R-i}$ représente la valeur de cavitation naissante. Expérimentalement, il peut être obtenu par les mesures de visualisation dans la pompe (turbine-pompe).
- $NPSH_{R-ero}$ représente la valeur où l'intensité de la cavitation est suffisamment élevée pour provoquer l'érosion sur les aubes de la pompe.
- $NPSH_{R-3\%}$ représente le niveau de cavitation pour lequel la chute de performances, en raison de la présence de la cavitation, atteint 3% de la chute de référence sans cavitation H_0. $NPSH_{R-3\%}$ peut être obtenu par les mesures globales des performances de la pompe (turbine-pompe) qui sont décrites dans la norme internationale IEC 60193 [12].

Une légère augmentation de la performance peut être parfois observée sur la courbe de chute principale $NPSH_R$ pour un débit réduit. L'angle d'écollement au bord d'attaque

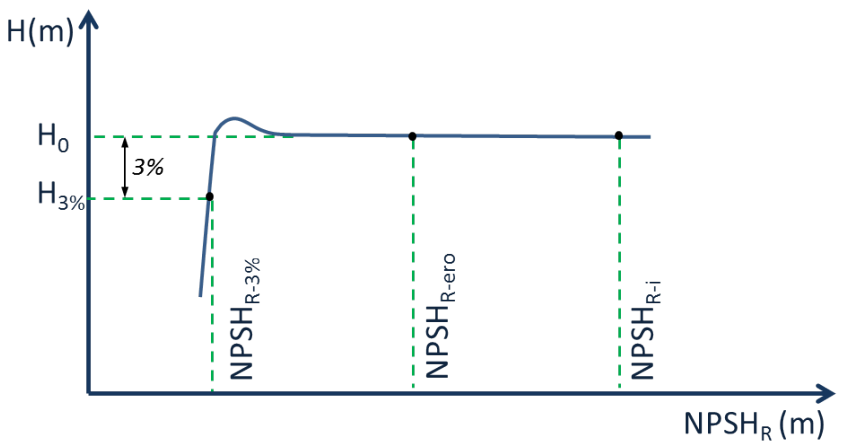

Figure B.9: Caractéristique $NPSH_R$ typique pour Q = const.

de l'aube est optimisé par la présence de la poche de cavitation. Comme mentionné précédemment, les valeurs $NPSH_R$ sont habituellement obtenues par des mesures de visualisations. Cependant, les simulations numériques peuvent être ainsi utilisées pour prédire les valeurs de $NPSH$ et les formes de cavitation pour certaines valeurs, ce qui est également l'un des nombreux objectifs de la thèse de doctorat présentée.

Les valeurs de $NPSH_R$ sont fortement influencées par le débit. La valeur minimale de la courbe de cavitation naissante correspond au débit optimal, tel que présenté sur la figure B.10. En raison des triangles de vitesse, la cavitation naissante à débit réduit se produit sur le côté aspiration des pales. En revanche, pour les sur-débits, elle se produit sur le côté pression de la pale. La cavitation sur le côté pression de la pale a plus d'effet sur la performance de la turbine-pompe que la cavitation sur le côté aspiration. En effet, la valeur de $NPSH_{R-3\%}$ est plus élevée pour les sur-débits que pour les sous-débits comme on le voit sur la figure B.10.

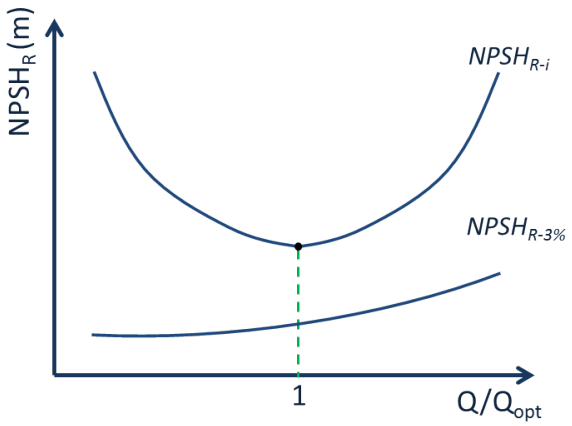

Figure B.10: Influence du débit sur les valeurs de $NPSH_R$

B.3 Objectifs de la thèse

Les simulations CFD nous fournissent un outil utile et rentable pour analyser les phénomènes d'écoulement dans les machines hydrauliques. L'étude présentée porte sur la prédiction et l'analyse de l'écoulement dans des conditions complexes en régime hors-nominal en mode de pompage. La géométrie étudiée est le modéle réduit d'une turbine-pompe à haute chute ($n_q = 27$). A des régimes de charge partielle, le fonctionnement continu de la machine peut être limité par le décollement tournant et la cavitation. Les objectifs de la thèse sont les suivants:

- Le premier objectif est d'utiliser un code commercial, testé auparavant dans le laboratoire, pour développer une approche numérique afin de permettre la prédiction précise des phénomènes observés en régime hors-nominal. Le but est d'utiliser le code et de proposer une méthodologie numérique pour prédire avec précision les régimes de cavitation, les chutes de performance dues à la cavitation, et effectuer des analyses locales des écoulements cavitants. Des analyses globales de l'impact de la cavitation sur les découlements tournants et le feston seront également proposées. Le code devra donner une prévision globale et précise de la zone de feston cadre sur la courbe de performance de la machine. Il devra également permettre l'analyse de l'écoulements instables observés pour une large gamme de débits et de valeurs de $NPSH$. Par conséquent, les simulations doivent être numériquement stables et robustes, tout en restant précises.

- Un autre objectif est de développer une méthodologie globale de calcul à bas coût qui permet de détecter les zones d'exploitation stables et instables. Les méthodologies mentionnées peuvent être très utiles pour une analyse rapide et pratique des écoulements et pour l'évaluation de l'influence de différents paramétres tels les angles d'ouverture des aubes, la géométrie des aubes directrices et des avant-directrices, la taille de jeu radial entre la roue et le distributeur entre autres. Il devra fournir de résultats globaux précis pour un grand nombre de points de fonctionnement pour un coût de calcul relativement faible.

- L'objectif final est de faire une analyse détaillée du comportement et des origines de décollement tournant en effectuant des simulations instationnaires sur toute la géométrie. L'analyse inclura l'étude des champs de vitesse et de pression dans le distributeur. De plus, l'influence de la vitesse d'écoulement, les angles d'ouverture des aubes directrices, la géométrie des aubes directrices et la taille de jeu radial seront étudiées en détail afin de donner une image globale de le phénomène. L'analyse proposée, ainsi que les outils et des méthodologies développés pourront être une base importante pour les futures études sur les phénomènes d'écoulement instables en régime hors-nominal, pas seulement pour la géométrie de turbine-pompe présentée, mais aussi pour d'autres géométries de turbine-pompe et de pompes centrifuges.

B.4 Modélisation physique et numérique

Les études numériques basées sur la CFD sont devenues fréquentes dans le domaine de la mécanique des fluides. Le développement des ordinateurs et des logiciels a assuré aux universitaires et industries des outils utiles pour analyser, prévoir et améliorer le comportement de l'écoulement au sein des circuits et machines hydrauliques. En comparaison aux études expérimentales, l'approche CFD est normalement moins couteuse

et peut fournir des informations plus détaillées sur les phénomènes auxquels les scientifiques et les ingénieurs sont intéressés. Cependant, cette approche a encore ses limites en termes de puissance de calcul et de précision des résultats obtenus. C'est pourquoi, la validation de ces résultats est toujours nécessaire. Typiquement, la combinaison d'études expérimentales et numériques donne les résultats les plus efficaces.

B.4.1 Les approches CFD

Pour obtenir de bons résultats des simulations numériques, il est important de savoir quels types de simulations sont disponibles et quelles sont leurs limites. En règle générale, trois approches différentes sont disponibles pour simuler le comportement d'un écoulement. La simulation numérique directe (DNS) résout des équations instationnaires de Navier-Stokes et calcule les structures turbulents sur toutes les échelles. Si la discrétisation en temps et en l'espace est adéquate, les DNS doivent fournir les résultats les plus exactes. Jusqu'à présent, les plus grands et plus rapides superordinateurs ne sont capables de calculer que de géométries simples avec d'écoulements à faibles nombres de Reynolds. Compte tenu de l'évolution attendue de la puissance de calcul, les DNS pour des géométries complexes avec grand nombre de Reynolds ne seront pas disponibles avant quelques décennies.

La deuxième approche est connue par le nom Large Eddy Simulation (LES). C'est un compromis entre les DNS et les simulations RANS. Cette approche calcule les structures turbulentes, mais pas sur toutes les échelles. Par conséquent, avec une sélection de filtres, il faut choisir la taille des structures turbulentes qui seront calculées. Le défi est de trouver un bon compromis entre l'exactitude et la discrétisation. Les turbulences se produisent sur une grande échelle, mais se dissipent sur les petites échelles. Par conséquent, il est essentiel de trouver une discrétisation spatiale adéquate. En outre, la modélisation des couches limites peut être très exigeante en raison des besoins de maillage très dense près des bords. Une étude de faisabilité sur le maillage doit être effectuée avant les simulations numériques réelles. La méthode LES a gagné en popularité ces dernières années dans le domaine académique, mais elle n'est pas encore utilisée fréquemment pour les applications industrielles.

La seule approche restante est de résoudre les équations de Navier-Stokes moyennées à l'aide de la décomposition de Reynolds (RANS). Jusqu'à présent, elle est largement utilisée dans l'industrie ainsi que par les universitaires. L'approche est économique, car elle peut être utilisée pour une large gamme d'applications, sans besoin de moyens de calculs importants. L'inconvénient est que l'approche RANS nous fournit des solutions statistiquement moyennes pour le comportement turbulent. Choisir le bon modèle turbulent est très important. Les équations RANS peuvent être modifiées comme des équations RANS instationnaire (URANS) pour effectuer les calculs instationnaires.

B.4.2 Schéma numérique appliqué

Le code FINE^{TM}/Turbo de Numeca a été utilisé pour toutes les simulations numériques présentées.

Le tableau B.1 résume les informations sur le schéma numérique. Les deux types de simulations, stationnaire et instationnaire, ont été effectuées en utilisant les équations RANS et URANS. Le modèle de turbulence $k - \epsilon$ (Extended Wall Function) a été utilisé pour toutes les simulations, car il a été validé comme étant le plus précis pour notre genre de simulations. Les simulations de l'écoulement de cavitation ont été effectuées uniquement pour des simulations stationnaires en utilisant la loi d'état barotrope pour

le transfert de masse. Dans le cas de régimes de fonctionnement cavitants, des résultats non cavitants ont été utilisés comme solution initiale. Un plan de mélange a été utilisé sur l'interface entre le rotor et les directrices pour les simulations stationnaires. Entre la roue et le tube d'aspiration, le plan de mélange n'a pas été appliqué et une interface permettant le bon transfert de données fut créée. Le solveur utilise un schéma centré pour la discrétisation spatiale [47]. Un pas de temps local est utilisé pour les simulations stationnaires. L'approche par pas de temps dual a été appliquée pour les simulations instationnaires (voir description dans [47]).

Type de Simulation	Stationnaire	Instationnaire
Modèle physique	RANS	URANS
Modèle de turbulence	$k-\epsilon$ (Ext. Wall Function)	$k-\epsilon$ (Ext. Wall Function)
Modèle de cavitation	Barotrope	/
Discrétisation spatiale	Central (2nd order)	Central (2nd order)
Discrétisation temporelle	Local time stepping	Dual time stepping
Pas de temps	/	2° de tour
Max iter/pas de temps	2000 - 15000 iter	2700 pas de temps

Table B.1: Schéma numérique

Le pas de temps choisi pour les simulations instationnaires est 2° de la révolution de la roue, ce qui correspond à $0,00033s$ pour une vitesse de rotation de 1000 tours par minute. Le nombre d'itérations internes est limité à 35 pour chaque pas de temps. Une convergence satisfaisante pour les simulations stationnaires est généralement atteinte après environ 2000 itérations pour des points de fonctionnement stables et jusqu'à 15000 itérations pour les points de fonctionnement instables qui sont influencés par la cavitation, le décollement tournant ou par d'autres types d'instabilités.

B.4.3 Moyens de calcul

Plusieurs paramètres de maillage différents ont été analysés au cours de l'étude présentée. Cependant, pour l'analyse finale et les résultats, un seul type de maillage a été utilisé dans le but d'avoir une bonne comparaison entre les différentes conditions aux limites et les différents types de simulations. En d'autres termes, dans tous les cas la densité du maillage ne change pas, le domaine numérique ne change pas, la périodicité entre les pales change, et le type de simulations (stationnaires et instationnaires) change aussi.

Une estimation des ressources informatiques nécessaires pour des points de fonctionnement non-cavitant est présentée dans le tableau B.2. Colonne 'periodic' indique que des conditions de périodicité ont été appliquées dans le roue et dans le distributeur. Cela signifie que seulement un canal de la roue mobile et un canal du distributeur sont calculés. Le maillage 'combined' se compose d'une chaîne à mailles dans la zone de la roue à aubes et un distributeur entièrement maillé. Le 'full mesh' représente le type de maillage où la périodicité n'a pas été utilisée et pour lequel la machine a été maillée complétement.

Les simulations de l'écoulement de cavitation exige 2 à 5 fois plus de temps de calcul, en comparaison aux calculs non cavitant. Le temps de calcul dépend beaucoup de l'intensité de la cavitation, par conséquent, il est difficile de faire une estimation générale.

Comme le montre le tableau B.2, la taille de maille diffère de manière significative. D'une part, les calculs sur le maillage périodique peuvent être facilement effectués sur un ordinateur personnel normal, puisque seuls 7 à 20 heures de calcul sont nécessaires pour

	periodic	combined	full mesh	full mesh
type	steady	steady	steady	unsteady
N° de cellules	0,87 M	10,7 M	13,4 M	13,4 M
CPU h	7 - 20	250	320	270/rev
Output	0,2 Gb	1,9 Gb	2,3 Gb	1,7 Gb/ts

Table B.2: Analyse de maillage, CPU temps, taille des données

atteindre une bonne convergence pour l'écoulement non-cavitant. D'autre part, pour le combiné et pour le maillage complet, il faut déjà plusieurs processeurs supplémentaires et plus de 250 heures de calcul pour les simulations stables. En outre, la taille typique de mémoire vive (RAM) dans un ordinateur personnel ne suffit plus.

La prédiction exacte du décollement tournant nécessite la réalisation de simulations instationnaires, en utilisant un maillage complète de la machine. Cependant, dans ce cas, les moyens de calcul nécessaires sont trop important. Pour une bonne détection du décollement tournant, il faut utiliser un pas de temp équivalent à environ un rotation de 2° de la roue. Cela correspond à, au moins, 180 pas de temps par un tour de la machine. Étant donné que chaque pas de temps nous fournit environ 1,7 Gb de données, nous avons besoin d'environ 300 Gb de stockage pour enregistrer les données et environ 270 heures de calcul CPU pour un tour de la turbine-pompe. Néanmoins, pour détecter la fréquence caractéristique de décollement tournant, qui est normalement comprise entre 2% et 6% de la fréquence nominale de la machine, plus de 10 tours devraient être calculés pour chaque point de fonctionnement. L'un des objectifs de l'étude est de proposer une approche numérique efficace, robuste et à bas coût pour simuler des points de fonctionnement instables en mode de pompage. Tous les calculs ont été effectués sur le serveur du LEGI, en utilisant au maximum 12 processeurs. Le temps de calcul de la plus longue des simulations présentées a été d'environ 2 semaines. Cela signifie que tous les calculs effectués dans la thèse ont été relativement rapides et n'ont pas bénéficié de moyens de calcul important.

B.5 Les résultats globaux

Ce paragraphe est consacré à l'analyse du phénomène de cavitation. Tous les calculs effectués sont stationnaires et ont été réalisés sur un maillage périodique. L'angle d'ouverture de 14° est considéré. La plupart des résultats a été présentée dans [48]. L'analyse de la cavitation est principalement axé sur la prédiction des valeurs de NPSH pour la cavitation naissante, sur les formes de structures de cavitation et sur les effets de la cavitation sur la courbe de performance.

Les premiers résultats globaux, présentés sur la figure B.11, ont été obtenus pour des régimes permanents non-cavitant. Comme représenté sur la figure B.11, la position de la zone de feston peut être détectée numériquement avec une précision de 2% sur la valeur de débit. La prédiction d'amplitude du feston correspond bien aux résultats d'essais, avec un écart d'environ 1% sur la performance de la machine.

Cette diminution de la performance dans le zone de feston (B.11;. $\phi = 0,031$, numériquement; $\phi = 0,032$, expérimentalement) se produit en raison du décollement de l'écoulement dans de distribution, ce qui conduit plus tard au phénomène de décollement tournant. Cependant, il est important de souligner que, selon les calculs effectués, la diminution de la performance se produit en raison de l'augmentation des pertes dans le distributeur.

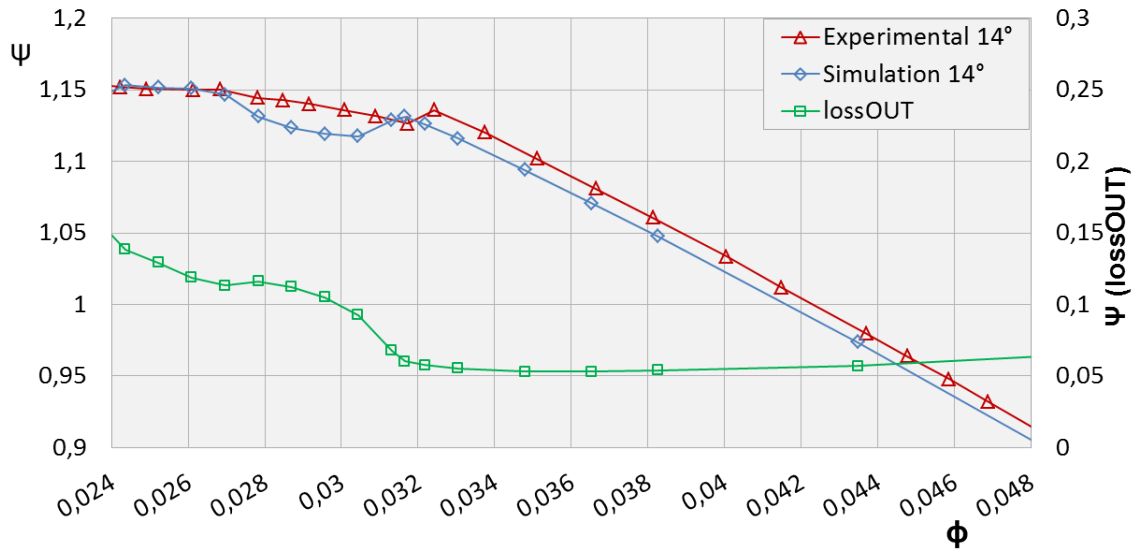

Figure B.11: La performance globale, les pertes dans le distributeur - lossOUT (ouverture 14°, géométrie GVI, régime non-cavitant)

B.5.1 Validation du modèle de cavitation

Afin d'évaluer le niveau de la cavitation dans le régime de pompage, la définition numérique de la valeur de NPSH requis est importante. Dans notre cas, il est calculé pour chaque point que d'exploitation:

$$NPSH(m) = \frac{p_{ref} - p_v}{\rho_l \; g}. \tag{B.9}$$

Dans l'équation B.9, p_{ref} représente la valeur totale de pression à l'entrée du domaine, p_v la pression de vaporisation de l'eau à 20°C, ρ_l la densité de l'eau, tandis que g est l'accélération gravitationnelle. Puisque les conditions à l'entrée et à la sortie du domaine numérique ont été fixées, la valeur NPSH a été modifiée en changeant la valeur de la pression de vaporisation p_v dans le but de maintenir la stabilité de la simulation ainsi qu'un bon niveau de convergence.

B.5.2 Cavitation naissante

La possibilité de pouvoir valider les simulations numériques en régime cavitant par comparison avec les résultats expérimentaux est d'une importance considérable. La valeur de cavitation naissante (fig. B.12) fait référence aux simulations numériques ainsi qu'à l'expérience. Expérimentalement, la valeur est obtenue par l'observation visuelle d'entrée de roue de turbine-pompe. La valeur à différents débits est définie comme l'apparition des premières bulles de cavitation.

L'approche industrielle numérique classique ne se sert pas du modèle de cavitation pour prédire la valeur de cavitation naissante. Il est simplifié, définissant la pression de référence p_{ref} (eq. B.9) par la différence entre la pression totale à l'entrée du domaine et la pression statique minimale dans le domaine étudié. Bien que cette approche se soit révélée assez précise pour prédire la valeur de cavitation naissante, il ne peut pas nous offrir d'informations supplémentaires si la cavitation est plus développée.

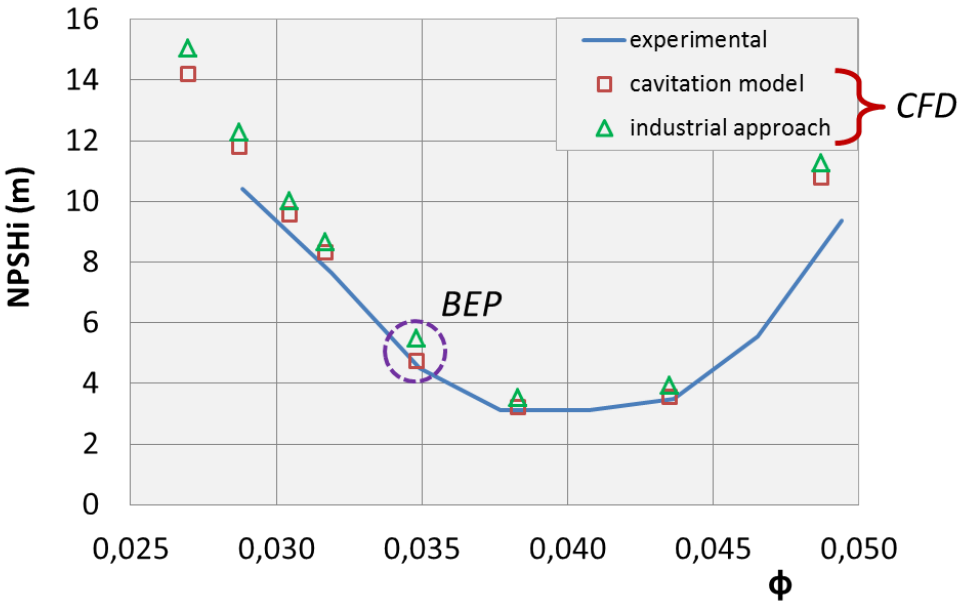

Figure B.12: Valeurs de cavitation naissante

Lorsqu'on utilise le modéle de cavitation, les critères pour définir la cavitation naissante peuvent être définis par le taux de vide α. Dans notre cas, quand le taux de vide est de $\alpha = 0,2$ (20% de la vapeur dans la cellule), la valeur NPSH correspondante a été prise comme valeur de cavitation naissante. L'accord entre l'approche industrielle sans modèle de cavitation et l'approche se servant du modèle de cavitation pour le transfert de masse est très bon. Les simulations avec le modèle de cavitation peuvent toutefois nous fournir assez d'informations supplémentaires sur le comportement des ecoulements cavitants par rapport à l'approche numérique industrielle.

Comme la figure B.12 l'indique, la mise en correspondance entre les valeurs numériques et expérimentales fonctionne bien dans une gamme considérable de débits. L'écart est estimé à $\pm 0,5m$. Un écart plus important peut être observé dans le cas du point de fonctionnement de $\phi = 0,048$. Cela est probablement dû à la méthodologie expérimentale appliquée pour estimer l'apparition de la première bulle. Dans la plupart des points de fonctionnement que nous avons étudiés, la première bulle de cavitation s'est produite sur le côté aspiration de la pale de la roue. En revanche, pour $\phi = 0,048$, la cavitation survient en premier lieu sur le côté pression de la pale, ce qui est plus difficile à observer expérimentalement et pourrait expliquer l'écart observé.

B.5.3 Courbes de NPSH

Les courbes de NPSH peuvent être produites pour diverses conditions de débit. La figure B.13 montre quatre courbes NPSH différentes, correspondant aux quatre différents débits. La courbe $\phi = 0,0348$ représente le régime de fonctionnement, à proximité du meilleur point de rendement pour GV ouverture 14°, ce qui est également relativement proche de la zone de feston. $\phi = 0,0278$ représente le débit partiel. La courbe $\phi = 0,0435$ est proche de la limite maximale de fonctionnement normal, tandis que la courbe $\phi = 0,0487$ représente le point de fonctionnement à sur-débit. Dans trois cas, nous pouvons observer les résultats expérimentaux pour 1% de perte de performance qui est due à l'occurrence de la cavitation. Les résultats numériques sont en relativement bon accord avec les données

expérimentales.

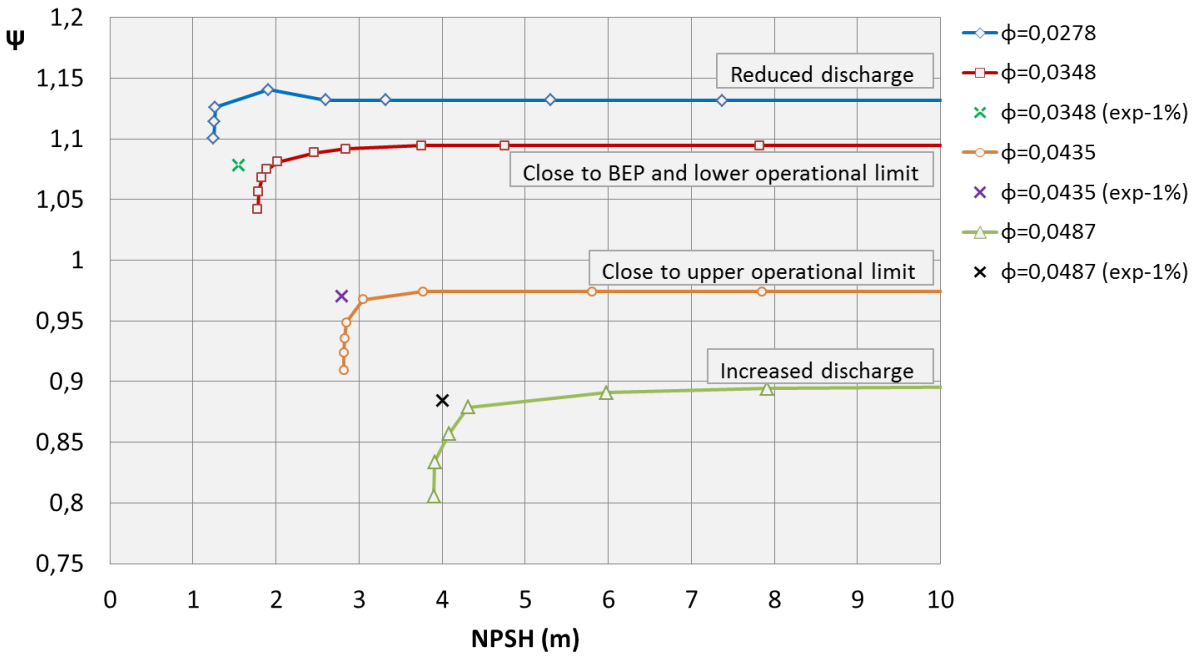

Figure B.13: Courbes de NPSH

Comme la figure B.13 le montre, la perte de chute simulée peut atteindre 10% à cause de la cavitation sur le côté pression de la pale de la roue. Tous les points où la perte de performance se produit sont considérés comme dangereux puisque la machine peut être exposée à de fortes vibrations, à l'érosion et à des points de fonctionnement instables. Tout cela est provoqué par le phénomène de la cavitation.

Dans le cas de débit réduit, une performance augmentée peut être observée avant la chute de pression à environ $NPSH = 2m$. À ce point-là, la cavitation augmente l'incidence de l'écoulement au bord d'attaque de la pale de la roue et améliore la performance.

Il est connu que la cavitation n'est pas un phénomène stationnaire quand les valeurs NPSH sont basses. Toutefois, les simulations stationnaires nous permettent d'obtenir la forme et la taille moyen de poches de cavitation pour chaque valeur de NPSH ainsi que la perte estimée. Pour évaluer la fréquence de lâcher des structures de cavitation, de simulations instationnaires couteuses sont nécessaires et n'ont pas été effectuées dans la cadre de cette thèse.

B.5.4 Formes de cavitation, débit $\phi = 0,0348$

Sur la figure B.13, nous pouvons observer les formes de cavitations correspondant à différents débits. La figure B.14 indique les trois niveaux de cavitation dans la turbine-pompe à débit de $\phi = 0,0348$, ce qui correspond au point de fonctionnement de meilleur rendement pour l'ouverture considérée. La valeur de cavitation naissante dans ce cas-là est d'environ $NPSHi = 4,8m$. Tout d'abord, la cavitation survient sur le côté aspiration de la roue. Quand la valeur de NPSH baisse, la cavitation est présente principalement sur une grande surface du côté aspiration de la pale, plus près de carter. Quand les valeurs NPSH sont extrêmement faibles ($NPSH = 1,78m$), les poches de cavitation se forment

sur le côté pression de la pale également. Quand $NPSH = 1,78m$, la chute de pression parvient à 5% environ de la hauteur d'élévation nominale correspondant au débit et à l'ouverture de directrice considérés.

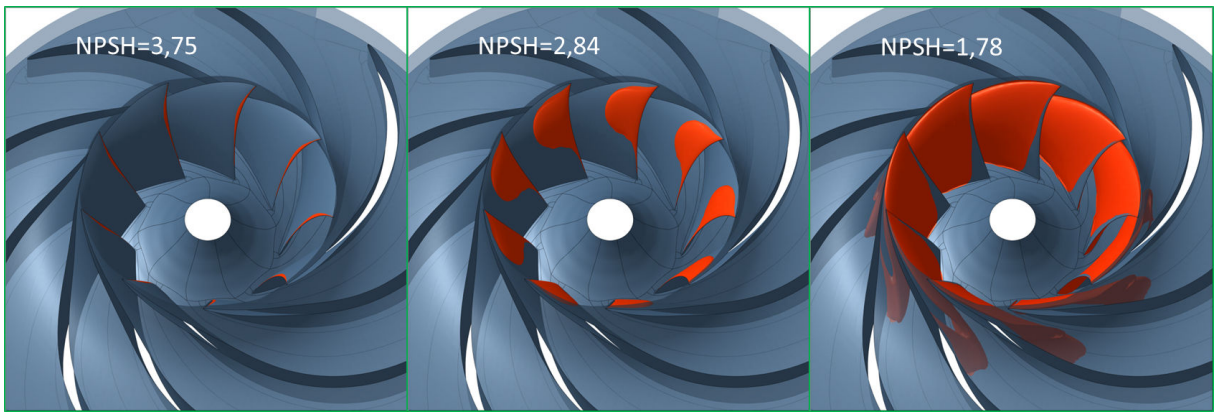

Figure B.14: Formes de cavitation de côté aspiration pour $\phi = 0,0348$ ($\alpha = 0,05$)

B.5.5 Influence de la cavitation sur le feston cadre

L'influence de cavitation sur le feston a été étudiée dans les mêmes conditions numériques et pour la même ouverture que dans les analyses de cavitation précédentes. La figure B.15 illustre la zone de feston sous conditions non-cavitantes, ainsi que sous conditions de cavitation relativement fortes (valeurs NPSH constantes). La courbe de performance pour l'ecoulement non-cavitatnt a été comparée aux deux courbes de performance à NPSH constant. Dans les deux cas ($NPSH = 2,7m$ et $NPSH = 2m$), les valeurs de NPSH ont un effet important sur le feston cadre.

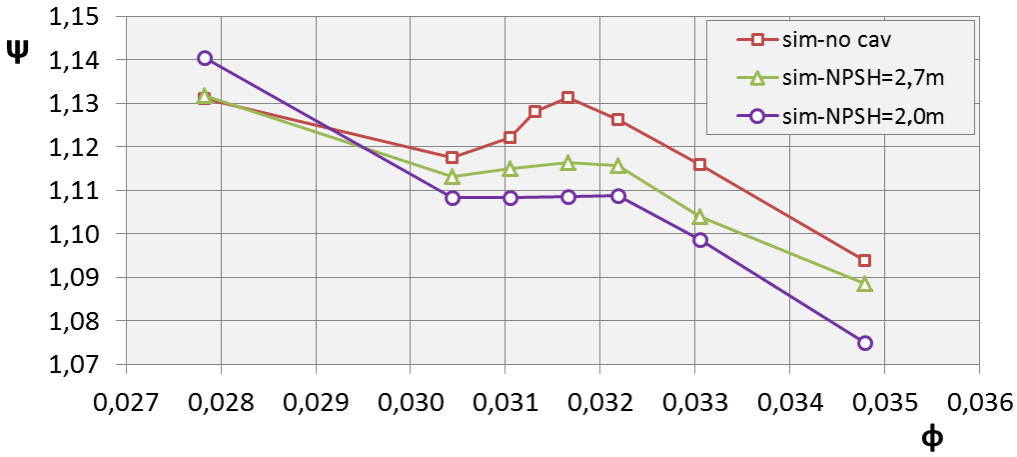

Figure B.15: Influence de la cavitation sur le feston cadre

La présence d'une cavitation forte réduit l'amplitude de feston et l'inclinaison positive dH/dQ n'est plus observée dans le cas des régimes de cavitation aux valeurs de $NPSH = 2,7m$ et $NPSH = 2m$. Comme déjà constaté, dans le cas de $\phi = 0,0278$ et $NPSH = 2m$, la performance s'améliore grâce aux conditions optimisées dans la roue.

On peut anticiper que les formes développées de cavitation causent des pertes plus importantes dans la roue, cependant, cela n'est pas évident dans le cas du distributeur. Les pertes dans le distributeur et la baisse de performance dans la roue ont été étudiées pour les points de fonctionnement cavitant ($NPSH = 2,7m$ et $NPSH = 2m$) et ont été comparées au régime non-cavitant (fig. B.16). Les valeurs négatives désignent l'augmentation des pertes ($\Delta\Psi$, fig. B.16).

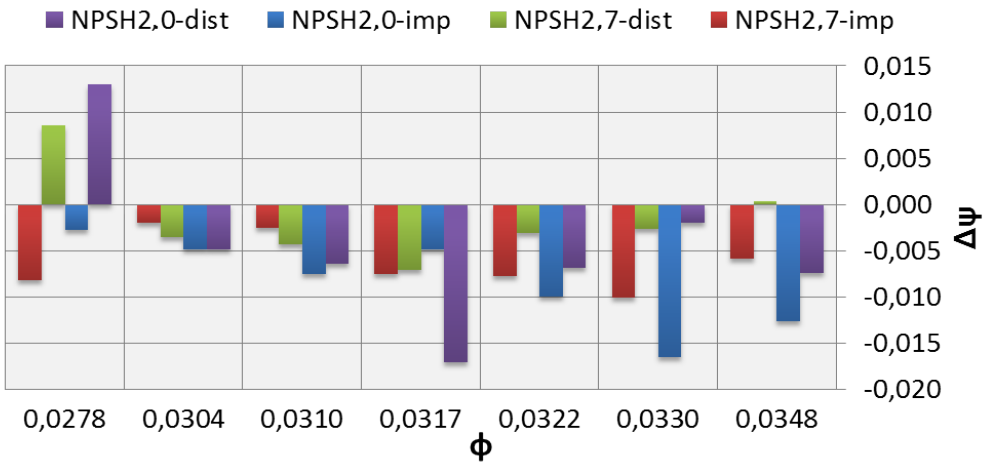

Figure B.16: Variations des pertes dans le distributeur et des performances de la roue dues à la cavitation, par rapport au régime non-cavitant

Les effets de la cavitation sur la performance sont plus considérables lorsque le débit est plus élevé. Quelques fois, à débit partiel ($\phi = 0,0278$), la présence de cavitation améliore la courbe de performance grâce aux meilleures conditions dans le distributeur, comme l'indique la figure B.16. En outre, l'analyse montre que dans la majorité des cas, la cavitation augmente les pertes dans la roue ainsi que dans le distributeur, bien que la cavitation se produise sur le bord d'attaque de la pale de la roue.

B.6 Analyse stationnaire à débit partiel

Tous les calculs analysés dans ce paragraphe sont stationnaires et non-cavitant. Les analyses se concentrent sur la prédiction globale de la position du feston, sur l'amplitude du feston et sur l'écoulement dans la zone du distributeur. L'analyse a servi à prédire les zones de fonctionnement stables, complètement instables et légèrement instables en fonction des ouvertures de distributeur et des débits considérés.

B.6.1 GV ouverture 14°

La ligne intitulée 'Sim-periodic 14°' (fig. B.17) comporte les calculs avec maillage périodique. La position de feston a été détectée avec une précision de 2% sur l'axe de débit. L'amplitude de chute parvient à plus ou moins 1% dans les deux cas - numérique ainsi que expérimentale. Il a été montré que la chute de performance dans le région de feston est liée aux pertes qui se produisissent à cause du comportement de l'écoulement à l'intérieur du distributeur.

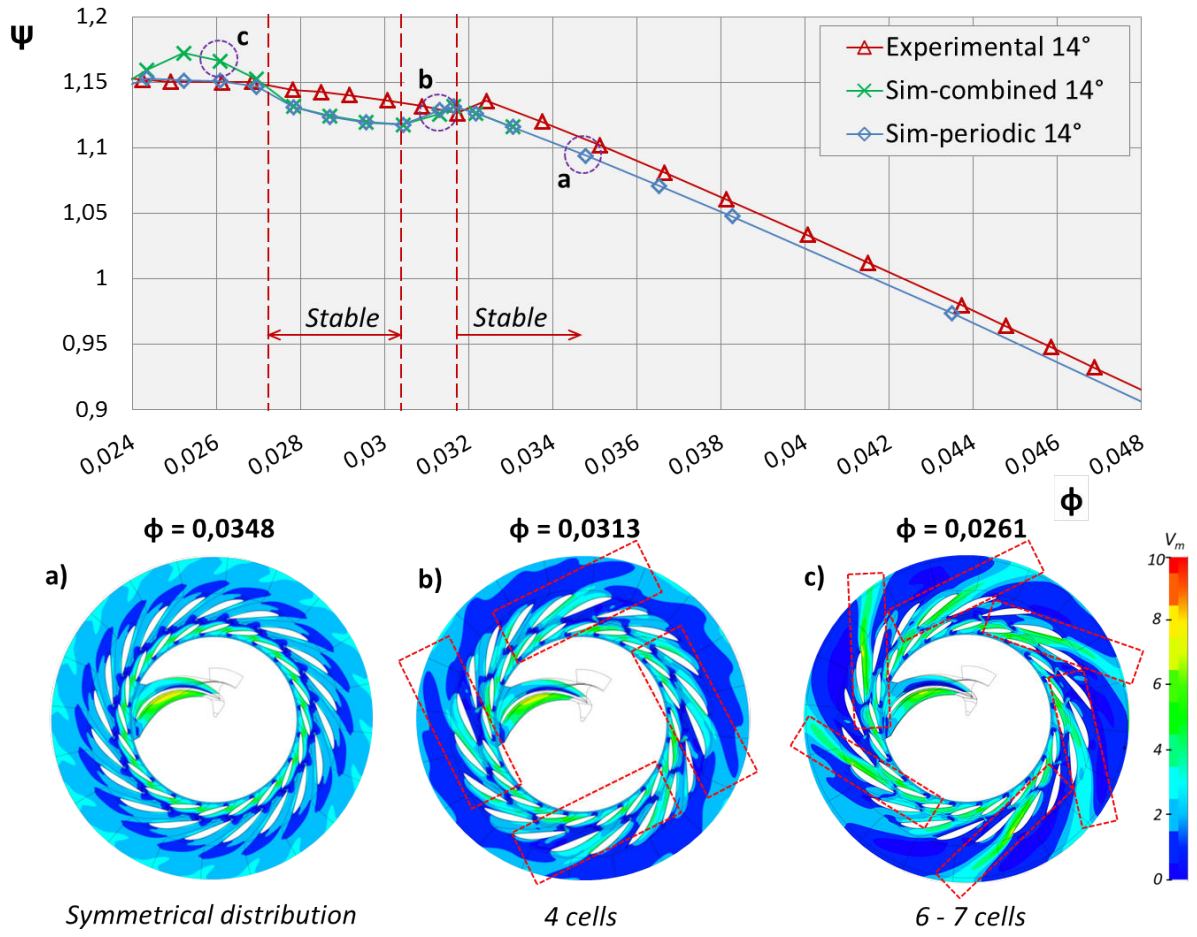

Figure B.17: Courbe de performance pour GV ouverture 14°; la géométrie GV I; analyse des configurations d'écoulement

Dans le but d'étudier les effets de conditions de périodicité, un maillage combiné (Sim-combined 14°, fig. B.17) a été créé en utilisant la périodicité dans la roue et un maillage complet dans directrice. La différence entre les résultats numériques se produit seulement à débits partiels lorsque les débits sont à environ $\phi = 0,025$. Plusieurs analyses des écoulements obtenus avec le maillage combiné ont été réalisées sur un plan de coupe à mi-envergure, comparant les distributions de vitesse méridienne. L'analyse a révélé une distribution symétrique de l'écoulement pour tous les débits supérieurs à $\phi = 0,0317$ (exemple a $\phi = 0,0348$, fig. B.17). En revanche, pour le débit partiel dans le zone du feston ($\phi = 0,0313$), l'instabilité se montre comme un écollement réparti asymétriquement, comme l'indique la figure B.17, exemple b. En outre, l'analyse de l'écollement indique quatre cellules de sous-débit à côté des régions de sur-débit. Ce phénomène détecté est lié à un phénomène instable de décollement tournant, qui sera présenté en détail dans le chapitre suivant.

En réduisant le débit, différents formes et nombres de cellules de décollement tournant peuvent être prédits. Dans la gamme $\phi = 0,0275$ et $\phi = 0,0304$, l'écoulement semble presque symétriquement distribué autour du distributeur. La performance est légèrement sous-estimée comme dans tous les cas de régime de fonctionnement stable. D'autre part, l'écollement semble être très instable quand la valeur est inférieure à $\phi = 0,027$, ce qui se traduit en 5 à 7 cellules de sur-débit (exemple c, $\phi = 0,0261$, fig. B.17).

Les régions stables sont marquées sur la figure B.17. La stabilité est définie comme une distribution symétrique de l'écollement dans les régions de directrice et avant-directrice. Les régions de fonctionnement qui ne sont pas marquées comme stables sont considérées instables. Il est donc fort probable que le décollement tournant se produira dans ces régions instables. Les résultats stationnaires calculés sur maillage combiné surestime la performance aux points fortement instables ($\phi < 0,028$). Des calculs instationnaires devraient être effectués pour ces points, vu que l'instabilité de l'écollement dans le distributeur joue un rôle important dans la prédiction des pertes dans cette partie de la machine.

B.7 Analyse du décollement tournant

Nous avons obtenus les résultats ci-dessous en effectuant des simulations instationnaires sur la géométrie complète en le régime non-cavitant. Entre 2 et 3 tours de roue ont été nécessaires pour stabiliser les calculs, et puis environ 10 à 15 révolutions ont été effectuées pour analyser le phénomène de décollement tournant. Les comportements et les caractéristiques des écoulements instables tels que la fréquence et l'intensité de décollement tournant ont été étudiés et analysés. Dans le but d'étudier ces phénomènes d'instabilité, une analyse détaillée de ecoulement local pour le débit $\phi = 0,0313$ et l'ouverture de 14°, a été réalisée.

B.7.1 Résultats globaux 14°

Nous avons comparé les résultats instables globaux pour l'ouverture GV de 14° aux données expérimentales et aux simulations stationnaires présentées ci-dessus, comme le montre la figure B.18. En plus, nous pouvons voir que les résultats stationnaires sur la géométrie compléte ne diffèrent pas des résultats stationnaires sur le maillage combiné. Cela indique que dans le cas de l'ouverture et la géométries considérées, la périodicité dans la région de roue peut être appliquée pour les simulations stationnaires. Les résultats instationnaires révèlent une amélioration importante de la prédiction de la courbe de performance par rapport aux simulations stationnaires. Par ailleurs, la comparaison entre les données expérimentales et les simulations instables indique un très bon accord dans les deux régions de fonctionnement, stable ainsi qu'instable.

Dans la zone du feston (fig. B.18b; $\phi = 0,0313$), quatre cellules de sur-débit et sous-débit ont été observées. Les cellules semblent plus développées que dans le cas des simulations stationnaires. La fréquence de rotation des cellules est d'environ 3,5% de la fréquence de rotation de la turbine-pompe (tab. B.3). Les fluctuations d'énergie spécifiques pour ce débit atteignent environ $\pm 0,5\%$ et indiquent un point de fonctionnement instable, potentiellement dangereux.

Alors que le débit continue à décroître, nous pouvons observer huit cellules de décollement tournant à $\phi = 0,0296$. La fréquence de décollement tournant est inférieure par rapport à $\phi = 0,0313$ et parvient à environ 2% de la fréquence de fonctionnement (fig. B.18c; tab.B.3). En outre, les cellules paraissent moins intenses dans ce cas-là et la performance ne fluctue pas. En comparaison aux simulations stationnaires sur le maillage combiné (fig. B.17), le comportement est un peu plus instable quand le flux est à $\phi = 0,0296$. Cela est le cas dans la plupart de points de fonctionnement.

L'écoulement devient encore plus instable au débit très faible de $\phi = 0,0261$. Trois cellules de décollement tournant peuvent être observées (fig. B.18d). La fréquence de

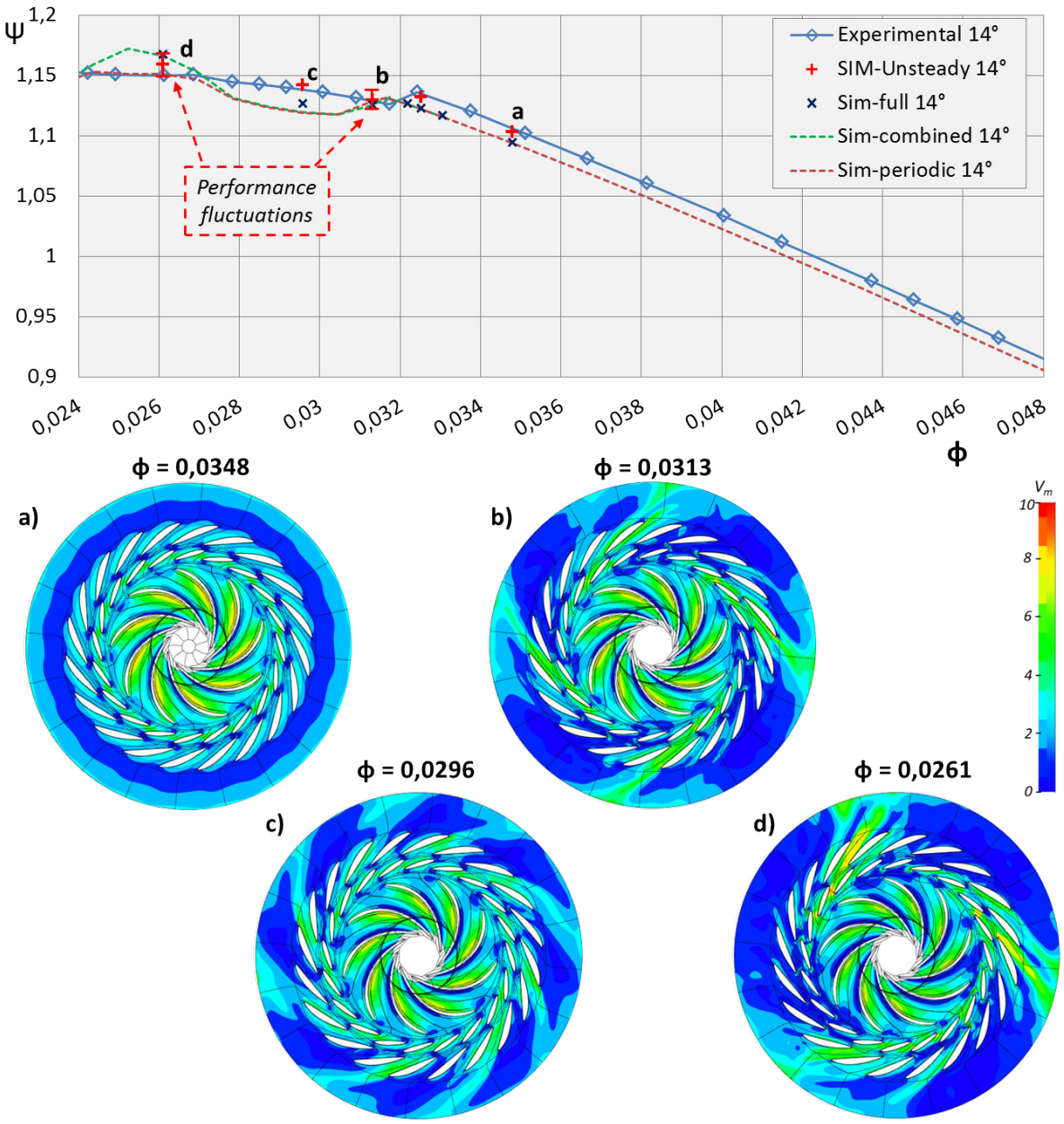

Figure B.18: Courbe de performance pour GV ouverture 14°, analyse du décollement tournant

Débit	N° des cellules	Fréquence	Intensité
$\Phi = 0,0348$	/	/	0
$\Phi = 0,0325$	/	/	0
$\Phi = 0,0313$	4	3,5%	++
$\Phi = 0,0296$	8	2%	+
$\Phi = 0,0261$	3	5,5%	+++

Table B.3: Cellules de décollement tournant, la fréquence and l'intensité pour ouverture 14°

décollement tournant parvient à 5,5% de la fréquence de fonctionnement de la turbine-pompe. La fluctuation du coefficient d'énergie spécifique ϕ atteint environ $\pm 0,5\%$, ce qui

est un autre indicateur d'un point de fonctionnement fortement instable. Les simulations stationnaires pour ce débit ont abouti à un nombre plus élevé et de cellules décollées de format réduit. Cela confirme les conclusions générales que les simulations instationnaires sur la géométrie complet prédisent des écoulements légèrement plus instables. Ils sont donc nécessaires pour une prédiction précise du décollement tournant.

B.7.2 Évolution du décollement tournant

L'évolution du décollement tournant peut être décrite de manière simplifiée comme une décomposition des cellules bloquées.

- **Phase 1.** Le débit augmente dans le canal en raison de conditions favorables, telles que la basse pression au milieu du canal et angle d'attaque adapté aux GV. Il atteint progressivement la valeur maximale de l'ordre de 130% du débit nominal à travers le canal.

- **Phase 2.** L'angle d'attaque à l'entrée du canal (décrit à l'aide des vecteurs de vitesse) commence à tourner doucement vers le canal aval. Entre temps, la pression statique dans le canal commence à augmenter, ce qui provoque une gradient de pression adverse forte entre le milieu du canal et la région près du bord d'attaque de la prochaine GV sur le côté pression de l'aube. Cela aboutit à une forte séparation de l'écoulement dans le canal, à la croissance de la zone de séparation et à la déviation de l'écoulement vers le canal aval. Le débit diminue d'abord au milieu du canal et baisse ensuite sur le moyeu et carter du canal, provoquant une réduction supplémentaire de débit à environ 45% du débit nominal.

- **Phase 3.** Gradient de pression adverse commence à diminuer conjointement avec la zone de recirculation, entraînant progressivement des conditions plus favorables et en augmentant le débit dans le canal. La cellule bloquée se déplace vers canal aval, ce qui entraine une augmentation supplémentaire de débit dans le canal.

B.8 Conclusions

Des outils de calcul ont été utilisés dans le travail ci-présent pour prédire et analyser des instabilities en mode pompage. Toutes les simulations décrites ont été effectuées au LEGI avec au maximum 12 processeurs, ce qui constitue aujourd'hui une puissance de calcul largement accessible.

Le premier objectif du projet a été de réaliser et de développer des simulations des phénomènes de cavitation dans la géométrie de turbine-pompe considérée. Les calculs stationnaires sur maillage périodique ont été réalisés pour différents débits et valeurs de NPSH. Même dans le cas des points de fonctionnement hors nominaux et fortement instables, nous avons obtenu des résultats fiables. Les données expérimentales (bien que limitées) s'accordent bien avec les simulations. Le code est capable de prédire avec précision les valeurs de cavitation naissante, les courbes de NPSH et les formes de cavitation moyennes avec de temps de calcul raisonnables (20 heures CPU au maximum).

Les simulations stationnaires offrent un bon aperçu de la stabilité des points de fonctionnement. Des maillage du type 'combiné' peuvent également être appliqués aux analyses de décollement tournant dans le distributeur. Les points de fonctionnement stables,

légèrement instables et fortement instables peuvent être détectés en utilisant cette approche. Cela constitue une solution de compromis entre des simulations instationnaires plus coûteuses sur la géométrie complète et des simulations stationnaires sur le maillage périodique. L'auteur souligne le besoin d'une attention particulière sur la modélisation des interactions entre le roue et le distributeur lorsque les jeux entre la roue et le distributeur sont relativement faibles et les points de fonctionnement sont à débits partiels.

Les résultats obtenus par les simulations instationnaires, en utilisant les équations URANS, se comparent bien aux résultats dans la littérature. D'ailleurs, ils prouvent que les outils CFD peuvent être très exacts en prédisant la performance, même dans des conditions hors nominales, par exemple adèbit partiel. En outre, des simulations CFD nous donnent un aperçu détaillé des écoulements dans la machine qui nécessitent des études expérimentales très exigeantes, quelques fois même impossibles à réaliser.

Les décollement tournants peuvent être caractérisés par de formes et intensités diverses. Le nombre ainsi que la fréquence du décollement tournant peuvent varier. Bien que cela doive être confirmé par des expériences, il semble que le nombre faible de cellules indique une fréquence de décollement tournant plus élevée. Par conséquent, un tel point de fonctionnement semble être plus dangereux pour la machine. L'analyse de l'écoulement local montre que le décollement tournant peut être décrit par l'augmentation ou la décomposition de cellules bloquées ainsi que par la rotation de ces cellules autour du distributeur. La forme de zones de recirculation et de séparation de l'écoulement, qui changent complètement les conditions au bord d'attaque des directrices sont les paramètres qui jouent le rôle le plus important sur l'evolution du décollement tournant. Les champs de pression, en particulier la direction et la magnitude du gradient pression adverse, entraînent une déviation de l'écoulement vers canal aval et causent ce que l'on appelle la rotation de cellules. Tenant compte de tous les mécanismes de décollement tournant mentionnés, nous pouvons souligner plusieurs façons possibles de modifier les effets du décollement tournant:

- Diminution/augementation de l'angle d'ouverture des directrices
- Modification de la géométrie de directrices
- Réduction du jeu roue-distributeur
- Modification de la géométrie de la roue

B.9 Perspectives

Premièrement, des expériences devraient être effectuées pour que la précision de simulations numériques présentées puisse être évaluée. L'exactitude de la fréquence de décollement tournant et le nombre de cellules devraient être validés par mesures expérimentales pour la même géométrie dans les mêmes conditions de fonctionnement.

Les résultats présentés, particulièrement les calculs instationnaires, offrent des grandes possibilités pour le développement d'un outil général et accessible qui donnerait des résultats fiables pour une large gamme de débits, même dans des conditions de fonctionnement hors nominales, avec l'apparition de la cavitation et de décollement tournant. Pour y parvenir, des simulations instationnaires pourraient être effectuées également sous des conditions de cavitation.

Finalement, l'idée principale de cette étude était d'étudier le feston cadre et le décollement tournant dans le but de minimaliser leurs effets sur la performance de turbine-pompe. Les outils numériques maintenant disponibles peuvent être utilisés pour toute géométrie exposée au problème de décollements tournants. Des études supplémentaires du point de vue industriel et/ou académique devraient être réalisées afin de proposer des solutions pratiques pour réduire ou éliminer les effets négatifs de décollement tournant sur les performances et la stabilité de machines hydrauliques.